High Quality Colloidal Crystals with Different Architectures and their Optical Properties

Dissertation zur Erlangung des Grades
„Doktor der Naturwissenschaften“
am Fachbereich Chemie, Pharmazie und Geowissenschaften
der Johannes Gutenberg-Universität in Mainz

vorgelegt von

Jianhui Ye

geboren
in Jiangsu, V. R. China

Mainz 2006

Contents

1. Introduction

Photonic crystals are a class of materials with a periodic varying refractive index. Such materials can create a range of 'forbidden' frequencies called a photonic bandgap (PBG), and then they are well known as PBG materials. Photons with energies lying in the bandgap cannot propagate through the medium. This provides the opportunity to shape and mould the flow of light for photonic information technology.[1] The concept of this new class of material was first proposed independently by Yablonovich[2] and John in 1987,[3] and since then a huge effort has been devoted to developing materials and structures that could support and expand their initial hypotheses. A wide variety of applications has been envisioned or demonstrated for these materials.

The photonic crystal can be thought of as optical analogue of the semiconductor. In a semiconductor the atomic lattice presents a periodic potential to an electron propagating through the electronic crystal. Moreover, the geometry of the lattice and the strength of the potential are such that, owing to Bragg-like diffraction from the atoms, a gap in allowed energies opens up for which an electron is forbidden to propagate in any direction. In a photonic crystal, the periodic 'potential' is due to a lattice of macroscopic dielectric media instead of atoms. If the dielectric constants of the constituent media are different enough, Bragg scattering off the dielectric interfaces can produce many of the same phenomena for photons as the atomic potential does for electrons.[1] Just as Bragg diffraction of electrons in silicon atomic lattices enabled electronic devices like the transistor and gave birth to the microelectronics revolution. Bragg diffraction of photons in dielectric lattices is leading to photonic crystal devices poised to ignite a microphotonics revolution.[4]

Photonic crystals offer a completely new way to confine, control, and manipulate photons in all of space: for example, to block the propagation of photons irrespective of their polarization or direction; to localize photons to a specific area at restricted frequencies; to inhibit the spontaneous emission of an excited chromophore; to modulate or control stimulated emission; and to serve as a lossless waveguide to direct the propagation of photons along a specific direction[1,5,6]. All of these properties are important for optoelectronic applications. They can be exploited, in principle, to produce light-emitting diodes (LEDs) that display coherence properties, to fabricate thresholdless semiconductor diode lasers, and significantly to enhance the performance of many other types of optical, electro-optical, and quantum electronic devices.[7]

The periodic structure of photonic crystals has been demonstrated in nature. The most prominent feature of such structures is that they present iridescences as a result of diffraction. Some natural examples are the multilayered structure of pearls, the flashing wings of several insects,[8] and natural opals.[9] The same effect appears in familiar man-made objects such as compact discs. However, while the periodic arrangement of atoms occurs naturally in semiconductors, photonic crystals need to be fabricated artificially. It is noted that the lattice constant of the photonic crystal must be comparable to the wavelength of the light. For the optoelectronics industry, for instance, where the usual operating frequency is around 1.5 μm (in the infrared), the lattice constant of useful photonic crystal must be of the order of 0.5 μm, therefore, the photonic crystals that work in the microwave and far-infrared regions are relatively easy to fabricate. Those that work for wavelengths shorter than near-infrared, especially 3D ones are difficult to fabricate because of their small lattice constants. To appreciate fully the challenge of fabricating these structures, various technologies have been developed. For their idiosyncratic nature, colloidal systems lend themselves to be used as natural starting points for the purpose of creating and using photonic crystals, and, as such, occupy still an important place in current research in this field now.

This work focuses on the fabrication and characterization of functional 3D photonic crystals based on colloidal systems. Such materials can serve as models for investigating the properties of photonic crystals which are important for photonic technology.

1.1 Background

The description of light in photonic crystals involves the solution of Maxwell's equations in a periodic dielectric medium. Generally, all of macroscopic electromagnetism, including the propagation of light in a photonic crystal, is governed by the four macroscopic Maxwell equations. They are[10]

$$\nabla\cdot\mathbf{B}=0 \qquad \nabla\times\mathbf{E}+\frac{1}{c}\frac{\partial\mathbf{B}}{\partial t}=0$$

$$\nabla\cdot\mathbf{D}=4\pi\rho \quad \nabla\times\mathbf{H}-\frac{1}{\mathrm{c}}\frac{\partial\mathbf{D}}{\partial t}=\frac{4\pi}{c}\mathbf{J} \tag{1}$$

where (respectively) **E** and **H** are the macroscopic electric and magnetic fields. **D** and **B** are the displacement and magnetic induction field, ρ and **J** are the free charges and currents, and c is the speed of light.

In the absence of free charges and the electric current, in addition the following assumptions are permitted:

- The field strengths are small enough so that the system is in the linear regime.
- The material is macroscopic and isotropic, so that the electric field **E** and the displacement **D** are related by a scalar dielectric constant ε.
- The magnetic permeability of dielectric materials is very close to unity, **B** = **H**.
- The dielectric constant ε is real, isotropic, perfectly periodic with respect to the spatial coordinate **r**, and does not depend on frequency. The periodicity of $\varepsilon(\mathbf{r})$ implies

$$\varepsilon(\mathbf{r}+\mathbf{a}_{\mathrm{i}})=\varepsilon(\mathbf{r}) \qquad (i=1,2,3) \tag{2}$$

where $\{\mathbf{a_i}\}$ is the elementary lattice vector. Because of this spatial periodicity, $\varepsilon^{-1}(\mathbf{r})$ can be expanded in a Fourier series

$$\frac{1}{\varepsilon(\mathbf{r})}=\sum_{\mathbf{G}}\kappa(\mathbf{G})\exp(i\mathbf{G}\cdot\mathbf{r}) \tag{3}$$

where $\{\mathbf{G}\}$ is the reciprocal lattice vector.

With all of these assumptions in place, after a little manipulation, the Maxwell equation can be then reduced to a wave equation of the form:

$$\nabla\times\left[\frac{1}{\varepsilon(\mathbf{r})}\nabla\times\mathbf{H}(\mathbf{r})\right]=\frac{\omega^2}{c^2}\mathbf{H}(\mathbf{r}) \tag{4}$$

which is an eigenvalue problem for **H**(**r**), the magnetic field, where ω is the eigen-angular frequency. It can be shown that the operator acting on the **H**(**r**) field ($\Theta=\nabla\times[\frac{1}{\varepsilon(r)}\nabla\times\ ]$) is Hermitian, and as a consequence, its eigenvalues are real and positive. Since $\varepsilon(\mathbf{r})$ is periodic, Bloch's theorem can be used.[11] **H** (**r**) are thus characterized by a wave vector **k** in the first Brillouin zone and a band index n and expressed as

$$\mathbf{H}(\mathbf{r}) = \mathbf{H}_{\mathbf{k}\mathrm{n}}(\mathbf{r}) = \mathbf{v}_{\mathbf{k}n}(\mathbf{r})e^{i\mathbf{k}\cdot\mathbf{r}} \qquad (5)$$

where v_{kn} (**r**) stands for periodic vectorial functions that satisfy the following relation:

$$\mathbf{v}_{\mathbf{k}n}(\mathbf{r}+\mathbf{a}_i) = \mathbf{v}_{\mathbf{k}n}(\mathbf{r}) \qquad (i = 1, 2, 3) \qquad (6)$$

Hence, it can be expanded in Fourier series. As a result, (5) is modified to

$$\mathbf{H}_{\mathbf{k}n}(\mathbf{r}) = \sum_{\mathbf{G}} \mathbf{H}_{\mathbf{k}n}(\mathbf{G}) \exp\{i(\mathbf{k}+\mathbf{G})\cdot\mathbf{r}\} \qquad (7)$$

where $\{\mathbf{H}_{\mathbf{k}\mathrm{n}}(\mathbf{G})\}$ is the Fourier coefficients in reciprocal lattice space. Substituting (3) and (7) into (4), the following eigenvalue equation for the expansion coefficient $\{\mathbf{H}_{\mathbf{k}\mathrm{n}}(\mathbf{G})\}$ is obtained:

$$-\sum_{\mathbf{G}'} \kappa(\mathbf{G}-\mathbf{G}')(\mathbf{k}+\mathbf{G}) \times \{(\mathbf{k}+\mathbf{G}') \times \mathbf{H}_{\mathbf{k}n}(\mathbf{G}')\} = \frac{\omega_{\mathbf{k}n}^2}{c^2} \mathbf{H}_{\mathbf{k}n}(\mathbf{G}) \quad (8)$$

where $\omega_{\mathbf{k}\mathrm{n}}$ is the eigen-angular frequency of $\mathbf{H}_{\mathbf{k}\mathrm{n}}$ (**r**). By solving this equation numerically, the dispersion relation of the eigenmodes, or the photonic band structure can be obtained.

This is universally acknowledged to be the correct description of the photon states in a periodic medium. An appealing aspect of Maxwell's equations is that they can be solved exactly. This means that theoretical computations can provide very accurate descriptions and predications of the properties of photons and therefore be very useful and complementary to experimental investigations. Another appealing aspect of Maxwell's equations is that there is no fundamental length scale. If we ignore changes in the dielectric function with frequency, a photonic crystal designed at one length scale will have the same fractional gap as the crystal at any other length scale.

The theoretical calculation of the photonic band structure can be confirmed by experimental measurements, for example, by transmission or reflection measurements. In Figure 1.1[12] is a dispersion diagram from a photonic crystal made of silica spheres in a compact face centered cubic (fcc) structure. The abscissa represents the wave vector in the first Brillouin zone of 3D dimension. The ordinate represents energy measured in units: a/λ, where a is the lattice parameter. For these structures the lattice parameter is given by $a = \sqrt{2}D$, where D is the sphere diameter.

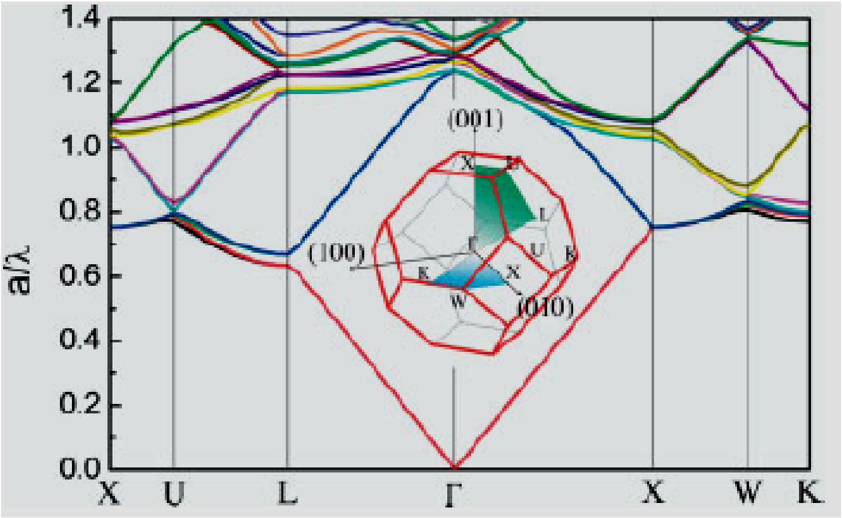

Figure 1.1. Dispersion relation for a photonic crystal made of silica spheres in a compact face centered cubic (fcc) structure.[12]

1.2 1D, 2D, and 3D Photonic Crystals and their Applications

Photonic crystals are classified mainly into three categories, i.e., one-dimensional (1D), two-dimensional (2D), and three-dimensional (3D) crystals. Fig. 1.2[10] shows the simple examples of 1D, 2D, and 3D photonic crystals. The different colors represent materials with different dielectric constants and demonstrate the periodicity of photonic crystals in one, two, or three directions.

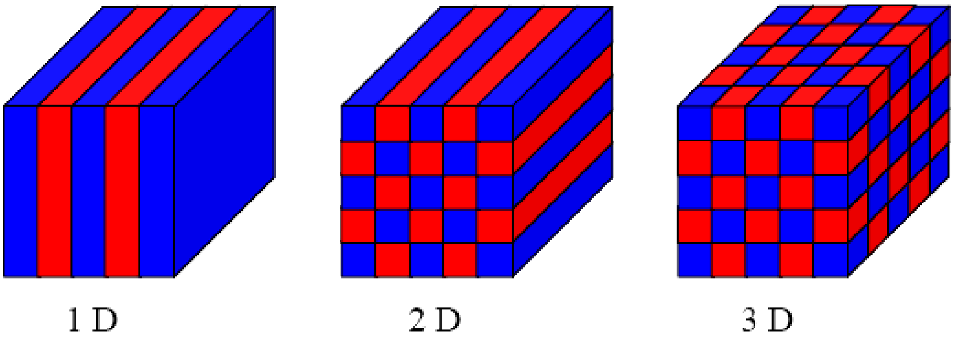

Figure 1.2. Schematic illustration of one-dimensional (1D), two-dimensional (2D), and three-dimensional (3D) photonic crystals. The defining feature of a photonic crystal is the periodicity of dielectric material along one or more axes.

1.2.1 1D Photonic Crystals

Dielectric mirrors (Bragg reflector) and interference filters were actually the 1D photonic crystal. However, they usually are not referred to as crystals because the name crystal is normally reserved for 2D or 3D structures. Typically, these 1D photonic crystals are prepared by layer-by-layer deposition of alternating materials with different reflective index (RI). For example, a layered stack of TiO_2/SiO_2 deposited by sputtering techniques can be used as an optical coating for windows. Recently 1D multilayer structure can be also realized by using the method of layer by layer electrostatic assembly of polyelectrolytes combined with the in situ synthesis of inorganic nanoparticles. Using this technique can lead to the formation of 1D structures with tuned morphologic (thickness) and dielectric properties (RI contrast).[13]

However, there are two problems with simple dielectric filters or mirrors for use in micro-optoelectronics.[14] First, for an angle of incidence greater than a critical angle, light whose frequency lies in the bandgap of the 1D crystal can penetrate through the film (except for omnidirectional reflectors, which consist of very high index material[15]). Second, there is no guidance of the light, which lies energetically outside the photonic bandgap or within a defect band.

1.2.2 2D Photonic Crystals

2D photonic crystal is periodic along two of its axes and homogeneous along the third. This can be realized, for example, by cylindrical holes from air in a high refractive material, or rods in the air periodically arranged parallel to one another. In this case, the dielectric function varies periodically in xy-plane but is independent of the position along the z-axis. The lattice parameter of this photonic crystal can be varied by changing the diameters of tubes or rods.[14,16,17,18] This 2D photonic crystal can have a photonic band gap in the plane. Inside this gap, no light propagation is permitted and incident light is reflected. While the 1D photonic crystal only reflects light at normal incidence, this 2D photonic crystal can reflect light incident from any direction in the plane. In Fig. 1.3 are examples of the realized 2D photonic crystals. In Fig. 1.3 (left)[14] are hexagonal ordered pores made from etched silicon wafer. The pore separation is 1.5 µm and the height of the porous is 100 µm. In Fig. 1.3 (right)[19] are PMMA tubes with long-range hexagonal order obtained by wetting of a macroporous silicon pore. These tubes were arrayed after complete removal of the template.

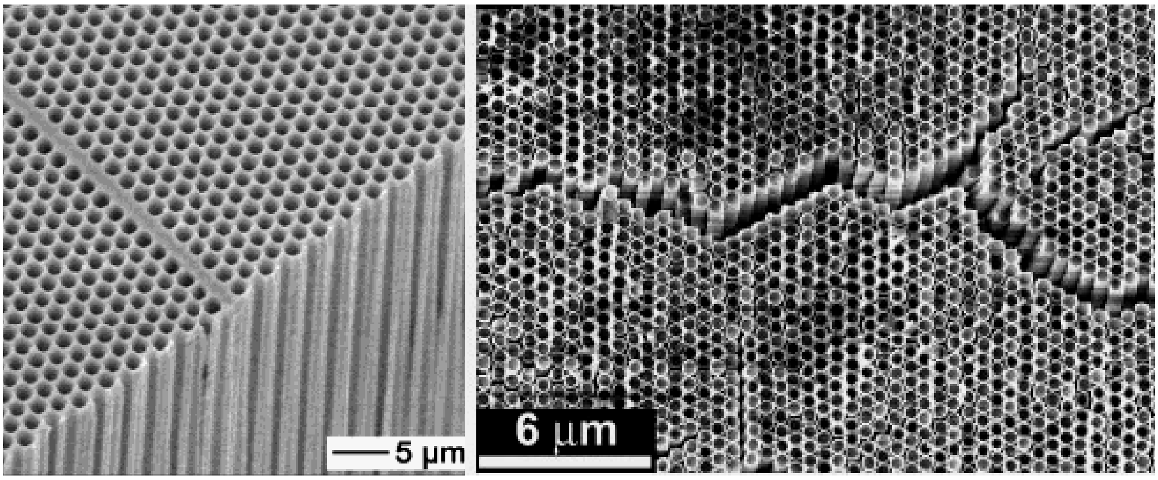

Figure 1.3. Examples of 2D photonic crystals. Left: Pore formed in macroporous silicon with the separation of 1.5 µm and the height of 100 µm[14]; right: PMMA tubes obtained by wetting of a macroporous silicon pore.[19]

Lehmann's group at Siemens Corp[20] has developed a process of fabrication of 2D photonic crystals by growing electrochemically ordered macropores in silicon. The structures obtained with this method for the first time showed a complete 2D bandgap in the near-infrared (near-IR) at a wavelength of about 4.9 µm. The fabrication of 2D photonic crystals has experienced the greatest development, mainly boosted by using microelectronic technology techniques, such as photolithography, electron beam lithography, etc. They are used more and more often for microphotonic applications.

1.2.3 3D Photonic Crystals

1D and 2D systems do not possess a complete photonic bandgap. A complete gap, a range of frequencies for which light propagation is completely forbidden in any directions, is defined as one that extends throughout the entire Brillouin zone in the photonic band structure.[10] It is only possible to realize in a 3D system. However, the evolution of a full bandgap strongly depends on the crystal structure as well the dielectric contrast. Although the band structure of classical scalar waves readily yields complete three-dimensional gaps for simple structures such as a face centered cubic lattice of spherical scatters,[21] the vector nature of the electromagnetic wave equation leads to much more restrictive conditions on the dielectric microstructure for the formation of a photonic bandgap.[22] The breakthrough came from the theoretical group at Iowa State University.[23] They discovered a complete photonic bandgap for an arrangement of photonic atoms in diamond structure, an fcc structure with a two-atom basis, which lifts the polarization degeneracy of the one-atom fcc structure.

The first-fabricated photonic crystal that possessed a complete bandgap for microwave frequencies was manufactured by the group of Yablonovitch[24] and which is now known as "Yablonovite" (Fig. 1.4). It was fabricated by simply drilling cylindrical holes in a bulk dielectric material (with a refractive index of 3.5). Since then, numerous structures amenable to layer by layer fabrication and drilling that possess complete PBG have been suggested.[25,26,27,28] A number of structures have already been fabricated with PBGs in the range of millimeter waves.[29] These structures have interesting applications[22] in the microwave to millimeter wave range. For instance, an antenna mounted on a conventional dielectric constant substrate radiates the majority of its radiation into the substrate itself. If the substrate is engineered into the form of a PBG material with a gap at the radiation frequency, the losses can be minimized, leading to highly directional transmitters.[30,31] Other applications include angular filters[32] and cladding material for preventing losses in waveguide structures that contain bends or junctions.[33,34,35]

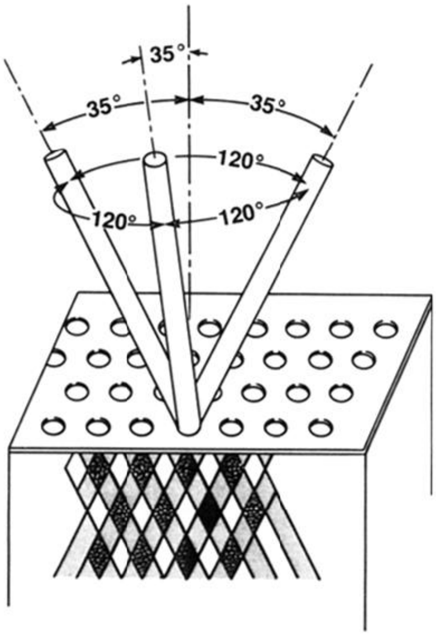

Figure 1.4. Scheme of production of Yablonovite

The biggest disadvantage of a “Yablonovite” was that it could not be miniaturized easily. Another structure that is easier to miniaturize than the “Yablonvite” is the so-called “Lincoln-log” or “Woodpile” structure (Fig. 1.5 left).[36] This structure resembles a stack of wooden logs in parallel orientation to each layer. Within each layer, SiO_2 was first deposited, patterned, and etched, in such a way that two successive layers are oriented perpendicular to each other. The resulting trenches are then filled by poly-si layers and finally the SiO_2 is removed completely. This structure has been revealed as one of the best suited to sustain a complete photonic bandgap. The first of these crystals had a bandgap at a frequency of about 13 GHz (corresponding to a wavelength of about 2.3 cm). Nevertheless, applications in telecommunications may require the fabrication of large-scale 3D PBG materials with a gap centered around 1.5 µm. These applications may include the design of zero-threshold microlaser, light emitting diodes that exhibit coherence properties at the single photon level, subpicosecond optical switches, and all-optical transistors. The late fabricated crystals at Sandia National Laboratories[36] exhibit a bandgap at a wavelength of about 1.5 µm. However, the vertical extensions that have been achieved by using the above-mentioned method are rather small, consists of only five layers, i.e. 1.25 unit cells in the vertical direction. Instead of depositing each layer, Noda et al. have applied wafer-fusion technology on III-V semiconductor substrates (Fig. 1.5 right).[37] Using this technique, a stack of eight layers has been achieved, corresponding to two units cells in the vertical direction. Fig. 1.5 (right) shows the top view SEM image of 3D photonic crystal prepared via the Noda approach. The lattice constant a is 0.7 µm, resulting in a bandgap around 1.3 µm.

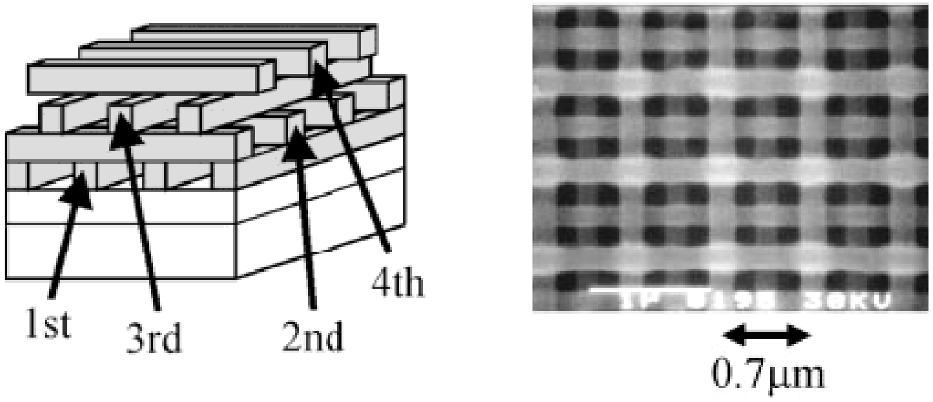

Figure 1.5. Left: Schematic drawing of one unit cell of the woodpile-structure 3D photonic crystal. Right: Top view SEM image of 3D photonic crystal prepared via the Noda approach. The lattice constant a is 0.7 µm, resulting in a bandgap around 1.3 µm.[37]

The development of new holographic lithography makes it possible to produce precise 3D photonic crystal structure in large-scalar.[38,39,40] For fabrication of the structures which possess a 3D periodic lattice four laser beams were used, while three beams produce a 2D pattern. This set-up applied to a photosensitive polymer can lead to a 3D network if the exposed polymer is crosslinked and the unexposed polymer is dissolved. Fig. 1.6 shows some examples made from this technology.[39] An unsatisfactory aspect of this technique is that the available photosensitive polymers have a low refractive index. This makes a second process of templated infiltration necessary for the enhancement of the dielectric contrast. Nanolithography is already widely used by the semiconductor industry and is an expensive, precise and painstaking step-by-step fabrication process. This technique enables the calculated construction of photonic crystal structures, defects and defect networks.

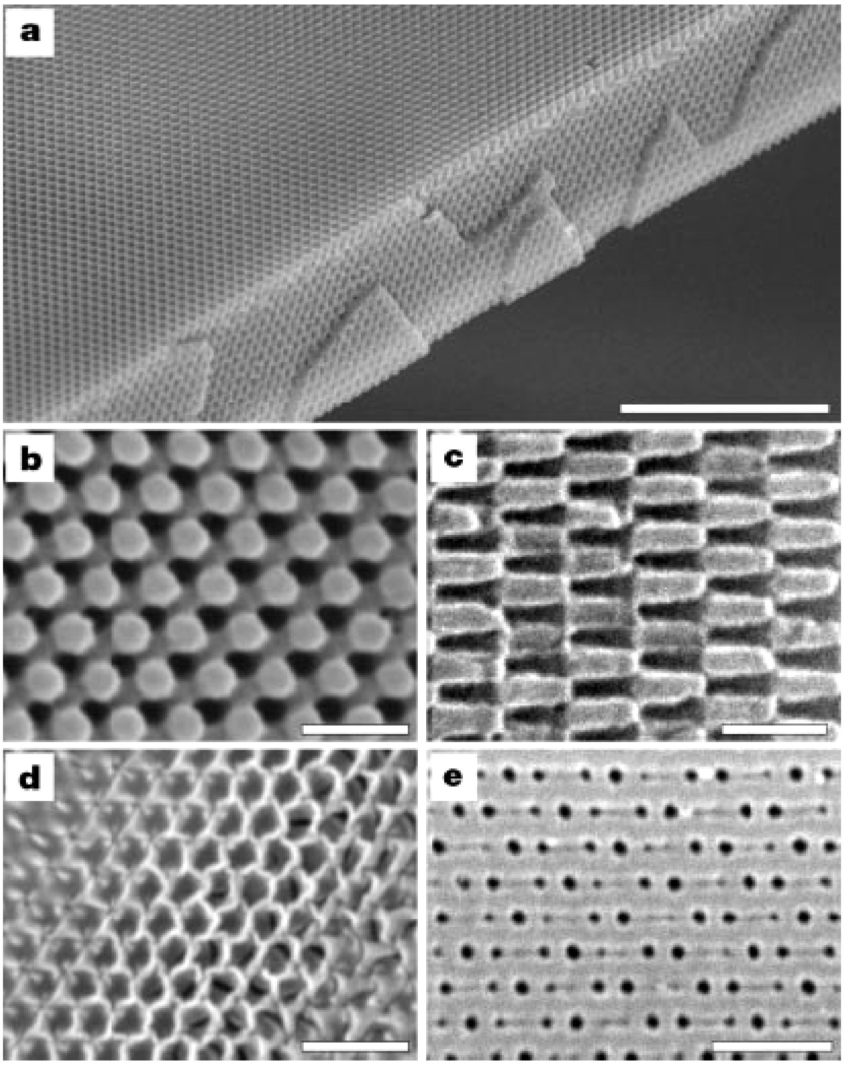

Figure 1.6. SEM pictures of different structure obtained by the holography technique.[39]

In comparison with nanolithography the spontaneous crystallization of colloids provides a much simpler, faster and cheaper way to obtain three-dimensionally periodic structure.[7,12,41] This approach involves the natural self-assembly of polymer or silica microspheres from colloidal suspension. They present the typical fingerprint of photonic crystals: they are iridescent (artificial opals). These synthetic opals offer a simple and easily prepared model system to probe experimentally the photonic band diagrams of certain types of 3D periodic structures and have inspired a whole branch of research in the photonic crystal field. Fig. 1.7 shows an example of poly(methyl methacrylate) (PMMA) opals from this work.

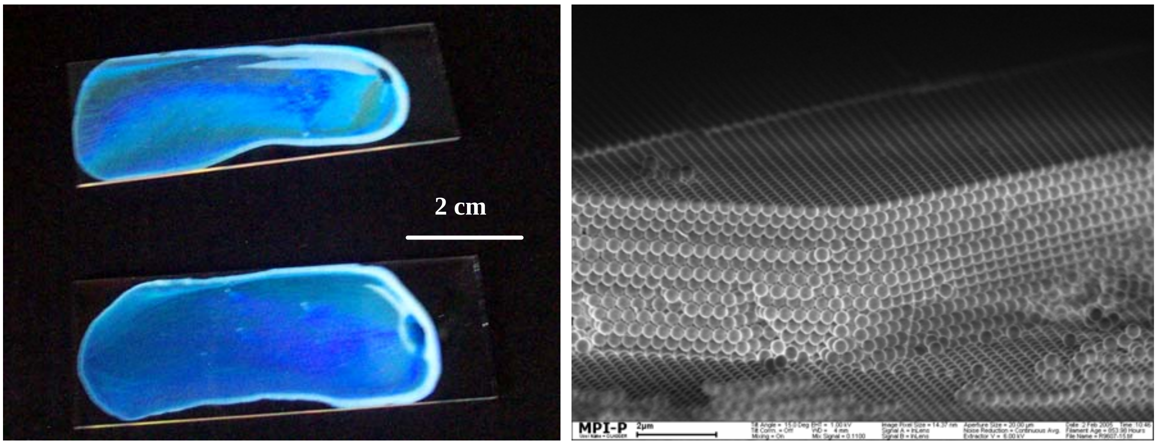

Figure 1.7. Opals fabricated from PMMA spheres of a diameter of 370 nm. Left: Optical microscopy. Right: SEM image.

Owing to the underlying structure present in these systems the colloidal crystals cannot possess a complete photonic bandgap. However, the inverse structure, the so-called inverse opal, does have a complete bandgap in the higher bands.[22] Fig. 1.8 presents the band structure and corresponding total photon density of states (DOS) of an inverted fcc structure consisting of close-packed air spheres in a silicon matrix with dielectric constant $\varepsilon \approx 11.9$. In Fig. 1.8 it is observed that the fcc structure possesses a pseudogap (stop gap) between the fourth and fifth bands around $\tilde{\omega} \approx 0.524$ and a complete 4.25% band gap between the eighth and ninth bands with a center frequency of $\tilde{\omega} \approx 0.794$. Therefore artificial opals can act as a template for construction of the photonic crystal. The template contains voids that can be infiltrated by material of high refractive index and then removal of the original template by wet etching or sintering leads to the desired photonic crystal structure. The group at the University of Toronto reported the first successful fabrication of silicon-based inverse opals with a complete 5% photonic bandgap relative to its center frequency for center frequencies at the telecommunication window around 1.5 µm.[42] Here, the voids of the artificial opal were almost completely filled with silicon by chemical vapor deposition process (CVD).[43,44] Fig. 1.9 shows an SEM image of such a photonic crystal with a lattice constant of about 0.5 µm. Theoretically calculation has been also demonstrated that it is possible to double the size of the inverse opal PBG by fine tuning the material's synthesis by, for example, careful sintering and control of the infiltration process.[22]

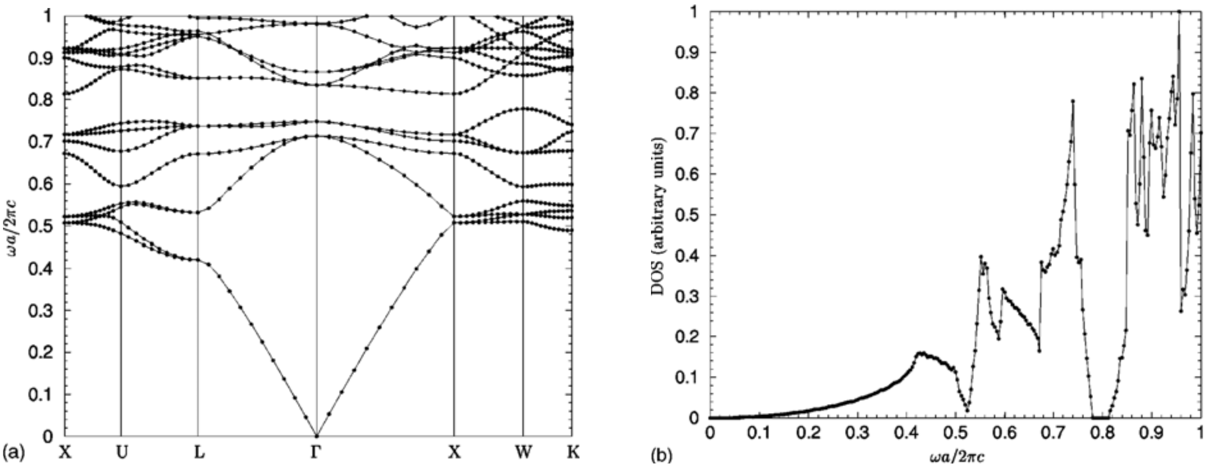

Figure 1.8. Band structure (a) and corresponding DOS (b) for a close-packed fcc lattice of air spheres in silicon ($\varepsilon \approx 11.9$).[22]

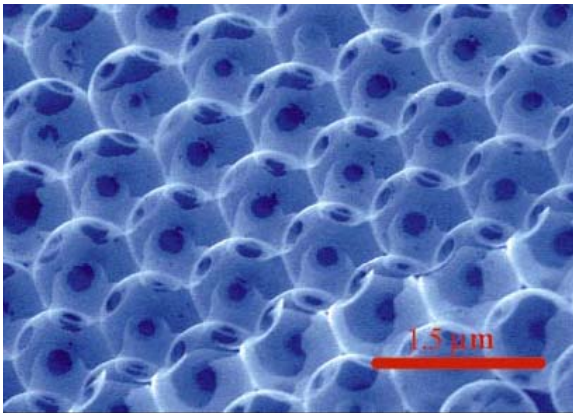

Figure 1.9. SEM image of spatially periodic structures that have been obtained by infiltrating an artificial opal with silicon and subsequent removal of the opal. The lattice constant is 500 nm.[42]

1.2.4 Functional Photonic Crystals

For the applications of 1D, 2D, and 3D photonic crystals, more interesting is the creation of photonic crystals with intentional defects, in an otherwise perfect periodic structure that can allow light to be trapped in the vicinity of the defect while being excluded from the medium surrounding it. A defect, or mistake in the periodicity, could lead to localized photonic states in the gap, whose shapes and properties would be dictated by the nature of the defect.[1] A point-like defect could serve as a microcavity to localize light, a line-defect as a linear waveguide to guide light, a planar defect as planar waveguide, and so on.[10] These properties provide a new mechanism for moulding or controlling the properties of light. Herein lies some exciting potential of photonic crystals.

An interesting example of 1D system has been pursued by the group of Kimerling[45]. A waveguide with a diameter of about 0.5 μm was structured on a silicon-insulator (SOI) substrate using X-ray lithography to provide a periodic arrangement of holes (Fig. 1.10). They omitted one pore in the center, which acts optically as a resonator having a drastically increased electromagnetic field at the defect site.

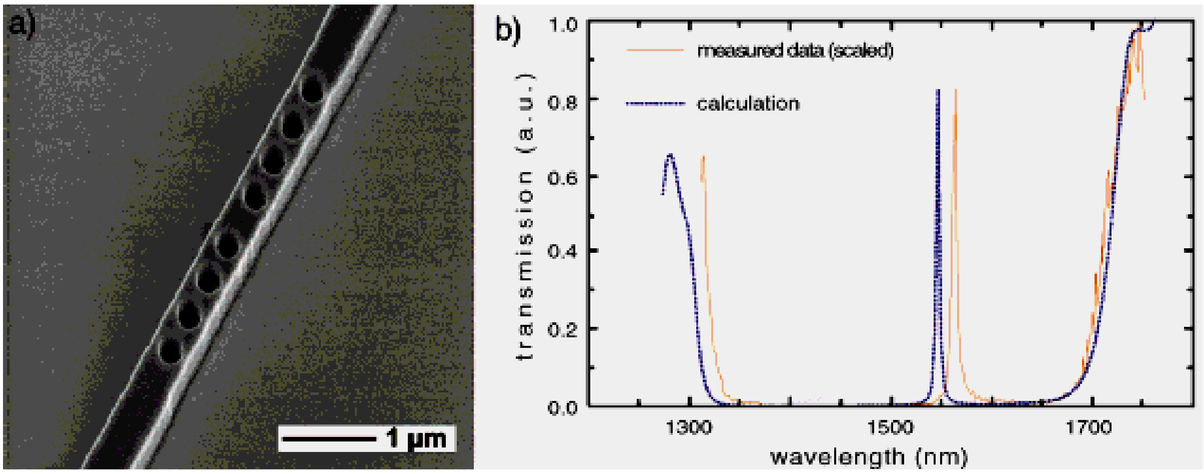

Figure 1.10. a) SEM image of a 1D waveguiding structure made of silicon. b) By incorporating holes at periodic distances one yields a resonator-like functioning of the waveguide, as was demonstrated by transmission calculations.[45]

A linear and bent waveguide structure could be fabricated, for example, by missing some pores of a 2D system, as shown in Fig. 1.11.[14] This can be realized, if some etch pits are omitted by using a suitable mask for the photolithography, the electronic holes that are generated at the back side through illumination are consumed by the neighbouring pores without influencing their position. Chaining together these missing pores, a rather perfect line structure can be produced and, under appropriate conditions, create defect modes with transmission bands inside the photonic bandgap. In addition, different defect structures, for instance, bent waveguide, Y-branch, and microresonator (Fig. 1.11), have been realized by using this procedure.

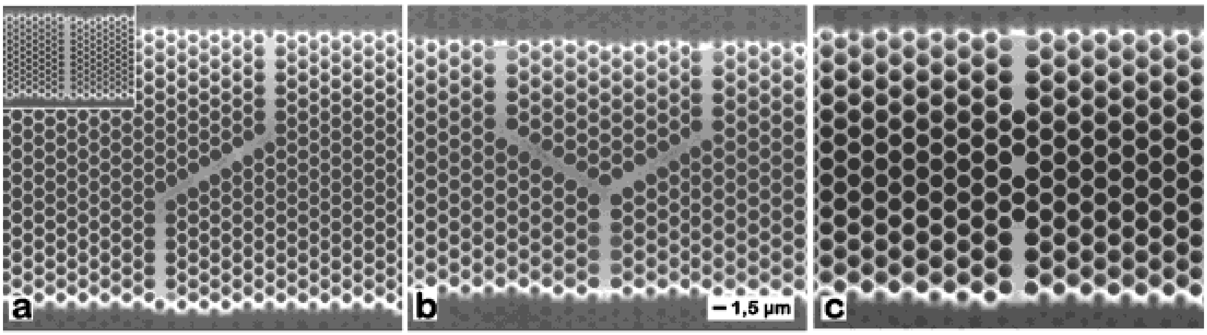

Figure 1.11. Different defect structures realized in macroporous silicon with 1.5 μm interpore distance.[14]

In comparison with 1D and 2D systems, it is much more complicated to introduce a defect into the 3D photonic crystals. Relatively accessible for this is the use of the top-down methods. For example, 3D waveguides containing sharp bends in woodpile PBG structures have been formed via lithographic techniques.[37] But it is still a great challenge to engineer defects into colloidal photonic crystals via a bottom–up approach. There is no straightforward way to introduce well-defined defects into these crystals. Recently various efforts have been made, for instance, several groups have reported introducing a planar defect in these crystals by using different methods.[46,47,48,49,50,51] Under certain conditions this 2D defect lattice can be inscribed with all kinds of functionalities like waveguides, splitters or cavities or used to test mode coupling. Theoretical calculation has demonstrated that this 2D-3D heterostructure achieved by intercalating two-dimensional photonic crystal layers containing engineered defects into a 3D PBG material enables flow of light without diffraction through micron-scale air waveguide networks. This provides a general and versatile solution to the problem of ‘‘leaky modes’’ and diffractive losses in integrated optics. More interesting is that the properties of this 2D-3D structure could be controlled strongly by variation of the 2D defect layer configuration. Jonsson et al. has presented a method, for example, for the artificial introduction of a lattice of such intentional defects in self-assembled PMMA photonic crystals by means of electron beam lithography (Fig. 1.12).[52] The inscribed defects are of the size of an individual bead, providing a broad spectral range between adjacent resonance peaks. This opens for devices with single line transmission in the photonic band gap, as well as for applications in modification and control of the diffraction properties and directionality of scattered light. Specific patterns in such monolayers have also been engineered by using micromanipulation[53] and by laser-induced breakdown.[54]

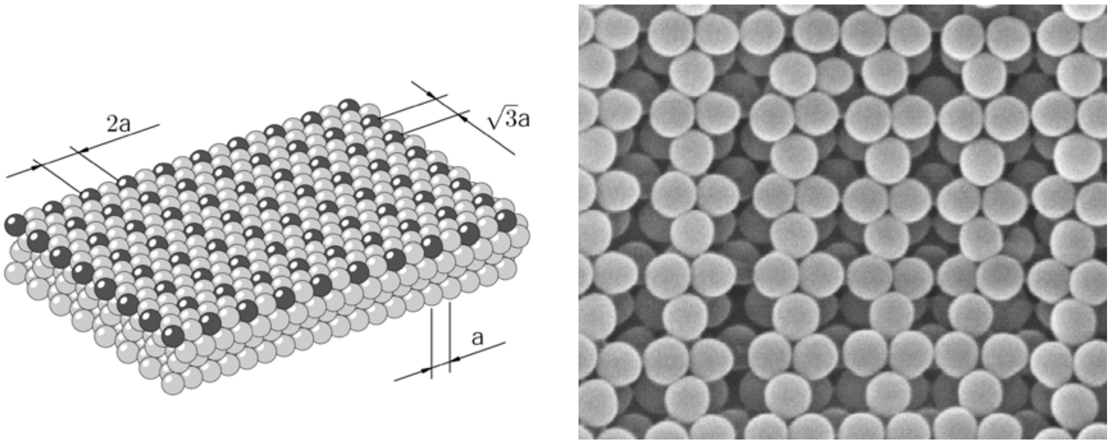

Figure 1.12. Left: Geometry of the lattice of defects, schematically drawn in black, written into the naturally grown opal, right: Scanning electron microscope image of the rectangular lattice of defects inscribed in the three-dimensional crystal of opal structure. The second layer of the face centred cubic lattice of beads is displayed in the sites of open defects.[52]

Another class of functional photonic crystals is the tuneable photonic crystals in which the novel functionalities can be realized by introducing materials with tuneable properties, for instance, tuneable refractive index, into periodic dielectric structures. One of the candidates of these materials is liquid crystals. Liquid crystals have a large optical anisotropy due to their anisotropic molecular shape and alignment, and its alignment is extremely sensitive to external parameters such as temperature or electric field. The change of alignment varies the refractive index and, as a result, when included in a periodic dielectric, the photonic band structure changes. Ozaki et al. has demonstrated a stop band shift upon change in temperature or application of an electric field in synthetic opals infiltrated with nematic and smectic liquid crystals.[55,56] They could be used to enable thermal or electric tuning of the optical properties. If a liquid crystal is filled into an inverse opal an abrupt change in the stop band can be observed because of higher volume fraction of the liquid crystal, which gives more influence to the optical properties.[57] More interestingly, if the infiltrated liquid crystal possesses a photochromic azo dye a photoswitchable photonic crystal is fabricated.[58]

Various materials can be used for this concept, organic dyes, for example, were infiltrated in inverse opals, in which inhibition and stimulated emission of these dyes was observed.[59] The effects of the photonic bandgap can also be observed in the luminescence lifetime.[60] These structures do not constitute a complete PBG and their stop band shifts with angle with the corresponding effect on luminescence.[61] This may be used to make laser even in the absence of a complete PBG through a gap-enhanced distributed feedback effect.[62] Lasing can occur in different directions depending on the interplay between the dye emission band and the stop band.[63]

Hydrogels are popularly used for such a purpose because of their ability to simulate biological tissues and to swell or collapse reversibly in response to external stimuli.[64] They usually consist of randomly crosslinked polymer chains and contain a large amount of water filling interstitial spaces of the network, resulting in amorphous structures. These structures can be easily functionalized, for example, by introducing a molecular recognition element which senses a given chemical agent, or certain metal ions through complexes.[65] If these functional hydrogels were fabricated in the presence of an opal, different specific sensors are created. So the tunability of hydrogel-opal can be controlled by temperature, pH, or ionic strength.[66,67,68,69]

1.3 Fabrication of Photonic Crystals from Colloidal Spheres

The ability spontaneously to assemble colloidal particles into crystalline arrays allows one to obtain interesting and useful functionalities not only from the constituent materials but also from the long-range, mesoscopic order that characterizes periodic structures,[70] which confer photonic properties.[9] As a result, the formation and utilization of highly ordered structures of colloidal particles has been an intriguing subject of research over the past several decades.

For fabrication of 3D photonic crystals that work in the visible region monodisperse colloidal spheres with a size range of 200 nm to 1000 nm are needed. These microspheres have been produced from numerous materials, both inorganic, for instance, inorganic oxides and organic such as polymers. A rich variety of chemical approaches are available for producing colloidal spheres that are monodispersed in size.[71] The best established and most commonly used methods seem to be controlled precipitation for inorganic oxides and emulsion polymerization for polymer latexes, respectively. Using these methods, inorganic oxides such as amorphous silica have been readily prepared as uniform spheres with diameter ranging from a few nm to 1 µm; polymer latexes of 20 nm to 1 µm in size have also been routinely produced as uniform beads.[7]

In order to obtain colloidal photonic crystals, these beads must be arranged into a crystalline lattice. However, it is not so straightforward to self-assemble them into high quality crystals with desired structures because of the nature of this crystallization process. Nevertheless, various methods have been developed that are described later.

1.3.1 Synthesis of Monodisperse Colloidal Spheres

We all know that nature opals consist of silica colloids. So it is no wonder that silica colloids play an important role in the fabrication of artificial opals. In 1968, Stöber et al. demonstrated an extremely useful procedure for preparing monodisperse silica colloids.[72] They hydrolyzed a dilute solution of tetraethylorthosilicate (TEOS) in ethanol at high pH and obtained uniform spheres of amorphous silica whose sizes could be varied from 50 nm to 2 µm simply by changing the concentrations of the reactants. This method was later improved by many others and now seems to be the simplest and most effective route to monodisperse silica spheres.[73]

Silica colloids represent one of the best characterized inorganic systems that have been manufactured as monodispersed samples in large quantities. Silica spheres are suitable for the fabrication of inverse opals, especially if the infiltration process requires high temperature, or using chemical reactants because silica is highly inert both chemically and thermally.

The most used polymer colloids are polystyrene (PS)-, and poly(methyl methacrylate) (PMMA) colloids. For the preparation of these spheres there are a lot of polymerization techniques, for example, suspension, emulsion, dispersion, and precipitation polymerization. These heterogeneous polymerization systems are distinguished on the basis of the four criteria: i) Initial state of the polymerization mixture; ii) Kinetics of polymerization; iii) Mechanism of particle formation; and iv) Shape and size of the final polymer particles.[74] Kinetic features and the size range of polymer particles produced by different heterogeneous polymerization processes are presented in Fig. 1.13.

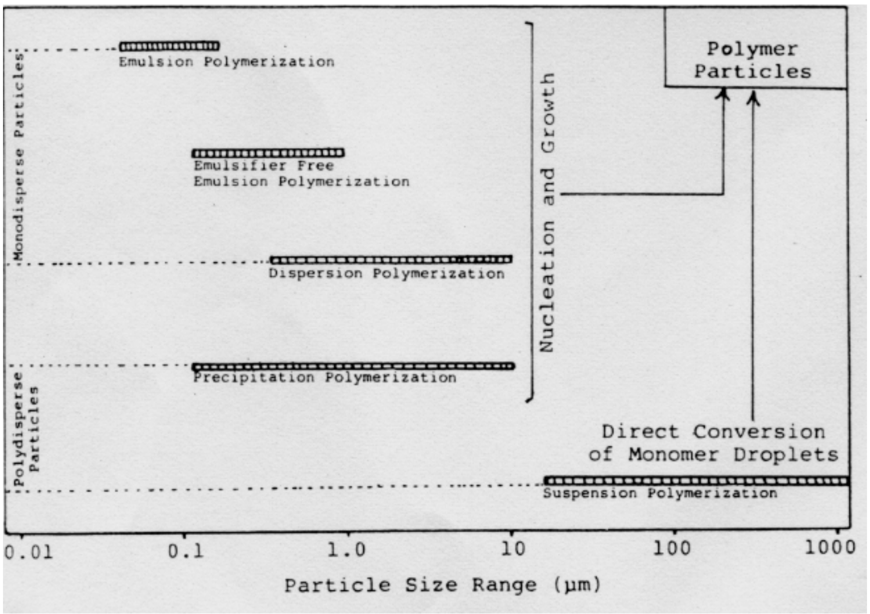

Figure 1.13. General kinetic features and particle size ranges of heterogeneous (particle forming) polymerization processes.[74]

The monodisperse polymer colloids in the size range of 20 nm to 1000 nm are usually produced by emulsion polymerisation.[75] In classical emulsion polymerization the major components of this process include a monomer, a dispersion medium (in most cases, water), an emulsifier (surfactant), and an initiator (usually water-soluble). The monomer is dispersed as an aqueous emulsion (~1±100 µm in diameter) with the help of the emulsifier. A small percentage of the monomer is also molecularly dissolved in the medium. Most surfactant molecules exist as micelles (~10 nm in diameter), depending on the nature and concentration of the emulsifier. The majority of these micelles have been swollen by the monomer. The formation of polymer latexes begins with the decomposition of the water-soluble initiator during which a burst of primary free radicals is generated. These radicals polymerize the small amount of monomer that is dissolved in the aqueous phase to form the oligomers (oligoradicals). These oligoradicals subsequently enter the micelles and eventually grow into latex particles until all the monomer dissolved in each micelle has been consumed. At the same time, the monomer encapsulated in emulsion droplets acts as a reservoir to provide a supply of repeating units to the growing polymer chains through diffusion. The growth of polymer latexes will stop at the point when all the monomer has been depleted.[75]

An attractive variation of emulsion polymerization and present most used method for preparation of monodisperse polymer colloids is the surfactant-free emulsion polymerization (SFEP),[76,77] in which the polymerization is carried out in same way as in classical emulsion polymerization, except that no emulsifier is used (Fig. 1.14). Accordingly, nucleation takes place by precipitation of macroradicals (oligomers) as compared with micelle formation in normal emulsion polymerization.[74] However, the mechanism of this process also has been described: The oligomers can act as surfactants because of their functional group at the chain ends formed by the decomposition of the radical initiator and aggregate into micelles. The advantage of this method (SFEP) is that the micelle concentration is low and all micelles grow for a long time (during polymerization) at equal rate. This leads to large and very monodisperse polymer colloids.[78]

When potassium peroxydisulfate is used as the water-soluble initiator, the surface of polymer latexes prepared by SFEP is negatively charged because of the sulfate group. As a result the polymer colloids are ionically stabilized, but with a rather low charge density. In addition the charges are chemically fixed on their surfaces. This is advantageous in comparison with using detergents as stabilizers which can migrate between colloids and make the crystallization problematic. Polymer latex stabilization by the use of amidinium initiators producing positively charged latex particles has also been studied by Goodwin et al..[77] Monodispersed polymer colloids such as polystyrene (PS) and poly(methyl methacrylate) (PMMA) have been produced in large quantities by using this technique. Polymer colloids tend to behave better than silica ones for the purpose of colloid crystallization. Therefore, they are very appropriate for optical and crystallization studies.[12]

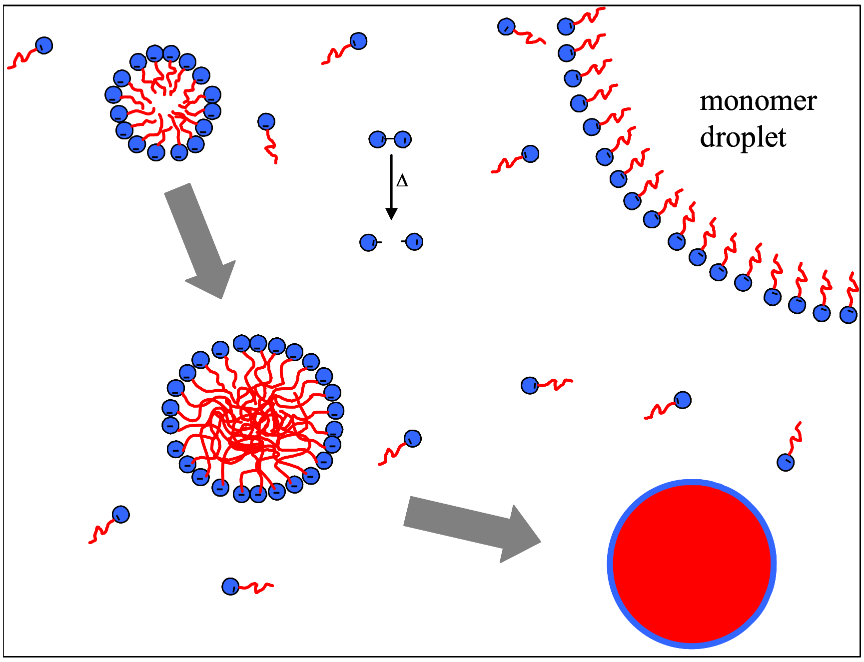

Figure 1.14. Schematic presentation of the surfactant-free emulsion polymerization.

Our group has worked on the synthesis of monodisperse polymer colloids form methacrylats for a long time and so far accumulated a lot of experiences about it.[79,80,81] The SFEP method for the preparation of these polymer spheres, especially the size control, has been investigated intensively. It has been realized from previously work[82] that the size of the individual polymer colloids can be tailored by varying the ratio of monomer to water. This result is important and useful for the further work. The efforts that have been done are not only restricted to optimise the process conditions, but much more to aim at exploring the possibility of the preparation of polymer spheres which may be used for the fabrication of functional photonic crystals. The chemical and physical properties of polymer spheres can be modified by using different monomers,[80] for instance, the glass transition temperature, which determines the thermal stability of the resulting polymer opals, can be varied between 80°C and 160°C, the refractive index of the polymers can be varied between 1.35 (fluorinated monomers) and a value slightly above 1.6 (bromine containing monomers), and the use of chemically labile monomers allows a chemical modification of the beads after crystallization, while crosslinking leads to an increase of the thermal stability.[78,83]

1.3.2 Crystallization of Monodisperse Spheres

Sedimentation is the natural way to obtain solid opals, in which a particle suspension is standing undisturbed over a long period of time.[84,85] The colloids settle at the bottom of the container due to gravity and form dense 3D crystalline structures. It seems to be the simplest approach to the formation of 3D crystalline. Silica colloids are usually employed in sedimentation because of their high density. However, in reality, this method could be successful only when several parameters such as the size and density of the colloidal spheres, as well as the sedimentation rate, which has to be slow enough to allow a disorder-to-order transition to occur, were controlled tightly. The major drawbacks of this method are the long time needed to obtain colloidal crystals (days to months), the restricted control over the morphology of the top surface and over the number of layers, and the limited size range of colloidal spheres that can be used (300-550 nm). Generally, these sedimented opals contain numerous defects such as vacancies, dislocation and stacking faults.[86] They are often polycrystalline by nature.[87] To improve this situation, more recent research has explored alternative approaches to form synthetic opals. For example, the sedimentation rate can be controlled by using an electric field;[88,89] van Blaaderen et al. have developed a method of epitaxal growing 3D crystalline arrays with desired spatial structures by using the lithographically defined surfaces as templates to obtain highly ordered and well-controlled arrays,[90] and Kumacheva and co-workers have reported that sedimentation under an oscillatory shear could enhance greatly the crystallinity and ordering.[91]

A convenient and versatile way to obtain colloidal crystals is the vertical deposition technique, in which a hydrophilic substrate is vertically immersed into a colloidal suspension while the liquid medium is allowed to evaporate.[92,93] In this case colloid crystallization is initiated in a particle layer on a substrate by the strong attractive capillary forces[94] mediated by a bridging meniscus, which tends to minimize its free surface area due to the surface tension of liquid. Such a meniscus is formed between the particles at the drying front when the liquid film reaches a thickness equal to the particle diameter. This effect drives particle aggregation in the top layer and creates a mesoporous structure with a high surface area. The large surface area facilitates solvent evaporation and induces as a secondary process a solvent flux from the suspension bulk through the growing crystal front to the drying particle layer.[95] Particles from the suspension bulk are dragged to the growing crystal front by this solvent flux and settle epitaxially there. If the colloid suspension is quite stable the thickness of the crystal can be controlled precisely by adjusting the concentration of suspension and the size of the spheres. This method is especially suitable for crystallization of polymer colloids because their density is close to that of the dispersion medium (mostly water) which leads to the maintenance of a stable suspension over a long time. Ethanol is usually used as the suspending medium for crystallization of silica spheres because of its relatively fast evaporation rate at room temperature. Colvin and co-workers have reported[92] that by using this method thin opaline films which have a tightly controlled number of layers along the (111) direction have been prepared. Such planar opals are extremely attractive as templates for photonic bandgap materials since they can be single crystals that contain defect densities that are significantly lower than in sedimented opals.

A variant of the vertical deposition technique has been developed, where the substrate is withdrawn from an aqueous suspension by using a "drawing apparatus" at a controlled speed instead of letting the solvent evaporate.[96,97] The withdrawing speed provides an additional parameter to control the thickness and can substantially decrease the preparation time. This method is advantageous to producing colloidal crystals with heretostructure, for instance, multilayer crystalline which consist of similar or different particles, or colloidal crystals on patterned substrates, in which the flexible and effective thickness control is crucial. In addition, by lifting the substrate slowly away from the suspension surface the solvent evaporation is accelerated due to enhancing the area of drying zone. As a result the arrayed spheres in the meniscus soon can be solidified in the substrate before they are eventually resolved again in solvent. Thus large size and well-ordered colloidal crystals can easily be obtained.

However, for large spheres, especially large silica spheres, this vertical deposition technique is unsuccessful because sedimentation of large particles away from the meniscus is usually faster than the process of solvent evaporation, so this method was believed to be limited to particles with diameters less than 0.4 µm. For commercial (near-infrared) application the particles have to be at least twice as large. Vlasov and collaborators overcame this problem by adding a temperature gradient (and therefore inducing convection) along the suspension.[93] The convective flow combats sedimentation and provides a continuous flow of particles to the meniscus region. Ozin's group has reported[98] using slow stirring as a help in keeping the colloidal spheres in a levitated state. Crystallization of large silica spheres (with diameter of 890 nm) is one of the tasks of this present work, in which high quality silica opals were successfully fabricated either on flat or patterned substrates by using a drawing apparatus in combination with stirring. The advantages of this method are discussed later.

1.3.3 Photonic Properties of Colloidal Crystals

The colloidal crystals fabricated by the above-mentioned methods generally possess a face centred cubic (fcc) lattice structure in which the (111)-plane is parallel to the substrate surface. They present iridescent colors resulting from their Bragg reflection. Although these crystals do not exhibit the complete bandgaps, they are very useful as a simple and easily prepared model system for the experimental investigation of 3D photonic bandgap materials. López and co-workers,[99] Vlasov and co-workers,[100] Zhang and co-workers,[101] and Colvin and co-workers[102] have investigated extensively the photonic properties of artificial opals fabricated from monodisperse silica colloids.

Bragg reflection plays a prominent role in optical experiments on photonic crystals. It occurs whenever there is constructive interference of waves reflected from a set of lattice planes. The central wavelength of the stop band (Bragg diffraction band) λ_B from these colloidal crystals follows the Bragg-Snell law condition well:

$$\lambda_B = 2d\,(n_{eff}^2 - \sin^2\Theta)^{0.5} \qquad (9)$$

where λ_B is the peak wavelength, $d = (2/3)^{1/2}D$ is the lattice constant along the (111)-axis, involving the sphere diameter D of the close-packed fcc lattice, Θ is the angle between the incident beam and the normal to the (111)-plane, and n_{eff} is the effective refractive index determined by $n_{eff}^2 = n_{sphere}^2\Phi + n_{air}^2(1-\Phi)$, with Φ being the volume fraction of spheres. For the close-packed fcc structure $\Phi = 0.74$. If $\Theta = 0°$ and D instead of d, the equation (9) can be simplified to:

$$\lambda_B = 1.633 \cdot D \cdot n_{eff} \qquad (10)$$

This means that the spectral position of stop band can be controlled through the size of colloidal spheres. Conversely the sphere diameter D can be calculated from equation (10) if λ_B is known from optical experimental data. This provides an indirect but quick way to determine the sphere diameter.

The optical measurements are usually used to examine the quality of the colloidal crystals. If a crystal is sufficiently well-ordered the Bragg reflection will be very strong, close to 100%. The associated extinction will be very large, increasing exponentially with sample thickness. Therefore the optical properties of the colloidal crystals reflect their quality. The criteria for acceptable structural quality of the colloidal crystal film is the observation of the low energy stop band with resolved Fabry–Pérot fringes, as well as with resolved high energy bands of its transmittance spectra.[4] The number of layers of this film can also be determined by optical measurements.[102]

1.4 Motive and Goals of this Work

Photonic crystals, optical equivalents of semiconductors, become more and more important for the technological development of current planar optical circuits, which plays a central role in the photonics industry. As Joannopoulus presented his "photonic crystal micropolis" (Fig. 1.15)[103] it was considered as a possible model for the all-optical chip of the future. Meanwhile, however, for many materials researchers and scientists it is not only a dream but also has been envisioned as a great goal to strive for. The all-optical chip is comprised of integrated microphotonic crystals, for instance, Joannopoulus's all-optical chip is formed in form 1D, 2D, and 3D photonic crystals, having the remarkable property of being able to control light in micron-scale optical circuits very much smaller than those currently utilized in optical networks. In the envisioned operation of such a futuristic optical chip, light from a conventional optical fiber is coupled to a planar waveguide on the chip, which is then coupled to photonic crystal optical components with minimal light losses. Therefore, integrated photonic crystal components on all-optical chips are imagined to function as low threshold lasers, wavelength division multiplexers, wavelength dispersion compensators and switches.[4]

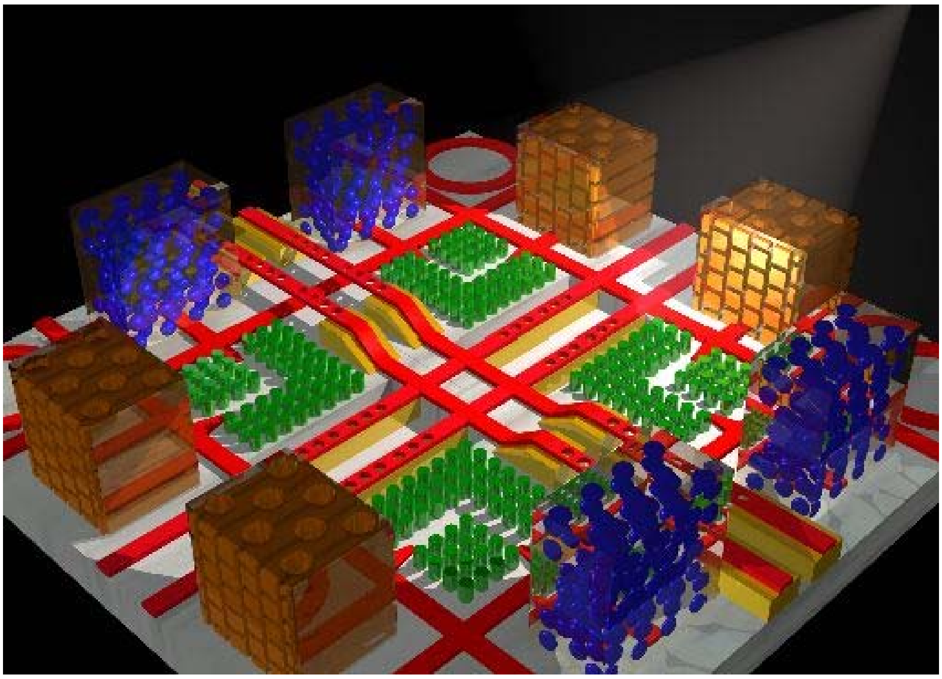

Figure 1.15. Joannopoulus photonic crystal micropolis.[103]

In order to create new photonic crystal devices and chips which are user-friendly it is important to develop the process of making optically functional photonic crystals in a controllable way and at a reasonable cost. Self-assembly of monodisperse microspheres into opal structures remains the favourite route towards templates for platform-integrated photonic materials, due to its simplicity, flexibility and low cost. These bottom-up colloidal photonic crystal constructs, through the phenomenon of optical Bragg diffraction in all three spatial dimensions, have demonstrated their ability to control the flow of photons at the light scale. However, it is still difficult to understand and to control this 'natural' self-assembly process. The greatest challenge that remains to be overcome before colloidal crystals can be engineered as photonic crystal devices is their experimentally achievable degree of structural perfection and optical quality.

This work based on polymer colloidal crystals shall serve as a contribution to explore the potentials of these colloidal photonic crystals. General goals of this work are the preparation of polymer photonic crystals with high quality characterized thought their excellent optical properties and development of crystallization methods for fabrication of heterostructure colloidal photonic crystals. The major tasks of this work are as follows:

- High monodisperse PMMA spheres with different sizes shall be prepared and subsequently crystallized to PMMA photonic crystals by using different crystallization methods. The optical properties of PMMA photonic crystals should be investigated.
- A new method of crystallization of large silica spheres shall be developed in order to obtain a large size and high quality of these silica opals.
- The conditions of crystallization opals on patterned substrates shall be optimised. The crystallisation shall take place very selectively and precisely. The quality of these photonic opals shall satisfy to all requirements the realization of perfectly crystalline low refractive index 3D templates.
- Multilayer opals shall be fabricated. The optical properties of these herterostructure opals shall be investigated.
- Inverse opals with different materials shall be fabricated.

2. Fabrication of 3D Photonic Crystals from Colloidal Spheres

For fabrication of colloidal photonic crystals highly monodisperse colloidal spheres are required. In this work, for the historic reason, monodisperse PMMA spheres were used. The PMMA spheres of different sizes were synthesized at first by surfactant-free emulsion polymerization (SFEP) and then their properties, including polydispersity and surface property, were characterized. As a second step these spheres were crystallized to crystalline films by using a “drawing apparatus”. The quality of these crystalline films was examined by different methods. Especially the optical properties of PMMA opals were investigated intensively.

The influences on the quality of colloidal crystals, for instance, the properties of PMMA spheres and the conditions of crystallization, including the environment concentrations, as well as the methods which were used for the crystallization, have been studied. The PMMA spheres prepared from this work have very high monodispersity, polydispersity less than 2%. This is an important prerequisite for the fabrication of high quality PMMA opals.

This work has also explored a new way for the fabrication of silica opals from large size spheres. The large silica spheres which were used for this work were acquired from Prof. Unger of the Inorganic Chemical Institute of the University of Mainz.

2.1 Preparation of Monodisperse PMMA Spheres by SFEP

The SFEP is the most frequently used method for preparation of monodisperse colloidal spheres. PMMA spheres used in this work were produced by it. In this process a water-insoluble monomer is dispersed in water with a charged water-soluble radical initiator (mostly potassium peroxydisulfate ($K_2S_2O_8$)). The reaction takes place at 90°C in the presence of nitrogen. In Fig. 2.1 the mechanism of the synthesis of PMMA spheres by SFEP is described: (a) The potassium peroxydisulfate molecule is split thermally to the charged sulfate radicals. (b) These radicals initiate the polymerization of traces of monomer, which are dissolved in equilibrium in water. (c) The oligoradicals, which possess charge at the one end resulting from the initiator, but are otherwise hydrophobic because of their polymer chain, are formed. (d) If the polymer chain of the growing oligoradicals becomes long enough nucleation takes place by precipitation of macroradicals. The nuclei are stabilized by the orientation of their own polymer chains, notably the chain ends originating from initiator molecules. (e) Subsequently, charge-stabilized polymer nuclei become the main loci of polymerization by absorbing further oligoradicals and monomer molecules from the medium and form increasingly larger latex particles. (f) In this way, the latex particles grow gradually until the monomer is completely consumed. As the particles grow, their surface charge increases and the particles become stabilized by their own electrostatic charge.

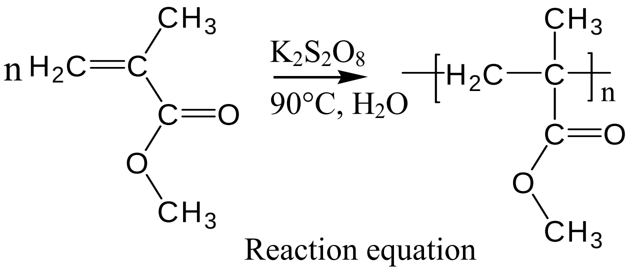

Reaction equation

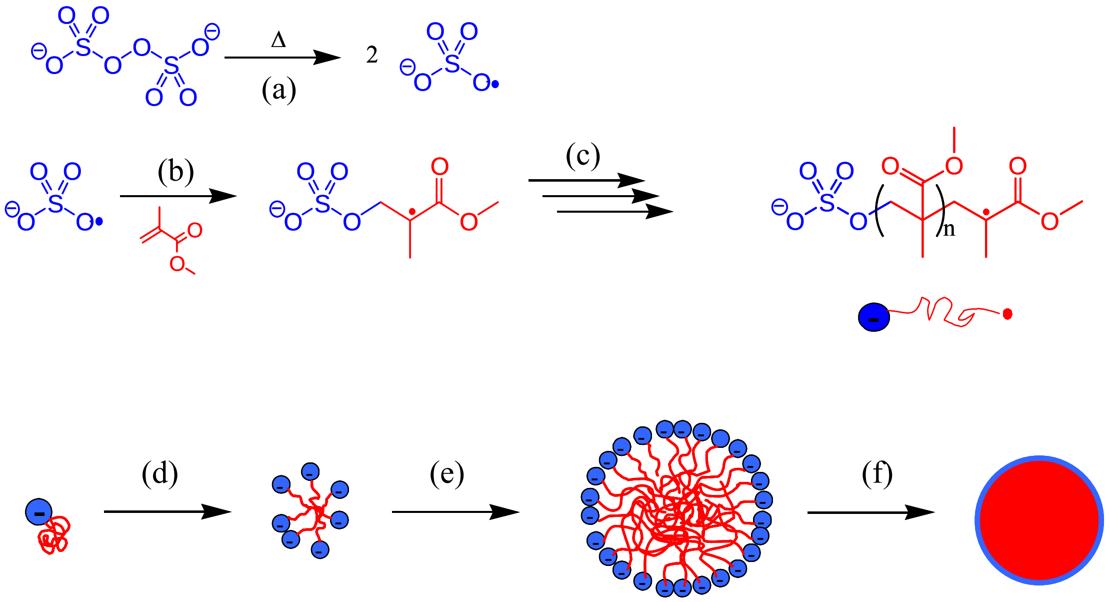

Figure 2.1 Schematic outline of the synthesis of PMMA spheres by SFEP.

The sphere size can be easily controlled by varying the ratio of monomer to water. Generally, the monomer to water ratio in SFEP is much smaller than that in normal emulsion polymerisation. If the monomer concentration is too high, the disperse system becomes unstable. The latex particles aggregation could take place before they are stabilized. This means, SFEP is not suitable for the preparation of large monodisperse spheres (diameter > 450 nm for PMMA spheres). However, monodisperse PMMA spheres of the diameter larger than 450 nm could be obtained by addition of the monomers afterwards during the polymerization procedure in principle like seed polymerisation.

In the present work the monodisperse PMMA spheres with different size are prepared in large batch size. Table 2.1 is a list of samples regarding batch size and sphere size. The polymerization conditions from sample No. 1 to No. 6 are the same, apart from the MMA monomer amounts, which were varied from 30 ml to 300 ml depending on desired sphere size. Initiator $K_2S_2O_8$ was put into a reaction mix as 10% aqueous solution. For sample No. 7 the MMA monomers were added in batches during the polymerisation process because of the higher monomer to water ratio. The sphere sizes were determined from the position of the stop band obtained by UV-Vis-Spectroscopy. By precise control of the reaction conditions, for example, the temperature, the concentration of reactants and the method for the mixing of reactants, PMMA spheres with desired size and very narrow size contribution, polydispersity ~2% (Chapter 2.2), have been prepared. These spheres have slight negative charge and stabilize well in water.

Table 2.1 Listing of monodisperse PMMA spheres prepared by SFEP regarding batch size and sphere size

Sample No.	H_2O [ml]	MMA [ml]	MMA / H_2O	10 % $K_2S_2O_8$ solution [ml]	Sphere size* [nm]
1	1200	30	0,03	40	182
2	1200	50	0,04	40	227
3	1200	80	0,07	40	275
4	1200	100	0,08	40	305
5	1200	200	0,17	40	367
6	1200	300	0,25	40	418
7	180	93	0,52	15	540

* The sphere sizes were determined from the position of the stop band obtained by UV-Vis-Spectroscopy.

2.2 Characterizing of PMMA Spheres

In the following chapter the properties of the samples listed in Table 2.1 are studied. The sphere sizes and size distributions were determined by different methods, including UV-Vis spectroscopy, dynamic light scattering (DLS), Laser Aerosol Spectroscopy (LAS), and Malvern Mastersizer Microplus (MS). The surface charge of PMMA spheres was measured by the “Streaming Current Detection” (SCD) method.

2.2.1 Determination of the Sphere Sizes and Size Distributions

The sphere sizes can be determined by using the Bragg reflect condition as mentioned above (Chapter 1.3.3), in which the sphere size is calculated according to the Bragg-Snell equation from the maximal wavelength of the stop band λ_B obtained by UV-Vis spectroscopy measurement. In this present work the sphere sizes were mainly determined by this method because it can be performed in our laboratory. For the measurement first a thin crystal film was prepared and from it the UV-Vis spectroscopy measurement was performed. Unfortunately the UV-Vis Spectrometer in our laboratory has a measure range of 200 nm to 900 nm. The PMMA spheres of a diameter larger than 400 nm were measured at the Fraunhofer Institute in Golm. Fig. 2.2 is the UV-Vis spectra with the corresponding sphere sizes.

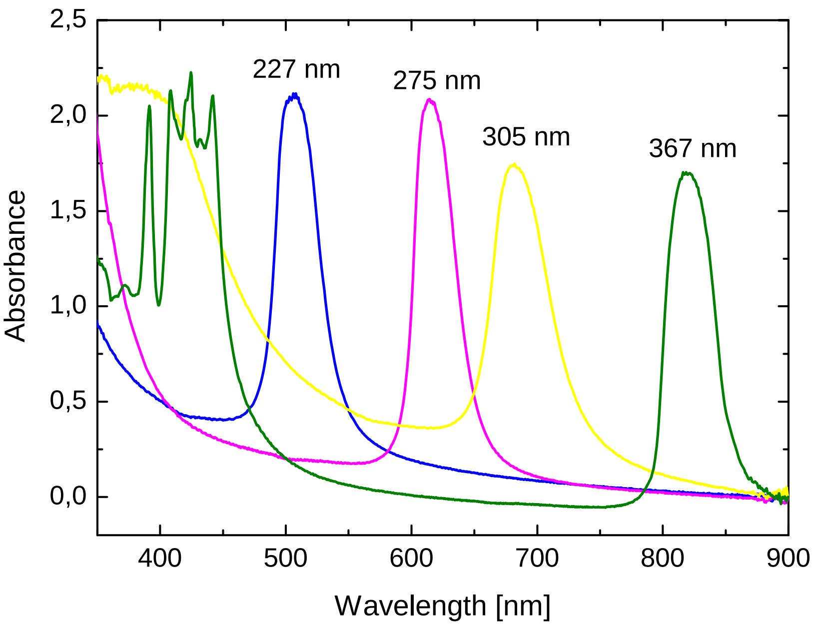

Figure 2.2 UV-Vis spectra with the corresponding sphere sizes.

The drawback of this method is that it is not possible to determine the size distribution. However, it is well known that for the fabrication of high quality colloidal crystals the polydispersity of the spheres should be lower than 2%. This means that by checking the crystal quality the sphere size distribution can be estimated qualitatively. Optical experiments are usually used for examining the crystal quality. Apart from the observation of the high order diffraction peaks and the Fabry-Pérot rings from optical spectra as the characteristic features for a good quality of the colloidal crystals, the relative bandwidth of the diffraction resonance, defined as the ratio of the full bandwidth at half height of the reflectance band to the band central wavelength, is also an important criterion of the crystal quality. The theoretically calculated value for the relative bandwidth along the (111)-axis of a perfect infinite opal is 0.056. Some transmission and reflection spectra from this present work are presented in Fig. 2.3, in which the above-mentioned criteria, including of the multiple diffraction peaks and the Fabry-Pérot rings are clearly observed and the relative bandwidth value (Δλ/λ) agrees well with the theoretical value. This confirms a very narrow size contribution of the spheres.

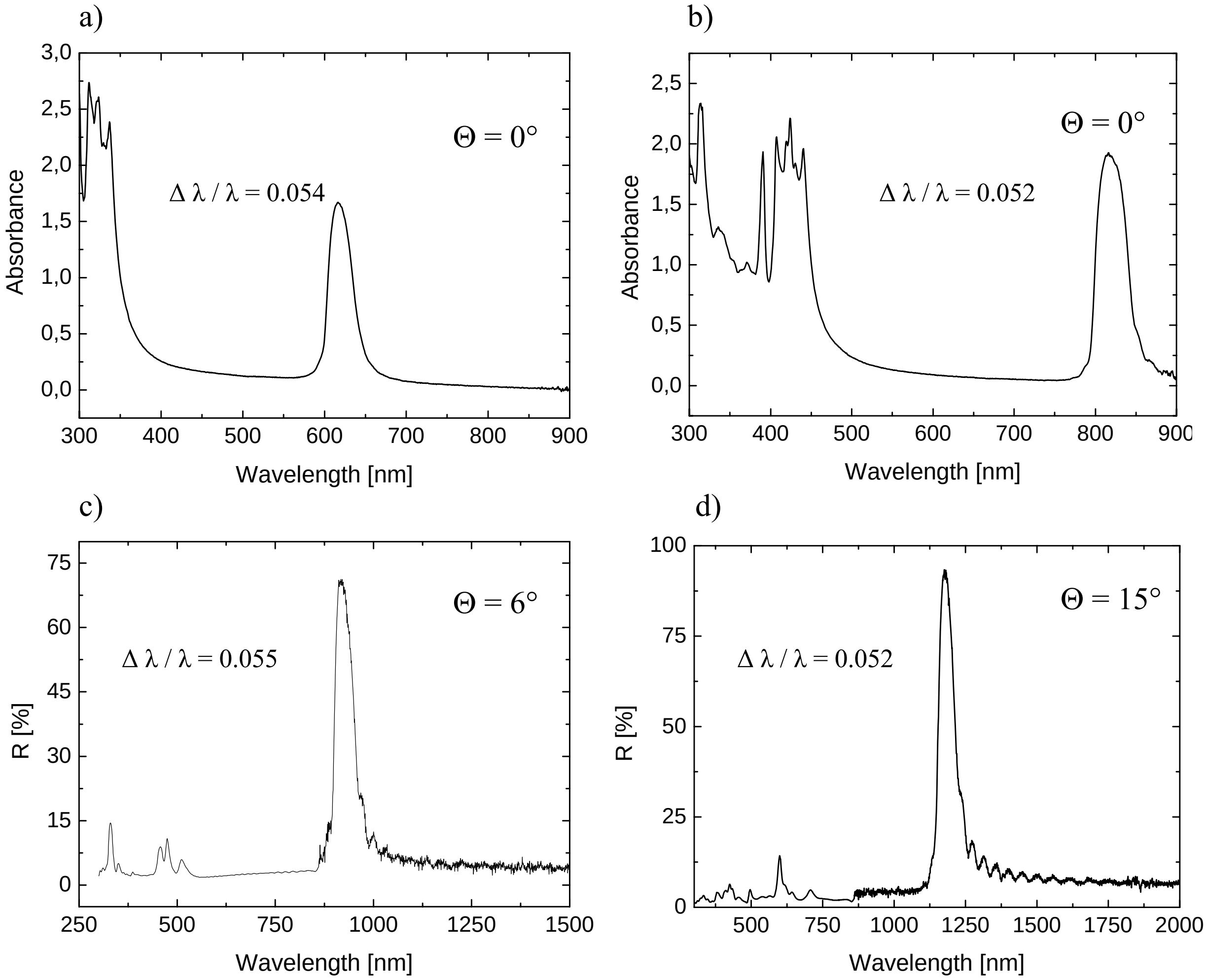

Figure 2.3. a) Absorption spectrum of sample No. 3 (sphere size 275 nm). b) Absorption spectrum of sample No. 5 (sphere size 367 nm). c) Reflection spectrum of sample No. 6 (sphere size 418 nm). d) Reflection spectrum of sample No. 7 (sphere size 540 nm). Θ is the angle between the incident beam and the normal to the substrate surface and Δλ/λ is the relative bandwidth value.

These PMMA spheres are also characterized by dynamic light scattering (DLS), Laser Aerosol Spectroscopy (LAS),[104] and Malvern Mastersizer Microplus (MA),[105] which were performed by Jürgen Gräbner in the colloid laboratory of the Celanese Emulsion GmbH company. In colloid industry the colloid size distribution is commonly described as polydispersity index (dw/dn), defined as the ratio of the weight mean diameter (dw) to number mean diameter (dn). The mostly frequently used method for such a purpose is DLS, based on measuring Doppler shifts due to Brownian motion of the particles, in which the hydrodynamic diameter is measured, which is higher than the diameters determined by the other methods. This measurement makes more deviation by measuring large particles because of the Doppler shifts effect. Table 2.2 is the experimental data from DLS measurement together with that from UV-Vis Spectroscopy. In Table 2.2 it is shown that the sphere size distributions are very narrow, polydispersity index close to 1 and polydispersity equal or smaller than 2 %, apart from samples No. 5 and 6, which are not sure by this method due to their relative large sizes.

Table 2.2. Determining sphere size and size distribution by DLS and UV-Vis Spectroscopy

	Dynamic light scattering			UV-Vis	
No.	Diameter [nm]	Polydispersity %	Polydispersity Index dw/dn	Stop-band λ_B [nm]	Diameter from λ_B [nm]
1	193	0,9	1,054	406	182
2	251	0,8	1,070	505	227
3	319	1,2	1,005	612	275
4	365	2,0	1,036	680	305
5	431	6,4	1,084	818	367
6	505	7,4	1,023	930	418

The method of LAS and MS both use laser technique, in which the kern diameter is determined. The method of LAS has very high resolution comparable to the electron microscopy but with a short measuring time. MS is based on laser diffraction principle and it is also suitable for measuring the large size particles. The experimental data resulted from LAS and MS are summarized in Table 2.3. Except for No. 7 the weight mean diameter determined by LAS is similar to that obtained from UV-Vis measurements (Table 2.2 and 2.3). In Table 2.3 it is noticeable that polydispersity measured by LAS is enhanced when the sphere size is increased. Here it is obvious that the larger the sphere size the broader the sphere size distribution (Fig. 2.4).

Table 2.3. Characterization of PMMA spheres by LAS and MS

No.	LAS			MS		
	dn [nm]	dw [nm]	Polydispersity Index dw/dn	dn [nm]	dw [nm]	Polydispersity Index dw/dn
1	168	179	1,070	239	247	1,033
2	175	212	1,212	270	280	1,040
3	204	263	1,291	280	290	1,040
4	199	301	1,514	290	300	1,030
5	199	359	1,804	300	320	1,070
6	180	425	2,361	360	370	1,030
7	137	343	2,510	476	501	1,053

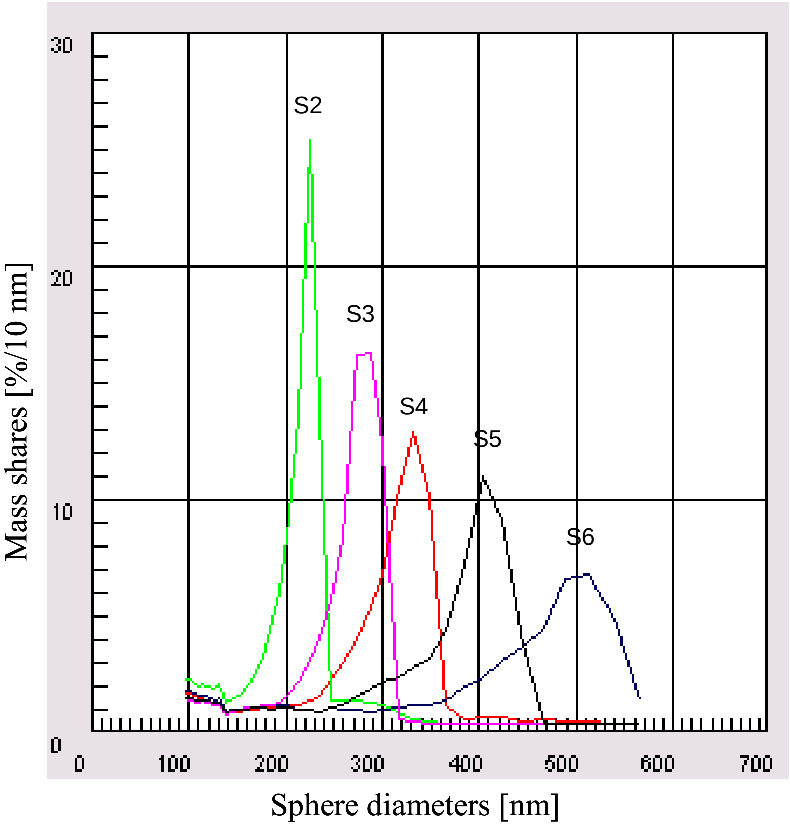

Figure 2.4. Sphere size distributions from sample No. 2 (S2) to 6 (S6) measured by LAS.

Sample No. 7 has a small faction of substantially smaller spheres (secondary seeds) built by adding monomers during polymerization procedure. Fig. 2.5b is the sphere size distribution of this sample measured by LAS, in which two peaks can be seen and evidently one of them belong to the fine particles. In comparison with the sample No. 1 (Fig. 2.5a) it seems that the sample No. 7 is binary latex. Really, the faction of the fine spheres is extremely small and can only be detected by the method that has excellent resolution.

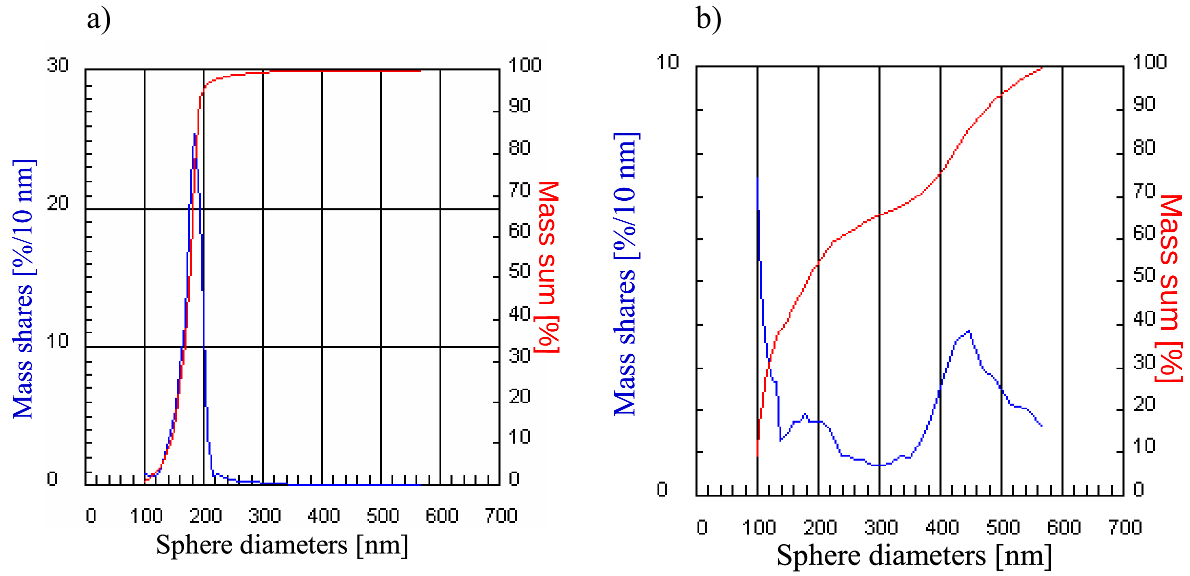

Figure 2.5. a) Sphere size distribution of sample No. 1 obtained by LAS. b) Sphere size distribution of sample No. 7 obtained by LAS.

It is worth mentioning that, although the small faction of the fine spheres turns out to have a minimal effect on the polydispersity index (Table 2.3), this has a major detrimental effect on the overall structural order of the crystal film. Fig. 2.6 is scanning electron microscopy (SEM) images of opaline film from sample No. 7. It shows the different crystalline arrays between the crystal with small spheres (Fig. 2.6 left) and the crystal without small spheres (Fig. 2.6 right). The elimination of these smaller spheres was done by consecutive centrifuging.

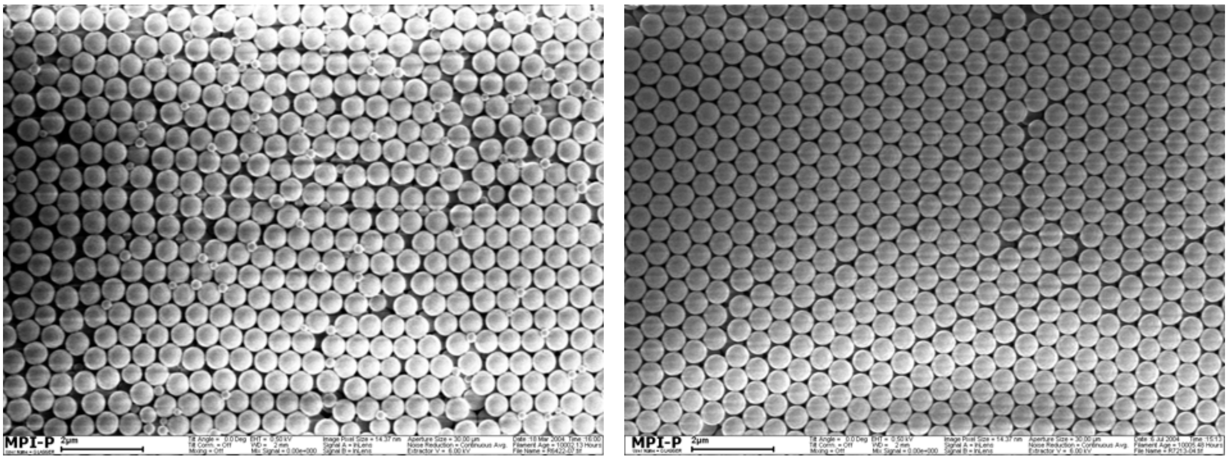

Figure 2.6. SEM images of opaline films from PMMA spheres of a diameter of 540 nm (sample No. 7). Left: crystal with small spheres. Right: crystal without small spheres.

2.2.2 Surface Charge Analysis

The PMMA spheres prepared by SFEP have slightly charges at the surface, which play a very important role for the sphere stability in suspension and the crystallization into colloidal opals. The surface charge of the samples was analysed by the ‘‘Streaming Current Detection’’ (SCD) method,[106] in which the negative charged colloidal solution is titrated at various pH values, with poly(diallyl dimethyl ammonium chloride) as a polycation, while an electrical current polarizes the electrolyte double layer at the surface of the colloids. From the amount of polycation necessary to compensate the electrolyte double layer, the charge per mass of colloid can be determined. The results of these measurements are presented in Fig. 2.7. The SCD measurements were done by Jürgen Gräbner in the colloid laboratory of the Celanese Emulsion GmbH company.

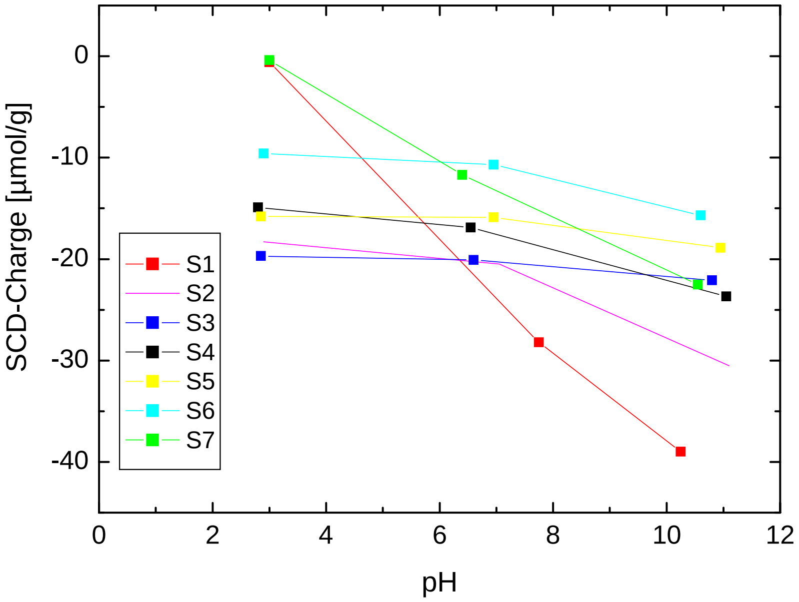

Figure 2.7. Results of SCD measurements.

In Fig. 2.7 it is shown that for samples No. 2 to No. 6 the charge per colloid does not depend on the pH value. This is expected for sulfonates (sulfonic acid as a strong acid) as a source of the negative surface charges. But it seems that the surface charge of sample No. 1 and No. 7 is pH dependent (Fig. 2.7). The reason is not clear. Next, it is evident that the absolute amount of surface charge is relatively low. This results from the fact that the incorporated initiator is the only ionic species. The fact of low density of surface charge of the PMMA spheres explains that they have a hard sphere character. This favours closely parking these spheres and reduces crack formation during drying, as the polymer opal reaches a volume density of the colloids of 74% (cubic densest packing). Fig. 2.8 is the relationship between the absolute amounts of surface charge and sphere size at pH value 7.0. It is obvious that the smaller the size the higher the surface charge (negative charge). This can be explained by the smaller sphere having a larger surface area.

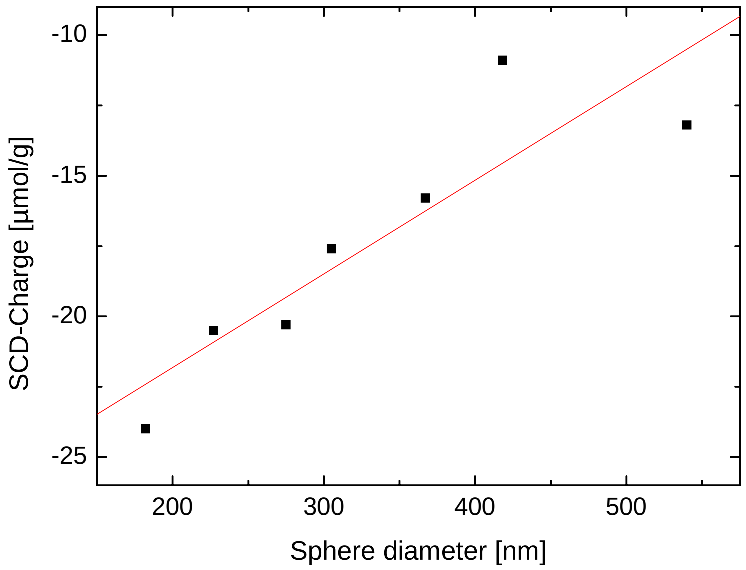

Figure 2.8. Relationship between the absolute amounts of surface charge and sphere size at pH value 7.0 (the values were obtained from Fig. 2.7).

2.3 Fabrication and Characterization of PMMA Opals

3D opaline lattices of colloidal spheres have been exploited as removable templates to generate highly ordered, macroporous materials; such as diffractive elements to fabricate sensors, filters, switches, PBG crystals, or other types of optical and electrooptical devices; and as a directly observable model system to study a wide variety of fundamental phenomena such as crystallization, phase transition, melting, and fracture mechanics. The success of all these applications strongly depends on the availability of colloidal spheres with tightly controlled sizes and surface properties, and on the ability to self-assemble them into ordered arrays with well-defined structures and sufficiently large domain sizes. This mean, the degree of structural perfection and optical quality of these crystals must meet an exceptionally high standard.

The colloidal crystals produced the by self-assembly approach have a face-centered-cubic (fcc) lattice with a packing density of ~74%. The preference of an fcc structure over a hexagonal-close-packed (hcp) one has been suggested to be a result of the difference in entropy between these two structures.[107] It seems that the fcc structure is more thermodynamically stable. Generally, when flat substrates were used as solid supports, the spontaneous crystallization of colloids provides fcc lattices with their (111) planes oriented parallel to these substrates.

The following chapter deals with crystallization of PMMA spheres. The crystallization methods, including crystallization in horizontal substrates and that in vertical direction, are described. The advantages and disadvantages of these different methods, as well as the influence of the important crystallization parameters, for instance, drying rate, temperature, and humidity on the crystallization are discussed. The structure perfection has been studied by optical microscopy, scanning electron microscopy (SEM), and spatially resolved microspectroscopy. The optical properties of these PMMA opals have been investigated intensively.

2.3.1 Crystallization on Horizontal Substrates

The simplest way to crystallize colloidal spheres is to spread a thin layer of a latex suspension onto a substrate and leave the suspension to dry.[108] This leads to the formation of densely packed colloid layers. If the particles are monodisperse highly ordered colloidal crystals are obtained. Fig. 2.9a is a picture of such a film, which was prepared by carefully spreading some microliter of a 1.5 vol. % suspension of monodisperse PMMA spheres of a diameter of 367 nm (Sample No. 5) on a glass substrate. The iridescent colour of the crystalline film reflects its good quality (Fig. 2.9a). Fig. 2.9b and 2.9c are also pictures of PMMA opaline films made of 275 nm diameter spheres (Fig. 2.9b) and 367 nm diameter spheres (Fig. 2.9c), which were taken by scanning in photo lab of the University of Mainz. Fig. 2.9a and 2.9c are the pictures taken from the same sample. Fig. 2.9b and 2.9c reveal how homogenous and transparent the samples were.

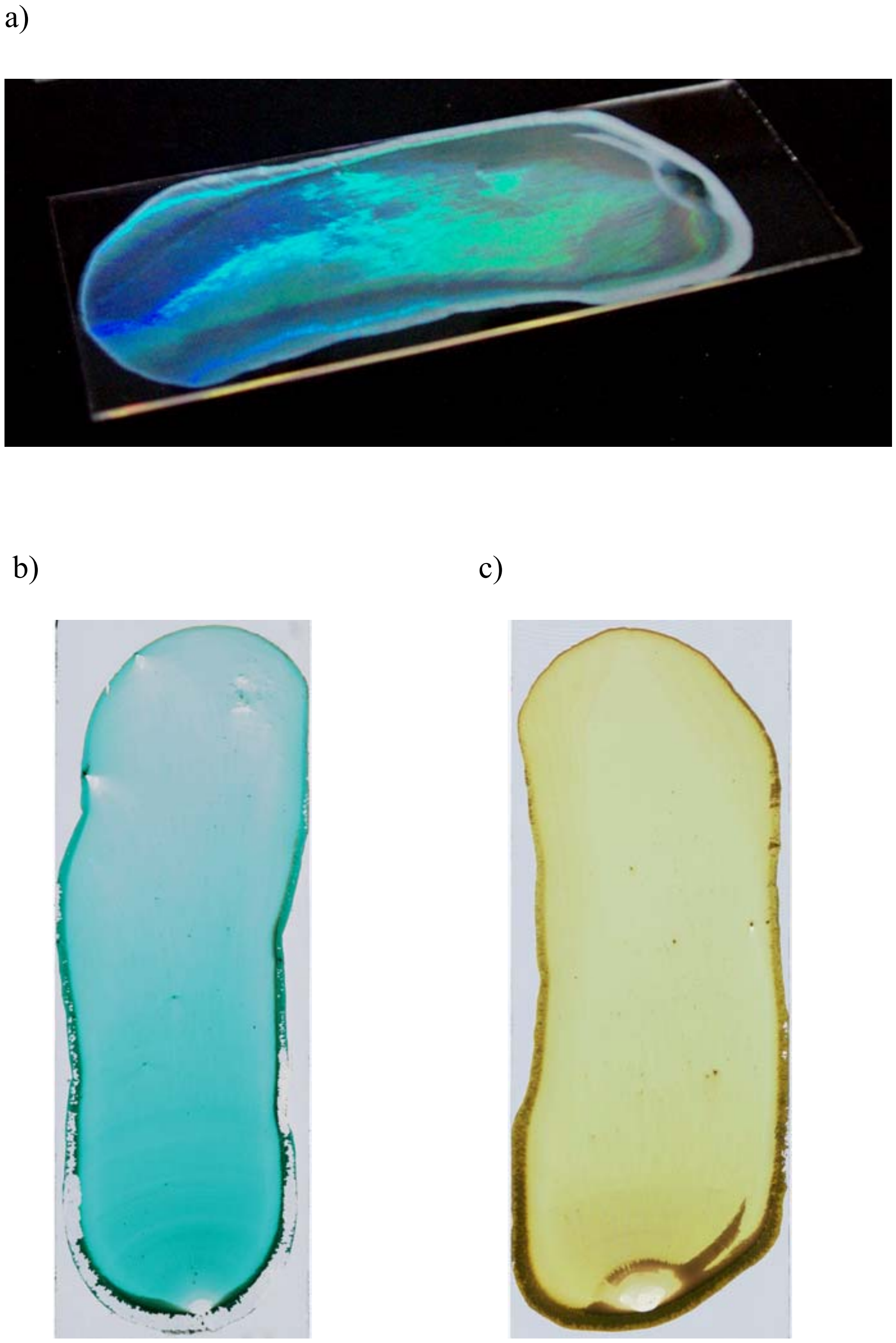

Figure 2.9. Pictures of the PMMA crystalline films prepared on a glass substrate: a) PMMA opals with 367 nm diameter spheres, b) PMMA opals with 275 nm diameter spheres (Sample No. 3), c) same sample as a).

The ordering process occurs where the thickness of the liquid film reaches the particle diameter and a meniscus is formed between the colloids, pulling them tightly together by capillary forces (Fig. 2.10). It has been observed that the crystallization begins mostly at the film edge where the position of the substrate is a little higher. The driving force is the high surface tension of water that tends to minimize the free liquid surface between the particles. In addition, water evaporation in the dense particle layer generates a convective flow of the surrounding liquid with its suspended particles toward the colloid layer (Fig. 2.10). The shape or slope of the drying meniscus controls the formation of multilayers, with a steeper meniscus producing thicker layers.

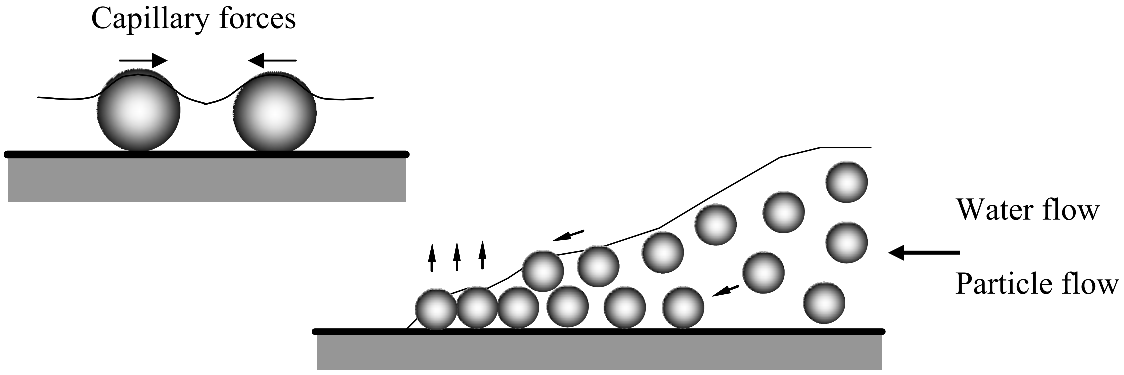

Figure 2.10. Schematic illustration of the crystallization of colloids on a horizontal substrate.

Figure 2.11 is a SEM image from such PMMA opal film similar to that in Fig. 2.9, which shows clear evidence for a highly ordered arrangement of PMMA spheres corresponding to the (111) plane of a face centred cubic (fcc) lattice. However, the domain size of the crystals from this thin film is small (Fig. 2.12) because of cracks, which appear due to volume shrinkage during drying of the colloidal crystal. Large crystallites can be obtained if the film is dried carefully, for example, the cracks can be reduced if the crystallization of this liquid film is performed in a chamber, in which the relative humidity is set to about 98% for a long time (several days to a week). Fig. 2.13 is the optical microscopy of the opaline film prepared by slowly drying, in which large crystallites (in the order of 100 μm^2) can be seen. The thicker crystalline film can only be obtained by slow drying. However, the thickness of this thicker film is usually not homogenous, which is thicker at the edge than in the center because of the changing of the suspension concentration during crystallization process.

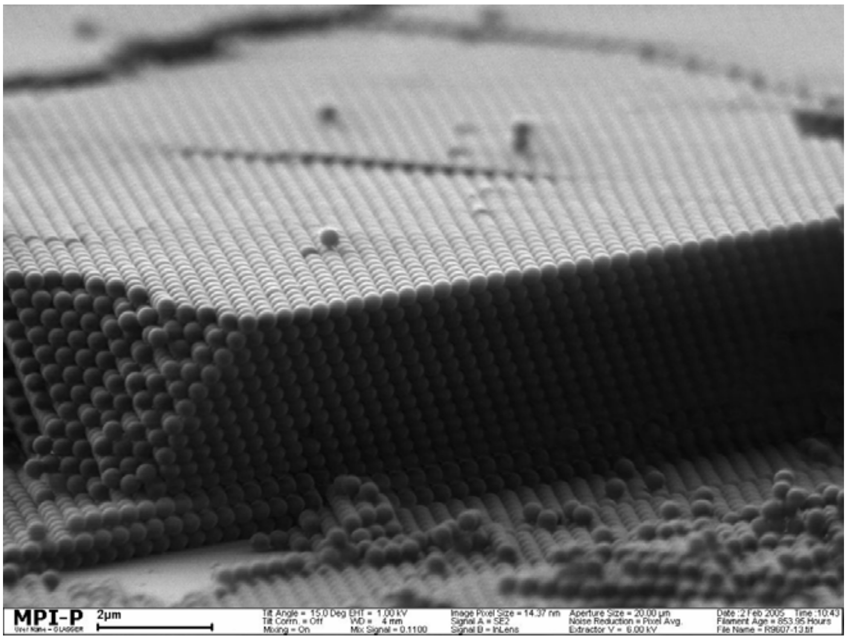

Figure 2.11. SEM image of PMMA opals with a sphere diameter of 367 nm fabricated on horizontal substrate.

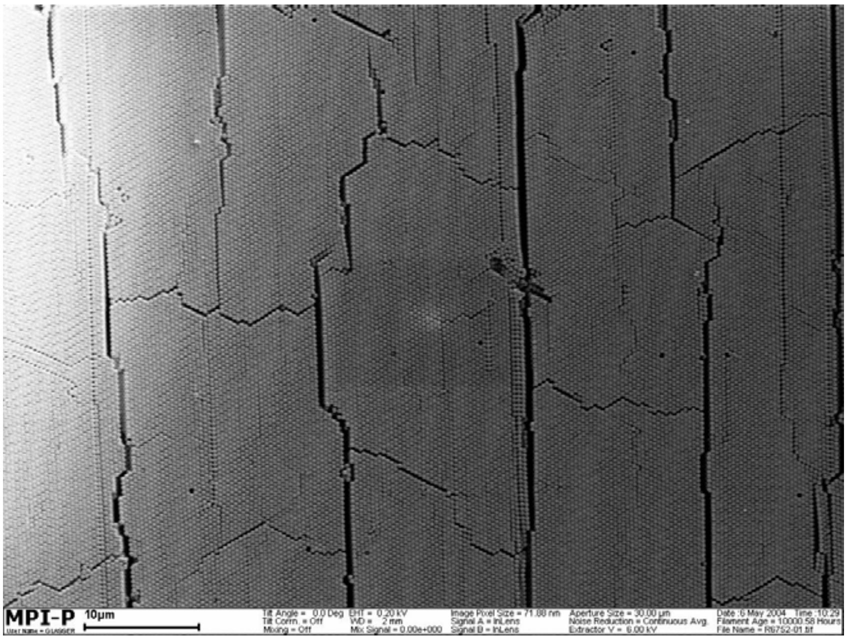

Figure 2.12. SEM image of the top view of PMMA opals with a sphere diameter of 367 nm fabricated on horizontal substrate.

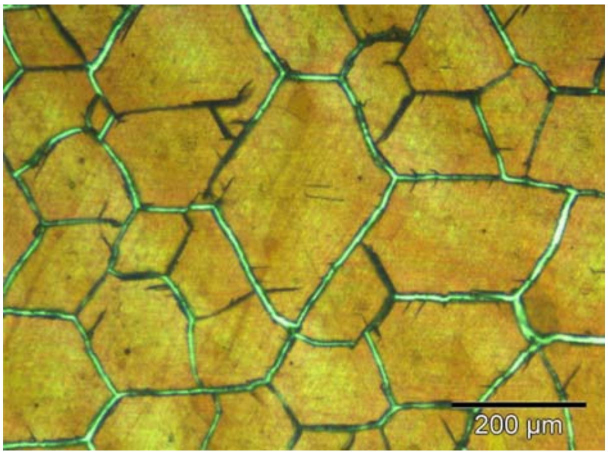

Figure 2.13. The optical microscopy of the PMMA opaline film (Sample No. 2 with a sphere diameter of 227 nm) prepared by slowly drying.

In principle the crystalline film thickness can be changed by adjusting the suspension concentration. But really, the control of the crystal thickness is difficult with this method because it depends not only on the concentration, but also on the drying rate, the amounts of suspension used for the formation of the liquid film, and the film size, as well as its shape. In addition the quality of these crystal films is also influenced by the suspension concentration and the drying rate.

2.3.2 Crystallization on Vertical Substrates

By spreading a thin suspension layer on a horizontal substrate the crystallization process proceeds randomly. It is hardly possible to control the crystalline film thickness and size. By contrast, the vertical deposition technique with a drawing apparatus is more calculable and reliable, in which the crystalline film size is dependent on the crystallization time and, if the temperature and humidity are constant, the thickness of the crystal film can be controlled flexibly by adjusting the suspension concentration and the drawing speed. In the present work this method was mostly used. The crystallization was performed by drawing up a hydrophilized substrate in a vertical position with a velocity of about 200 nm s^{-1} from a 1.5-3 vol. % suspension of PMMA spheres, and so large-area, well-ordered crystalline films were produced. Fig. 2.14 is a photo of such a film prepared from the PMMA spheres of a diameter of 275 nm (Sample No. 3). This photograph was taken in Golm by transmission (Fig. 2.14a) and reflection (Fig. 2.14b).

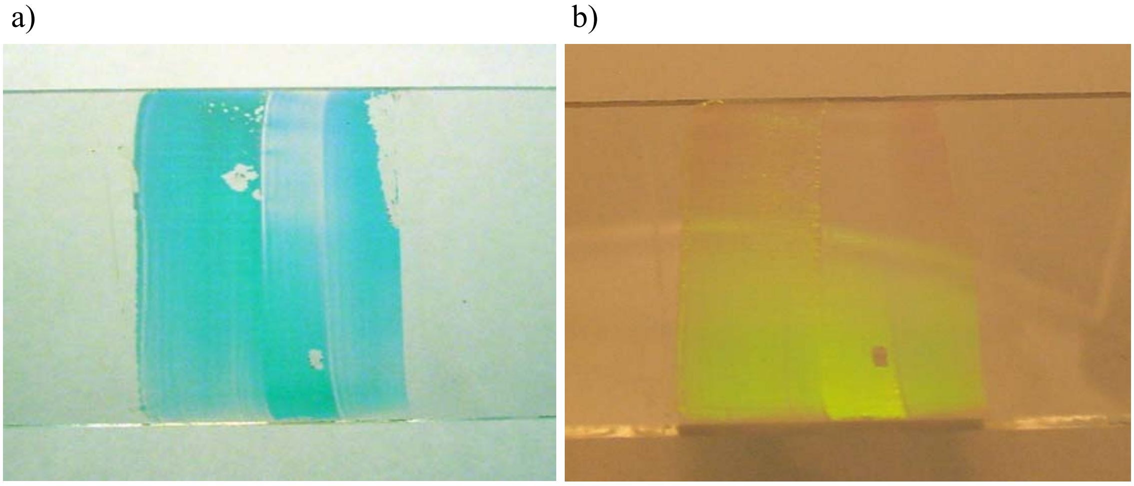

Figure 2.14. A photograph of PMMA crystal film having a sphere diameter of 275 nm prepared by vertical deposition technique: a) Taken by transmission, b) taken by reflection.

3D colloid crystallization is induced by attractive capillary forces present between particles at the solid-liquid-gas contact line. It has previously been shown that a concave meniscus between the monodisperse spheres and rather slow evaporation at the contact line are prerequisites to obtain highly ordered colloidal layers. If this meniscus is slowly swept across a vertically placed substrate by solvent evaporation, thin planar opals can be deposited (Fig. 2.15).

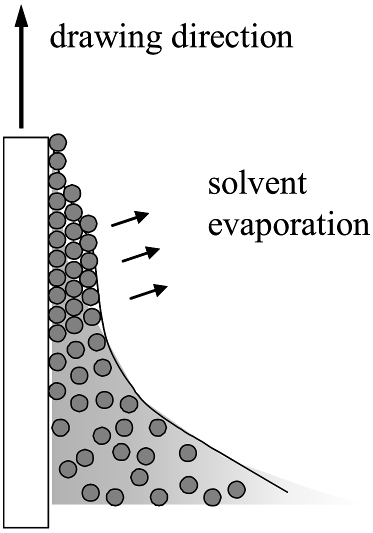

Figure 2.15. Schematic illustration of vertical deposition.

The thickness of this planar opal is dependent on suspension concentration and solvent evaporation, which is influenced by temperature, ambient humidity, and the drawing speed. Unfortunately, under our lab conditions it is not possible to control the ambient humidity and it changes day to day, sometimes from day to night, depending on the weather. As a result of this fact, the thickness of such films differs in the drawing direction (Fig. 2.14). However, principally it is possible to obtain the crystal films with a homogenous thickness of a size larger than one cm by this technique. The PMMA crystal films produced from this present work have the thickness of 5 – 50 layers. Fig. 2.16a is the optical microscopy from such a film. It is shown that the domain sizes are in the order of 100 µm^2. Fig. 2.16b is a single domain of PMMA colloidal crystals.

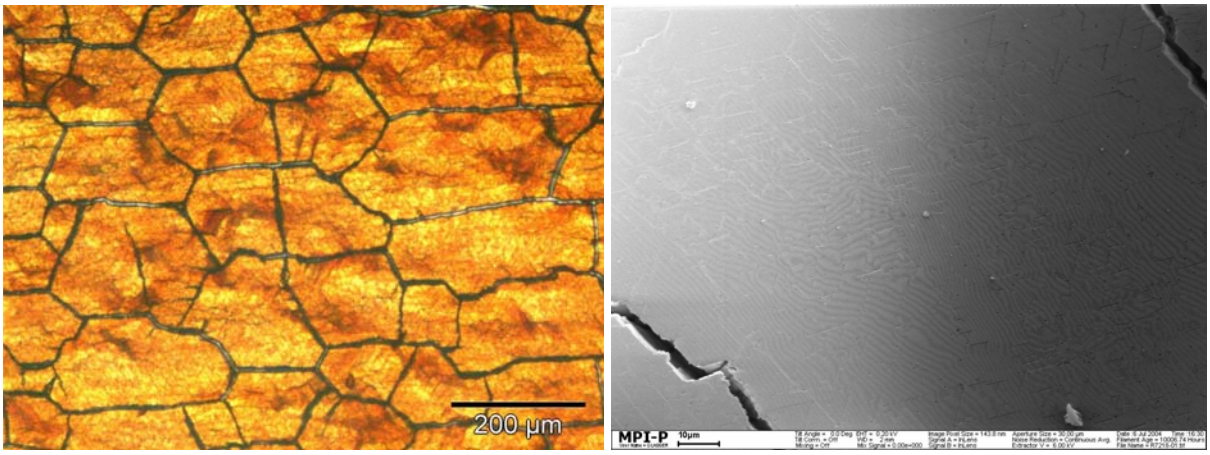

Figure 2.16. a) The optical microscopy of PMMA opals with a sphere diameter of 367 nm. b) SEM image of a single domain of these PMMA opals.

It is worth mentioning that this method works especially well in a polymer latex suspension system, in which water is usually used as a solvent (ethanol swells the polymer latex). The suspension of polymer latex and water is quite stable because of their similar densities. This is necessary for using successfully the vertical deposition technique. The drawback of using water as solvent is that water favours fluctuations, which leads to getting an uneven surface on the opaline film (Fig. 2.17). But this only has a visual effect and no influence on the optical property.

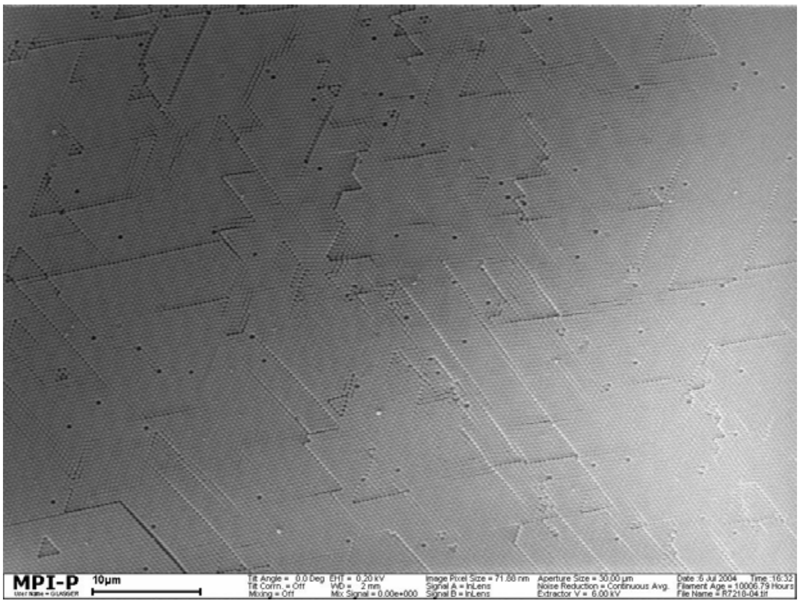

Figure 2.17. SEM image of PMMA opaline film produced from water dispersion.

2.3.3 PMMA Opal Structure Analysis by SEM

SEM is the best and most revealing method for investigating colloidal crystal structures. By this method silica opal structures have been exhaustively investigated from previous work[109] and the long range fcc packing of the silica spheres was observed. Fig. 2.18[12] shows SEM images of typical fcc planes taken from a real silica opal (Fig. 2.18a was from the growth surface and Fig. 2.18 b-d were from the facets) in comparison with a model crystal of fcc lattice. Fig. 2.18 a and b correspond both to a (111)-plane of an fcc structure, only they are oriented in different directions. Fig. 2.18c is an example of a (110) type surface. The arrangement here is a rectangular lattice where the particles array in different distances. Similar sorts of arrangements exist in the hcp structure, but there the ratio between the rectangle sides is larger. This facet is less frequently found due to its low density, which makes its appearance unlikely after cleavage. In Fig. 2.18d, a square arrangement can be clearly observed, which can only correspond to a (100) type face of an fcc structure. No facet of an hcp structure can show such an arrangement.

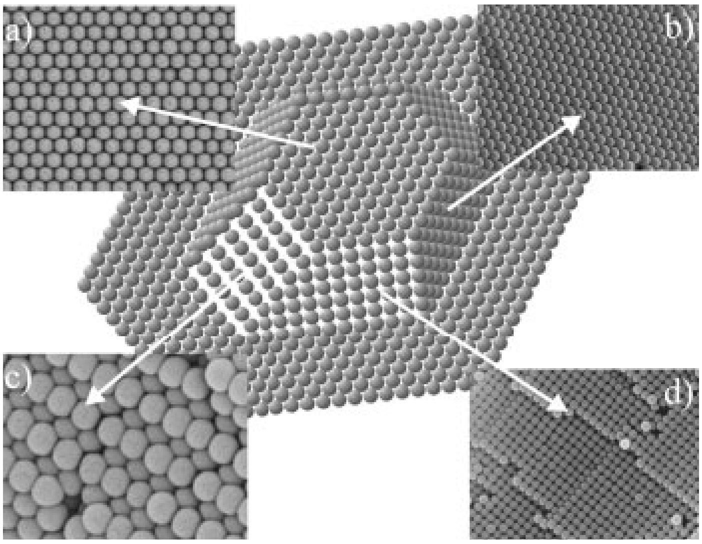

Figure 2.18. SEM images of four facets in a silica opal to be compared with a model crystal (center): a) Outer (111), b) inner (111), c) inner (110), and d) inner (100).[12]

These fcc lattice planes mentioned above have also been observed in PMMA opals from this present work. Fig. 2.19 to 2.22 are SEM images of some examples of the PMMA opals fabricated by growing PMMA spheres of a diameter of 367 nm on the horizontal substrates. The (111)-plane of an fcc structure can be observed either at the opal surface (Fig. 2.19a) or at its facet as obtained by sample cleavage (Fig. 2.19b). Fig. 2.20 to 2.21 show the lateral facets, which correspond to (110)-, and (100)-plane of an fcc structure respectively.

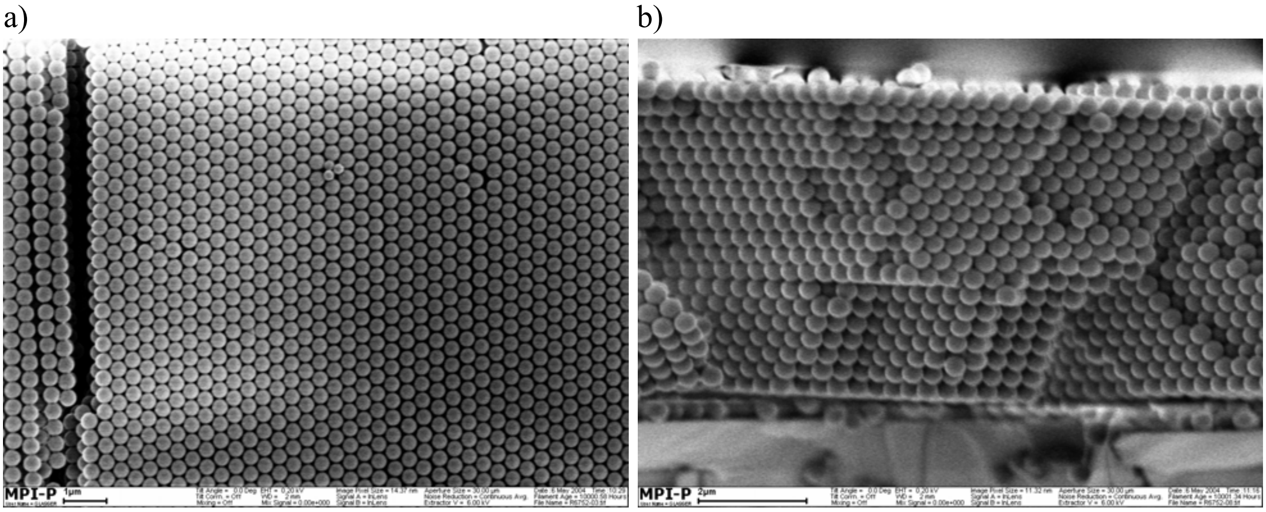
a)

b)

Figure 2.19. SEM image of top (a) and lateral surface (b) of a PMMA opal sample made of 367 nm diameter spheres, which correspond to a (111)-plane of an fcc structure.

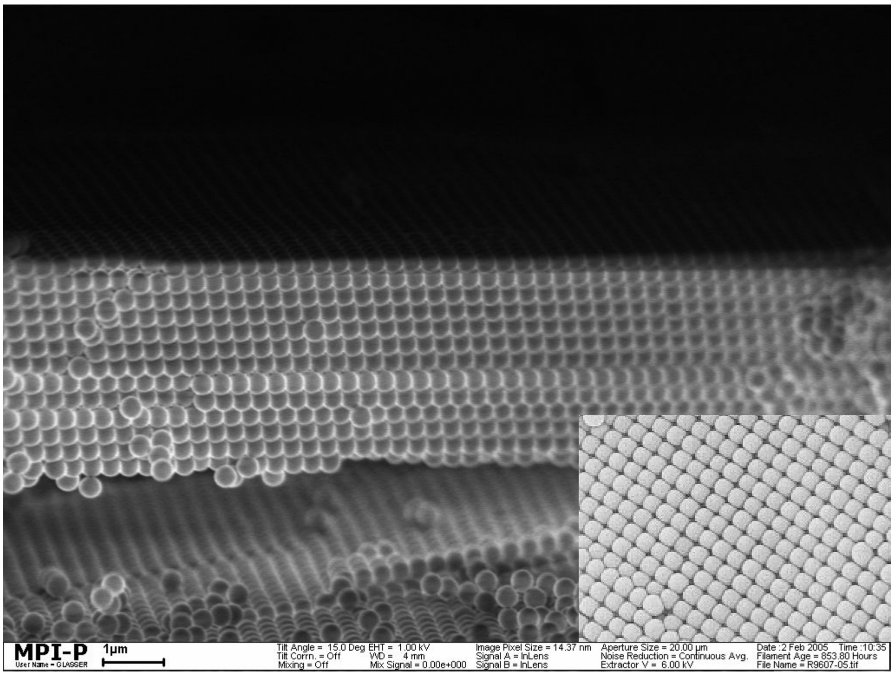

Figure 2.20. SEM image of a large (100) type facet obtained in a cleaved edge of a PMMA opal made of 367 nm diameter spheres. The figure in the inset is from silica opal.[109]

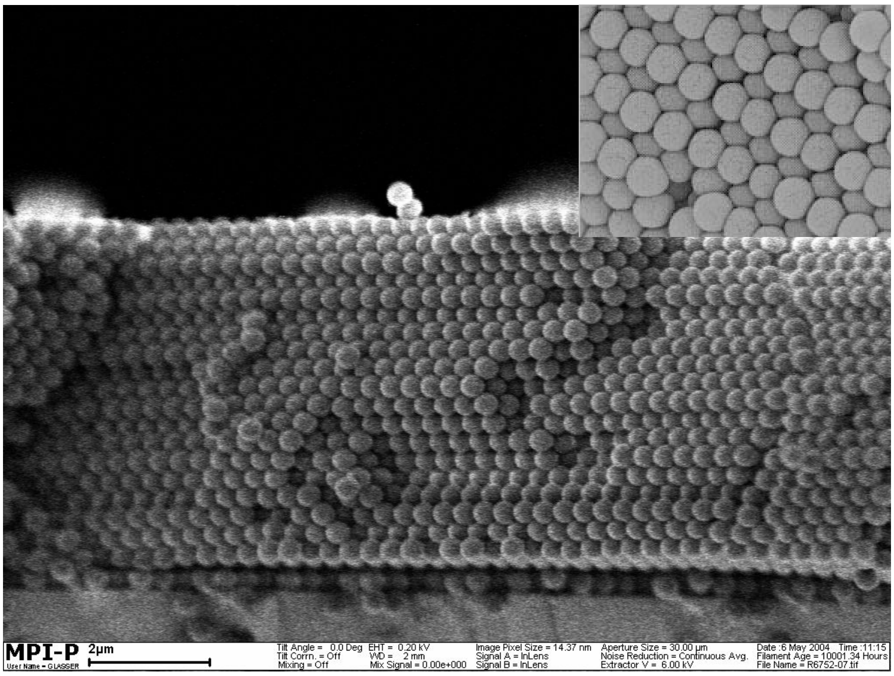

Figure 2.21. SEM image of a large (110) type facet obtained in a cleaved edge of a PMMA opal made of 367 nm diameter spheres. The figure in the inset is from silica opals.[109]

An interesting example is Fig. 2.22. It is a SEM image of a PMMA opal sample made of 367 nm diameter spheres, in which different crystalline planes corresponding to the (111)-, (110)-, and (100)-plane of an fcc structure respectively can be observed in the same piece of the sample. The analysis by SEM confirms that PMMA opals possess a well defined fcc lattice structure.

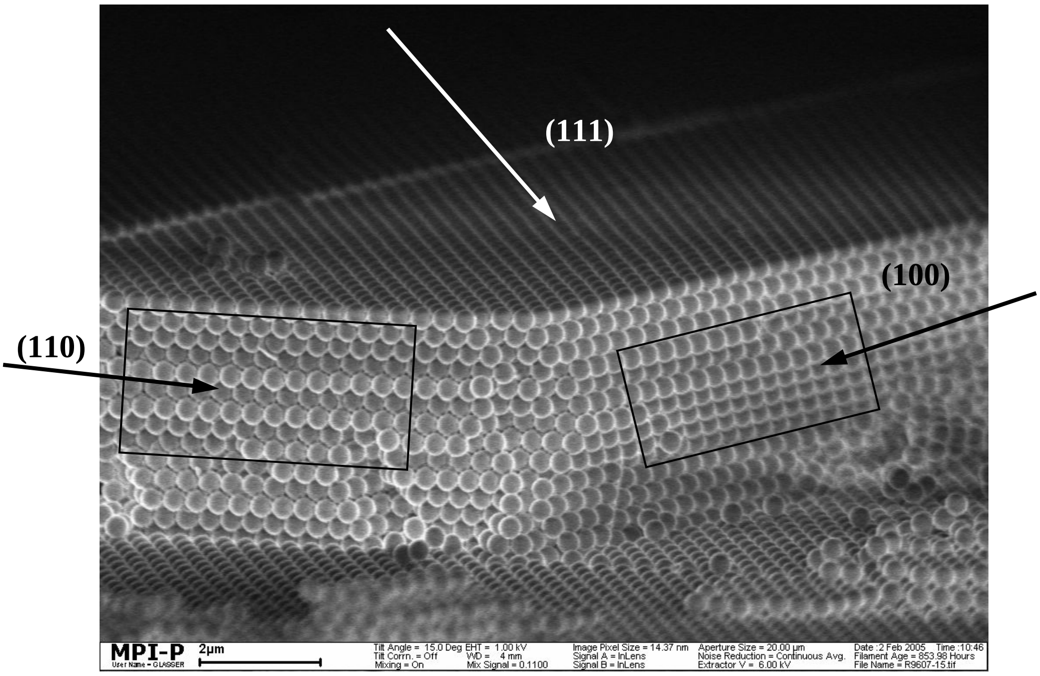

Figure 2.22. SEM image of different crystalline planes corresponding to the (111)-, (110)-, and (100)-plane of a fcc structure respectively in one piece of the PMMA opal sample made of 367 nm diameter spheres.

2.3.4 Optical Properties of PMMA Opaline Films

SEM is used to study the surface, i.e., it is limited to two dimensions. In order to determine the periodicity of the opal lattice in three dimensions, transmission and reflectance measurements were performed by a Perkin-Elmer Lambda 19 UV/VIS/NIR Spectrometer in Golm. The spectra were collected using a beam with a macroscopic spot size of 9x1 mm^2. Four samples (No. 3, 5, 6, and 7) were measured. The PMMA opals were self-assembled on hydrophilized glass substrates, from a 1.5-3 vol. % dispersion of PMMA spheres in de-ionized water, using the vertical deposition technique as illustrated in Fig. 2.15. These opals have about 15-35 layers. Fig. 2.23a shows the transmission spectra measured at normal incidence (Θ = 0°). The reflectance spectra were obtained at the incidence of angle Θ = 6° for sample No. 3, 5, 6, and at Θ = 15° for No. 7 (Fig. 2.23b). The relative bandwidth of the spectra is also determined (Fig. 2.23) and the values Δλ/λ from the reflectance spectra are very close to that from theoretical calculation Δλ/λ = 0.056. The nice high order diffraction peaks can be observed in both cases of transmission and reflection. In reflectance spectra the Fabry-Pérot fringes can be clearly seen (also in transmission spectra, but not so well developed). These confirm the high quality of the PMMA opals.

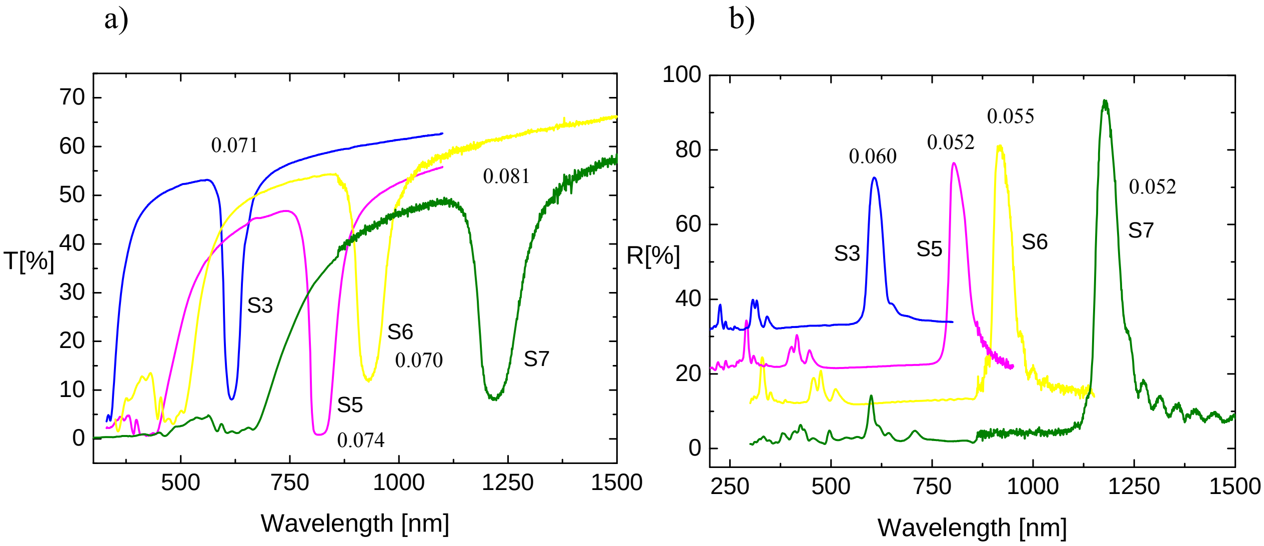

Figure 2.23. a) Transmission spectra and their relative bandwidth Δλ/λ, which were measured at normal incidence (Θ = 0°) from Sample No.3 (S3), 5 (S5), 6 (S6), and 7 (S7). b) The reflectance spectra and their relative bandwidth Δλ/λ, which were measured at the incidence of angle Θ = 6° for sample No. 3 (S3), 5 (S5), 6 (S6), and at Θ = 15° for No. 7 (S7).

2.3.4.1 Angular Dependent Transmission Spectra

Standard angular resolved reflectance/transmission measurements were carried out to study the PBG effect along the (111) direction in the opal photonic crystal.[99c,110] The angular dispersion of the stop band was studied by changing the angle of incidence Θ between the beam and the (111) axis of the fcc crystal from 0° to 70°. Transmission spectra of sample No. 3 collected at different angles Θ are shown in Fig. 2.24 (left). As the angle increases, band corresponding to the (111) Bragg reflection shifts to shorter wavelengths according to the Bragg law, while band from (200)-plane shifts to a longer wavelength. This is summarized in Fig. 2.24 (right), where both peaks' wavelengths are plotted against Θ°. Splitting of the Bragg resonance into two peaks was observed for angles between $\Theta \approx 50°$ and 70° (Fig. 2.27 and 2.28). This behaviour was attributed to the (200) Bragg reflection, when the specular conditions for reflectance are satisfied for both (111) and (200) sets of planes.[111] In Fig. 2.24 (left), a clear attenuation band can be seen in short wavelength range, which may correspond to the (220) Bragg reflection and seems hardly dependent on angles.

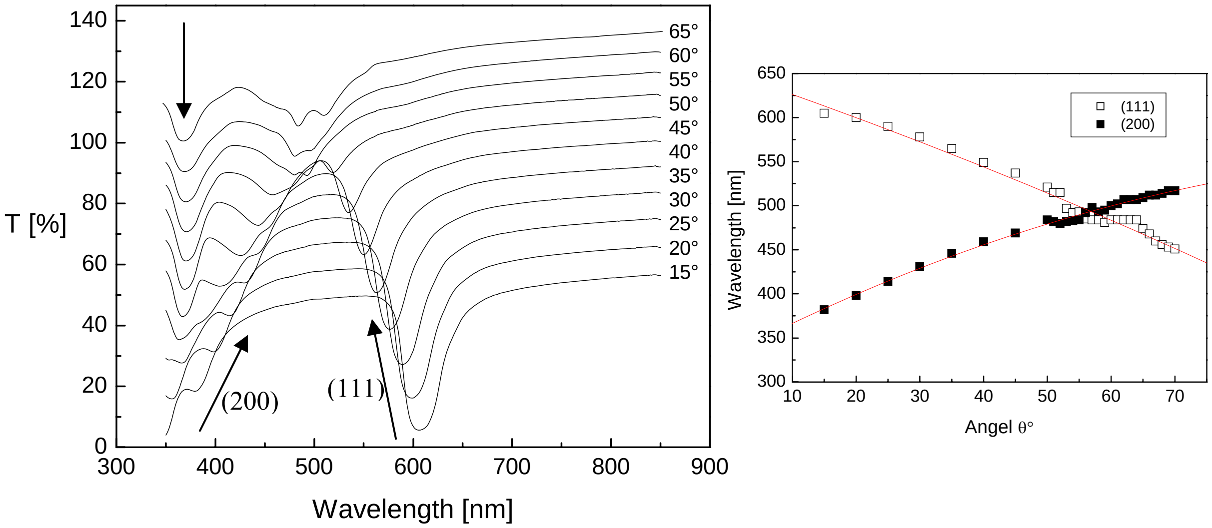

Figure 2.24. Left: Angle resolved transmission spectra of PMMA opal film (Sample No. 3) for angles between 15° and 65° from bottom to top with a 5° step. Spectra have been vertically shifted for the sake of clarity; right: Peak wavelength of the (111) and (200) are plotted against Θ° (empty and full squares, respectively). The lines are only for the eye.

Similar observations are also obtained from other samples. Fig. 2.25 is the angle resolved transmission spectra of sample No. 3, 5, 6, and 7 for angles between 0° and 60°. These follow well the Bragg condition (Fig. 2.25, inset) according to the equation

$$\lambda_B = 2d\,(n_{\mathrm{eff}}^2 - \sin^2\Theta)^{0.5},$$

where λ_B is the peak wavelength, $d = (2/3)^{1/2}D$ is the lattice constant along the (111)-axis, involving the sphere diameter D of the close-packed fcc lattice, Θ is the angle between the incident beam and the normal to the (111)-plane, and n_{eff} is the effective refractive index determined by $n_{eff}^2 = n_{sphere}^2\Phi + n_{air}^2(1-\Phi)$, with Φ being the volume fraction of PMMA spheres (1.3786 for PMMA by $\Phi = 0.74$). The value of n_{eff}, d, and D obtained by nonlinear fitting to the Bragg equation are collated in Table 2.4.

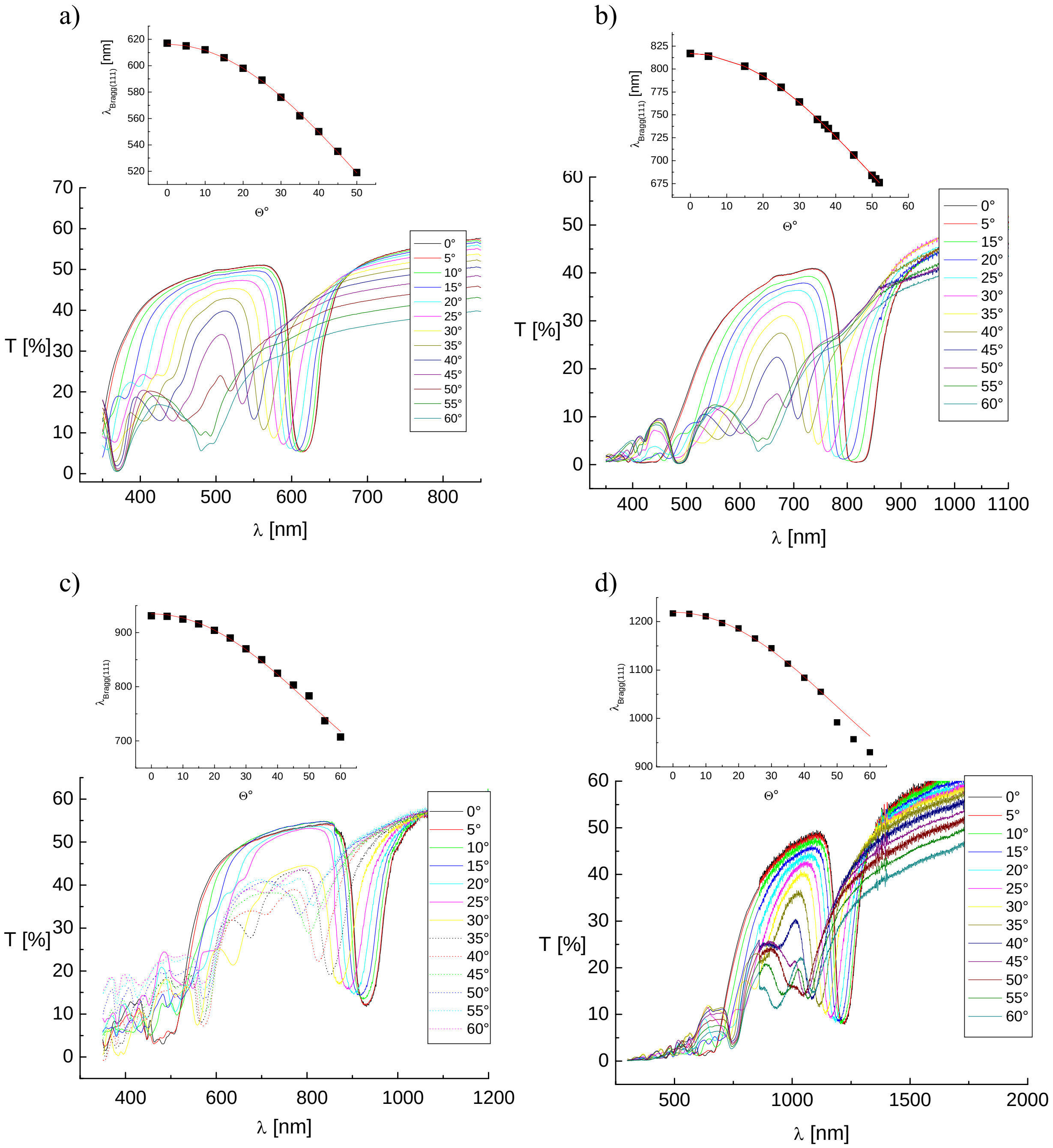

Figure 2.25. Angle resolved transmission spectra of PMMA opal films for angles between 0° and 60° with a 5° step: a) Sample No. 3; b) sample No. 5; c) sample No. 6; d) sample No. 7.

Table 2.4. Constants of PMMA opals and their sphere size obtained by nonlinear fitting to the Bragg equation

Sample No.	effective refractive index n_{eff}	grating constant d [nm]	particle diameter D [nm]
3	1,4189	217	266
5	1,4044	291	357
6	1,3510	346	424
7	1,3830	443	543

The effect of the angular dispersion of the stop band is also visually noticeable. Fig. 2.26 shows two pictures of the same PMMA opal film from sample No. 3, which were taken in Golm in different film positions: One was level (Fig. 2.26a); another was titled (Fig. 2.26b). They show totally different colours.

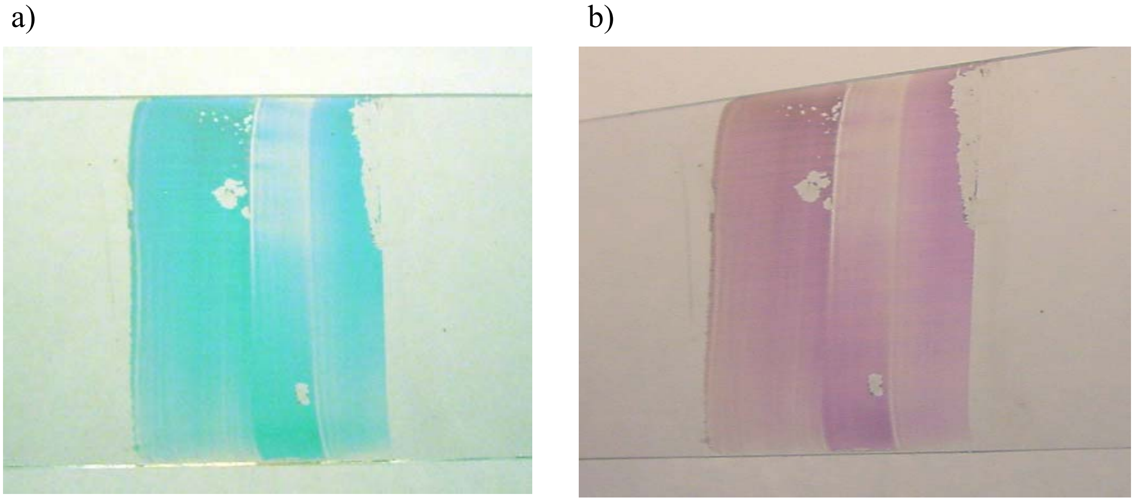

Figure 2.26. Pictures of PMMA opal film in different positions: a) Level; b) titled.

It is worth mentioning that the angle resolved transmission spectra of PMMA opal film for angle range between 50° and 70° look especially exciting. Fig. 2.27 and 2.28 are angle resolved transmission spectra of PMMA opal film (sample No. 5) collected at angles 50°-60° and 60°-70° respectively, in which not only the splitting of the Bragg resonance into two peaks was observed, but also the nice high order band structures could be detected, which shift very finely to longer wavelengths. Unfortunately, there is no theoretical calculation that could represent it, but this may be of interest in photonic band structure studies. In addition the high homogeneous angle resolved spectra reflect the excellent crystal quality.

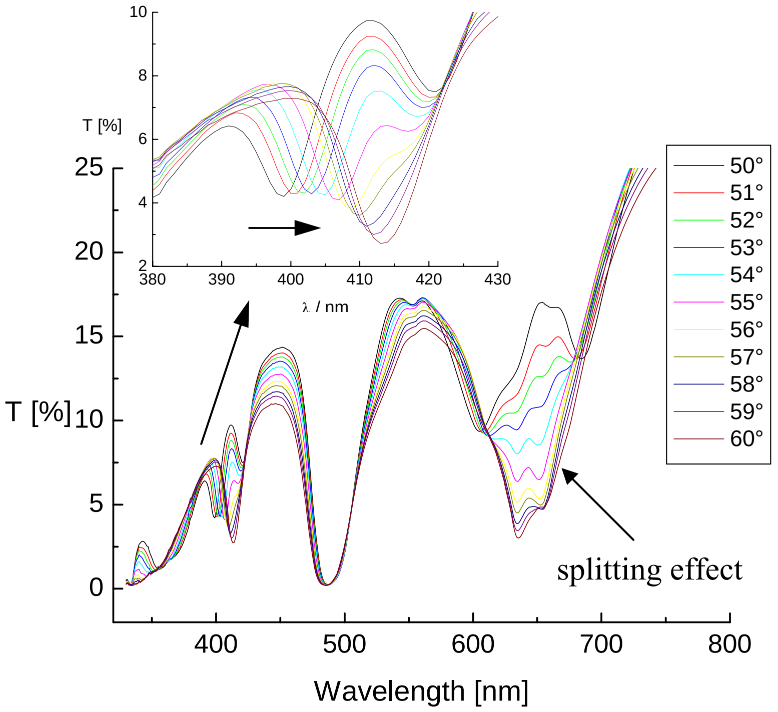

Figure 2.27. Angle resolved transmission spectra of PMMA opal film (Sample No. 5) for angles between 50° and 60° from bottom to top with 1° step.

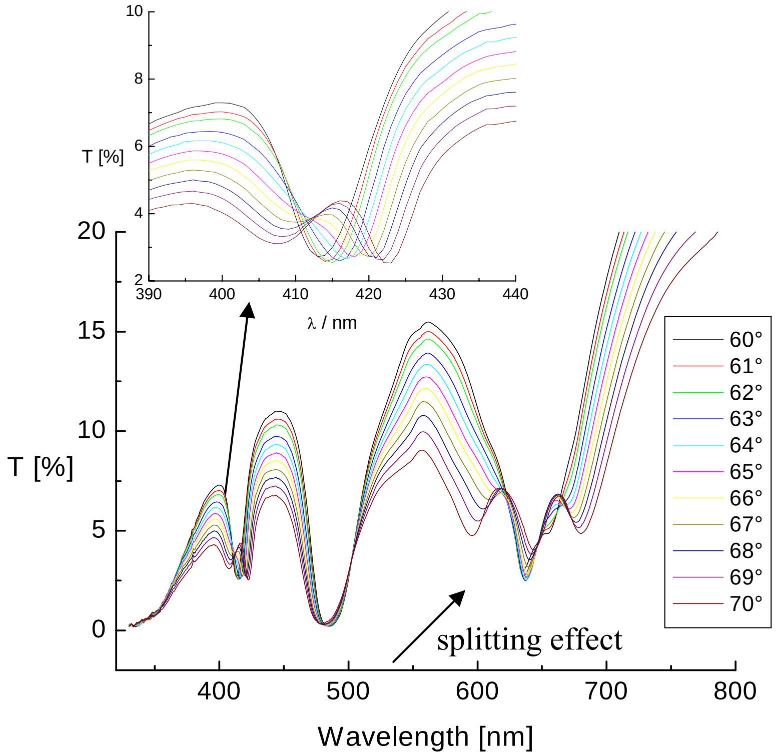

Figure 2.28. Angle resolved transmission spectra of PMMA opal film (Sample No. 5) for angles between 60° and 70° from bottom to top with 1° step.

2.3.4.2 Angular Dependent Reflectance Spectra

Figure 2.29 shows the angular resolved reflectance spectra of sample No. 5 for angles Θ between 6° and 65° (left) and the dispersion of the Bragg diffraction peaks (right). The value of the effective refractive index n_{eff} =1.361 and the lattice constant d =297 were obtained by nonlinear fitting to the Bragg equation from the reflectance spectra.

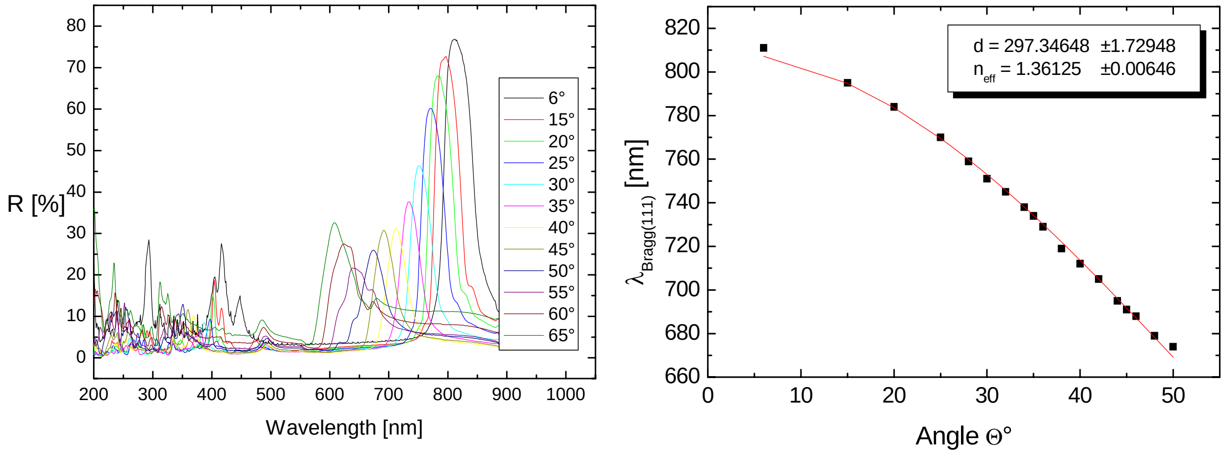

Figure 2.29. Angular resolved reflectance spectra of sample No. 5 for angles Θ between 6° and 65° (left) and the dispersion of the Bragg diffraction peaks (right).

The positions of diffraction stop bands for each set of (*hkl*) planes follow to the Bragg condition which is given by

$$\lambda = 2 d_{h,k,l} \sqrt{n_{eff}^{2} - \sin^{2}(\alpha - \Theta)}\ ,$$

where λ is a Bragg reflection wavelength, $d_{h,k,l}$ is the grating constant (interplanar spacing), Θ is the angle between the incident beam and the substrate normal. n_{eff} is the effective refractive index, α is the angle between a (*hkl*) plane and the (111) plane. For a fcc lattice (h,k,l –Millers indices) the inter-planar spacing (d_{hkl}) is related to the sphere diameter (D) and the unit cell parameter (a) according to

$$d_{h,k,l}^{2} = a^{2}/\left(h^{2} + k^{2} + l^{2}\right) \quad \text{, with } a = D \cdot \sqrt{2}\,.$$

In the case of highly fcc ordering, the Bragg reflections are predicted to occur for either all even or all odd h,k,l indices, i.e. (*hkl*) planes (111), (200), (220), (311), etc.[112] For sample No. 5 (Fig. 2.29), for example, multiple diffraction peaks could be indexed to different sets of planes for the reflectance spectra (6°) of the colloidal crystal template at 806nm (111), 447nm (220), 415nm (222), 402nm (311), 291nm (400). Fig. 2.30 shows angle dependence of the spectral position of Bragg peaks for different (*hkl*) planes from sample No.5. The full symbols represent the experimental date (splitting range (○); unknown reflections (∇)), while the solid lines come from the calculations.[99b,113] It can be seen in Fig. 2.30 that with a few exceptions, the experimental date corresponded well to the calculated wavelengths. Fig. 2.30 was made from Dr. Jürgen Wagner from Fraunhofer Institute in Golm. The identification of numerous diffraction planes from the reflectance spectra confirms the high quality of PMMA opals.

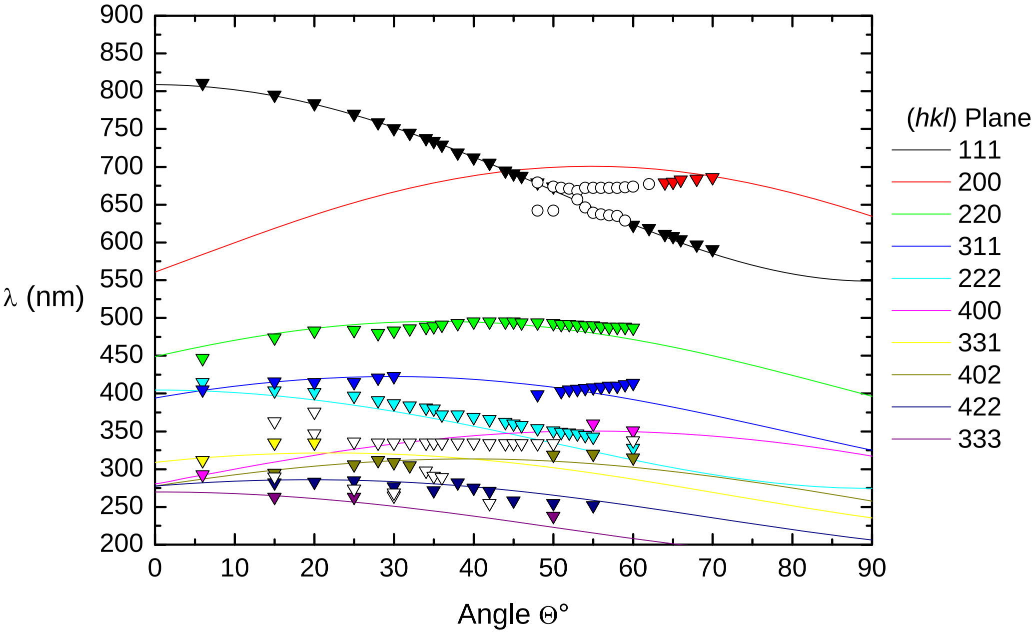

Figure 2.30. Angle dependence of the spectral position of Bragg peaks for different (*hkl*) planes from sample No.5. The full symbols represent the experimental date (splitting range (○); unknown reflections (∇)), while the solid lines come from the calculations.

2.3.4.3 High Order Diffraction Bands of PMMA Opals

One of the important criteria for high quality opaline films is the observation of the high order diffraction peaks. Defects in the array cause the diffraction peaks to widen. As a result they can be found close together which means that resolution of the diffraction peaks can be used as a measure of the quality of the arrays prepared.[114] For samples prepared from the same spheres, the difference in their spectra is due to defects and cracks, so it is easier to determine their quality by comparing spectra. The intensity of the diffracted peak increases approximately linearly with the number of layers. Fig. 2.31 shows the absorbance spectra of the PMMA opaline films made of 367 nm diameter spheres with the different thickness (from about 10 to 30 layers). However, it is also observed that the behaviour of the high order bands differed from the stop band with respect to absorbance intensity by increasing number of layers (Fig. 2.32). In fact the optical property of the high order bands is very complicated owing to many energy bands overlapping and they are extremely sensitive to the colloidal crystal misalignments and defects.

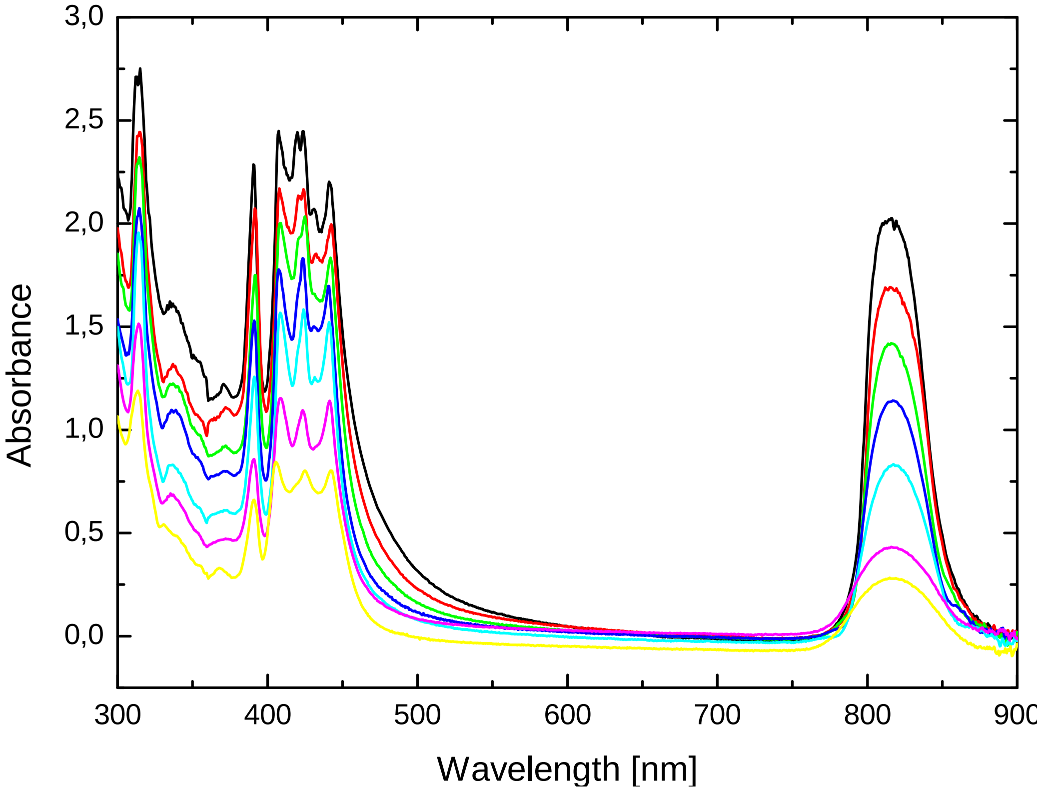

Figure 2.31. Absorbance spectra of the PMMA opaline films made of 367 nm diameter spheres with the different thickness (about 10 to 30 layers from bottom to top).

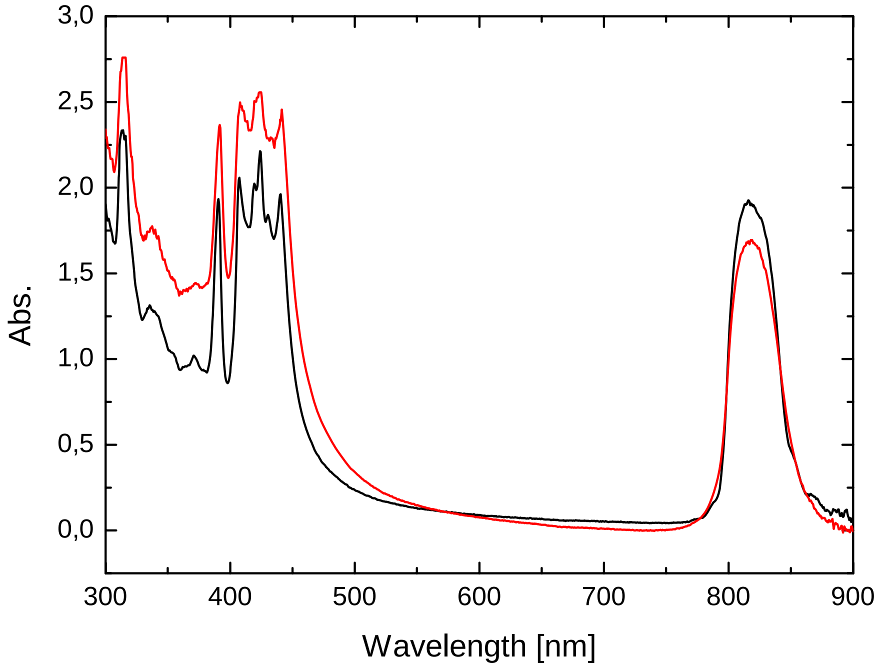

Figure 2.32. Comparison of the absorbance spectra of two PMMA opal samples made of 367 nm diameter spheres with different film thickness.

Figure 2.33 shows the comparison of absorbance spectra of three PMMA opal samples consisting of 367 nm diameter spheres with different film thickness. The blue line represents the spectrum from the film consisting of less than 10 layers, while the black line shows the film having about 25 layers and the red line represents the film composed of more than 35 layers. It can be seen in Fig. 2.33 that the spectrum of the film having about 25 layers has the best resolution of high order diffraction bands and the narrowest band width. It has been observed that the two diffraction peaks which are pointed out by arrows in Fig. 2.33 appeared only from the films with certain thickness (more than about 20 layers) and they were not found from the thin films (Fig. 2.31 and Fig. 2.33). However, the fusion of high order diffraction peaks has been observed (Fig. 2.33) if the opaline film is relative thick (more than 35 layers).

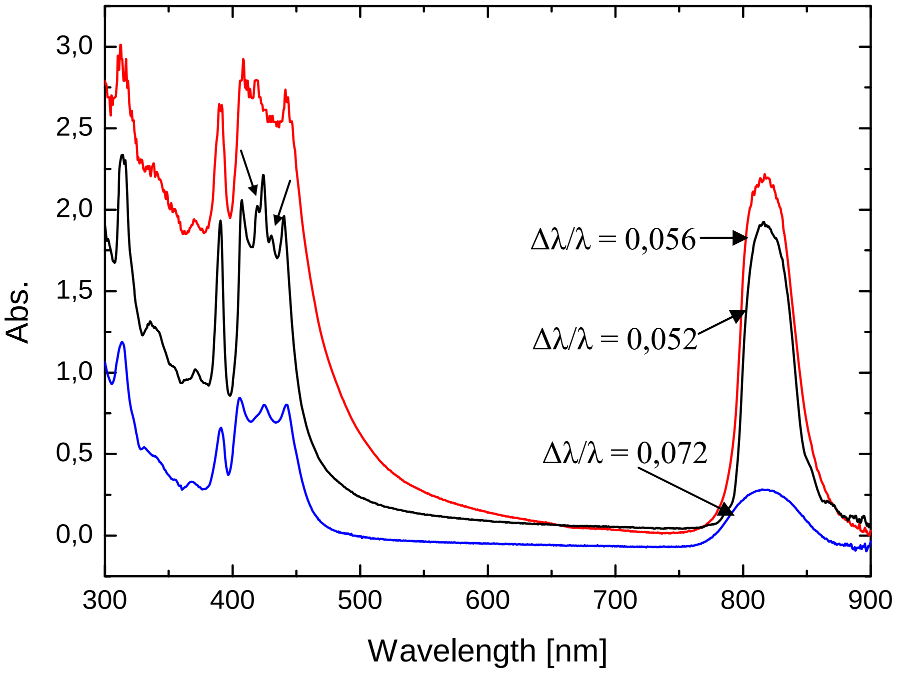

Figure 2.33. Comparison of absorbance spectra from three PMMA opal samples consisting of 367 nm diameter spheres with different film thickness. The blue line represents the spectrum from the film consisting of less than 10 layers, while the black line shows the film having about 25 layers and the red line represents the film composed of more than 35 layers.

Alternatively, the spectra can be reduced to the dimensionless units a/λ, where a is the lattice constant ($a = \sqrt{2}D$, where D is the sphere diameter). Fig. 2.34 shows the reduced transmission and reflectance spectra for PMMA opaline films made of 275 nm (Sample No. 3), 367 nm (Sample No. 5), 418 nm (Sample No. 6), and 540 nm (Sample No. 7) diameter spheres. It is evident that many diffraction peaks of the 367 nm, 418 nm, and 540 nm coincide and must be related to an intrinsic property of the photonic band gap materials. The position of the high order diffraction peaks of the opaline film prepared of 275 nm diameter spheres deviates from the position of that from 367 nm, 418 nm, and 540 nm large spheres. This deviation can be explained in terms of the PMMA refractive index dispersion. The scaling as described here only applies for systems possessing the same refractive index. The high order diffraction peaks of the opaline film made of 275 nm diameter spheres occur at wavelengths below 350 nm. At this wave range a significant change in the refractive index could be expected.

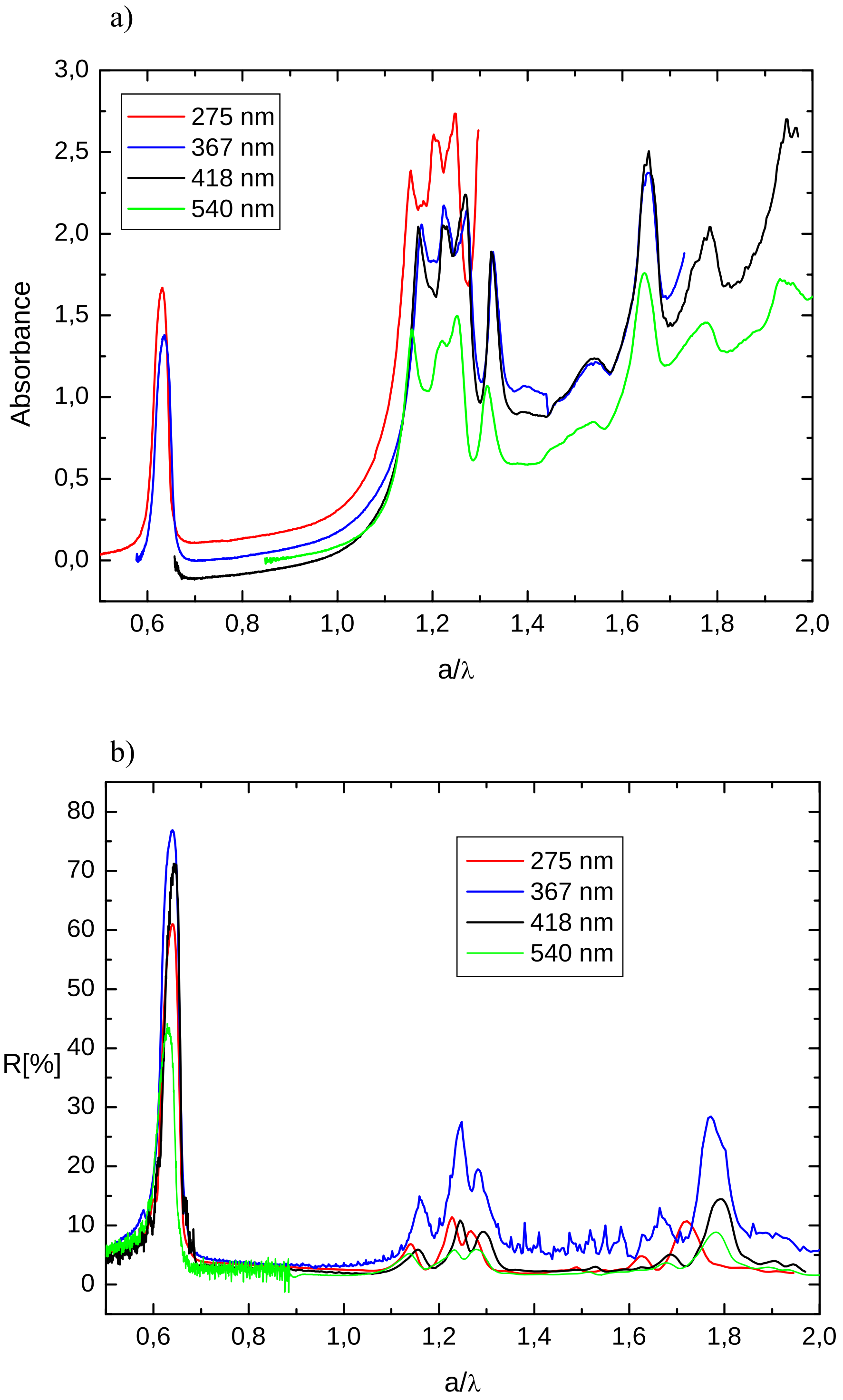

Figure 2.34. Reduced transmission and reflectance spectra for PMMA opline films made of 275 nm (red line), 367 nm (blue line), 418 nm (black line), and 540 nm (green line) diameter spheres: a) Transmission spectra, b) reflectance spectra.

2.3.5 Spatially Resolved Microscopy

A typical colloidal crystal film is comprised of many single crystals (Fig. 2.12, 2.13, and 2.16) and varies in size from several micrometers to hundred micrometers. In order to study the optical homogeneity of the PMMA opals with respect to crystal domain size, spatially resolved transmission measurements were performed by microscope spectroscopy, which were done by Dr. Martina Gerken in the Light Technical Institute of the University of Karlsruhe. A small beam spot from 1µm x 1µm to 10 µm x 10 µm was used. A PMMA opal film of sample No. 3 was measured, in which three measurements were performed:

a) A large crystallite of a size of about 0.1 mm was measured with a 0.001 mm step. The results are shown in Fig. 2.35. It can be seen that within this crystal at the area of 10 µm x 10 µm the transmission spectra are hardly changed.

b) Homogeneous small crystals of a size of about 0.05 mm were measured with a 0.001 mm step. Fig. 2.36 shows the transmission spectra, which are relatively constant within a crystal, but a few change constantly from one to another.

c) A large area consisting of different size crystals was measured with a 0.01 mm step. The results can be seen in Fig. 2.37. The significant variation of the transmission spectra has been observed.

In conclusion, the transmission spectra hardly changes within a crystal and changes relatively seldom within homogeneous crystals, but they change significantly within different size crystals.

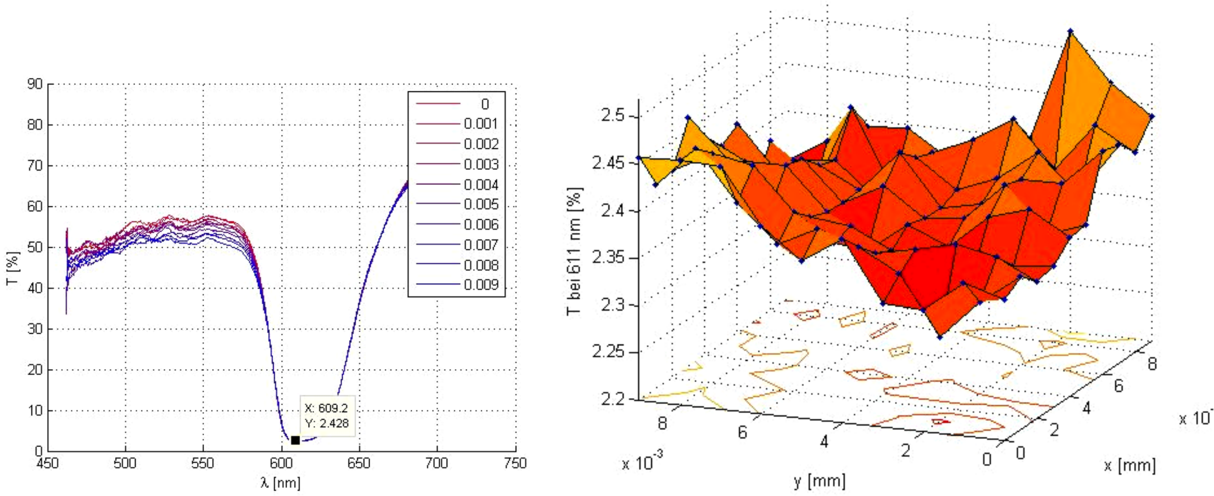

Figure 2.35. Spatially resolved transmission spectra of a single PMMA crystal (about 0.1mm, sample No. 3). Left: spectra in one direction; right: spectra in two directions, which were taken at the wavelength 611 nm.

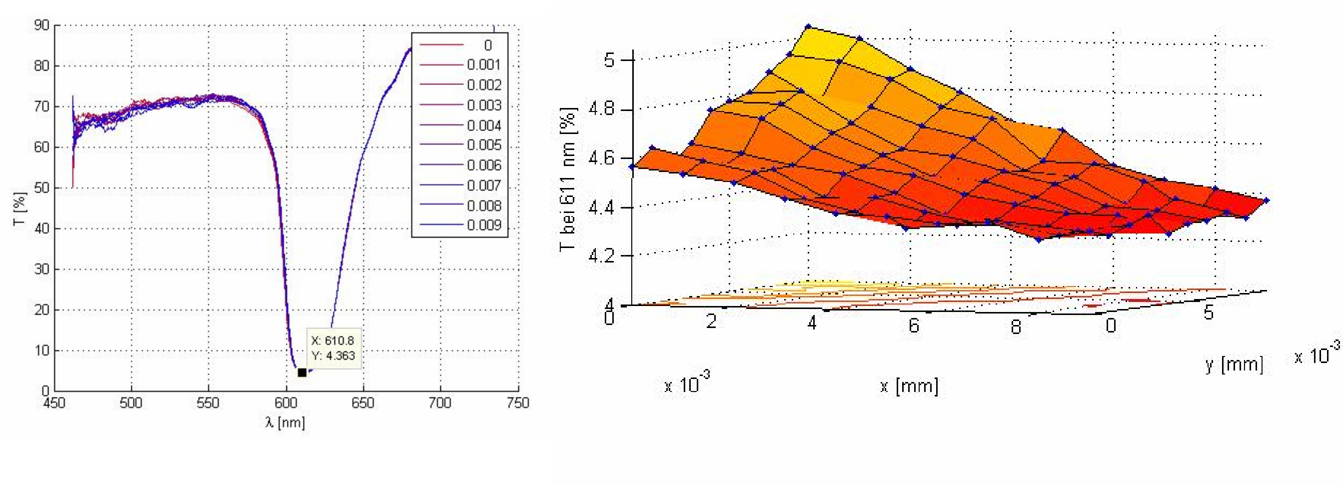

Figure 2.36. Spatially resolved transmission spectra of homogenous small PMMA crystals (about 0.05 mm, sample No. 3) with a 0.001 mm step. Left: spectra in one direction; right: spectra in two directions, which were taken at the wavelength 611 nm.

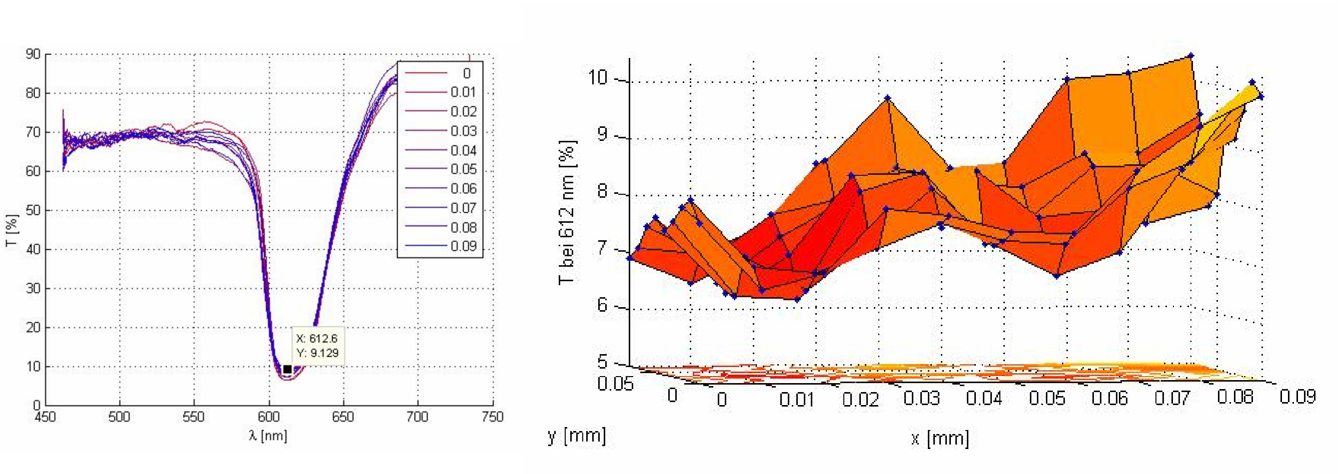

Figure 2.37. Spatially resolved transmission spectra of PMMA crystals (sample No. 3) with a 0.01mm step. Left: spectra in one direction; right: spectra in two directions, which were taken at the wavelength 611 nm.

2.4 Fabrication of Silica Opals from Large SiO_2 Spheres

In order to make silicon 3D photonic crystals, for which the photonic band gap of the replica is in the near infrared, micro-spheres made of silica with sizes greater than 850 nm are required. Such large micro-spheres have proven to be difficult to organize into large areas and well ordered lattice by the conventional methods. In the following chapter the problems of crystallizing large silica spheres are discussed and the way of solving the problem is also represented. The silica spheres used in the present work were of 890 nm diameter,[115,116] acquired from Prof. Unger from the Inorganic Chemical Institute of the University of Mainz.

2.4.1 Cleaning and Characterizing of Large SiO_2 Colloids

In the silica sphere sample fibrous dirt was observed by SEM-measurement (Fig. 2.38a). The spheres were cleaned by consecutive centrifuging, decanting and redispersing in water. The dirt was removed by sequential and multiple filtering. Fig. 2.38b shows that the cleaned SiO_2 colloids crystallize in regular arrays. Mastersizer measurements and scanning electron microscopy studies of the silica spheres showed high monodispersity, with the polydispersity index smaller than 2%.

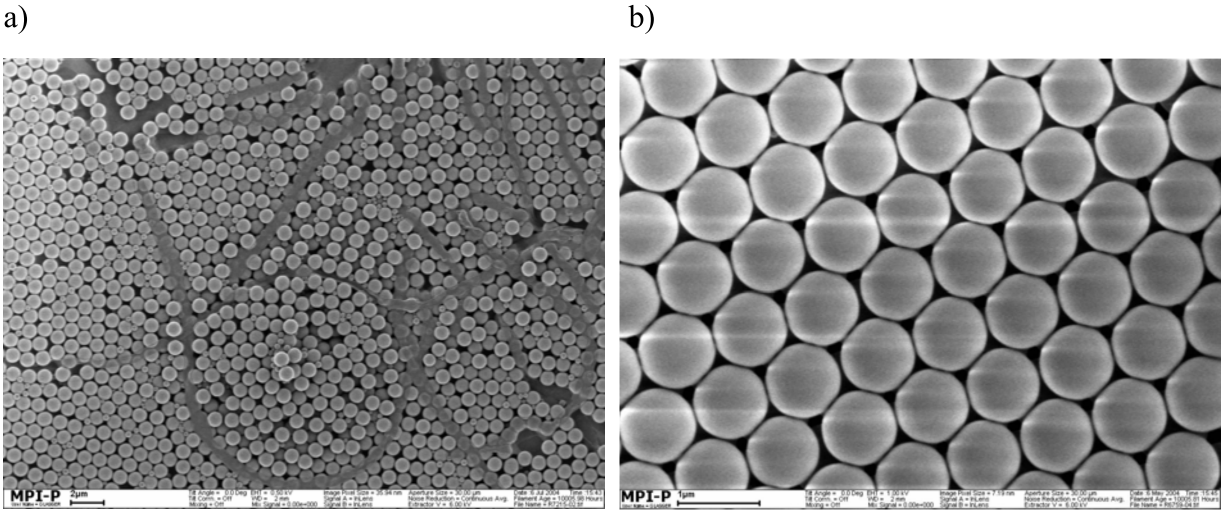

Figure 2.38. a) SEM image of silica sphere sample containing fibrous residues. b) SEM image of crystalline arrays from cleaned SiO_2 spheres.

These silica spheres have a slightly negative charge on the surface determined by the "Streaming Current Detection" (SCD) measurement (Chapter 2.2.2). Fig. 2.39 is the relationship between pH value and the charge per mass of the silica sphere.

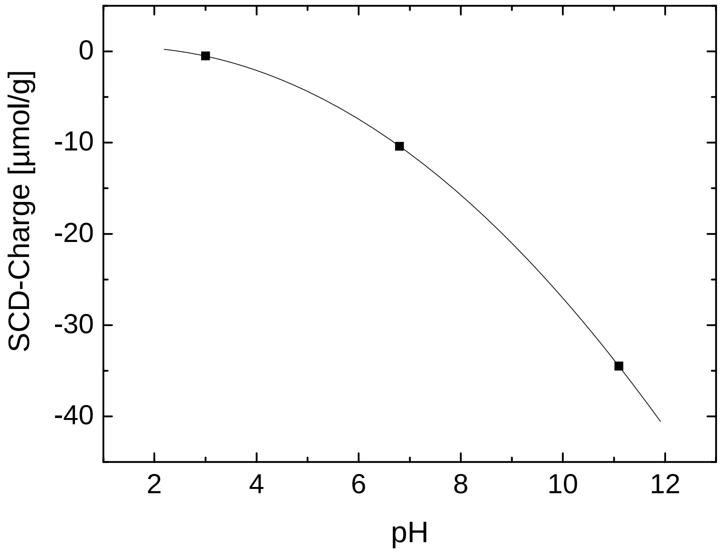

Figure 2.39. Relationship between pH value and the charge per mass of the silica sphere.

2.4.2 Crystallization of Large Silica Spheres by Lifting and Stirring

In comparison with work with polymer or small SiO_2 spheres, the main problem with large SiO_2 spheres is their rapid sedimentation in their suspension, due to their comparatively high mass. The suspension separate in a few minutes. In order to prevent sedimentation, a spinning magnetic bar at the bottom of the container was added as illustrated in Fig. 2.40, with slow stirring at 100 rpm. In this set-up, the surface of the suspension has to be far way enough from the spinning bar, so as to ensure that the suspension in the region of the meniscus contacting the substrate is maintained in a quiet state. Ethanol was used as a solvent because of its high vapour pressure. But for such large silica spheres the evaporation rate still can not match the sedimentation rate in normal condition, the arrayed spheres in front soon abandon the meniscus region. This problem was overcome by slowly lifting the substrate out of the suspension, in which the evaporation solvent was accelerated by enhancing the contact area between solvent and air and the spheres could solidify soon in substrate. Therefore, by the combined method of lifting and stirring large area and high quality colloidal crystals from large silica spheres could be obtained.

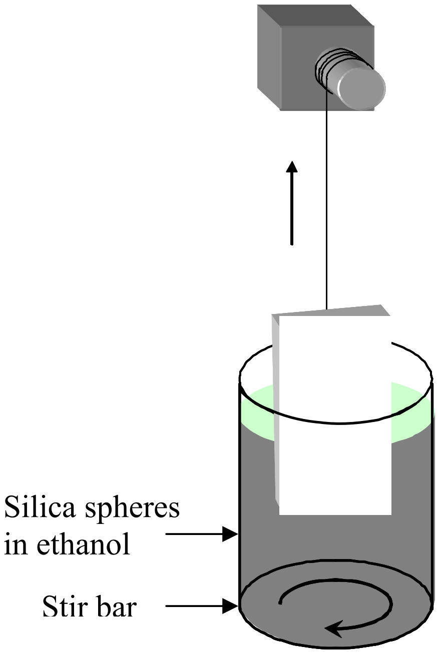

Figure 2.40. Schematic representation of the process of crystallization of large silica spheres by drawing up the substrate in a vertical position in combination with stirring.

2.4.3 Controlling of Silica Opal Quality

The important parameters for controlling the crystallization process are suspension concentration, stirring rate, and drawing speed. The crystallization was performed by drawing up the hydrophilized substrate in a vertical position with a velocity of about 200 nm s^{-1} from a 2-5 vol. % suspension of silica spheres at room temperature. Fig. 2.41 is a SEM image of silica opals on a glass substrate. In Fig. 2.41 a few very fine spheres can be observed. This is another problem of work on large silica spheres. The small faction of very fine spheres or sphere doublets, which always exist in a population of as-synthesized silica spheres, have a substantially detrimental effect on the overall arraying of the spheres. These should be separated as thoroughly as possible.

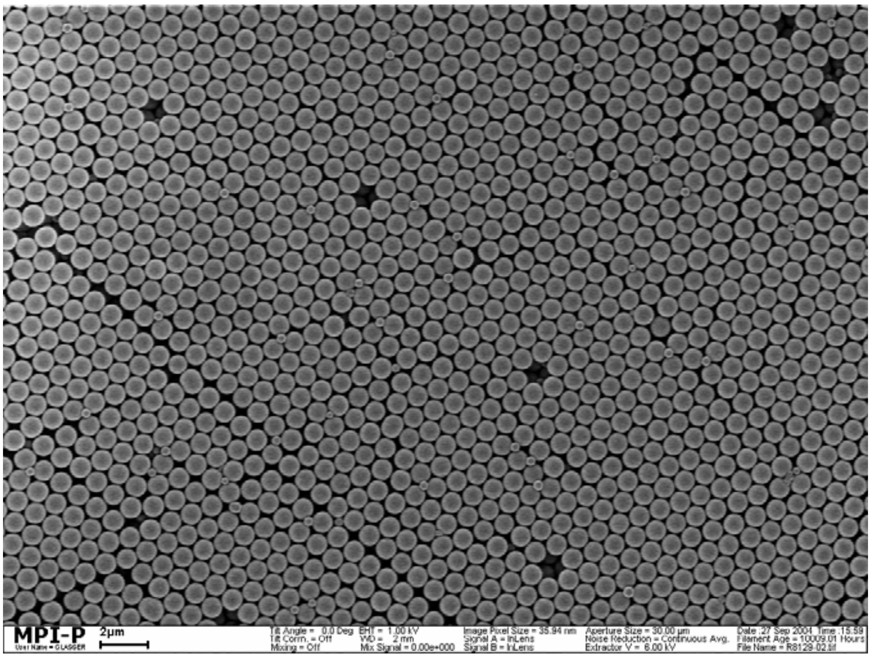

Figure 2.41. SEM image of silica opals made of silica spheres of a diameter of 890 nm on a glass substrate.

Figure 2.42 shows a SEM image of the resulting silica opal assembled on a silicon substrate after elimination of the fine spheres and sphere doublets. As shown in Fig. 2.42, a large and well ordered, nearly crack free opal film was obtained. The crystalline quality of the opal can be examined in the lateral dimension by applying the spatial Fourier transform to selected areas of the lattice images, as shown in Fig. 2.43. The Fourier transform in Fig. 2.43 shows nicely the hexagonal order of the (111) opaline crystal plane in both marked regions, which represent the corresponding size dependence of the pattern. For a sampling area of only 10 spheres the sharpness is comparable. The sharpness obtained for a large area shows well defined peaks in the spatial Fourier transform and hence proves the crystal quality.

Noteworthy is the absence of cracking even at large scales, as clearly illustrated in Fig. 2.42. This has been only observed from such silica opals made of large silica spheres. The possible reasons to explain it as follows: i) the colloidal sphere has a thin hydrodynamic shell from solvent, which forms capillary necks between the particles while the solvent evaporates in the crystal film. These capillary necks exert very strong attractions between the particles and may be responsible for the crack formation after complete drying and shrinkage of the particles. Larger sphere has thinner hydrodynamic shell in ratio to its diameter, which results in less shrinkage after drying; ii) if the spheres are mobile and they could move together as quickly as the solvent evaporating, there are no cracks. Large silica spheres are heavy and easy to move by a little force, for instance, the slight oscillation from the "lifting machine". This may be a reason for the tight packing of these silica spheres.

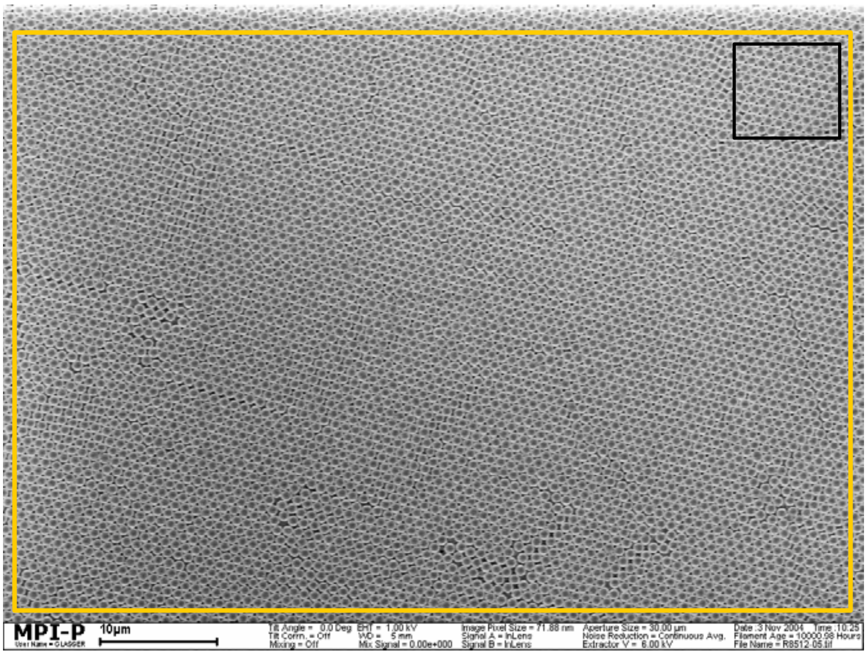

Figure 2.42. SEM image of silica opals made of silica spheres of a diameter of 890 nm on a plane Si-substrate. The small black and large white square represent the areas used for the calculation of the Fourier transforms in Fig. 2.43a and 2.43b.

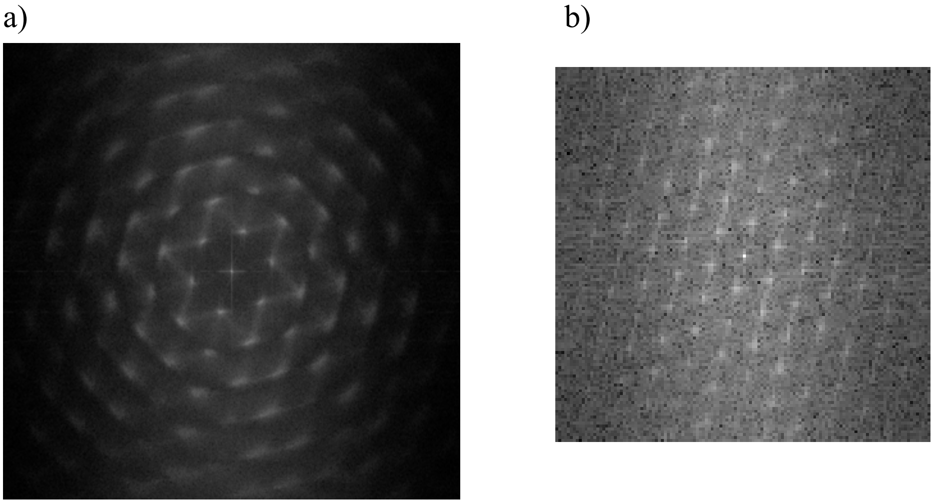

Figure 2.43. Fourier transform of Fig. 2.42: a) Large marked region about 70 µm x 50 µm; b) small marked region, about 10 x 10 spheres.

For optical characterization reflectance measurements were performed in Golm with a beam having a macroscopic spot size of 9×1 mm^2. Fig. 2.44a shows the reflectance spectrum at angle $\Theta = 6°$ with respect to the surface normal, corresponding to a Bragg peak centered at 1830 nm. The relative bandwidth of the diffraction resonance is 0.17. This value exceeds significantly the theoretically calculated value of 0.056 for the relative bandwidth along the (111)-axis of a perfect infinite opal. The major reason for this band gap broadening is, in this case, the small film thickness (about 4 layers),[102] which is emanates from the optical evaluation of the Fabry-Pérot oscillations (Fig. 2.44b).

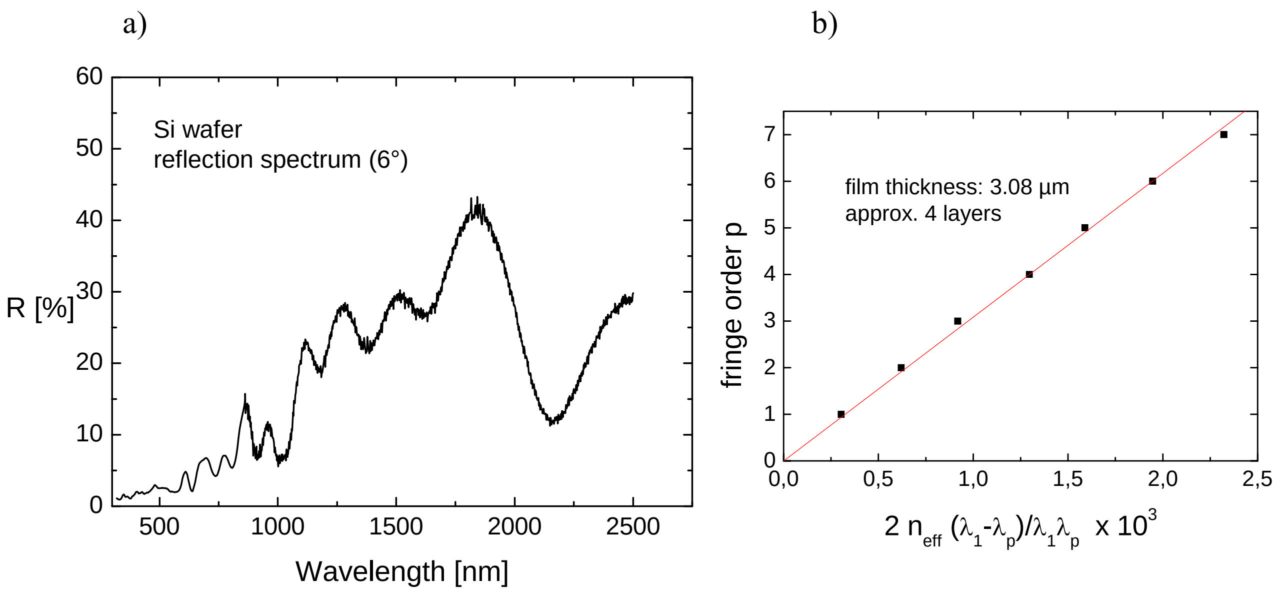

Figure 2.44. a) Reflectance spectrum of silica opal film at angle $\Theta = 6°$. b) Calculation of film thickness based on Fabry-Pérot fringes (4 layers).

Optical measurements were also performed at different angles $\Theta°$. The angularly dependent reflectance spectra are shown in Fig. 2.45a. The central wavelength of the Bragg diffraction band λ_B follows well the Bragg-Snell law condition (Fig. 2.45b). The best fit to the Bragg-Snell equation (Fig. 2.45b) gives d = 706 nm and n_{eff} = 1.3037. The inter-plane distance obtained from the Bragg fit agrees well with the 890 nm value estimated from Mastersizer and SEM measurements. The n_{eff} value of 1.304 is in the range expected for a close-packed fcc lattice, with 74 vol. % filling of SiO_2 spheres, if the refractive index of silica n_{silica} =1.42 is assumed.[117] In addition, the observation of well-defined Fabry-Pérot fringes by reflectance spectroscopy indicates the high quality of silica opals (Fig. 2.44a).

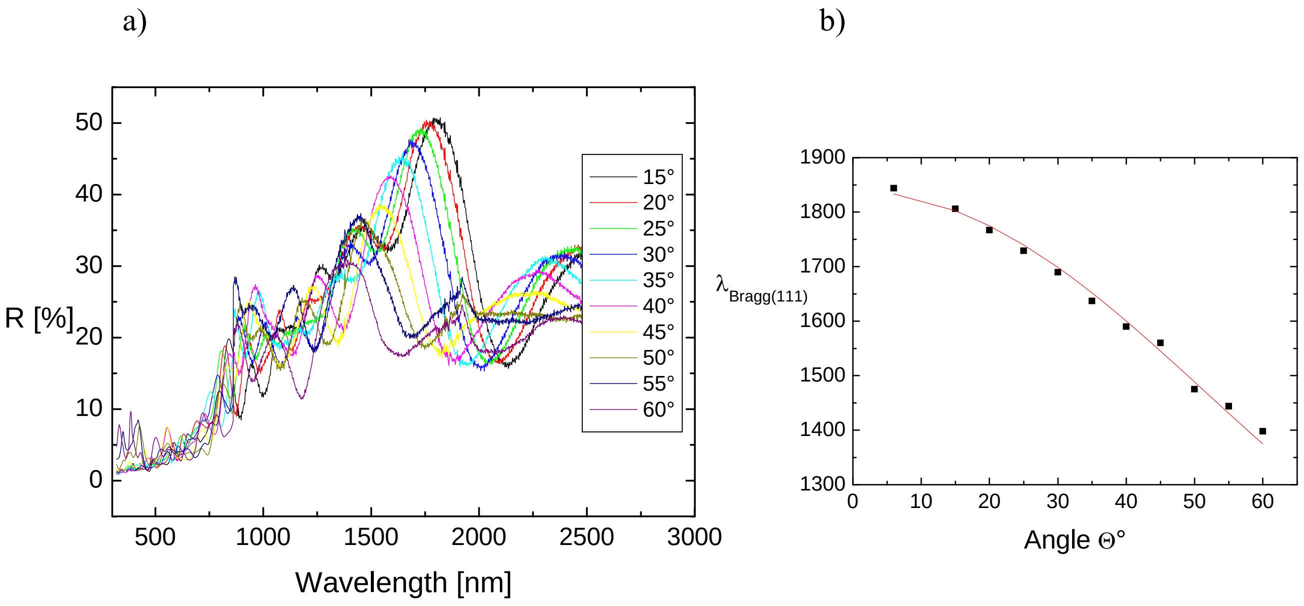

Figure 2.45. a) Angle resolved reflectance spectra of silica opal film for angles between 15° and 60° with a 5° step. b) Dependence of the peak position on the angle of incidence.

Recently, Schöpe et. al. have reported[118] that the structure and stacking sequence of hexagonally close packed structures are colour coded. The same colour means the same structure. This can be used for characterization of the homogeneity of opal films with respect to polycrystalline and defects. Fig. 2.46 to 2.48 show some optical micrographs of silica opal films prepared by different methods. The most homogenous color has been seen from the film produced by using a drawing machine.

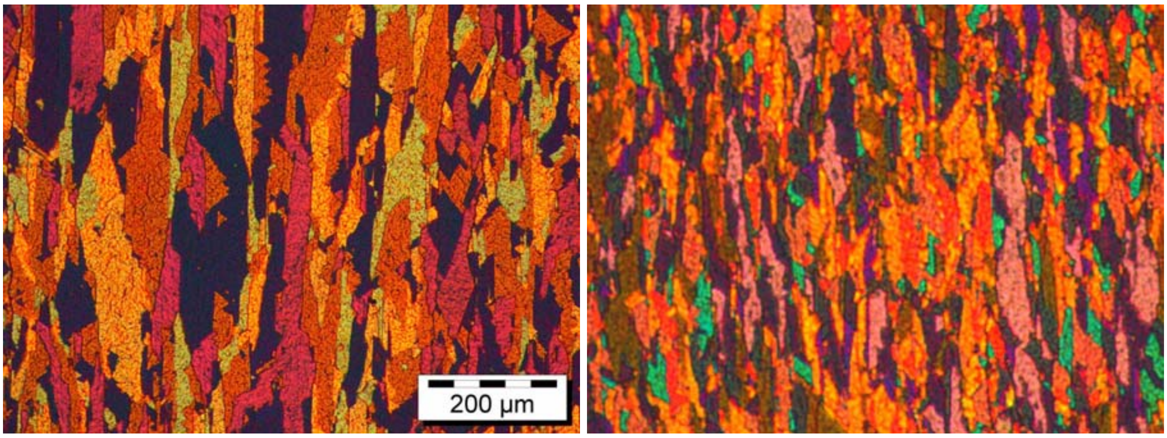

Figure 2.46. Optical micrographs (transmission) of the silica opal film on a glass substrate produced by crystallization on horizontal substrate.

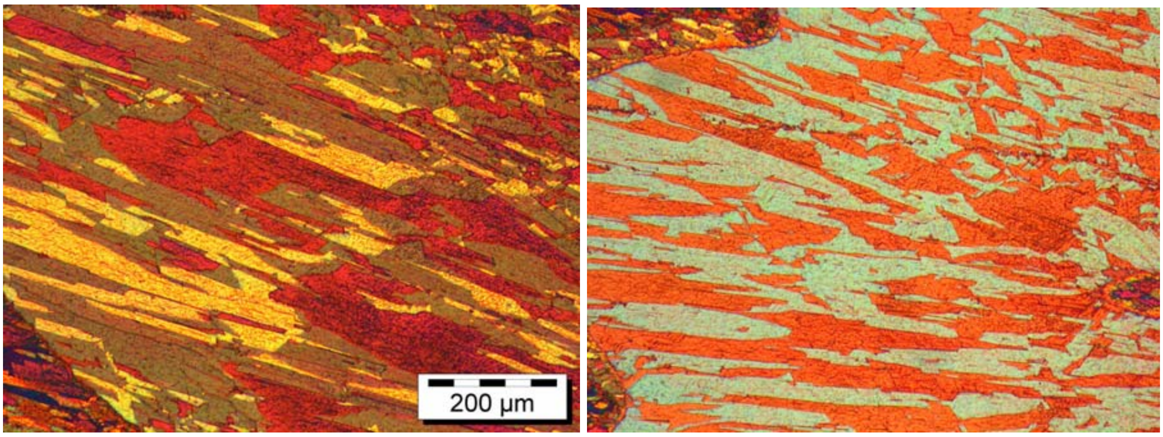

Figure 2.47. Optical micrographs (transmission) of the silica opal film on a glass substrate produced by using a drawing machine.

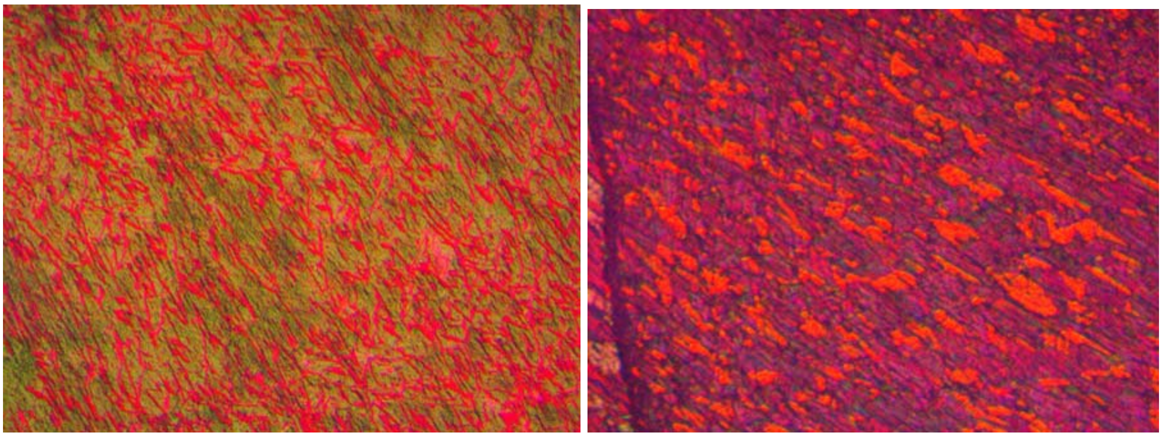

Figure 2.48. Optical micrographs (reflection) of the silica opal film on a silicon substrate produced by using a drawing machine.

3. Integration of 3D Photonic Crystals onto Structured Substrates

The strong research effort devoted to photonic crystals is motivated by their potential to design a novel generation of optoelectronic devices of reduced size, combining aspects of high integration and the ability to control the emission efficiency. In this respect, multi-functional photonic circuits will require architectures in which the positioning, shaping and coupling of high-quality two- and three-dimensional (2D and 3D) photonic crystals is of critical importance. In contrast to 2D photonic crystals, which can be fabricated in, for example, silicon-on-insulator platforms by means of well-developed 2D nanolithography,[119] the integration aspect of 3D photonic crystals poses a great challenge. Assembling 3D photonic crystals through wafer bonding has been proven as being a complicated and costly procedure,[37] with no straightforward prospect of further integration yet shown. Alternative 3D nanolithography, in which in-situ 3D patterning of polymer templates is followed by their infiltration by high refractive index semiconductors and completed by nanocomposite inversion, seems more efficient but still remains a costly process and requires sophisticated equipment. Moreover, 3D lithography methods are not free from limitations. For example, in the holographic technique,[39] the formation of photonic crystal templates in narrow trenches and cavities in substrates is complicated to achieve due to wall shadows and parasitic reflections, whereas the two-photon polymerization is restricted to dimensions less than one hundred micrometers.[120] Hence, self-assembly of monodisperse microspheres into opal structures[98,121,122,123,124,125] remains the favourite route towards templates for platform-integrated photonic materials, due to its simplicity, flexibility and low cost. In particular, the preparation of silicon-inverted photonic crystals on silicon platforms for the telecommunication frequency range is an important target. The accomplishment of this task, however, requires first of all the realization of perfectly crystalline low refractive index 3D templates.

The quality of self-assembled colloidal crystals on structured silicon wafers depends on the method of fabrication, commensurability of opal lattice constant and pattern dimensions, together with a spatial selectivity of opal growth. So far, opals have been crystallized in channel structures, whereby the deposition of opal on top of the wafer surface was mostly prevented by covering it with a slide[122] or by making this surface hydrophobic.[125] These methods are difficult to apply in assembly schemes in micrometer-sized isolated areas. Additional difficulties arise with crystallization of large spheres due to their lesser Brownian motion and quicker sedimentation, effectively reducing the bead concentration in the meniscus of the air-suspension interface close to the substrate. A combination of directed evaporation-induced self-assembly (DEISA process) and slow stirring to keep the spheres in a levitated state has been suggested as a method for assembling large spheres in channels.[98] However, this method is poor in its control of the opaline thickness, its influence on the selectivity of deposition and in obtaining large area opals with high quality. Ozin et al. have reported on control of the opaline film thickness by heating,[126] however this method is only suitable for silica spheres of diameters smaller than 500 nm, and the problem of cracks is not solved.

The following chapter deals with the fabrication of high quality opaline photonic crystals from large silica spheres of a diameter of 890 nm (Chapter 2.4) and PMMA spheres, self-assembled in hydrophilic trenches of silicon wafers by using a novel technique coined a combination of “lifting and stirring”. The achievements here represented comprise a spatial selectivity of opal crystallization without special treatment of the wafer surface, a filling of the trenches up to the top, leading to a spatially uniform film thickness, particularly an absence of cracks within the size of the trenches, and finally a good three-dimensional order of the opal lattice even in trenches with a complex confined geometry, verified using optical measurements. The opal lattice was found to match the pattern precisely in width as well as depth, providing an important step towards applications of opals in integrated optics.

3.1 Fabrication of Patterned Silicon Substrates

The patterned silicon substrates supplied by VTT Centre for Microelectronic, Finland were prepared from (100)-polished silicon substrate wafers by etching them in an inductively coupled plasma (ICP) reactor, using the standard Bosch process down to a depth of 5 micrometers. The substrates were cleaned for 20 minutes in a 7:3 solution of sulphuric acid (98%) and hydrogen peroxide (35%), followed by hydrophilization in a H_2O_2 (35%):NH_3 (28-30%):H_2O (1:1:5) bath at 65°C for 20 minutes. The substrates were finally rinsed in deionised water and dried using nitrogen gas. As a result of this process the whole wafer is highly hydrophilic, in low-lying etched parts as well as unetched high parts.

3.2 Selective Crystallization

To obtain the colloidal crystals grown in the microscopically structured substrates the profiled silicon substrates were vertically lifted out of a colloidal suspension at a controlled slow speed, in the order of some 100 nm/s (Fig. 3.1a). This deposition method, developed for homogeneous substrates,[97] has proved to be very suitable for the fabrication of opals on patterned substrates.[124] Highly monodisperse colloids together with a rather slow evaporation at the contact line are prerequisites to obtain highly ordered colloidal layers. As described by Jonas et al.,[127] the shape of the meniscus drives the crystallization. In the case of patterned substrate the capillary forces create a non-uniform meniscus pattern (Fig. 3.1b), which drives the crystallization to the etched trenches. Due to stronger capillary forces at the low lying etched trenches (diameter 1 – 100 μm) the meniscus at these parts extends higher (larger meniscus length L) than at the surface. This means that the crystallization first begins in the etched parts of the substrate. It is possible to deposit the spheres selectively if we can exactly control the growing opal film thickness. It has been realized by using a “lifting machine”. The main advantage of this deposition method, as compared to concepts which rely on evaporation, is the possibility of controlling the film thickness, not only by changing the suspension concentration, but also by adjusting the drawing speed.

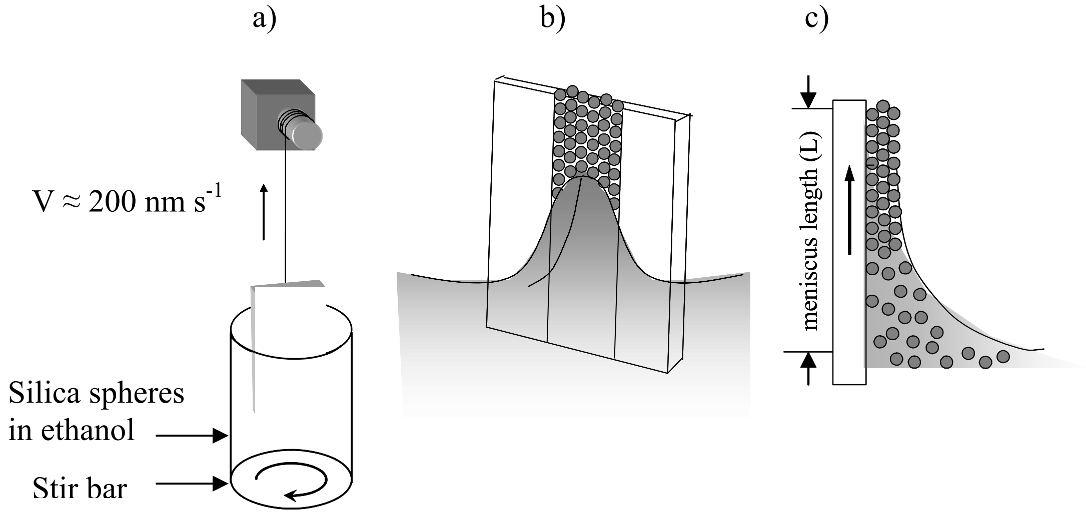

Figure 3.1. a) Schematic representation of the crystallization process by drawing up the substrate in a vertical direction with the help of stirring. b) Crystallization of colloidal crystal on patterned substrate during withdrawal. c) Colloid crystallization process at the drying zone.

3.3 Crystallization of Large SiO_2 Spheres on Patterned Substrates

As described in Chapter 2.4, for the growth of high quality colloidal crystals from large SiO_2 spheres of 890 nm diameter a drawing apparatus (providing control of the crystallization speed) in combination with stirring (providing counterbalancing of the sedimentation) was used. The choice of sphere diameter is dictated by the need to match the telecommunication wavelength range and the high-order photonic band-gaps of the inverted Si-opal targeted by the fabricated SiO_2 templates. Crystallization in a drawing apparatus allows a precise variation of parameters by changing the drawing speed compared to a control of the evaporation rate[126] and can be used to grow high quality opals. This opens the possibility of crystallization in selected areas of complex structured silicon wafers. Hence this work focused on optimizing the opal crystallization conditions in confined geometries of complex topology for sedimentation of such large SiO_2 spheres.

The samples were prepared at room temperature from a 2-5 vol. % suspension of 890 nm diameter silica spheres, at a drawing speed of 200 nm/s. The stirring rate was controlled in such a way that the solution meniscus is maintained in a quiescent state. Under these conditions, it was found to be possible to deposit the silica spheres rather selectively onto the profiled substrate. Fig. 3.2b shows an optical micrograph after the self-assembly of the opal. The figure clearly demonstrates that silica spheres on large scale crystallize exclusively into the etched low-lying trenches and that the unetched (high) parts remain uncovered. The excellent selectivity of the particle deposition for a large scale view of the substrate can also clearly be seen in the SEM image shown in Fig. 3.3.

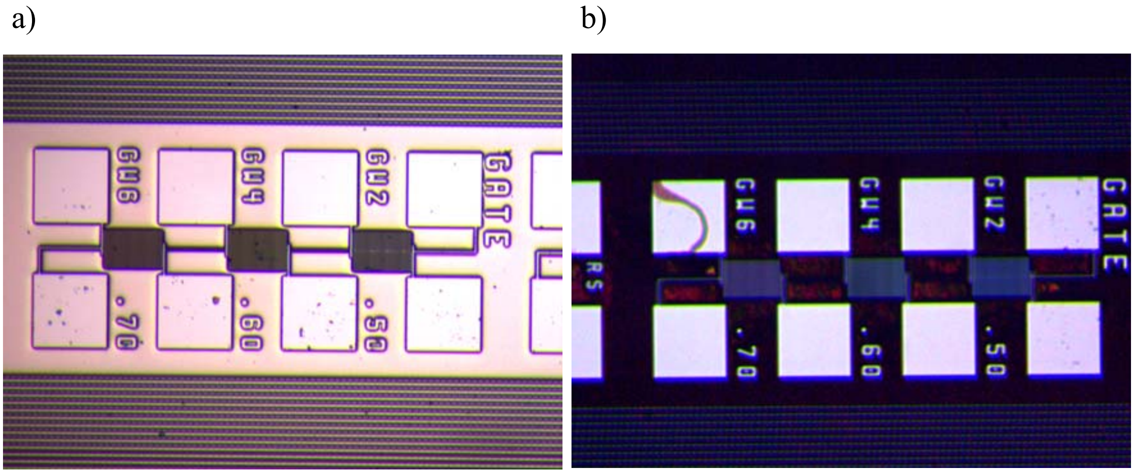

Figure 3.2. Optical micrographs: a) Bare etched silicon substrate; b) etched silicon substrate after crystallisation of silica opals (about 1 mm x 0.7 mm).

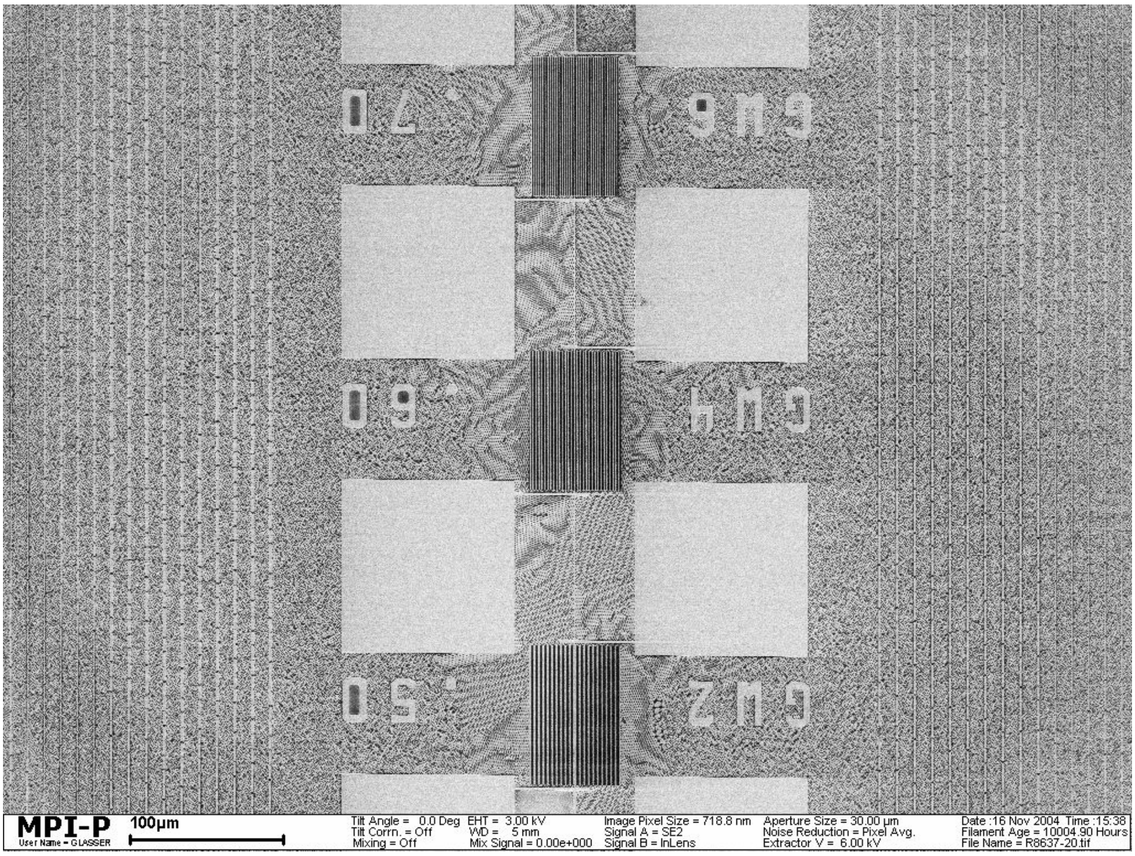

Figure 3.3. Representative SEM image of silica opals on a patterned silicon substrate.

Figure 3.4 and 3.5 show SEM images of silica opals on a patterned substrate with high magnification. As shown in the Figures, a large flat and well-ordered, nearly crack free opal film was obtained, which was exclusively inside the etched area.

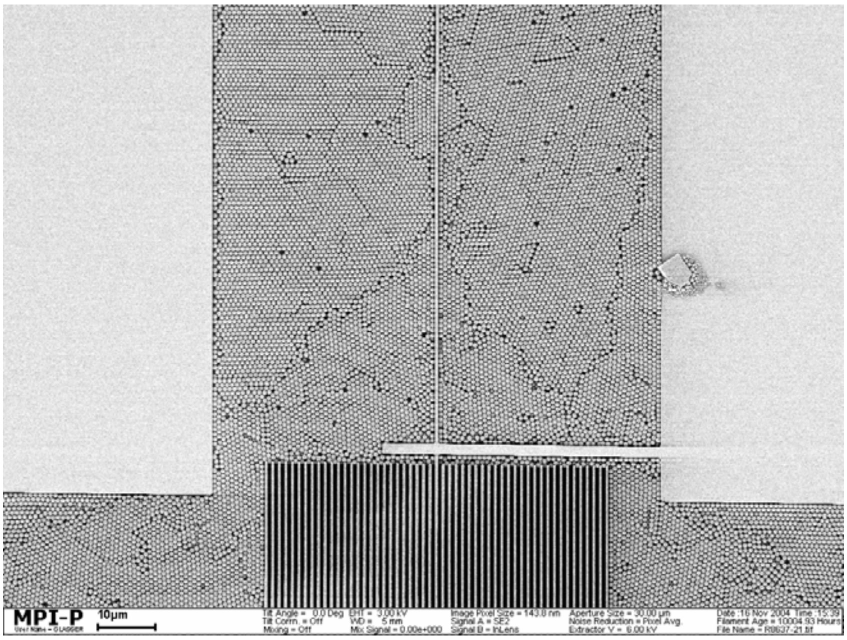

Figure 3.4. Representative SEM image of silica opals on a patterned silicon substrate.

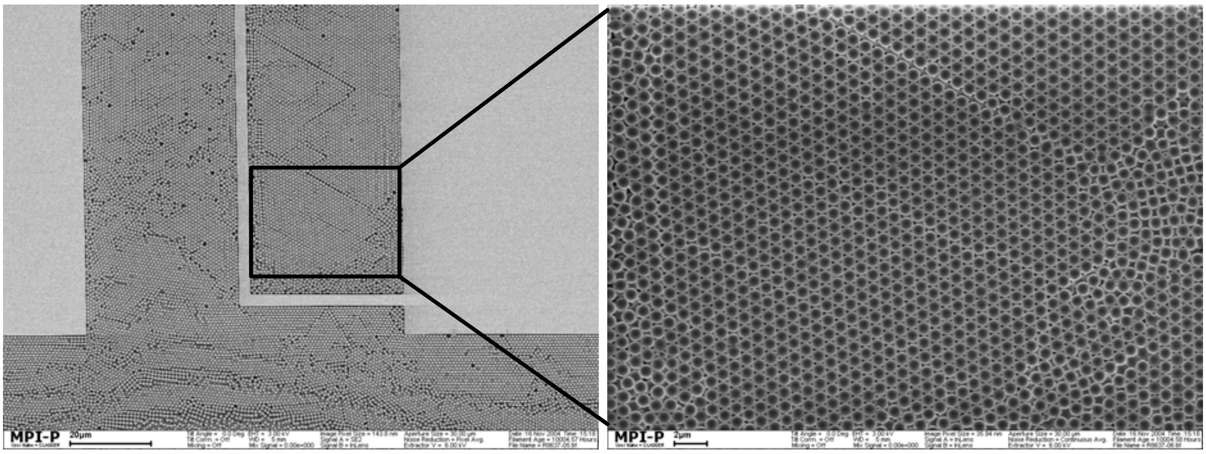

Figure 3.5. Representative SEM images of silica opals on a patterned silicon substrate, right: Close-up.

In Fig. 3.6 and 3.7, very good selectivity is shown also in areas with complex geometry. Even around complex patterns the filling is highly selective and the order is very good (Fig. 3.6). Independent of the substrate structure, the deposited film possesses a highly ordered arrangement of silica spheres corresponding to the (111)-plane of a face centered cubic (fcc) lattice.

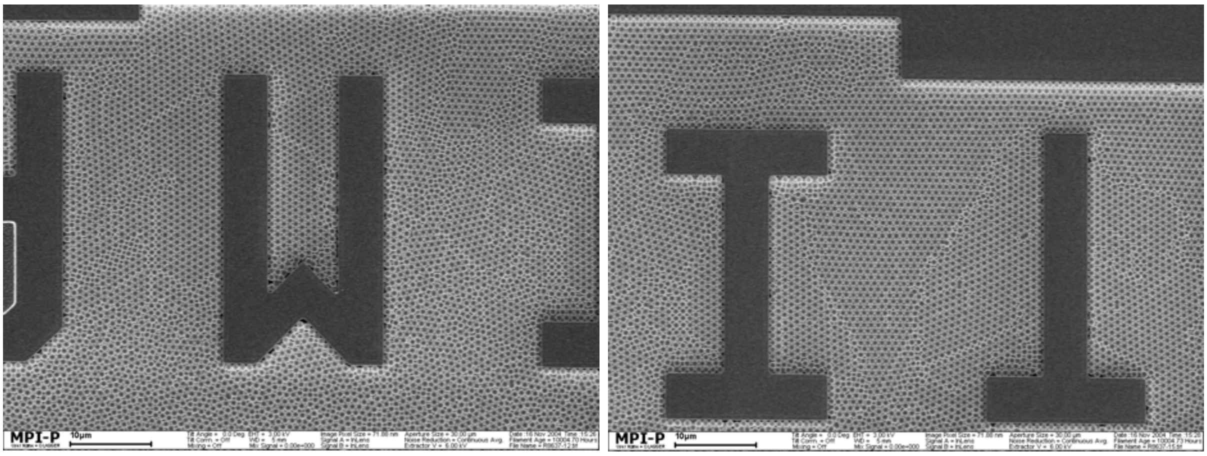

Figure 3.6. Representative SEM images of silica opals on a patterned silicon substrates with complex geometry.

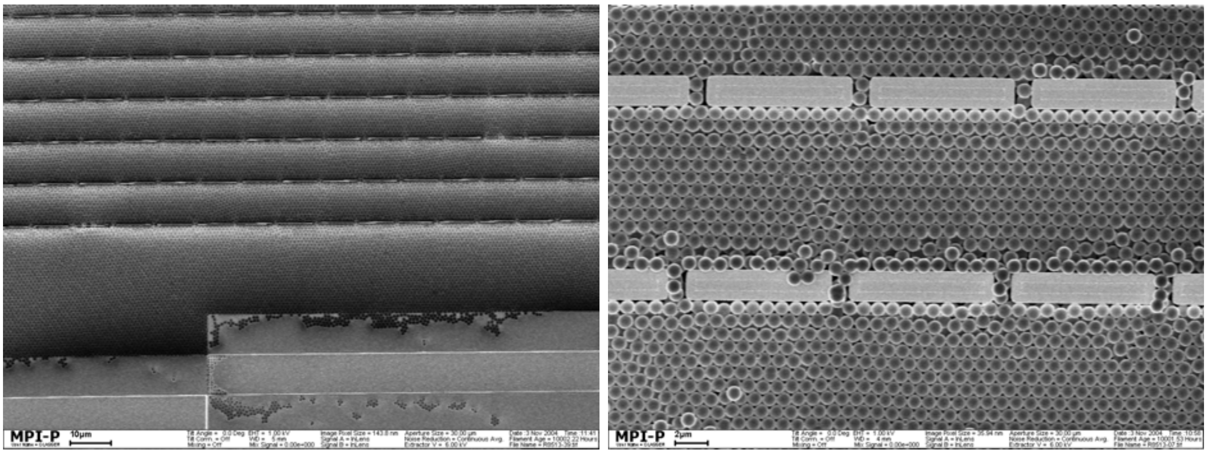

Figure 3.7. Representative SEM images of silica opals on a patterned silicon substrates with different geometry, right: Close-up from left picture.

The silica opals in the third dimension (depth) were also studied by SEM imaging of cleaved substrates. Representative SEM images of silica opals at the edges of the cut substrates are shown in Figs. 3.8, 3.9, and 3.10. These pictures nicely demonstrate that the top surface of the opal is very flat and the order quite good, in depth as well as in the plane. In particular, this is evident in Fig. 3.8. In Fig. 3.9 and 3.10, the order at the edge of a rather narrow trench is destroyed presumably by the cutting process. In this particular case, the crystal quality may be affected in such narrow trenches either by the slightly concave bottom profile of the etched trenches or by the potential misfit of the lattice dimension to the size of the trench. It is in addition noteworthy that the low-lying trenches are filled up to the top.

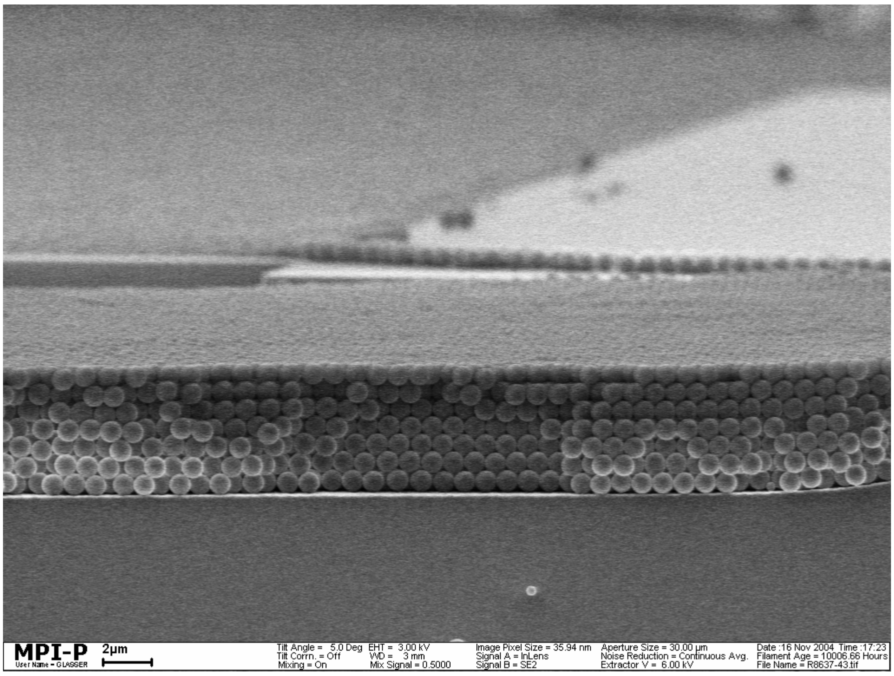

Figure 3.8. Representative SEM image of cross-section of silica opal on patterned silicon substrate.

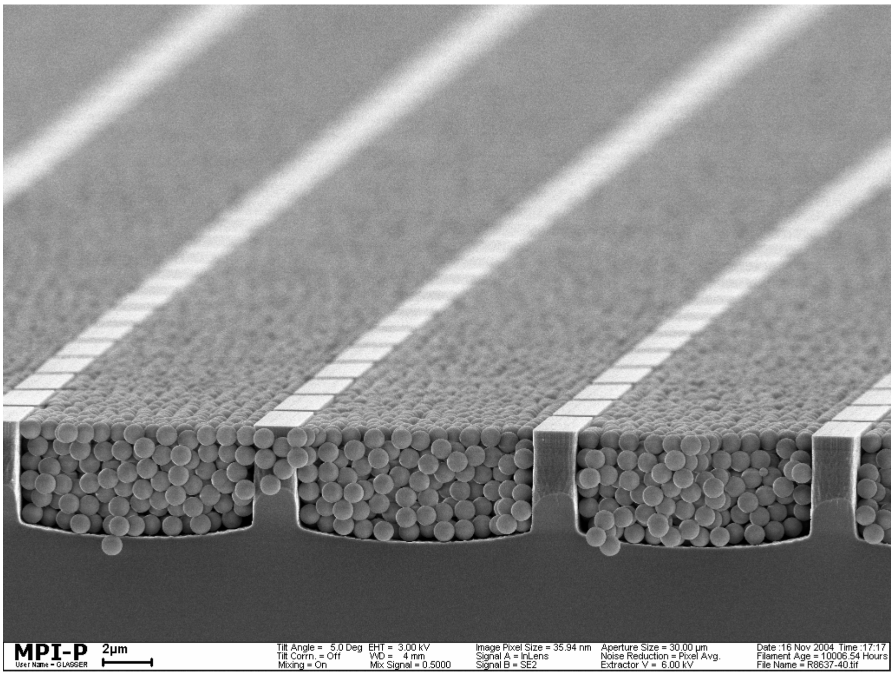

Figure 3.9. Representative SEM image of cross-section of silica opal on patterned silicon substrate.

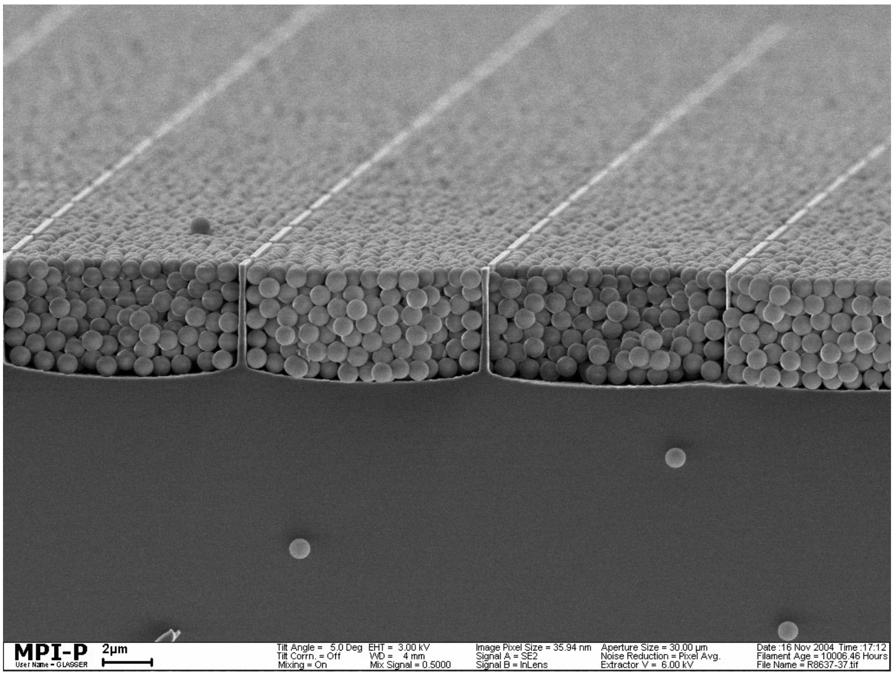

Figure 3.10. Representative SEM image of cross-section of silica opal on patterned silicon substrate.

3.4 Characterization of Silica Opals on Patterned Substrates

From the large number of SEM measurements as demonstrated above it is found that opal lattice matched the pattern precisely in width as well as depth and the ordering of silica spheres was excellent. In order to confirm the good quality of obtained silica opals on patterned substrates Fourier Transform studies and optical measurements were performed.

3.4.1 Fourier Transform Studies

The crystalline quality of the opal assembled on the patterned substrate can be examined in the lateral dimension by applying the spatial Fourier transform to selected areas of the lattice images, as shown in Fig. 3.11 to 3.12. The Fourier transform in these Figures nicely shows the hexagonal order of the (111) opaline crystal plane. The sharpness of the pattern is mostly limited by the lateral confinement of opal in trenches. For example, in Fig. 3.12 the peaks in the Fourier transform are much sharper in the horizontal than in the vertical direction, since only a few lattice periods are available in the vertical direction before the end of the channel. The sharpness which is comparable to silica opals on plane substrate (Fig. 2.43) shows well defined peaks in the spatial Fourier transform and hence proves the crystal quality.

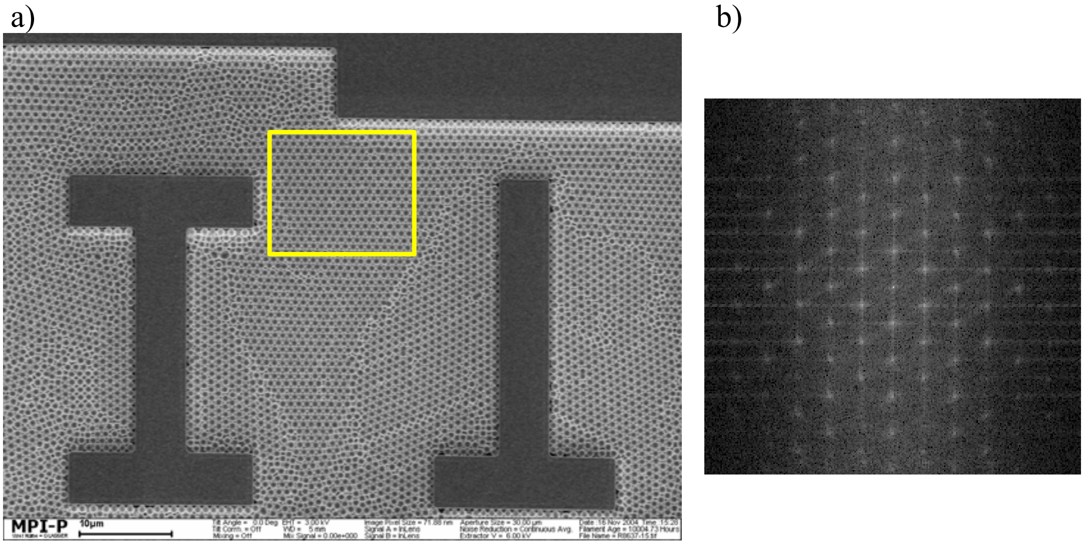

Figure 3.11. a) Representative SEM image of silica opal on a patterned Si-substrate with complex geometry. b) Fourier transform of marked region (about 17 x 17 spheres) of SEM image.

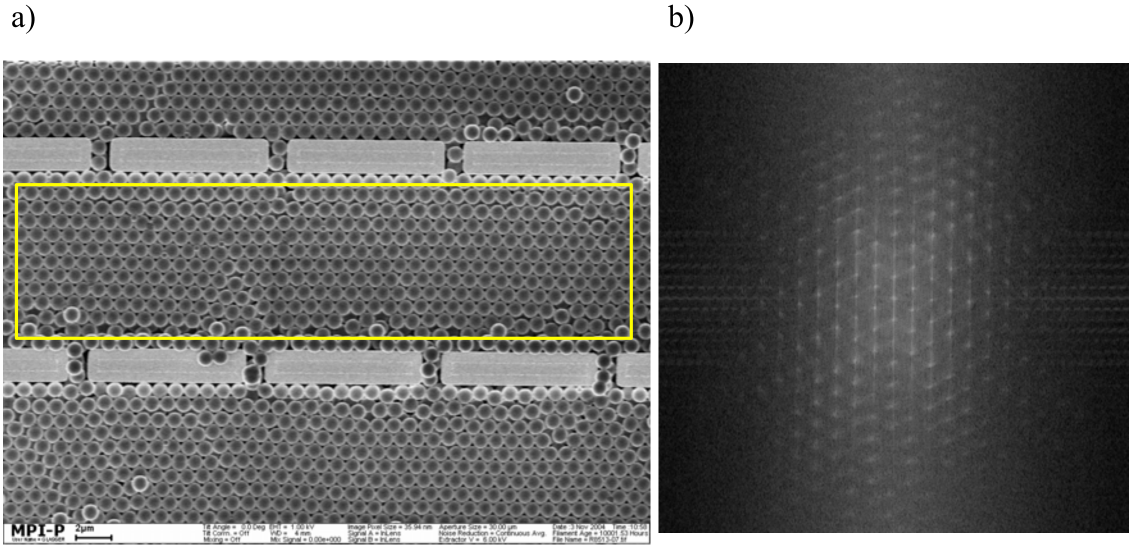

Figure 3.12. a) SEM image of same silica opal on another area of the patterned Si-substrate. b) Fourier transform of marked region (about 38 to 10 spheres) of SEM image.

3.4.2 Optical Measurements

In order to determine the periodicity of the opal lattice in depth of the trench, optical measurements were performed to compare extended opal crystals on flat substrates with the finite size crystals confined in trenches in the profiled substrate. The reflectance spectra were collected using a beam with a macroscopic spot size of 9×1 mm^2. In the case of profiled substrates, the spectrum is thus averaged over many trenches or realizations of opal lattice, with different lateral extension. Normalized spectra of opal films on flat and patterned substrates directly show the similarity with regard to the Bragg peak centered at 1830 nm and the spectrum shape, as shown in Fig.3.13. For a more refined comparison,[128] it is important to consider that an intense background due to the mirror-like reflectance at the uncovered parts of the silicon substrate is superimposed onto the spectrum of the opal on profiled substrates. This contribution sums up to 40% of the total reflectance intensity. In order to obtain an absolute magnitude of reflectance, this background was subtracted to fit the 5% background reflectance, characteristic to the opal film on flat substrate at wavelengths away from the diffraction resonance. The corrected spectrum for the opal on the patterned substrate (shown as curve 3 in Fig. 3.13) and the extended opal crystal on the flat substrate (curve 1) are rather similar. The relative bandwidth of the diffraction resonance, defined as the ratio of the full bandwidth at half height of the reflectance band to the band central wavelength, is 0.17 for the films on flat and 0.13 for the films on profiled substrates. These values significantly exceed the theoretically calculated value of 0.056 for the relative bandwidth along the (111)-axis of a perfect infinite opal. The major reason for this band gap broadening is, in this case, the small film thickness,[102] which emanates from the SEM pictures of cut samples and from the optical evaluation of the Fabry-Pérot oscillations. The film thickness of about 6 layers of spheres was found for opal films on the patterned substrates (Fig. 3.8, 3.9, and 3.10) and of 4 layers – for films on a flat substrate (Fig. 2.44b). In addition, inhomogeneous broadening of the diffraction resonance of films on patterned substrates increases due to averaging over many lattice realizations in different trenches. Microoptical studies of similar but thicker films in individual trenches on silicon substrate produced the narrower relative bandwidth of 0.08.[129] Taking into account the stronger resonance broadening for thinner films, the opals on patterned and flat substrates possess nearly the same quality.

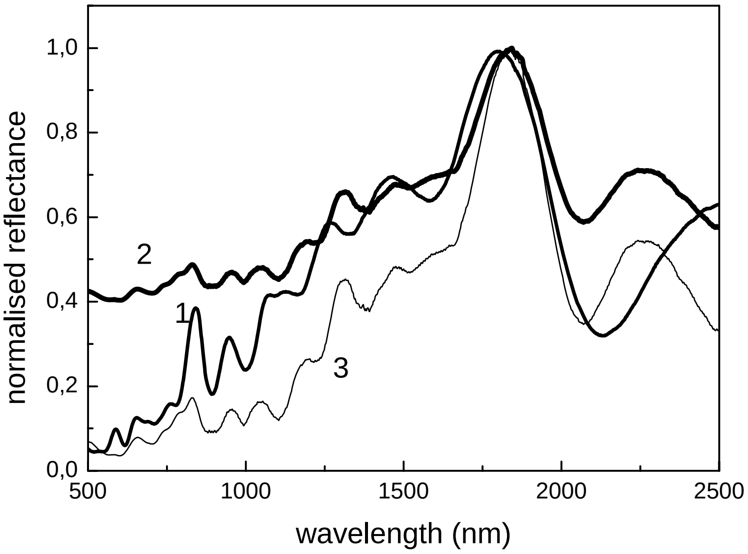

Figure 3.13. Normalised reflectance spectra of opal on flat (curve 1) and patterned (2) substrates. The spectrum 3 is obtained by subtracting the reflectance of uncovered silicon wafer from the spectrum 2.

Measurements of the angular dependence of reflection were performed to obtain more information on the crystal quality. Fig. 3.14a shows angularly dependent reflectance spectra of silica opals on patterned substrates. The central wavelength of the Bragg diffraction band λ_B follows well the Bragg-Snell law condition (Fig. 3.14b):

$$\lambda_B = 2d\,(n_{\mathrm{eff}}^2 - \sin^2\Theta)^{0.5},$$

where λ_B is the peak wavelength, $d = (2/3)^{1/2}D$ is the lattice constant along the (111)-axis, involving the sphere diameter D of the close-packed fcc lattice, Θ is the angle between the incident beam and the normal to the (111)-plane, and n_{eff} is the effective refractive index determined by $n_{eff}^2 = n_{sio2}^2\Phi + n_{air}^2(1-\Phi)$, with Φ being the volume fraction of silica spheres. The best fit to the Bragg-Snell equation (Fig. 3.14b) gives d = 709 nm and n_{eff} = 1.3099 for opals on patterned substrates. The *d*-value is identical with that obtained from opals on flat substrate within the experimental accuracy (Chapter 2.4.3).

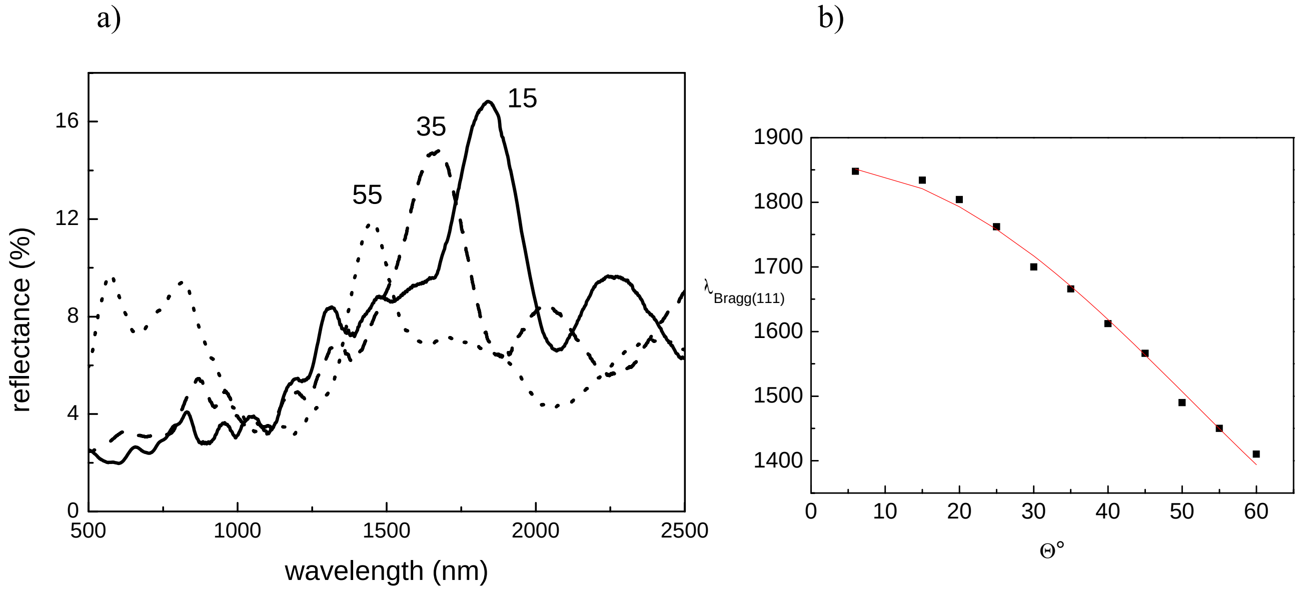

Figure 3.14. a) Reflectance spectra of opal film on the patterned Si-substrate at different angles of light incidence indicated by numbers at curves. Reflectance magnitude is corrected for reflectance of uncovered Si substrate. b) Bragg peak angle dispersion for the patterned wafer. Results from Bragg equation nonlinear fit: n_{eff} = 1.3099; d = 709 nm; particle diameter D = 869 nm.

In addition to the Bragg reflection, the Fabry-Pérot oscillations due to the finite film thickness were observed for opals assembled on both flat and patterned substrates. The observation of well-defined fringes by reflectance spectroscopy indicates[92] that the film thickness does not deviate more than 10% from the average value over the beam spot area of 9×1 mm^2.

3.5 Influence of Substrate Structure on Crystallization

The optical measurements have proved that the silica opals with the finite size confined in trenches in the profiled substrate have the same quality as that on flat substrates. However, it was observed that the ordering of the spheres in few trenches is not as good as in other ones (Fig. 3.9, 3.10). In following chapter the influence of substrate geometry on the crystallization and the limit of the structure with respect to selectivity are discussed.

3.5.1 Opals in Trenches with Rectangular Shape and Smooth Sidewalls

The patterned silicon substrates, as mentioned above, were fabricated by the standard Bosch process. The trenches of these substrates have some 200 nm sized roughness to the sidewalls and a somewhat concave bottom profile in larger features, which may affect the crystal ordering. VTT has developed a continuously passivated ICP-process that is able to create up to 6 micron deep wells with smooth sidewalls and smoother and less concave bottom profile. These new pattered silicon substrates have been used for sedimentation of silica opals. Under the same sedimentation conditions the opals crystallized in the new substrate (Fig. 3.15a) appear better ordered in comparison to the ones on the old substrate (Fig. 3.15b). It is noticeable that in the new substrates even very narrow trenches could be infiltrated well with silica spheres because of their rather straight sidewalls and sharp corner (Fig. 3.16). Other examples of infilling silica spheres in very narrow trenches are given in Fig. 3.17, 3.18, and 3.19.

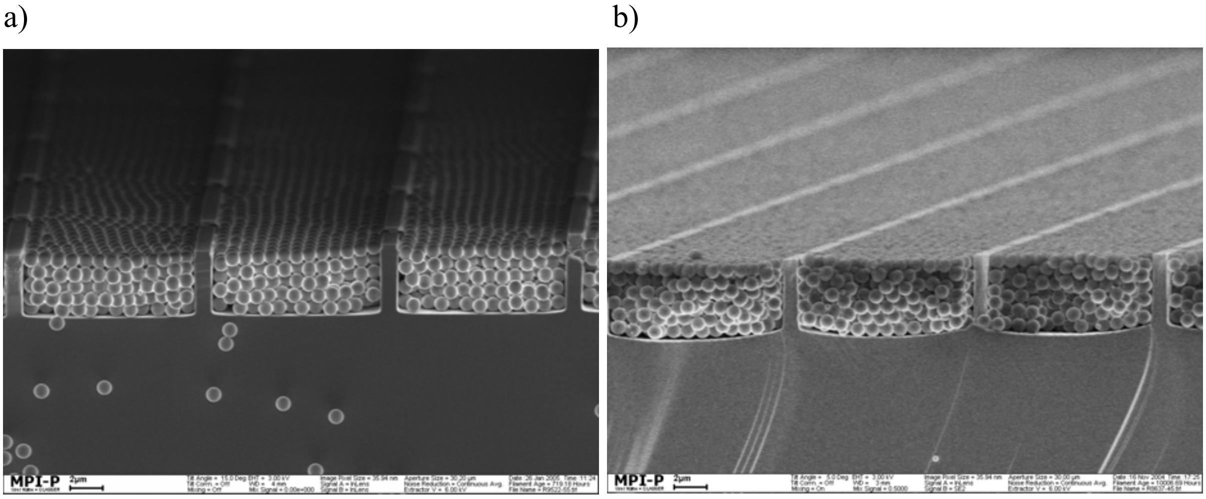

Figure 3.15. a) SEM image of opals in patterned Si-substrate made by continuously passivated ICP-process (new substrate); b) SEM image of opals in patterned Si-substrate made by standard Bosch process (old substrate).

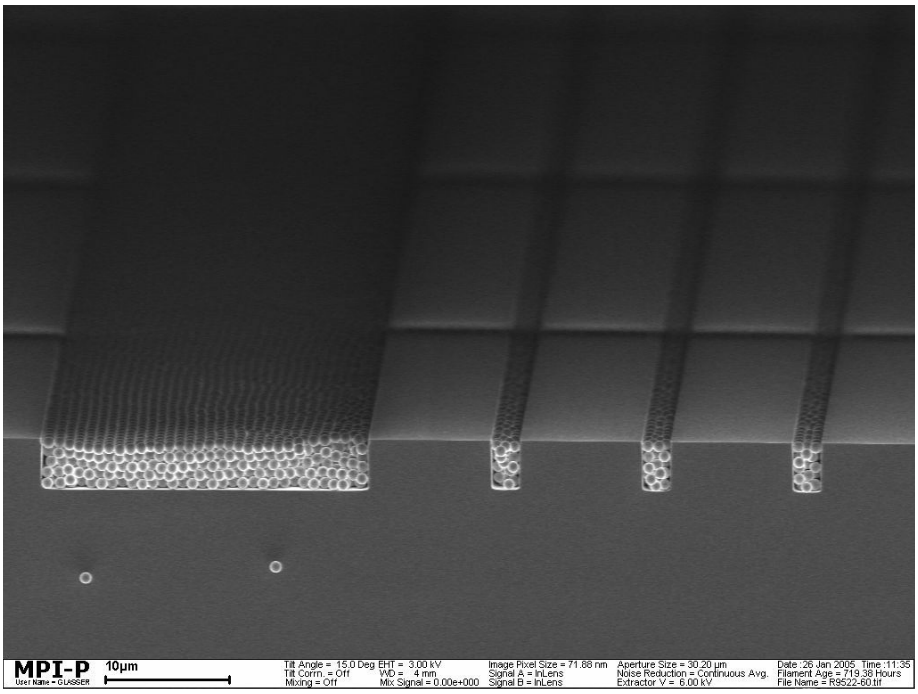

Figure 3.16. Representative SEM image of cross-section of silica opal on patterned Si-substrate made by continuously passivated ICP-process (new substrate).

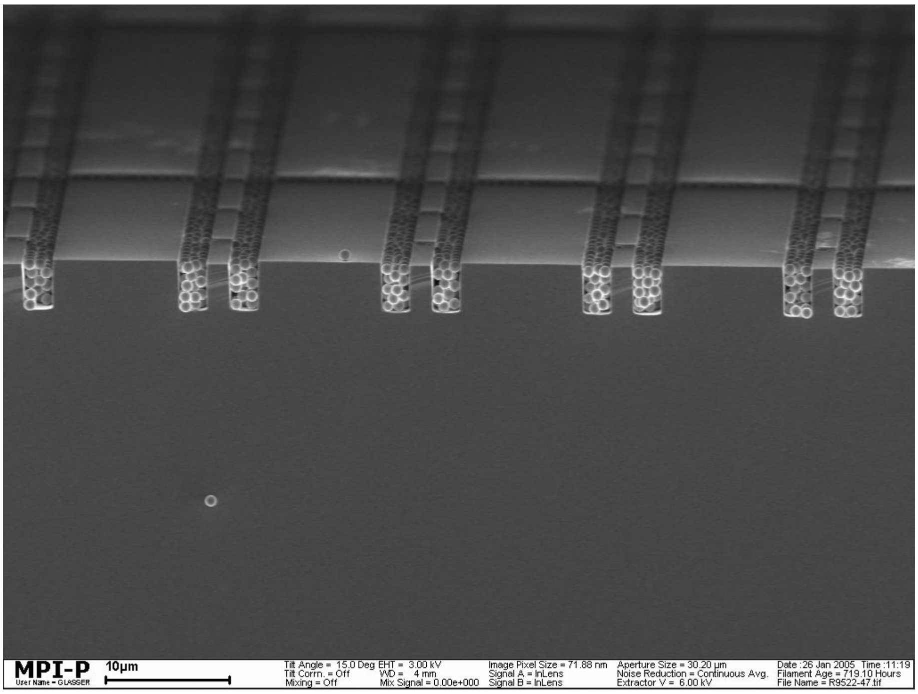

Figure 3.17. Representative SEM image of cross-section of silica opal on patterned Si-substrate with the structure of narrow trenches (three sphere arrays).

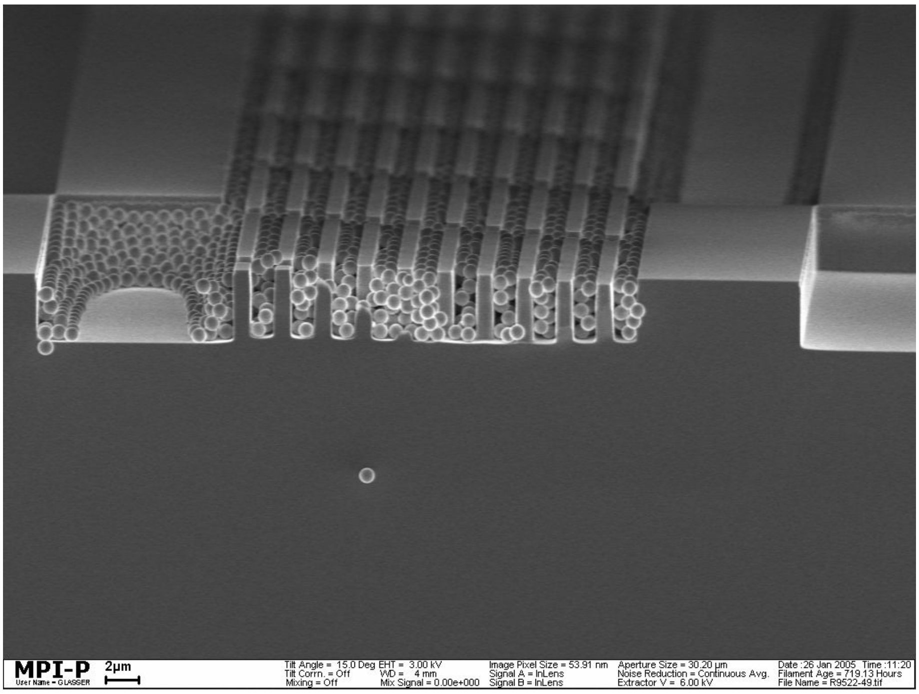

Figure 3.18. Representative SEM image of cross-section of silica opal on patterned Si-substrate with the structure of narrow trenches (two sphere arrays).

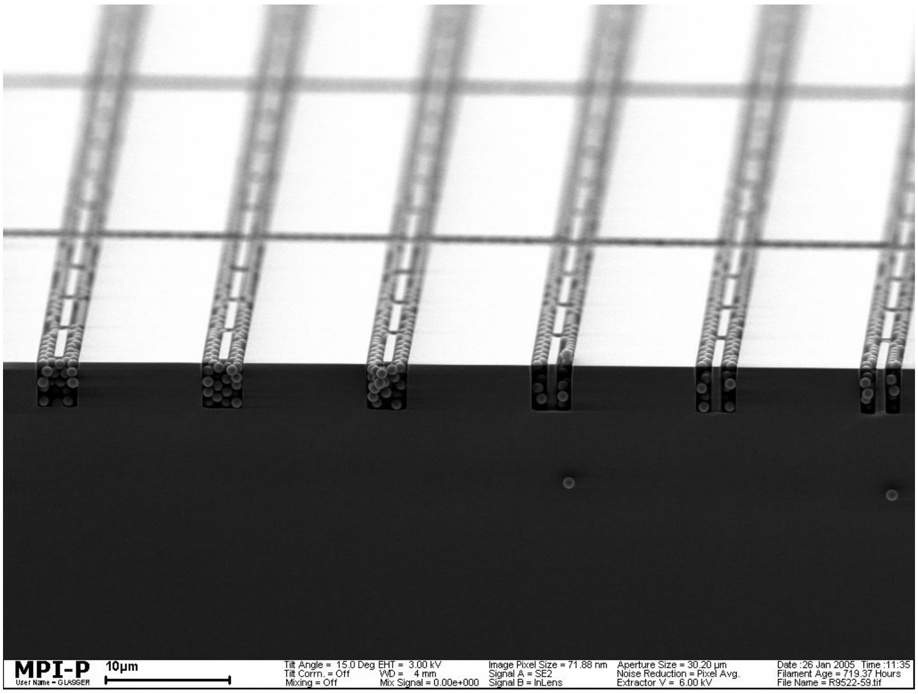

Figure 3.19. Representative SEM image of cross-section of silica opal on patterned Si-substrate with the structure of narrow trenches (one sphere arrays).

3.5.2 Opals in Trenches with Closed and Finite Shape Geometry

The selective deposition scheme as reported here has been realized for samples of 1 cm width and 2 cm height. By inspecting different samples and different regions it was found that trenches as wide as 110 μm are still completely filled, while the high parts stay sphere free. The lower limit for structures to be infilled is reached only if their diameter can only accommodate about 2 spheres. However, with regard to the whole profiled wafer some unfilled areas can be seen by SEM measurements, which depend on structures. Isolated regions are difficult to fill completely, for example, small closed shaped pits were always not filled (Fig. 3.20) because the capillary force is too weak to form a meniscus which is necessary for the crystallization.

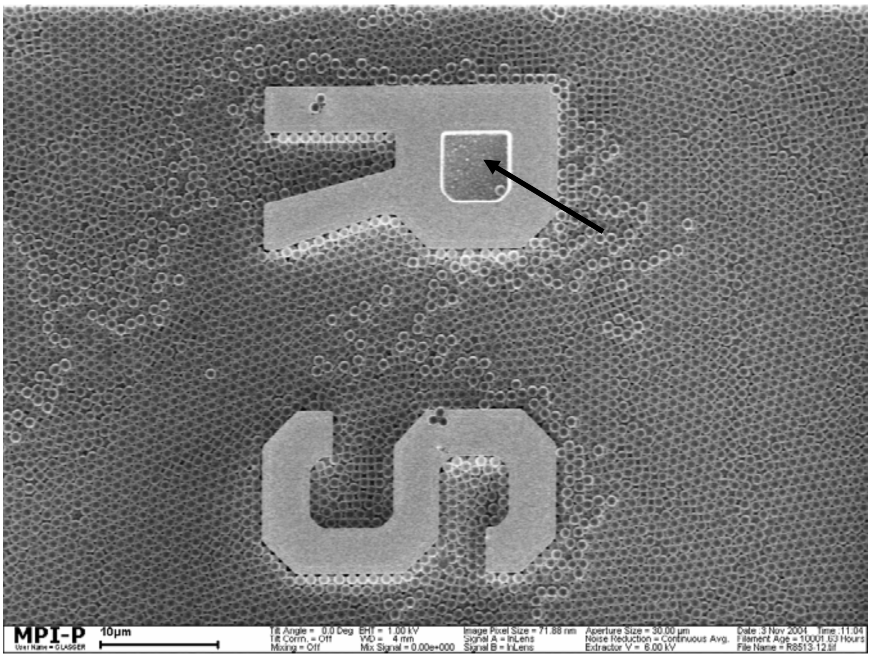

Figure 3.20. SEM image of silica opals with a sphere diameter of 890 nm on patterned Si-substrate. It shows unfilling area due to very weak capillary force.

In Fig. 3.21, it is shown that the isolated trenches of less than 100 µm length are not entirely filled, whereas trenches of the same length, which are connected to longer trenches, are completely filled. This result can be explained only by the fact that the driving force for selective crystallization is the larger meniscus length in the low-lying trenches due to capillary forces, as compared to higher lying areas. For this to happen the meniscus must extend far above the liquid surface. Therefore a low-lying trench cannot be filled immediately as it is lifted over the liquid surface. Crystallization starts only when a trench has reached a certain height above the surface of the liquid, enabling a sufficient length of the meniscus. For short isolated trenches this height obviously exceeds the trench length. This finding offers the selectivity of trench infiltration: trenches of the same cross-section can be either infilled or left empty depending on their length or their connection to a longer trench. In addition, a selective filling is only possible if the trenches are oriented perpendicular to the meniscus.

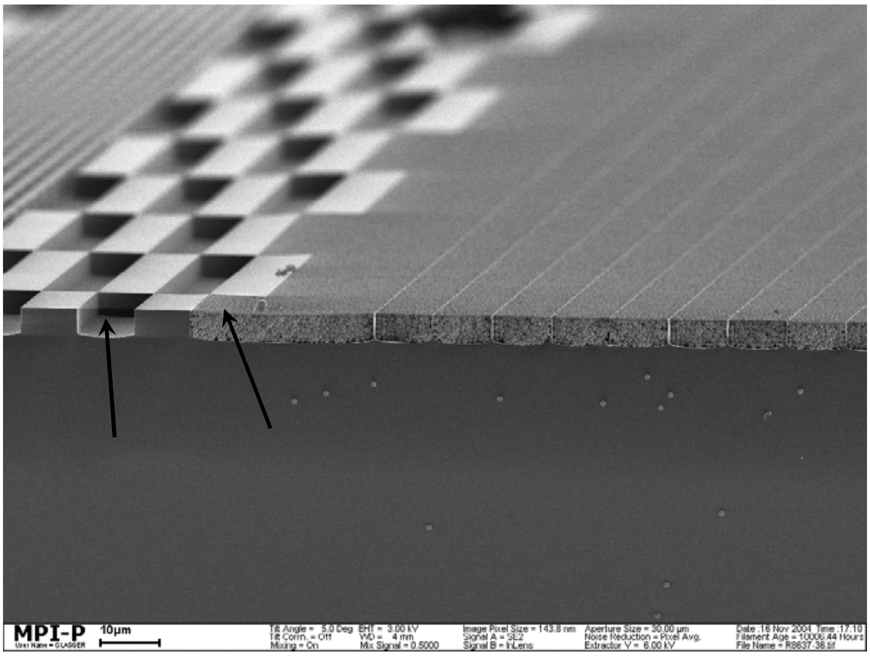

Figure 3.21. SEM image of silica opals with a sphere diameter of 890 nm on patterned Si-substrate. It shows unfilled area owing to meniscus rupture.

3.6 Influence of Substrate Surface on Crystallization

Selective deposition of colloids on patterned substrates based on capillary force difference has its limits, which is very strong dependent on substrate geometry and has been discussed in Chapter 3.5.2. In order to improve the spatial selectivity of the sedimentation patterned substrates on silicon and silicon-on-insulator (SOI) wafers with partially hydrophilic and hydrophobic surface were fabricated from VTT, Finland. The selectivity of these substrates for deposition of PMMA and silica spheres was studied.

3.6.1 LOCOS Substrate with Hydrophilic Bottoms and Sidewalls of Wells

Figure 3.22 shows a schematic representation of patterned silicon substrate with locally oxidized silicon (LOCOS). The bottom and sidewall of the trench in this substrate is covered by hydrophilic SiO_2. These substrates were used at first without HF pre-treatment for crystallization of PMMA spheres. The results are shown in Fig. 3.23 and 3.24. As shown in the Figures, silica opals were found only in trenches and they have a nice order.

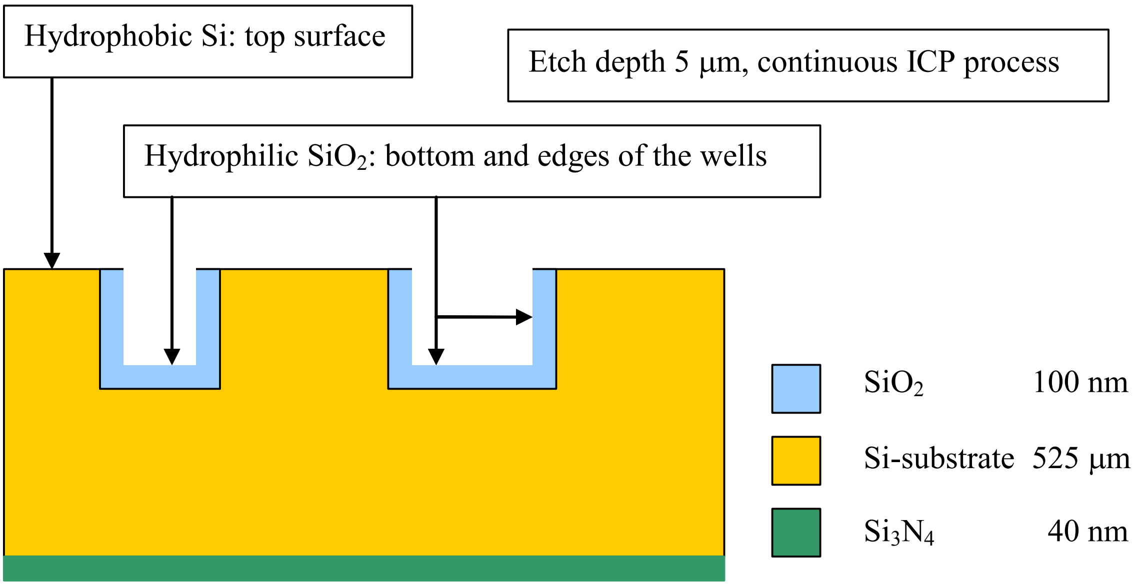

Figure 3.22. Schematic representation of LOCOS substrate.

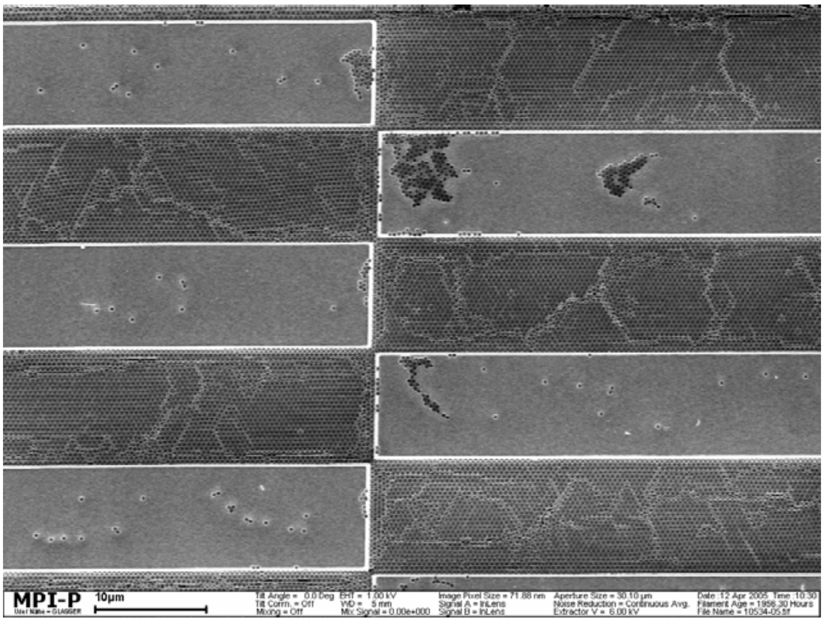

Figure 3.23. SEM image of PMMA opals with a sphere diameter of 420 nm (Sample No. 6) on LOCOS substrate.

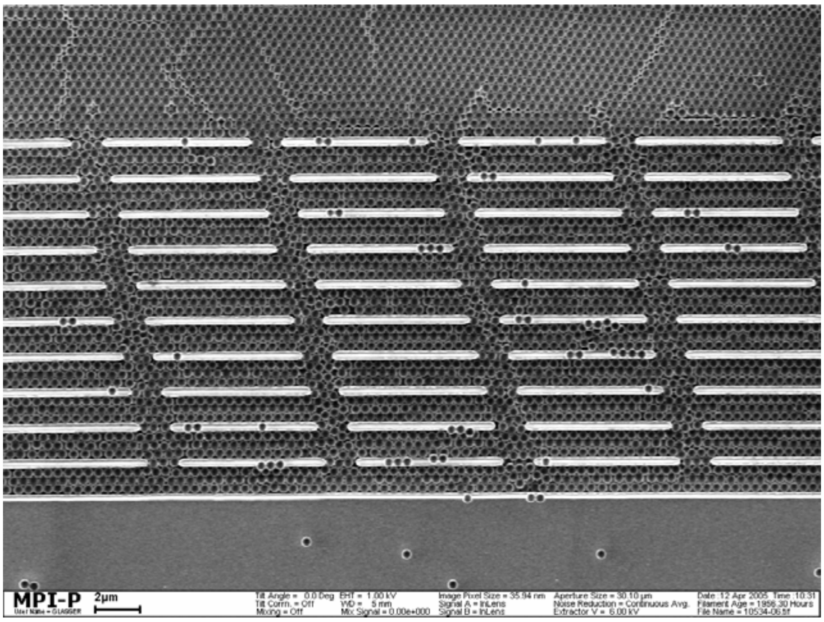

Figure 3.24. SEM image of PMMA opals with a sphere diameter of 420 nm (Sample No. 6) on LOCOS substrate.

Such substrates were also used for crystallization of silica spheres under the same condition as described in Chapter 3.3. Fig. 3.25 shows silica opals on a LOCOS substrate without treatment with dilute HF solution. In order to remove the native oxide layer of silicon surface, the LOCOS substrates were immersed in a dilute HF solution (about 2% aqueous HF solution) for 30 seconds before use. After rinsing them several times with de-ionized water they were used for the deposition of silica opals. However, no significant difference was found between using the LOCOS substrates with and without HF pre-treatment for the crystallization of silica spheres (Fig. 3.26).

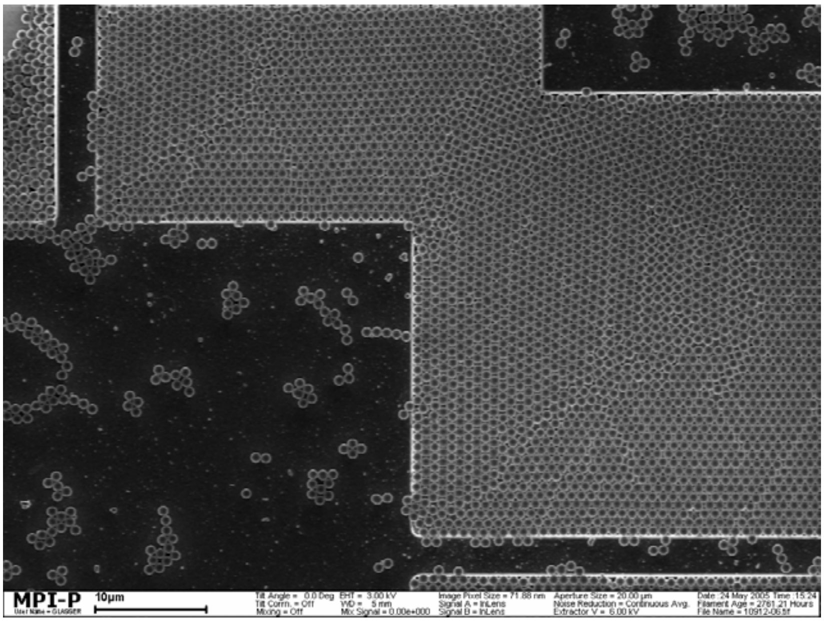

Figure 3.25. SEM image of silica opals with a sphere diameter of 890 nm on LOCOS substrate (without HF pre-treatment).

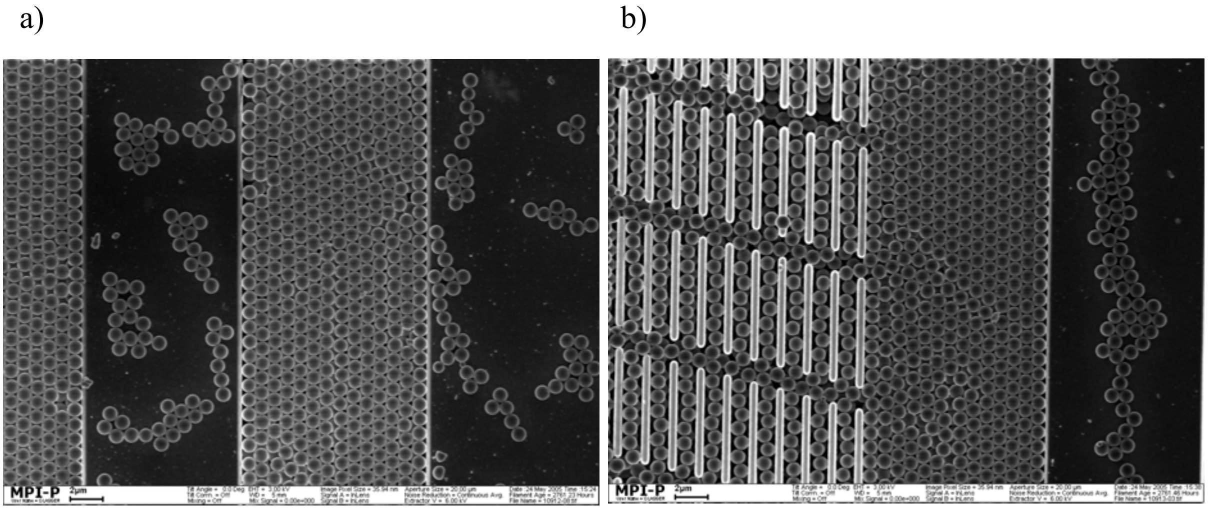

Figure 3.26. SEM images of silica opals with a sphere diameter of 890 nm on LOCOS substrate: a) Substrate without HF pre-treatment; b) substrate with HF pre-treatment.

Unfortunately, the problem with respect to isolated regions was not overcome as expected. In Fig.3.27 it is shown that small closed pits were not filled in LOCOS substrate independent of the fact whether the substrate was treated with dilute HF solution or not. Probably the SiO_2 film is not hydrophilic enough.

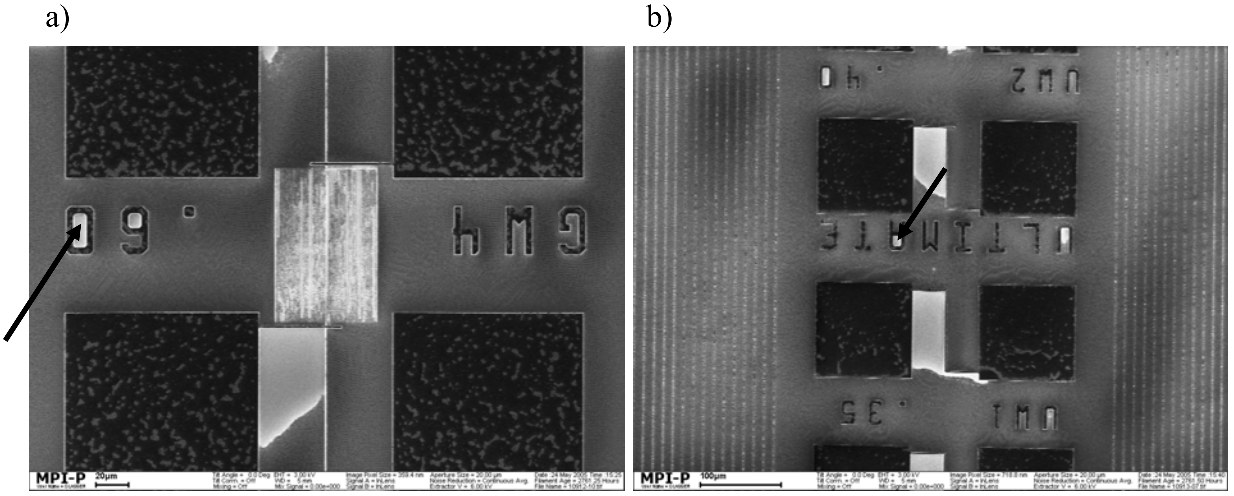

Figure 3.27. SEM images of silica opals with a sphere diameter of 890 nm on LOCOS substrate. The arrows show unfilling areas: a) Substrate without HF pre-treatment; b) substrate with HF pre-treatment.

3.6.2 SOI Substrate with Hydrophilic Bottoms and Hydrophobic Sidewalls of Wells

SOI substrates with spatial surface property were fabricated on SOI wafer by etching through the 10 µm SOI film with the ICP Bosch process from VTT, Finland. The bottoms of the wells are silicon dioxide and the sidewalls are rough crystalline silicon (Fig. 3.28).

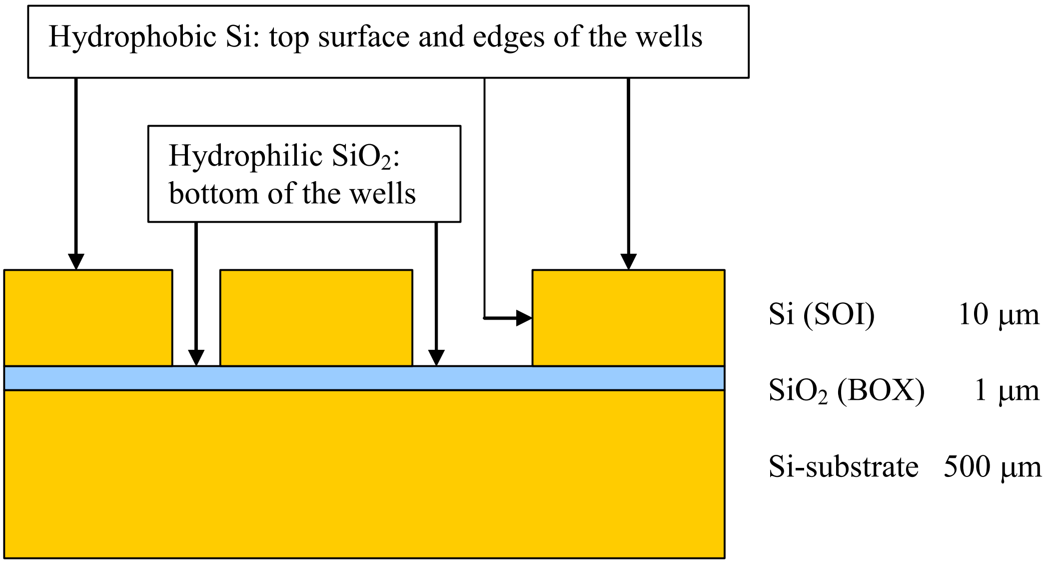

Figure 3.28. Schematic representation of SOI substrate.

SOI substrates were treated by immersing them in a dilute HF solution for 30 seconds and cleaned with de-ionized water. Then they were used for deposition of silica spheres under the same conditions as described above. It was observed that these substrates have similar selectivity as LOCOS substrates. It is remarkable that despite their hydrophobic sidewall surface it was possible to fill the depth parts under optimized conditions and there were no voids between silica opals and sidewalls (Fig. 3.29 and Fig. 3.30). But it was found that the ordering of silica opals in these substrates is not good. The reason for this is not clear.

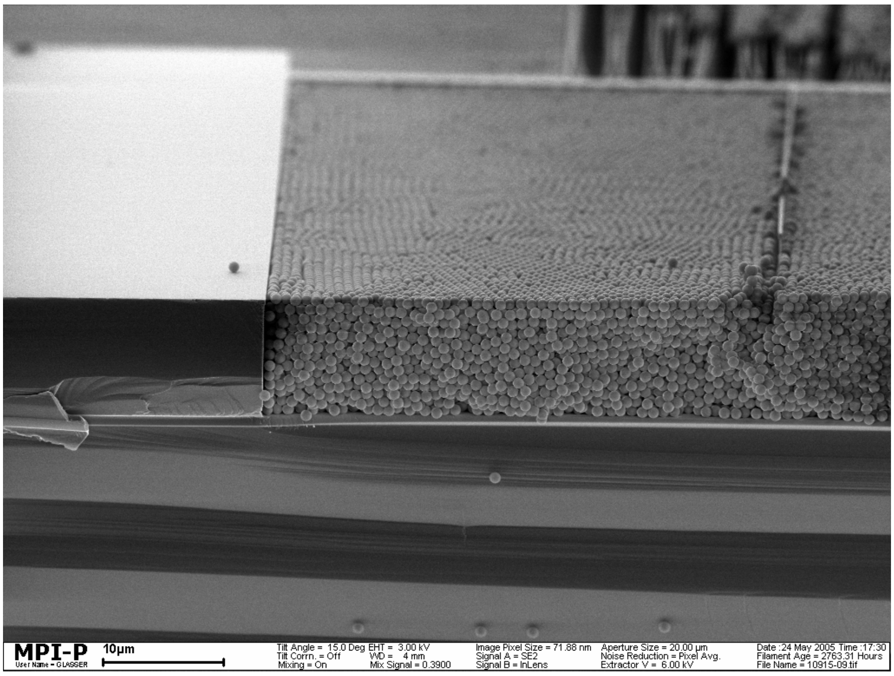

Figure 3.29. SEM image of cross-section of silica opals with a sphere diameter of 890 nm on SOI substrate.

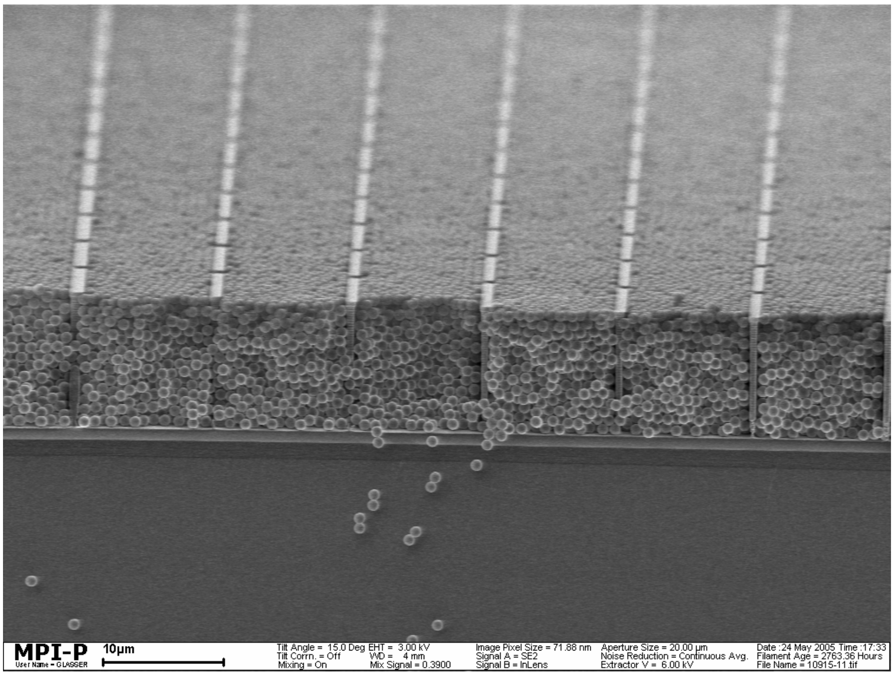

Figure 3.30. SEM image of cross-section of silica opals with a sphere diameter of 890 nm on SOI substrate.

3.7 Crystallization of PMMA Spheres on Patterned Silicon Substrates

For crystallization of PMMA spheres stirring is not necessary. The crystallization process is relative easier to control than that of large silica spheres. Therefore crystallization of PMMA spheres on patterned substrates has been used for investigation of structure influence on crystallization process with respect to the relationship between substrate structures, for instance, trench geometry and size, to sphere sizes. Fig. 3.31, 3.32, and 3.33 show typical samples of PMMA opals with a sphere diameter of 420 nm (Sample No. 6) on patterned Si-substrate fabricated by vertically lifting the substrate with a speed of about 200 nm s^{-1} from a 2 vol.% PMMA sphere suspension. Fig. 3.31 is an optical micrograph, while Fig. 3.32 and 3.33 are SEM images with different magnifications. As shown in these Figs. the well-ordered PMMA spheres were deposited rather selectively onto the profiled substrate. Unfortunately, in this case the cracks can not be overlooked.

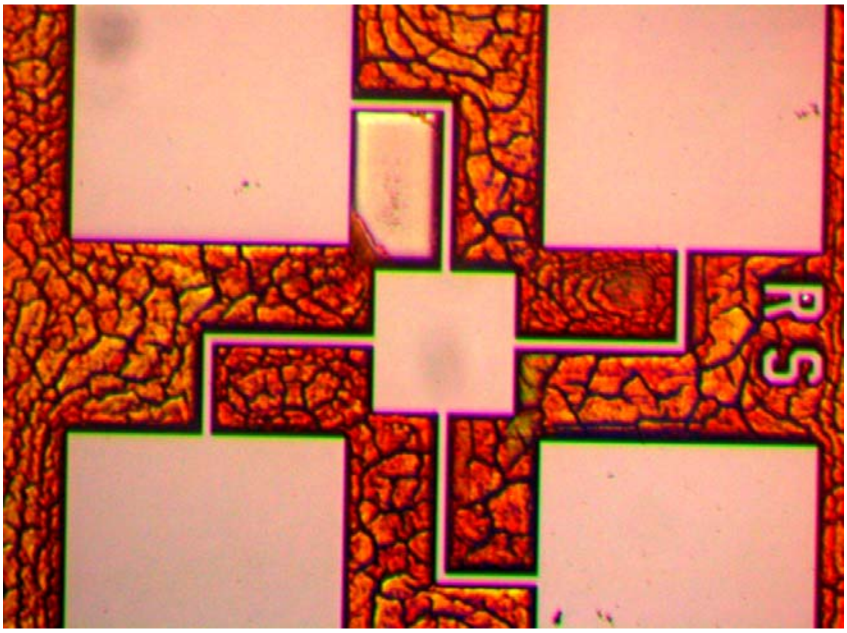

Figure 3.31. Optical micrograph of PMMA opals with a sphere diameter of 420 nm on patterned Si-substrate.

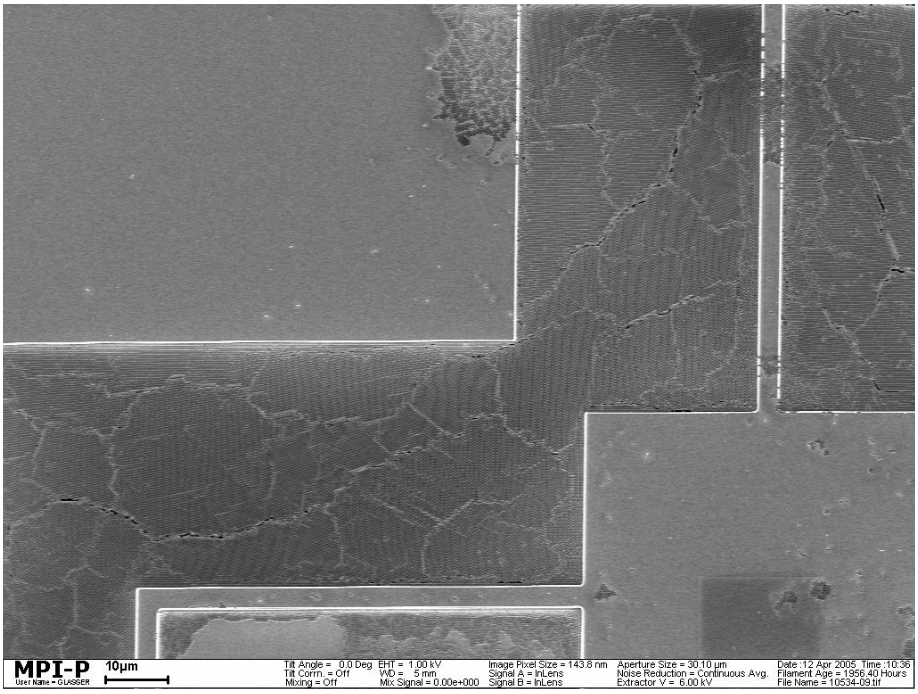

Figure 3.32. Representative SEM image of PMMA opals with a sphere diameter of 420 nm on patterned Si-substrate (LOCOS substrate).

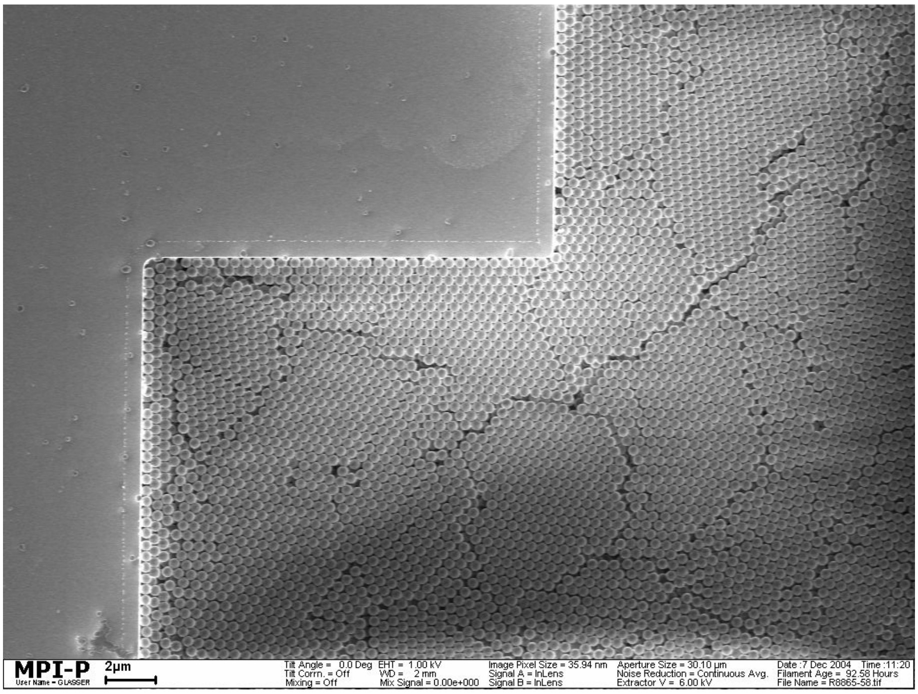

Figure 3.33. Representative SEM image of PMMA opals with a sphere diameter of 420 nm on patterned Si-substrate.

3.7.1 Factors of Precise Deposition of Spheres on Patterned Substrates

The same observation has been seen to be obtained as discussed in Chapter 3.5.2. The small closed pit was not filled even with small spheres, while the similar sized but not closed pit could be well filled (Fig. 3.34). Fig. 3.35 shows SEM images of an interesting comparison between two types of trenches after deposing PMMA spheres. These trenches have same size, but some of them are closed and empty (Fig.3.35a), while others are linked to each other and full infilled from spheres (Fig. 3.35b).

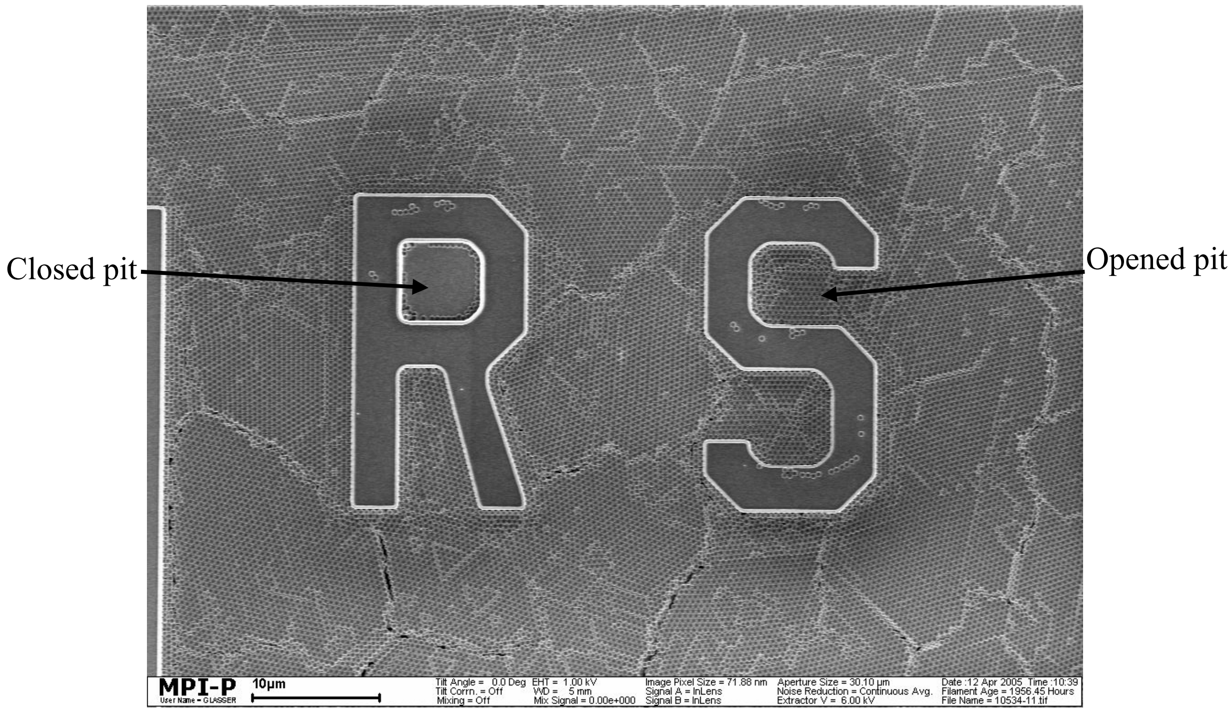

Figure 3.34. SEM image of PMMA opals (sphere diameter 420 nm) on patterned Si-substrate (LOCAS) with unfilled small closed pit.

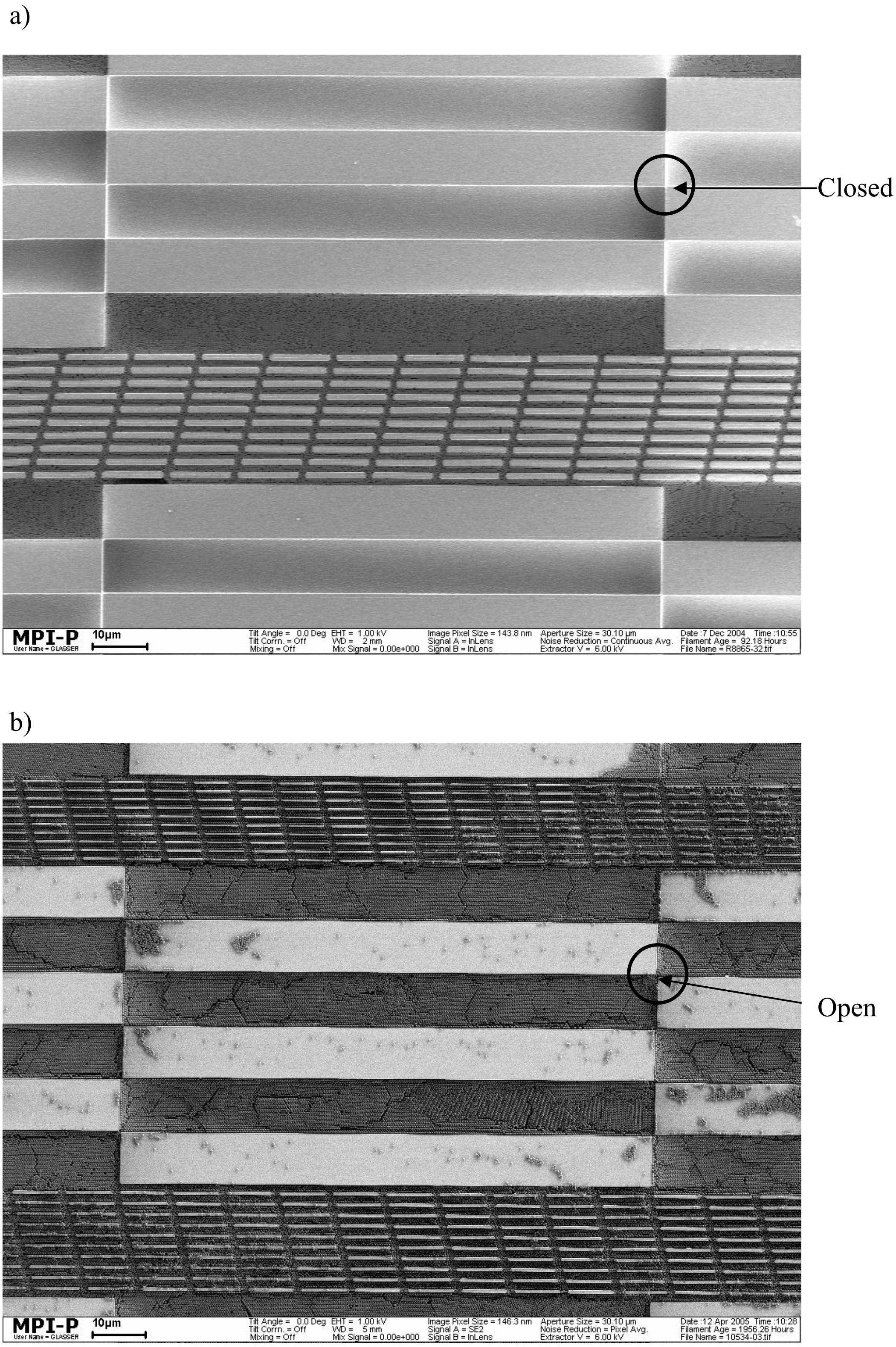

Figure 3.35. SEM images of trenches on Si-substrate after deposition of PMMA spheres of a diameter of 420 nm: a) Closed trenches, b) opened trenches.

For the precise filling the commensurability of the trench width with the sphere size is a critical parameter. Fig. 3.36 demonstrates an example of precise filling even in narrow trenches (Fig. 3.36b) in comparison with the similar situation with the width of the trenches was not exactly commensurate to the sphere size (Fig. 3.36a), in which the spheres could not park closely.

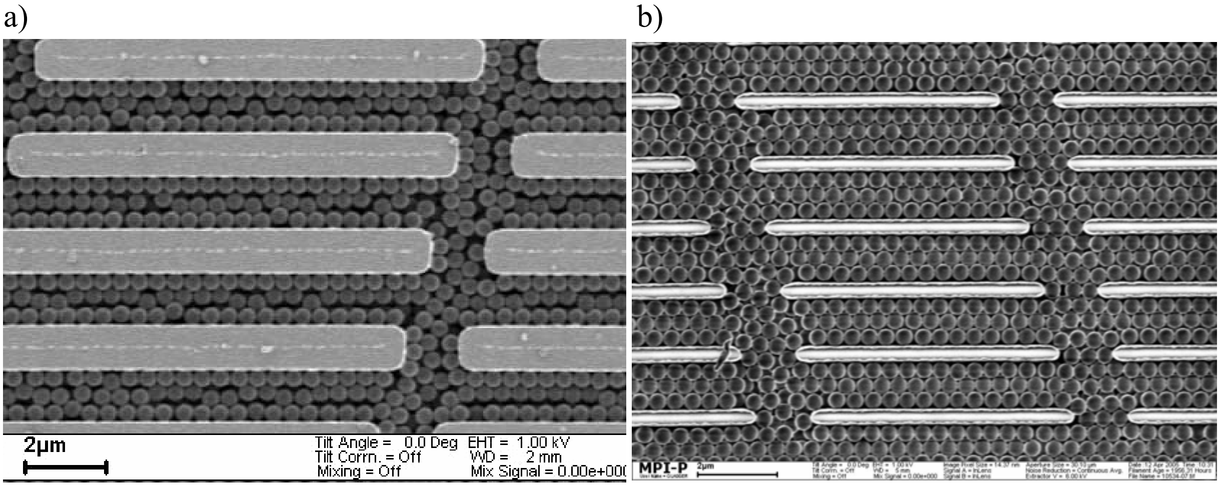

Figure 3.36. SEM images of PMMA opals with a sphere diameter of 420 nm in narrow trenches in patterned Si-substrates: a) The spheres were not closely parked; b) the spheres were closely parked.

Figures from 3.37 to 3.40 are SEM images of PMMA opals with sphere diameter of 270 nm (sample No. 3) on patterned Si-substrates. These opals made of small spheres have enormous volume shrinkage after total drying. The consequence is a great number of cracks emerging. The cracks appeared frequently along the side walls (Fig. 3.37 and 3.38) if the trench had the size in the order of a single crystal domain size, or if the side wall was not straight enough (Fig. 3.38). In a wide trench (Fig. 3.39 and 3.40) these cracks were almost randomly distributed over the surface as in the case of opal grown on a flat substrate and no preferred locations of them could be found (Fig. 3.39). Apart from the fact of cracks, the deposited film as shown in these Figs. possesses a highly ordered arrangement of PMMA spheres corresponding to the (111)-plane of a fcc lattice, in depth as well as in the plane, independent of the trench sizes.

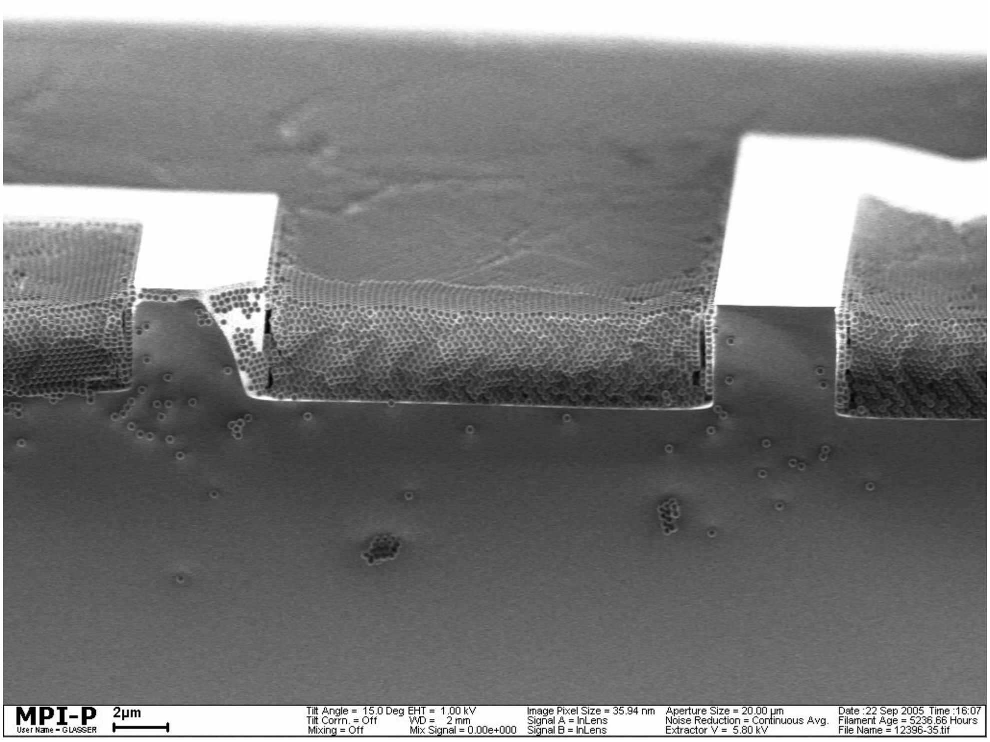

Figure 3.37. SEM image of PMMA opals made from spheres of a diameter of 270 nm on patterned Si-substrate.

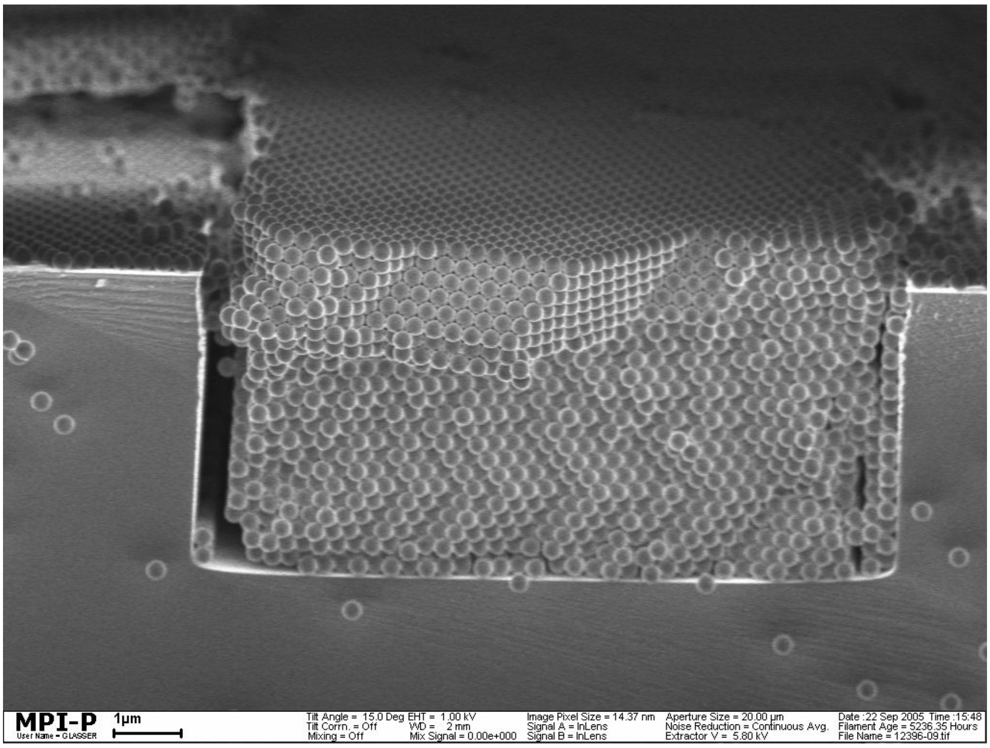

Figure 3.38. SEM image of PMMA opals made from spheres of a diameter of 270 nm on patterned Si-substrate.

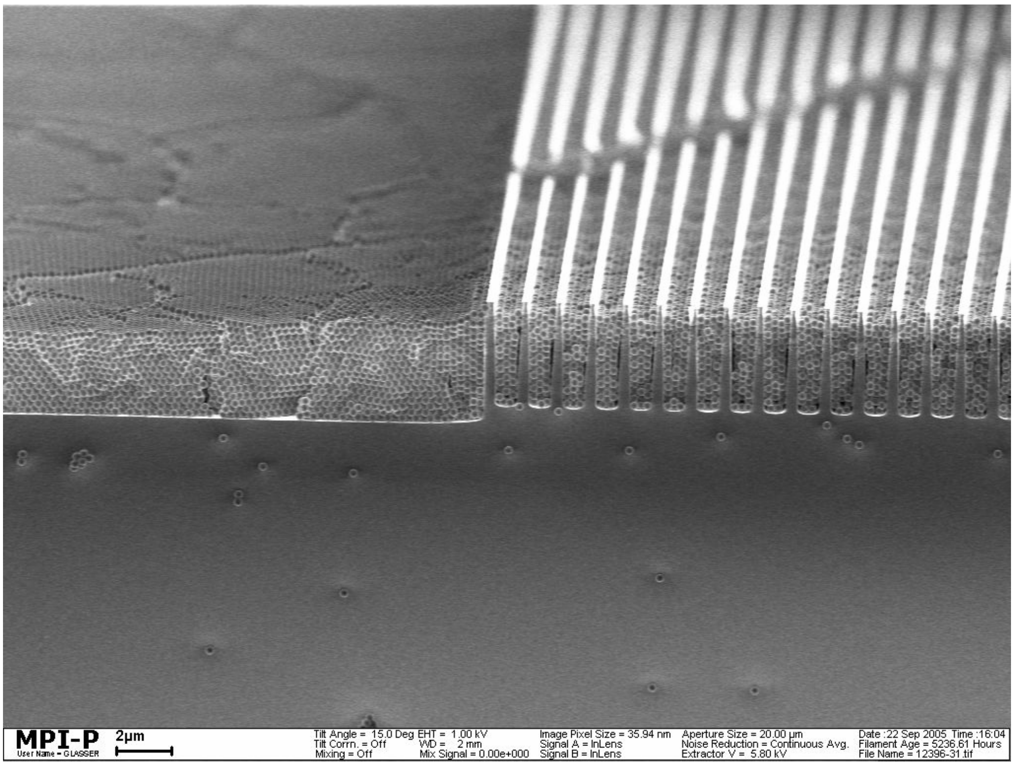

Figure 3.39. SEM image of PMMA opals made from spheres of a diameter of 270 nm on patterned Si-substrate.

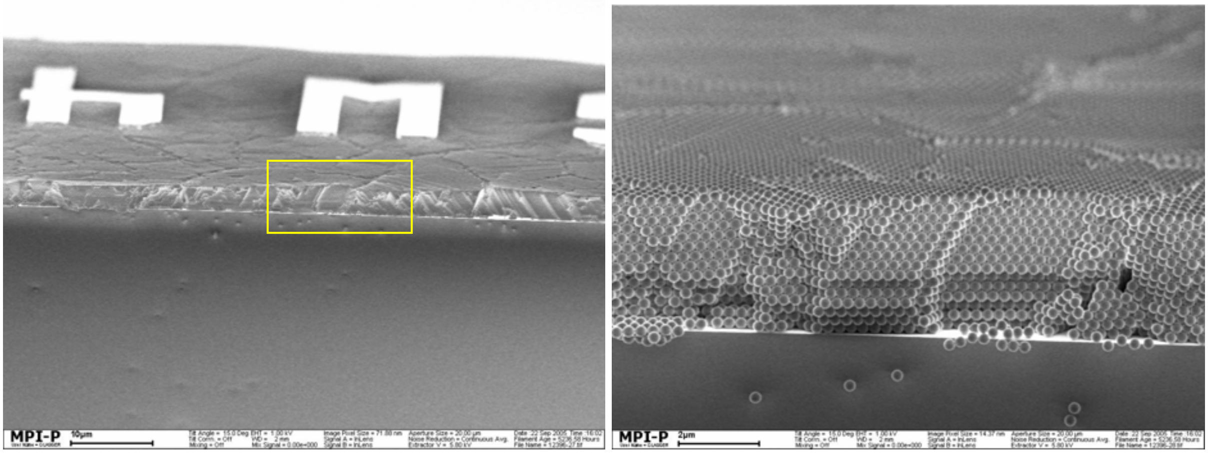

Figure 3.40. SEM images of PMMA opals made from spheres of a diameter of 270 nm on patterned Si-substrate. Right: Large magnification of the marked area (left).

3.7.2 Optical Characterization of PMMA Opals on Patterned Silicon Substrates

Optical characterization of PMMA opals on patterned Si-substrates was performed by reflectance spectroscopy in Golm. Fig. 3.41a is the reflectance spectrum of PMMA opals with a sphere diameter of 420 nm (sample No. 6) on patterned Si-substrate collected using a beam with a macroscopic spot size of 9x1 mm^2 at the angel $\Theta = 6°$ with respect to the surface normal. In this case, the spectrum is thus averaged over many trenches or realizations of opal lattice, with different lateral extension. This could be responsible for increasing inhomogeneous broadening of the diffraction resonance of the film and explain the high relative bandwidth value $\Delta\lambda/\lambda = 0.082$, which exceed significantly the theoretically calculated value of 0.056 for the relative bandwidth along the (111)-axis of a perfect infinite opal. Another reason for the band gap broadening is the small film thickness, which is about 13 layers emanating from optical evaluation of the Fabry-Pérot oscillations (Fig. 3.41b). The observation of Fabry-Pérot fringes by reflectance spectroscopy indicates the good crystal quality.

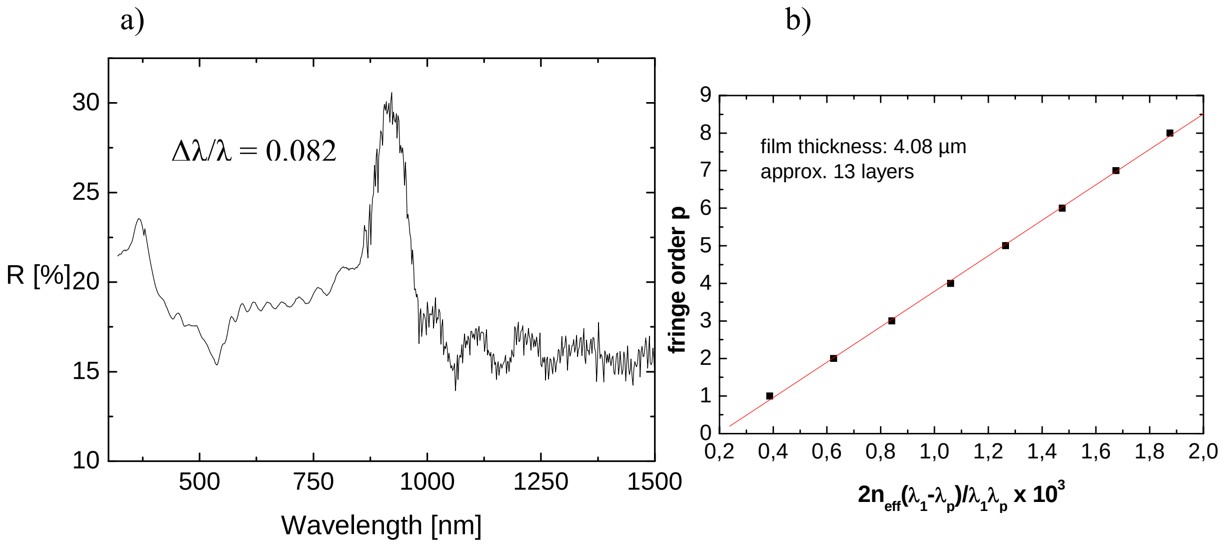

Figure 3.41. a) Reflectance spectrum of PMMA opals with a sphere diameter of 420 nm on patterned Si-substrate at angel $\Theta = 6°$. The relative bandwidth value $\Delta\lambda/\lambda = 0.082$. b) Calculation of film thickness based on Fabry-Pérot fringes (13 layers).

Reflectance measurements were also performed at different angels Θ. The results are shown in Fig. 3.42a. The reflectance spectra follow well the Bragg condition (Fig. 3.42b). The nonlinear fit to Bragg-Snell equation gives n_{eff} = 1.4152; d = 321 nm; particle diameter D = 394 nm, which is comparable to that obtained from flat glass substrate (Table 2.4) within the experimental accuracy.

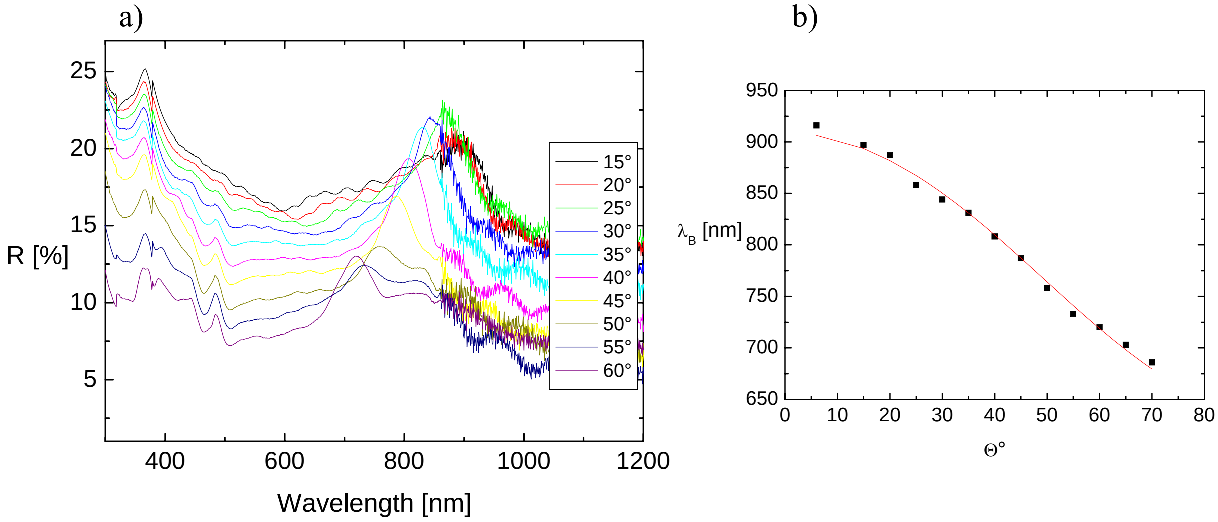

Figure 3.42. a) Reflectance spectra of PMMA opal film on the patterned Si-substrate at angles Θ from 15° to 60° with a 5° step. b). Bragg peak angle dispersion. Results from Bragg equation nonlinear fit: n_{eff} = 1.4152; d = 321 nm; particle diameter D = 394 nm.

3.7.3 Microspectroscopy Optical Analysis of Confined PMMA Crystals

For the optical characterization it is very interesting to know the optical properties of opals in an individual trench. To do this, the reflectance measurements were performed by using a UV-vis spectrometer coupled to a microscope (Leitz). Considering the spectrometer measure range, samples of a sphere diameter of 270 nm (Sample No. 3) were prepared. Fig. 3.43a, b, c, and d show optical micrographs of PMMA opals in different trenches. The white marked areas in these Figs. were selective regions for the reflectance measurements. The responding reflectance spectra are shown in Fig. 3.43e, and f. For the same trenches independent of trench numbers, as shown in Figs. 3.43e, and f, no significant difference of the spectra are observed in the intensity, width, and position of the main reflectance peak and side fringes. But for the different trenches large differences are observed for the shape of the reflectance spectra (Fig. 3.44).

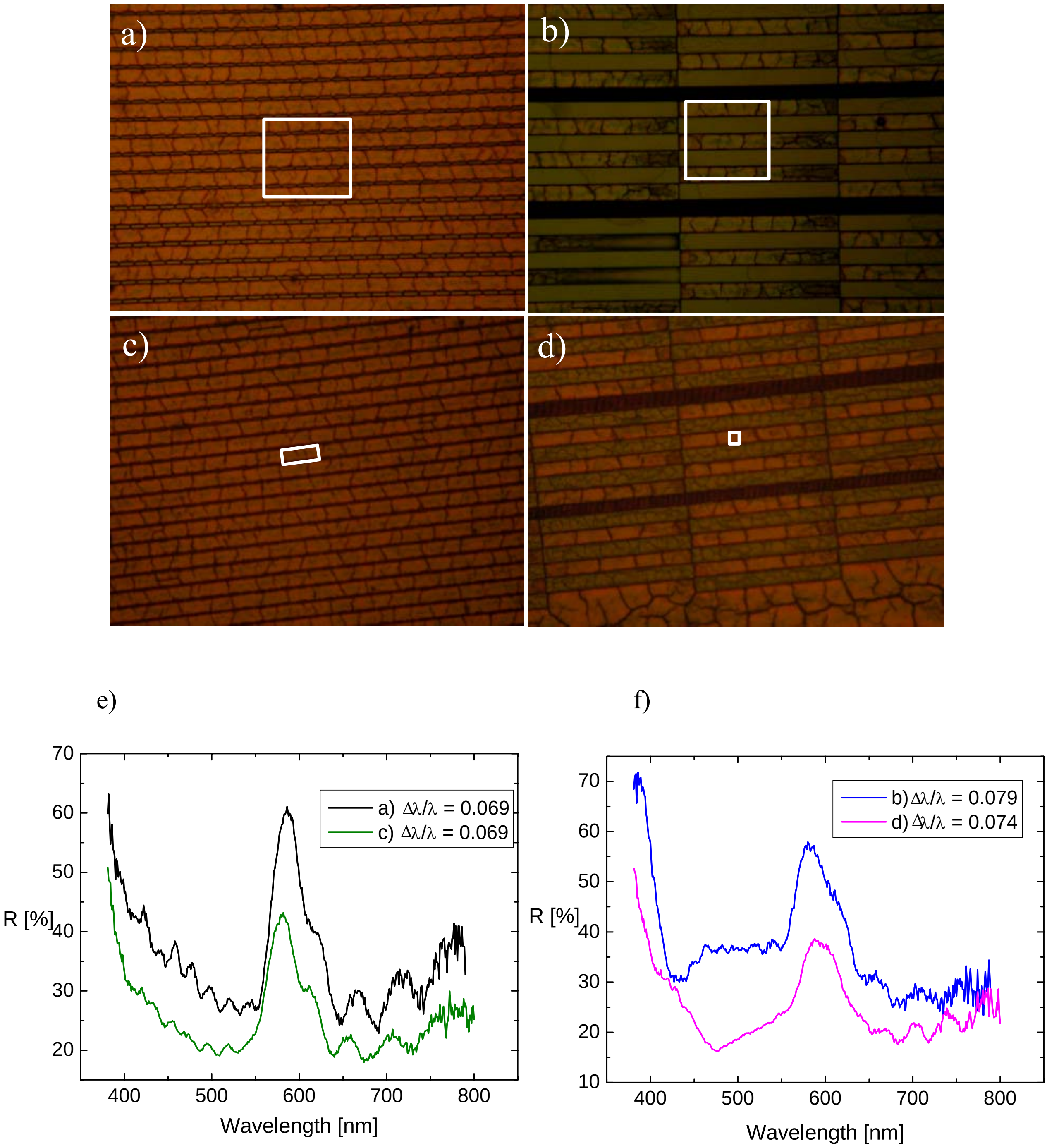

Figure 3.43. a-d) Optical micrographs of PMMA opals in different trenches. e) Reflectance spectra collected from marked area of a and c. f) Reflectance spectra collected from marked area of b and d. Δλ/λ is the relative bandwidth value.

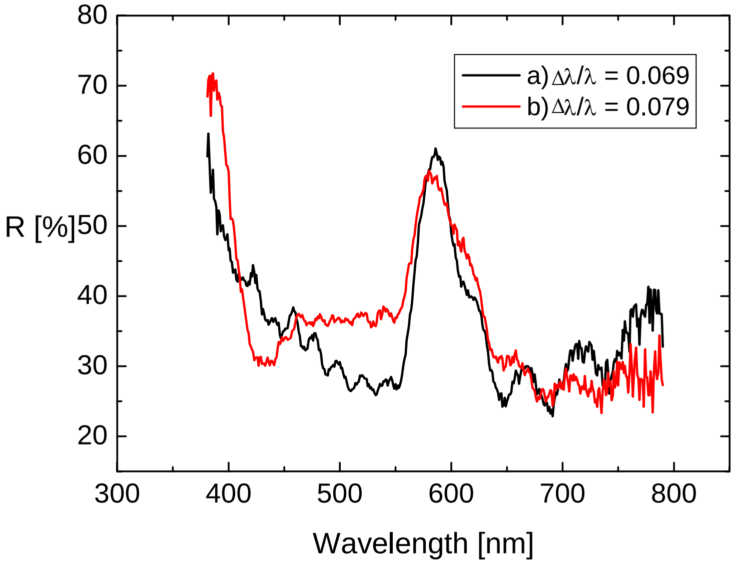

Figure 3.44. Reflectance spectra collected from marked area of Fig. 3.43a and b.

Figure 3.45 show the reflectance spectra collected from different regions (white marked areas): 1) No letter, 2) one letter, 3) two letters. It can be seen that they have similar shape but the spectrum collected from the area with two letters has relative low intensity.

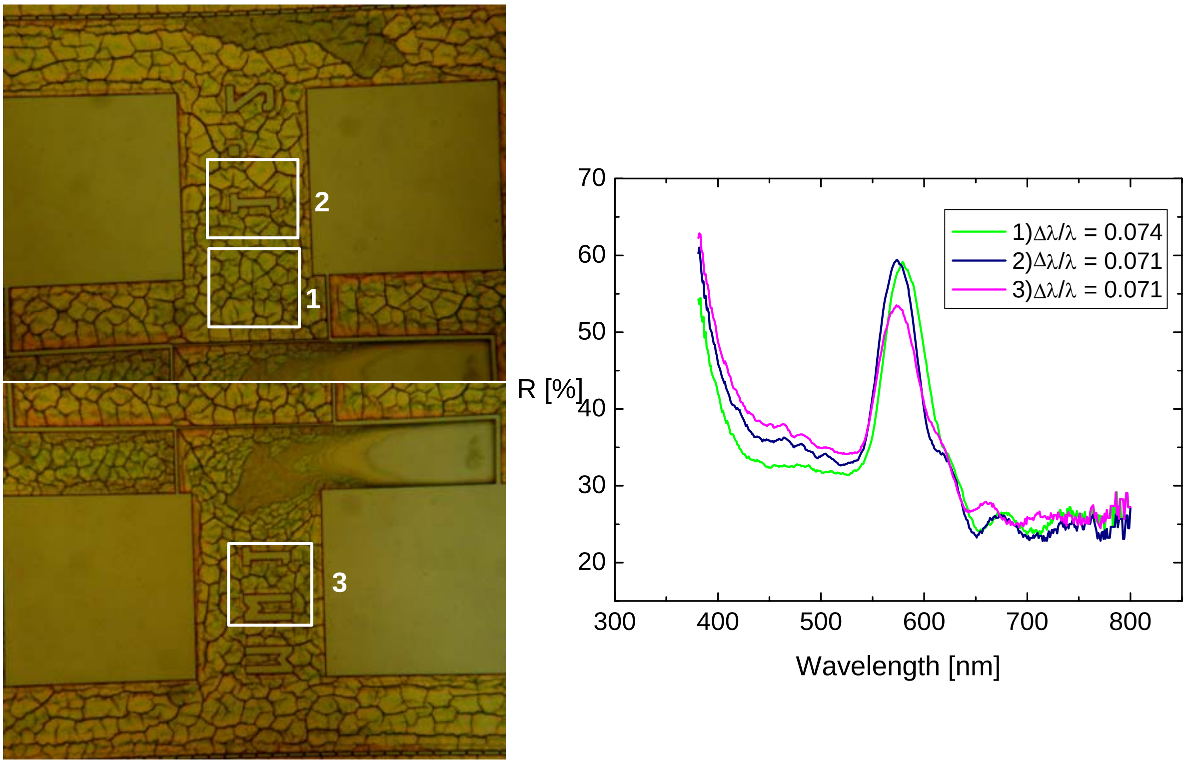

Figure 3.45. Reflectance spectra collected from different regions (white marked areas): 1) No letter, 2) one letter, 3) two letters.

Figure 3.46 shows reflectance spectra collected from single crystal in trenches with different widths: 1) very narrow, 2) wide, 3) narrow but wider than 1. These spectra are similar in intensity, relative bandwidth (Δλ/λ), and position of both the main reflectance peak and side fringes. But the shape of reflectance spectrum from the wide trench is a little different to that from the narrow trenches (Fig. 3.46).

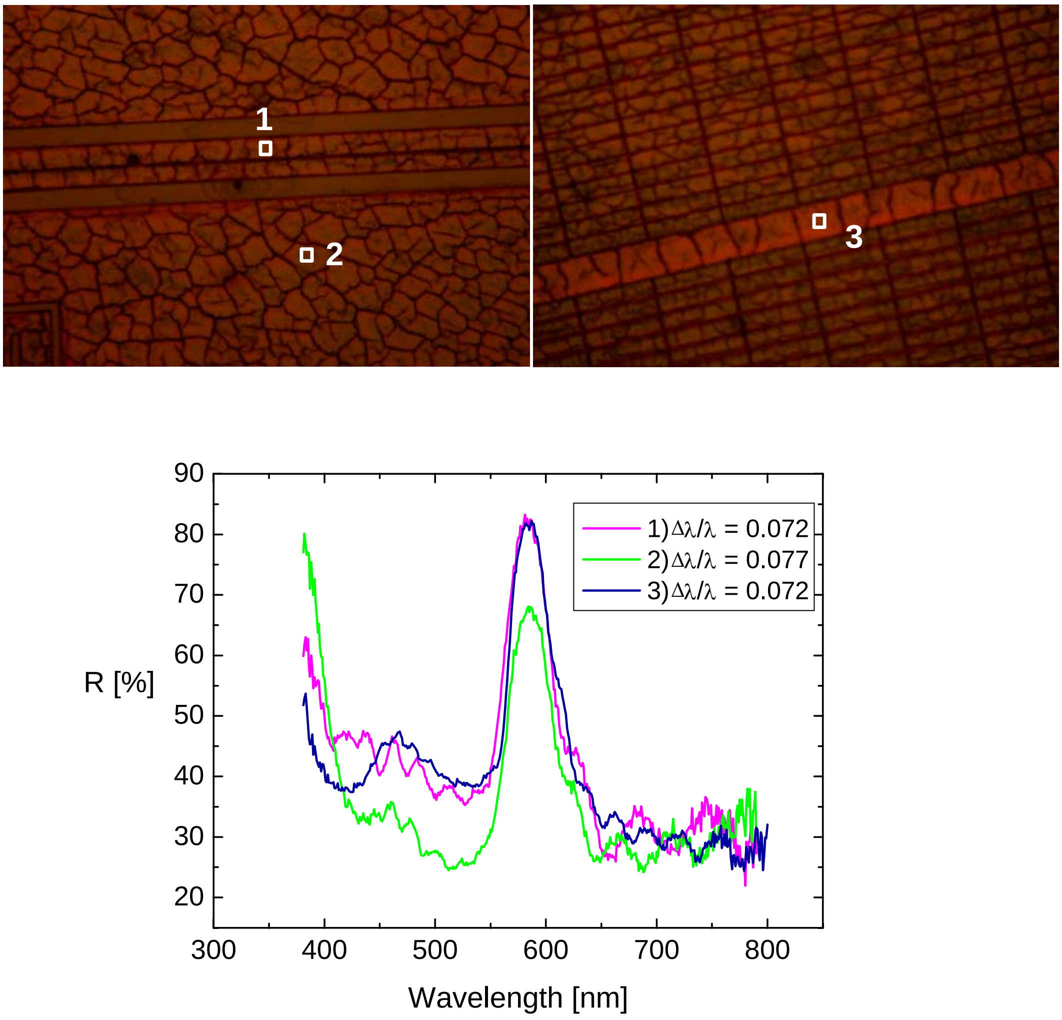

Figure 3.46. Reflectance spectra collected from single crystals in trenches with different widths: 1) very narrow, 2) wide, 3) narrow but wider than 1.

Figure 3.47 shows the reflectance spectrum collected from the marked area of a wide trench (Fig. 3.47a) in comparison with that from a flat substrate (Fig. 3.47b). As expected the spectra were nearly identical.

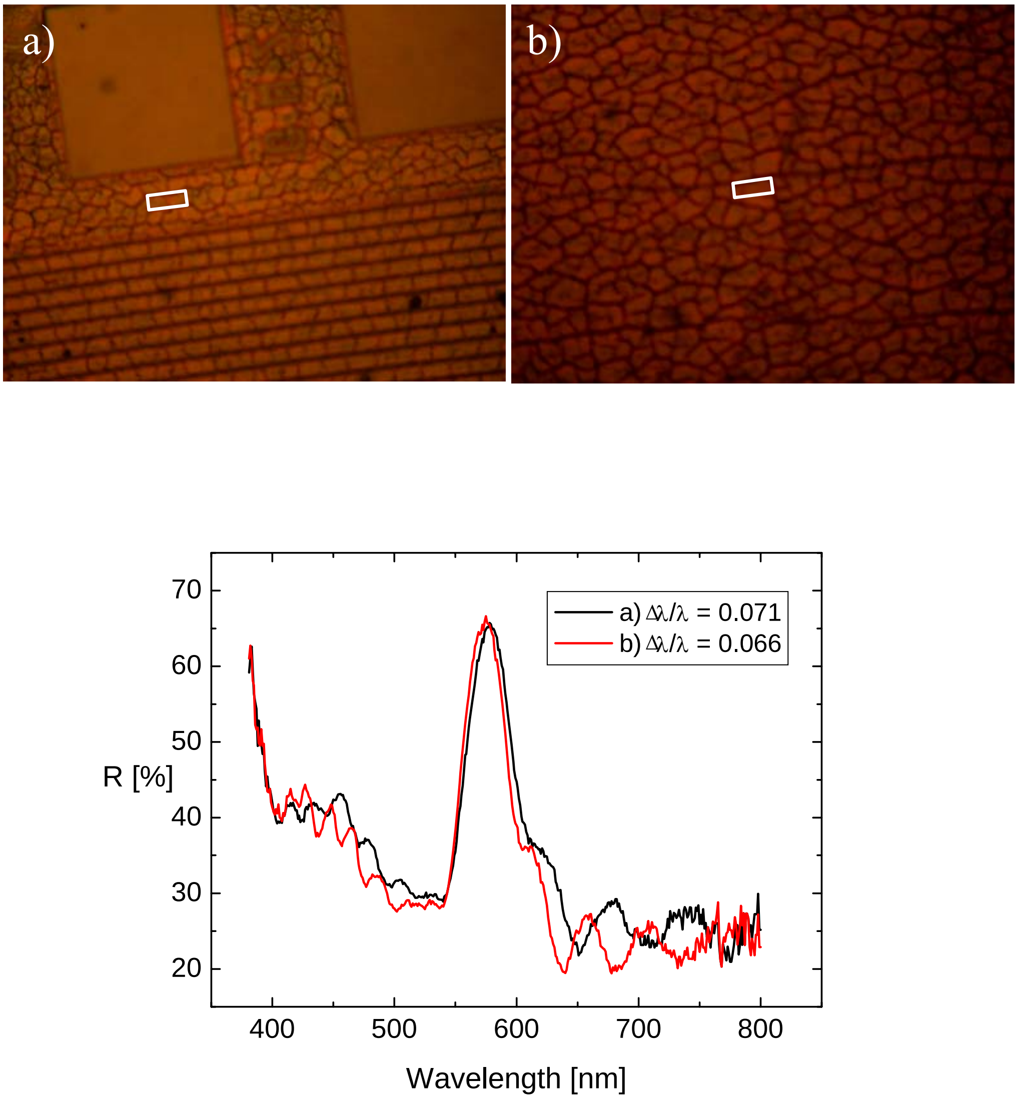

Figure 3.47. Reflectance spectrum collected from the marked area of a wide trench (a) in comparison with that from a flat substrate (b).

3.8 Crystallization of PMMA Spheres on Patterned Polymer Substrates

In order to open the optical accessing of the photonic crystals on the visible wavelength range patterned polymer substrates were fabricated by VTT, Finland. Fig. 3.48 is the schematic representation of such substrates, in which the trenches have a SU-8 polymer sidewall (hydrophobic) and a SiO_2 bottom (hydrophilic). For the crystallization PMMA spheres of a diameter of 420 nm (Sample No. 6) were used. Fig. 3.49, 3.50, and 3.51 show SEM images of opals on patterned polymer substrates. The results of deposition are strongly dependent on patterned structures (Chapter 3.5.2). As shown in these Figs. some of trenches were fully filled, while others were empty.

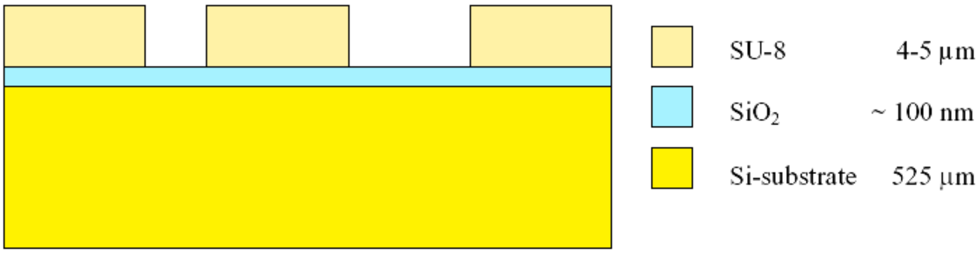

Figure 3.48. Schematic representation of polymer substrate.

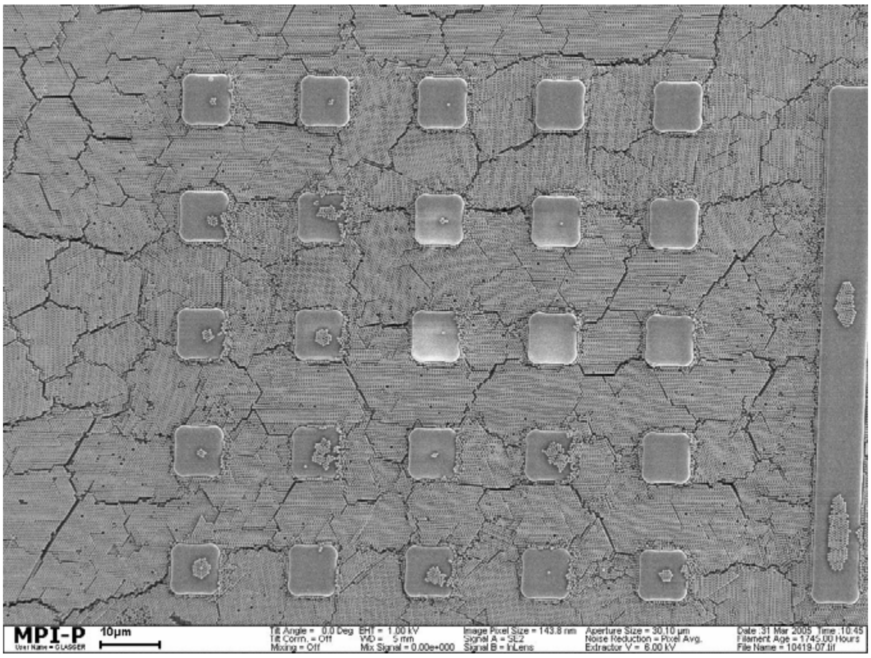

Figure 3.49. SEM image of PMMA opals of a sphere diameter of 420 nm on patterned polymer substrate.

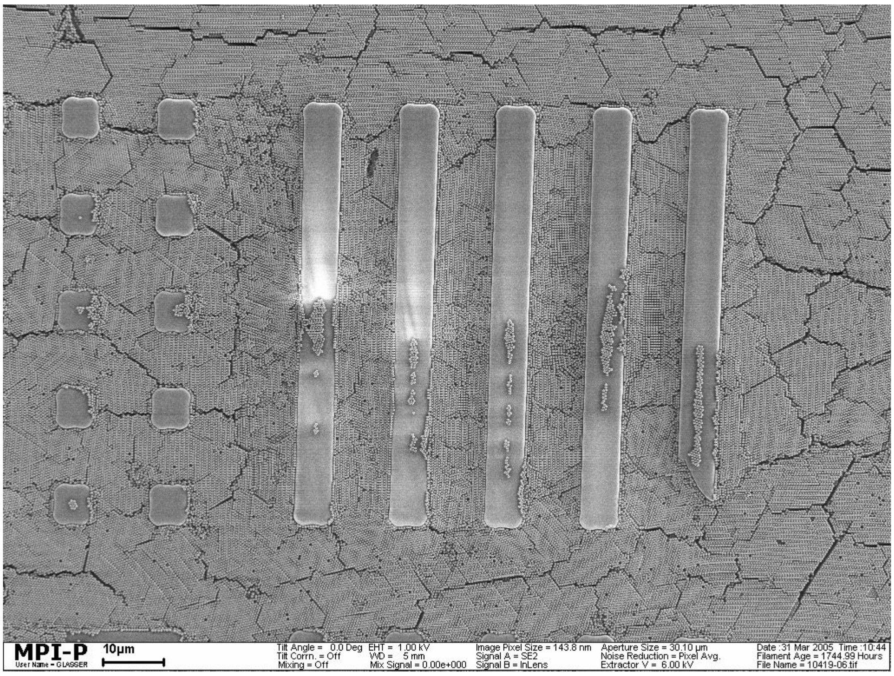

Figure 3.50. SEM image of PMMA opals of a sphere diameter of 420 nm on patterned polymer substrate.

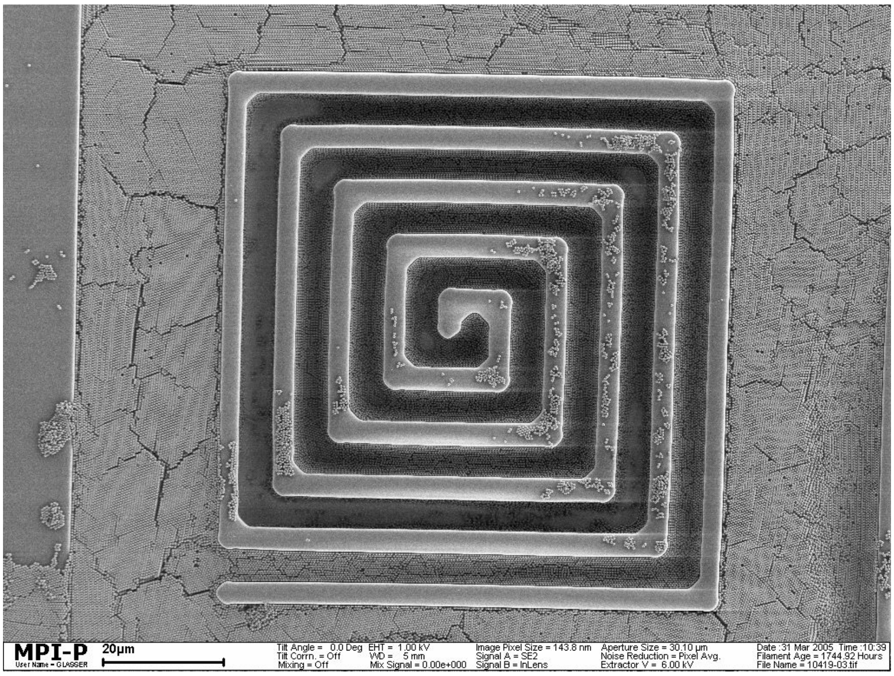

Figure 3.51. SEM image of PMMA opals of a sphere diameter of 420 nm on patterned polymer substrate.

Figure 3.52 and 3.53 show SEM images of opals on patterned polymer substrate in lateral section. It is remarkable that despite hydrophobic sidewall surface in certain conditions the spheres filled well in depth parts and no voids between opals and sidewall have been observed (Fig. 3.52 and 3.53). This indicated the fact that it is possible to introduce the polymer ridge waveguide into opals.

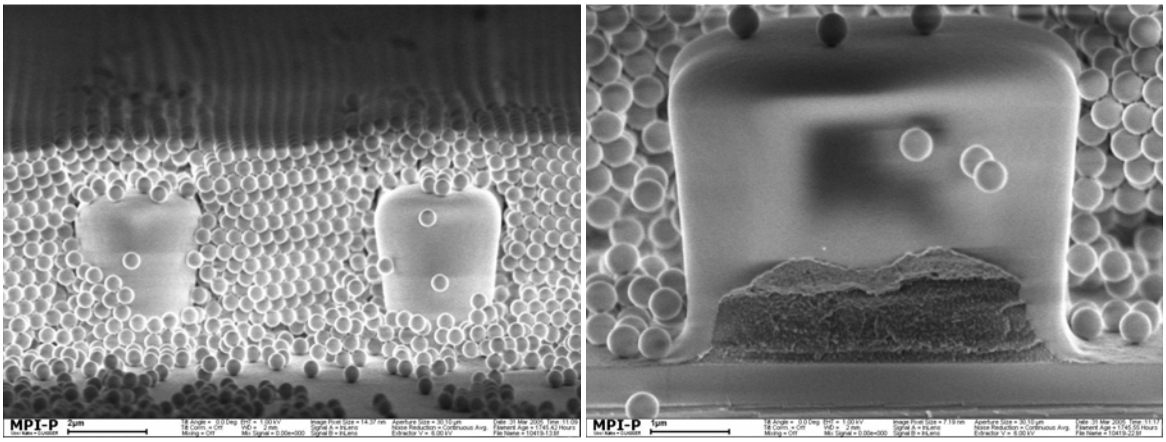

Figure 3.52. SEM images of PMMA opals of a sphere diameter of 420 nm on patterned polymer substrate.

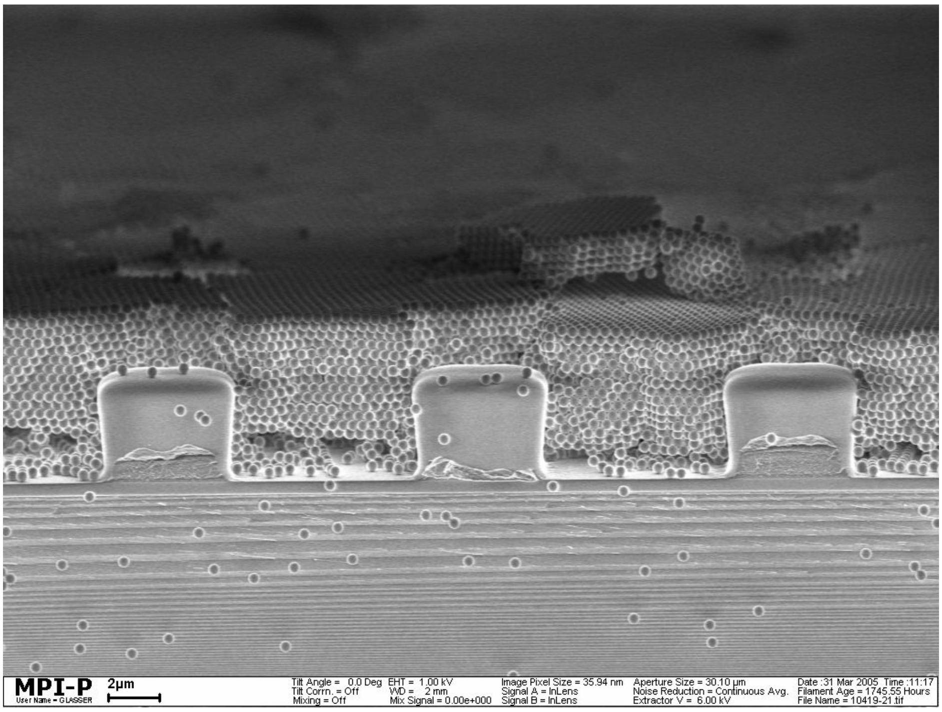

Figure 3.53. SEM image of PMMA opals of a sphere diameter of 420 nm on patterned polymer substrate.

4. Multilayer Opals as Functionalized Photonic Crystals

The impact of colloidal crystals as photonic crystals could be considerably enhanced if they possessed a heterogeneous structure. Recently the development of heterogeneous photonic crystals has attracted much attention owing to their complicated heterostructure. These photonic crystals change the light propagation and bring new physical phenomena. The basic component of these functionalized structures is the interface between two photonic crystals with different properties, which introduces a sharp distortion in the spatial distribution of the electromagnetic field.[130] This provides a possibility of interference of electromagnetic waves originating from different photonic crystal reservoirs, if they have the same frequency and wave vector but possess an arbitrary phase shift, which is a pre-condition for the appearance of a resonance at the photonic crystal interface. This phenomenon is a unique property of photonic crystal interfaces and has no analogy in electronic properties of semiconductor heterojunctions.[131] Hetero-opals are suitable candidates for heterogeneous functionalisation. They can be realized by combining films of different lattice using direct or inverted opal films.[46,130,132]

Multiple-layered structures contain the photonic bandgap interfaces affecting the light propagation. One example of these structures is the triple-film opals with a sandwich structure, whose top and bottom layer are the same opal film and the middle layer is either a opal film, but made of the spheres in different size as that in top and bottom layers, or a film of other material. If the middle layer is thin enough to be comparable to the wavelength of interest and it does not possess its own photonic band structure, it can serve as a planar defect. Otherwise a thick middle layer of opals can be characterized by its own photonic band structure. This leads to the necessity of coupling the light flow from one photonic crystal to another at each interface.[131] Studies of the transmission and forward scattering of light in triple-film hetero-opals revealed that its optical properties cannot be considered as the linear superposition of two independent photonic bandgaps.[133,134] The specifics of hetero-opal effects are the anomalous increase of the forward light scattering and changing the ballistic light propagation to diffuse one at frequencies of the planer defect,[133] as well as alteration of the transmission, such as the decrease of the polarization anisotropy and narrowing of the transmission minima.[134]

This chapter deals with fabrication of multilayer colloidal crystals formed from opaline films with different sphere sizes or different materials on a glass substrate. The characterization of these multilayer opals by SEM and optical measurements is demonstrated and the problems for the fabrication are also discussed.

4.1 Fabrication of Triple-Film Opals from PMMA Spheres with Different Sizes

The triple-film opals were prepared by sequential deposition of PMMA opal films on a glass substrate. The opal film A was fabricated by the vertical deposition method using a drawing machine as described in Chapter 2.3.2. The formed opal film was sintered at 80°C-95°C depending on sphere size for about 3 hours. After annealing, a second opaline film B was crystallized on top of the first one and so the process was repeated to assemble the top film A again. Each layer of the crystals consists of a three-dimensionally ordered array of closed-packed colloids. Fig. 4.1 shows the cross-sectional SEM images of a tri-layer opal film possessing an ABA structure, with three successive depositions. The two A layers were PMMA opaline films composed of 370 nm diameter spheres (Sample No. 5), while the middle B layer was PMMA opals with a sphere diameter of 270 nm (Sample No. 3). Below, this structure is denoted as 370 nm/270 nm/370 nm opal, with the first/second/third number representing the bottom/middle/top film. It is evident as shown in Fig. 4.1 that the interfaces between the layers are flat and well defined. Both the A and B layers have very nice sphere ordering. It should be noted that the individual layer of such multilayer opal film was relative thin because otherwise the film could be broken away from the substrate in the suspension and the entire process fails. If the temperature and humidity are constant the film thickness can be controlled by adjusting the suspension concentrations and the drawing speed of the lifting machine. Unfortunately this work was done in an open room. The room temperature did not change too much but the humidity did, which it was not possible to control. This made the controlling of the film thickness problematical.

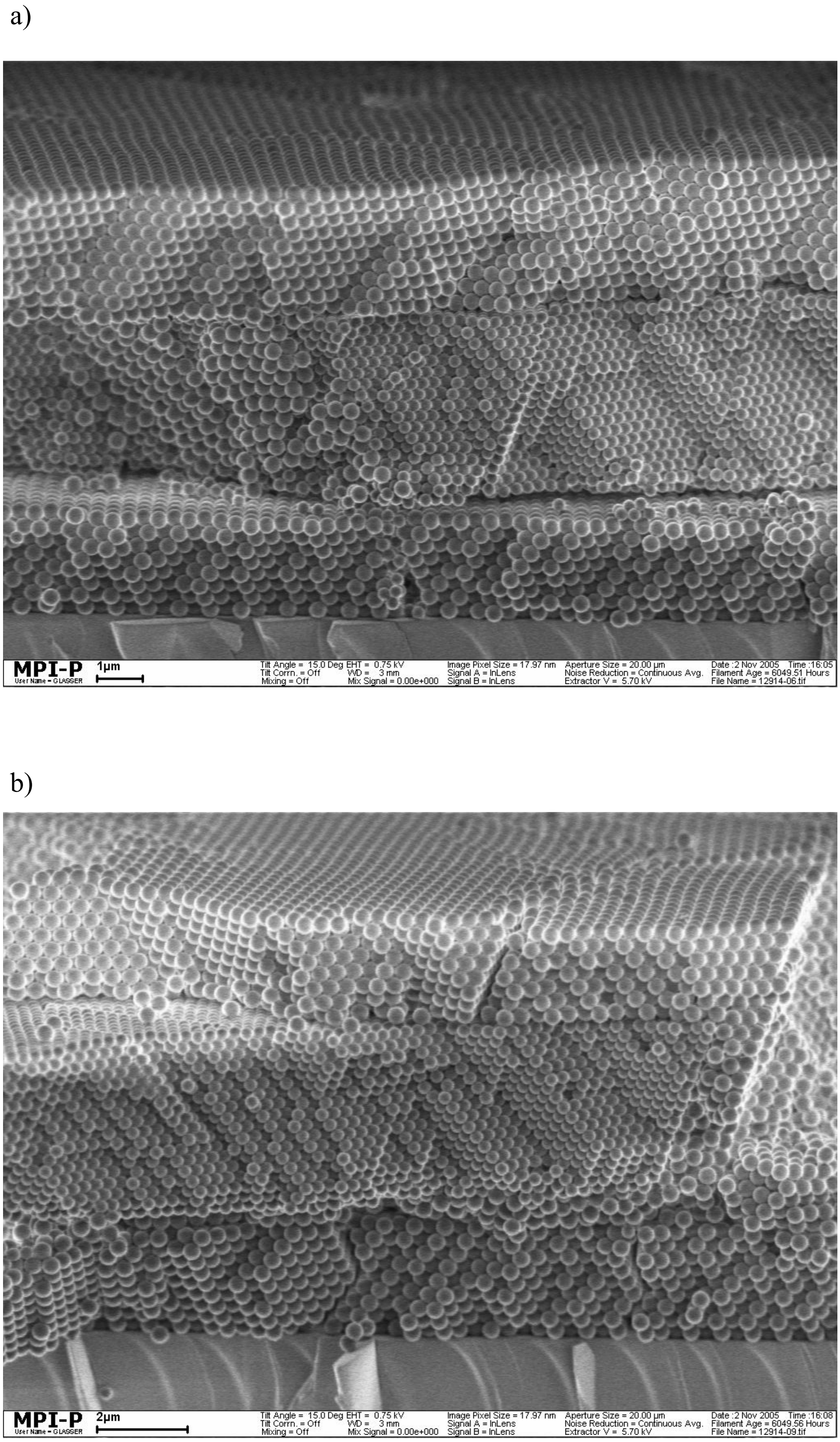

Figure 4.1. Representative SEM images of the cross-section of a 370 nm/270 nm/370 nm triple-film opals; a) and b) made from the same film but in different positions.

It has been observed that generally the assembling of colloidal spheres on an opal film works as well as their deposition on a glass substrate, no matter how the combination of the sphere sizes from the different individual layers and the stacking sequence is.[135] Some examples of bi-layer opal film composed of the opal layers having different sphere size combinations are given in Fig. 4.2. Fig. 4.3 shows SEM images of two tri-layer opal films made from same opal layer A with 370 nm diameter spheres and B with 420 nm diameter spheres (Sample No. 6) but in reverse layer stacking order. The Figs. 4.2 and 4.3 indicate highly ordered opaline films and good interfacial packing of the spheres with different sizes.

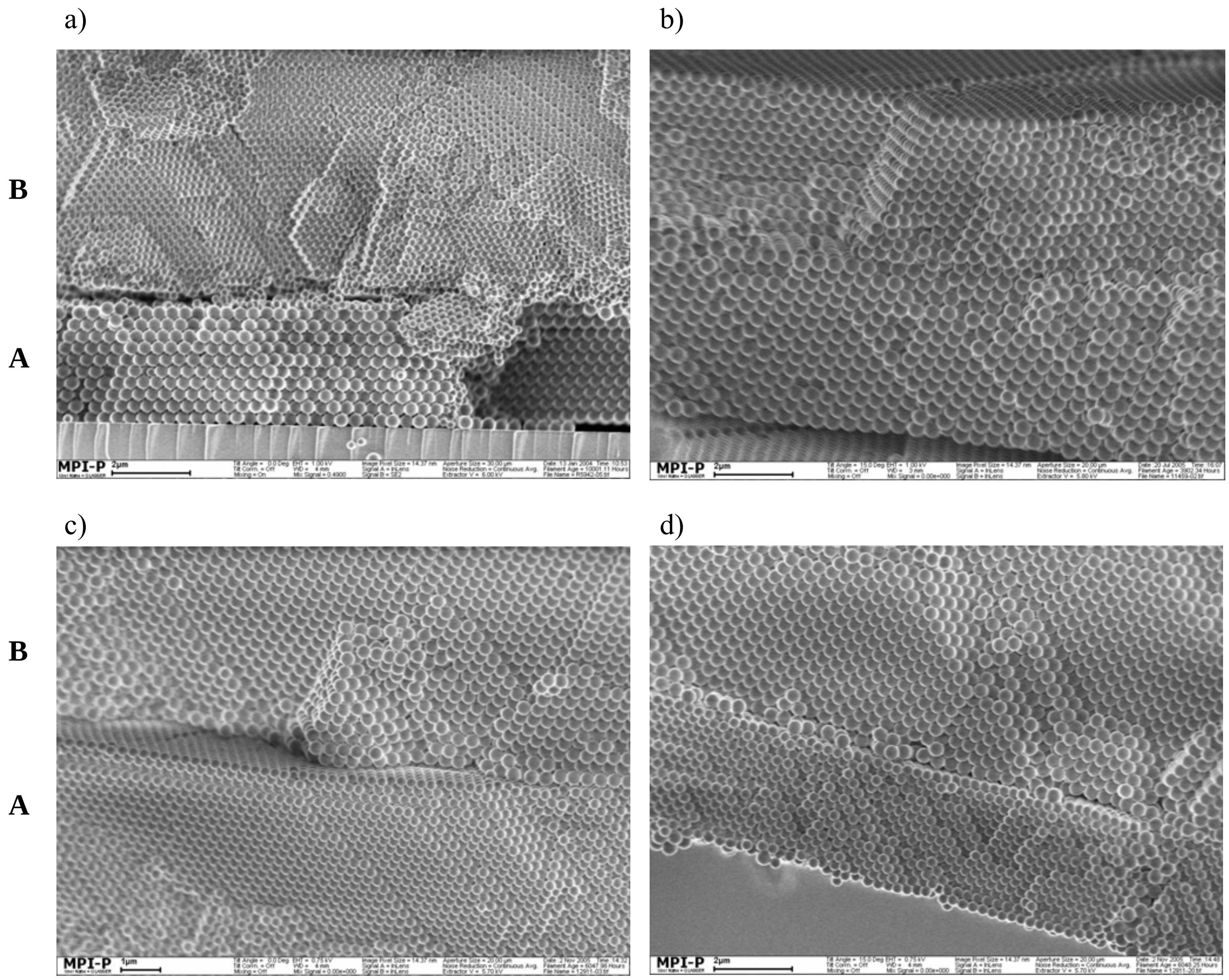

Figure 4.2. Representative SEM images of bi-layer opal films made from opal layers A/B with different size combinations: a) 370 nm/230 nm, b) 420 nm/370 nm, c) and d) 270 nm/370 nm.

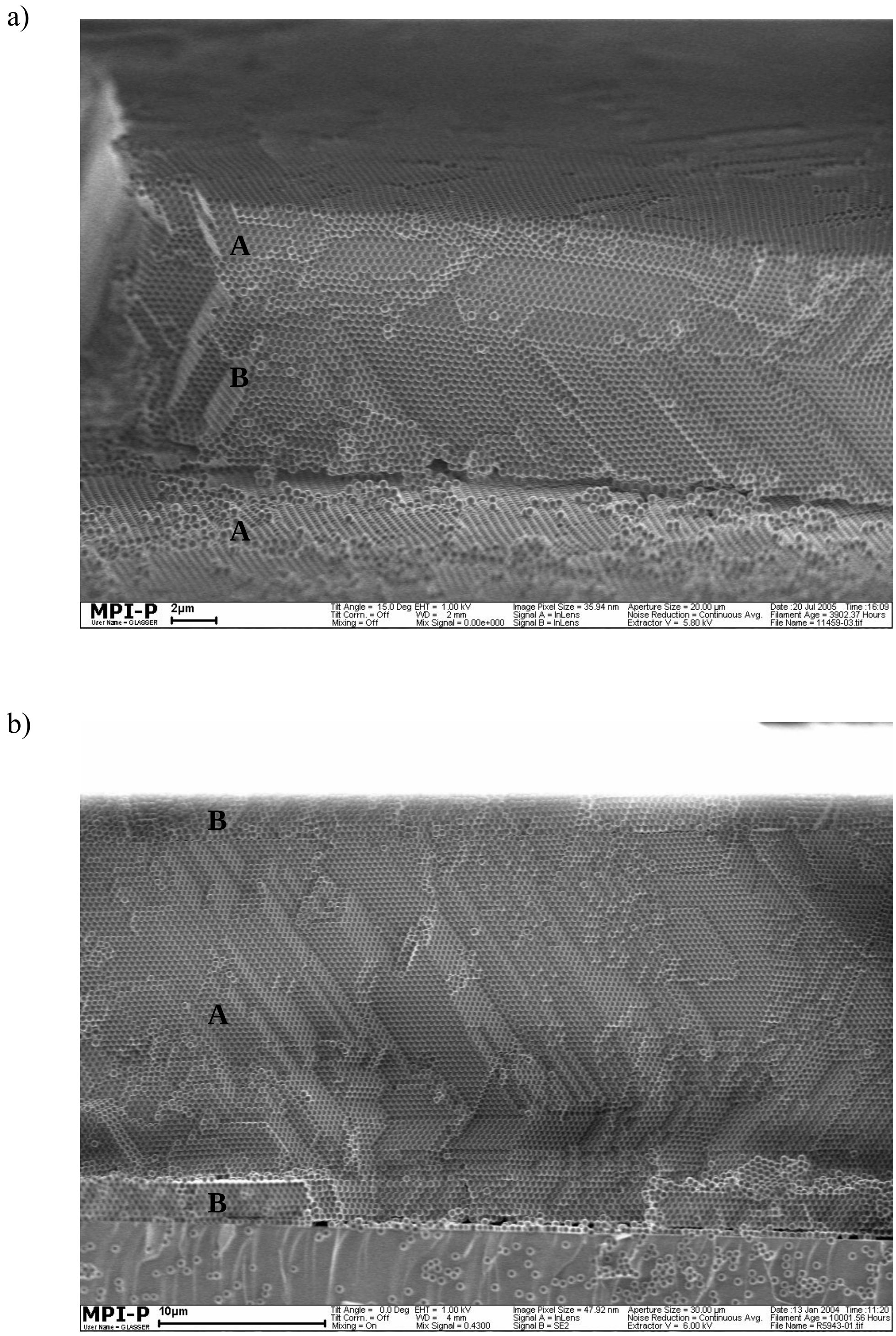

Figure 4.3. SEM images of triple-film opals made from the same opal layer A (sphere diameter 370 nm) and B (sphere diameter 420 nm) but in reverse layer order: a) 370 nm/420 nm/370 nm, b) 420 nm/370 nm/420 nm.

However, it was often observed that the opal layers separated from each other during drying (Fig. 4.4). This is the main problem in the fabrication of multilayer opals. The reason could be due to different shrinkage of each individual layers. The opal layer made of smaller spheres has higher shrinkage than that from larger spheres. Owing to the different shrinkages from the different layers there was strain in the interface between the layers. This resulted in more cracks and small crystallites in the multilayer opals (Fig. 4.5). At worst the opal film was broken. It has also been observed that the tri-layer opal film was very easily broken if the sphere size in the middle opal layer was larger than that in the other two layers (Fig. 4.6), while in reverse order of these layers the film was relative stable. The strain in the layer interface could be reduced by very careful drying. Nevertheless, it is more difficult to prepare multilayer opal film whose individual layers are made of the spheres with significant difference in their diameters. Fig. 4.7 shows SEM images of an extreme case in which the middle layer was a monolayer of large polystyrene (PS) spheres having a diameter of about 1 µm and the top and bottom layer were PMMA opal films made of spheres with a diameter of 370 nm; this tri-layer film broken explosively during drying. The large PS spheres were prepared by the Fraunhofer Institute in Golm. They had a hydrophobic surface and were deposited as a mono sphere layer on the top of the opaline film by the Langmuir-Blodgett-Transfer method. Another problem of the fabrication of multilayer opal film by this method is that the formed crystalline film was redispersed partially in the suspension by deposition of PMMA spheres on it again even after careful annealing. As a result this film possessed several holes.

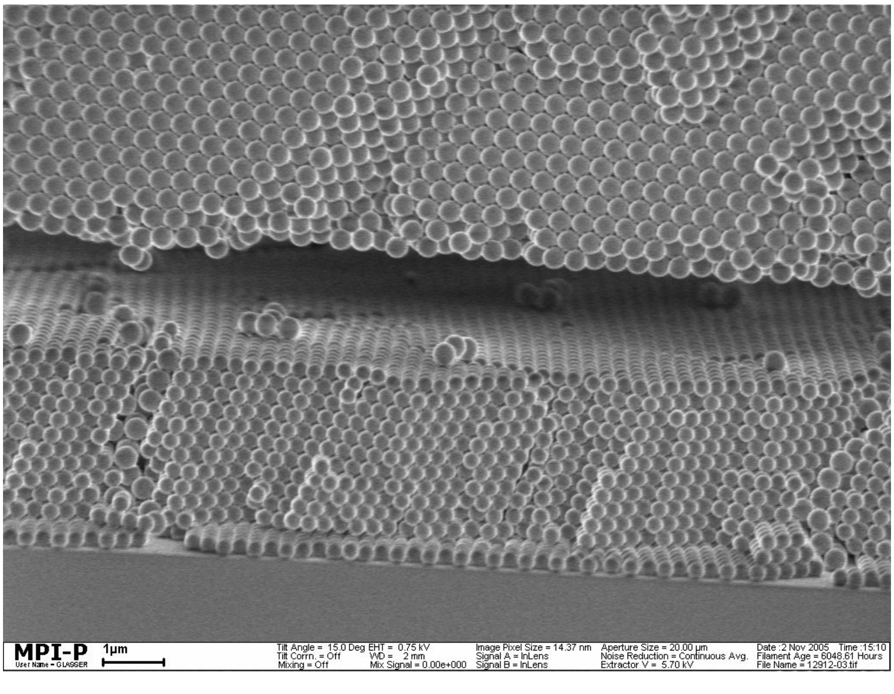

Figure 4.4. SEM image of bi-layer opal film made from PMMA spheres of the diameters of 270 nm (bottom layer) and 370 nm (top layer).

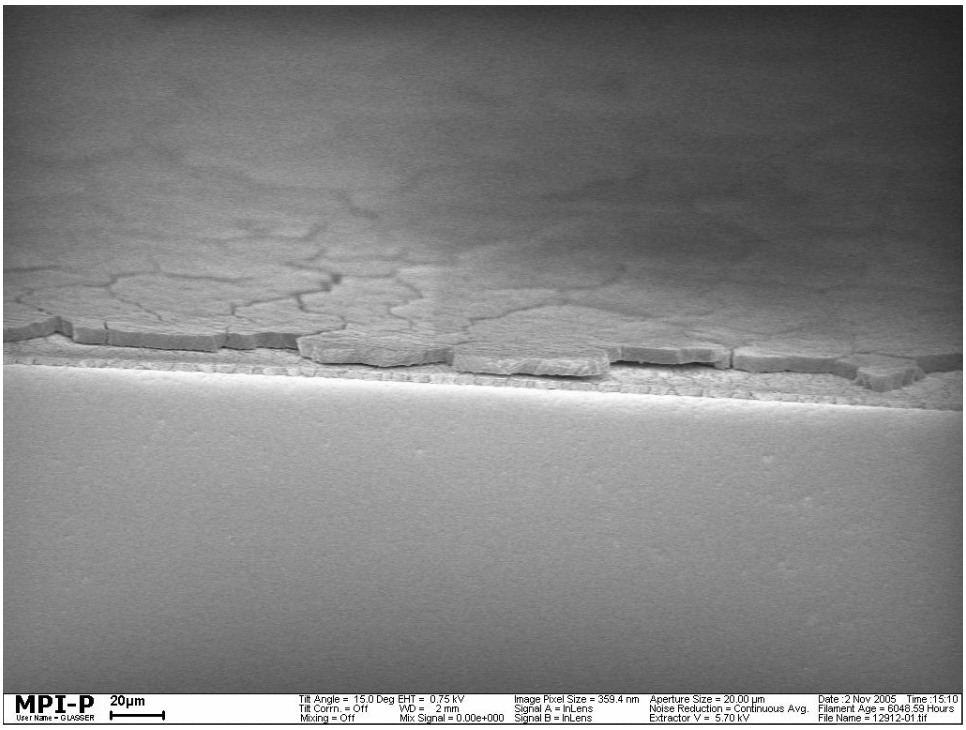

Figure 4.5. SEM image of bi-layer opal film made from PMMA spheres of diameters of 270 nm (bottom layer) and 370 nm (top layer).

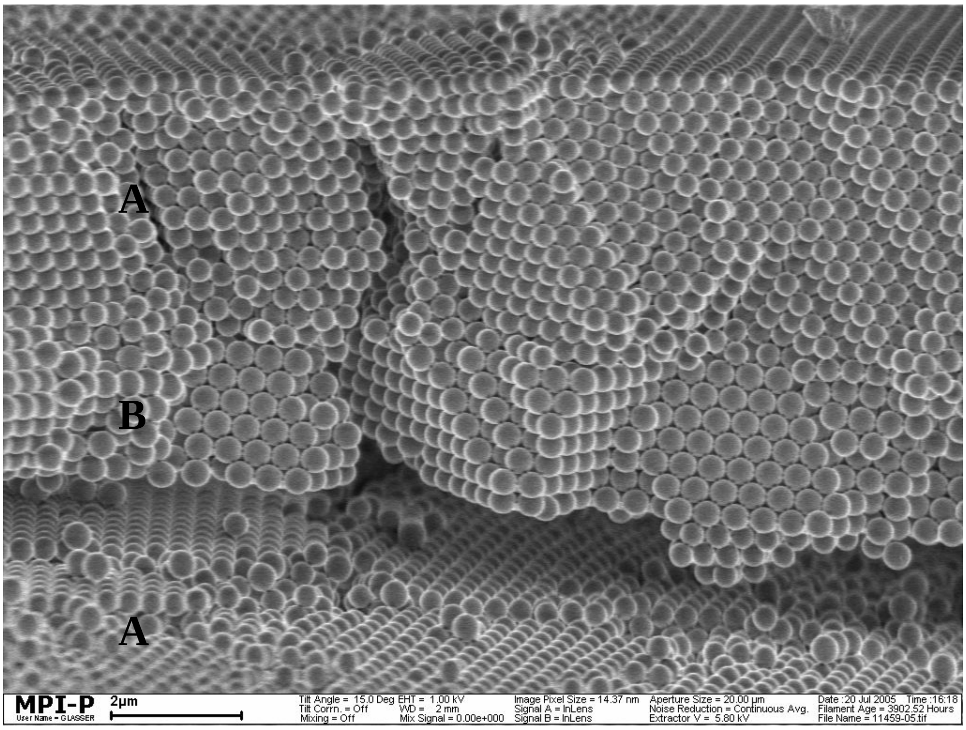

Figure 4.6. SEM image of tri-layer opal film made from PMMA spheres of diameters of 370 nm/420 nm/ 370 nm (A/B/A).

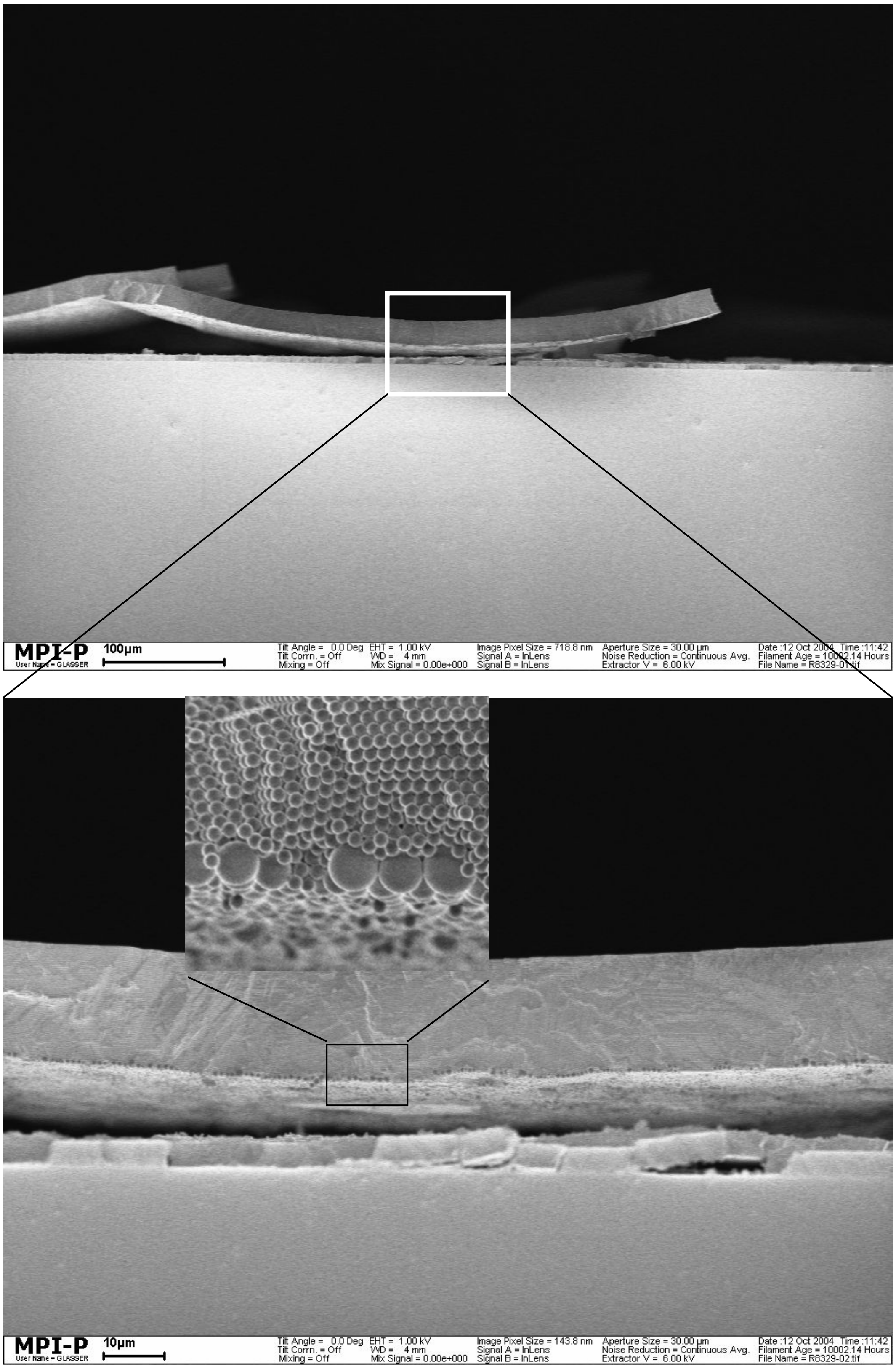

Figure 4.7. SEM images of the cross-section of the tri-layer opal film, whose middle layer was a monolayer of PS spheres of a diameter of about 1 µm (image in the inset) and top and bottom layers were PMMA opal films made of spheres with a diameter of 370 nm.

As mentioned above the sphere ordering in multilayer opals was quite good. However, it was observed that the sphere ordering got worse if the layer below was not made of monodisperse colloids. An example is given in Fig. 4.8. It can be seen that the sphere ordering in the top layer was not good because the PS spheres in the middle layer were of very different sizes. But if the top opal layer could grow further the sphere ordering would be better (Fig. 4.7).

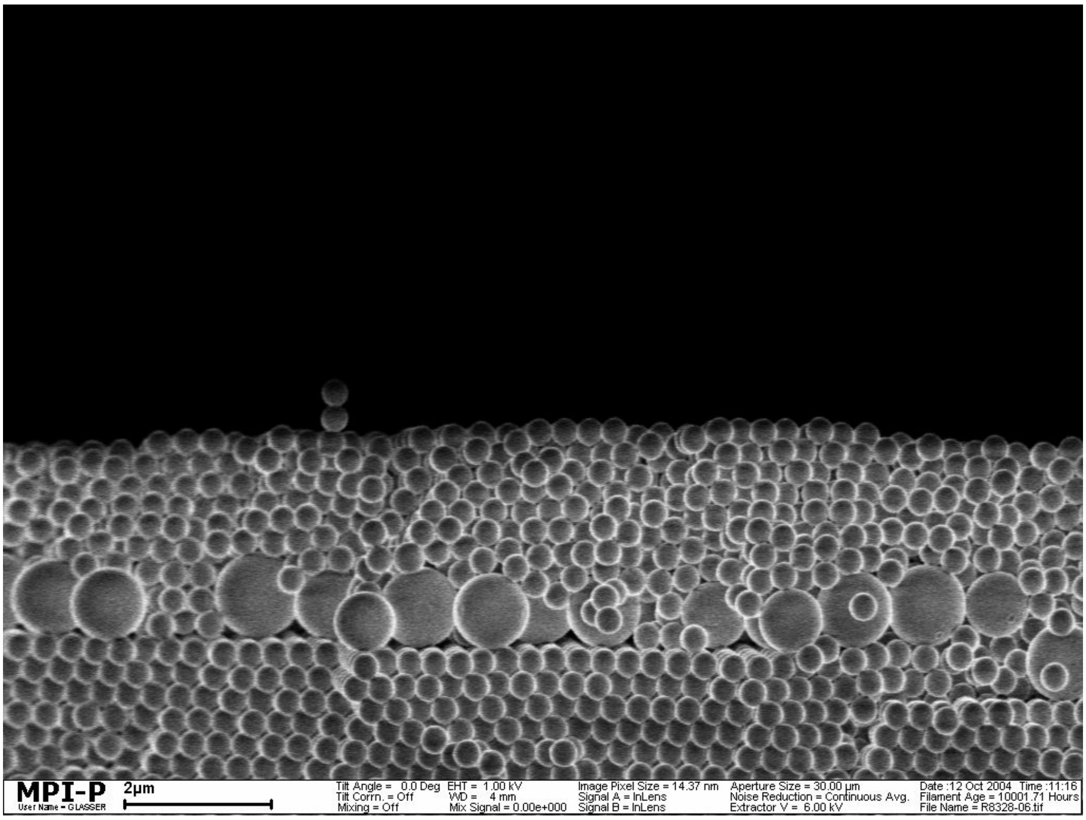

Figure 4.8. SEM image of the cross-section of the tri-layer opal film, whose middle layer was a monolayer of PS spheres of a diameter of about 1 µm and top and bottom layers were PMMA opal film made of spheres with a diameter of 370 nm.

4.2 Optical Characterization by UV-Vis Spectrometer

Optical characterization was performed by a UV-2102-PC UV-visible spectrometer from Shimadzu. Absorbance (transmission) spectra were collected using incident light beam normal to the substrate surface (perpendicular to the (111)-plane) at a range of 300 to 900 nm. It should be mentioned that within one sample the opal film thickness only changed after some millimetres because the atmospheric humidity changed during preparations. As the result the variation of the absorption intensities measured from different positions in one opal film was observed. Unfortunately it was hardly possible always to measure the monolayer opal, bi-layer opal, and three-layer opal film from the same sample in the same position owing to redispersing partially the opal film by immersing it in suspension again. This makes the comparison of the spectra after subsequent depositions complicated.

Figure 4.9 shows the transmission spectra of two bi-layer opal films composed of the same opal layers from 370 and 270 nm PMMA spheres but in reverse order. The black lines represent spectra from the monolayer opal (M), i.e. the first opal layer of the multilayer film, while the magenta lines show the double overlapped multilayer (B), and the black dash lines represent the single opal layers which were made of the same spheres and had the similar thickness as that of the second opal layer in the bi-layer film. It is evident in Fig. 4.9 that the Bragg diffraction peaks of the transmission spectra of each individual opal layers can be observed in the spectra of the bi-layer opal film again. Same observation has also been obtained from the spectra of tri-layer opal films (Fig. 4.10). The blue lines in Fig.4.10 represent the spectra of the tri-layer opal films.

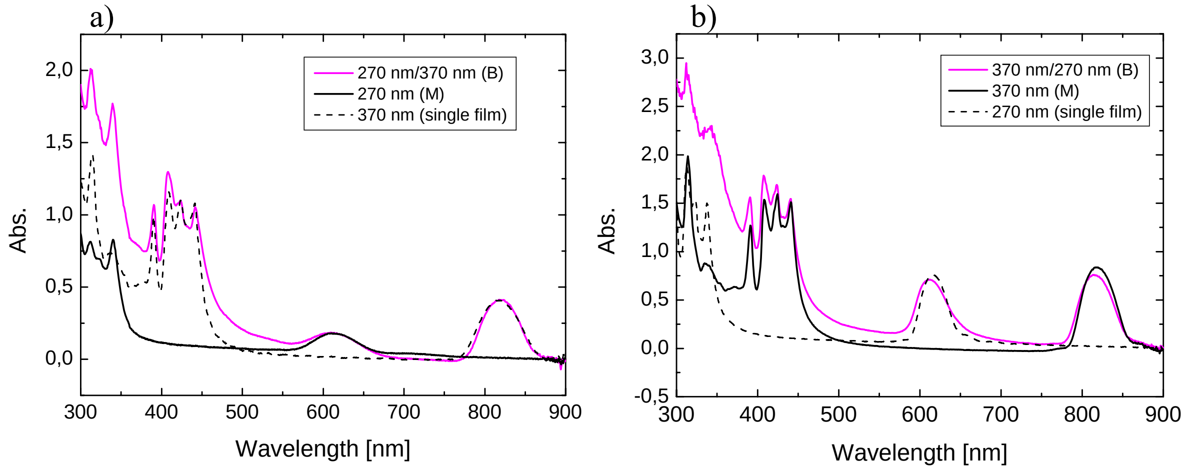

Figure 4.9. Transmission spectra of bi-layer opal film formed by 370 and 270 nm PMMA spheres in comparison with its single opal films: a) 270 nm/370 nm, b) 370 nm/270 nm.

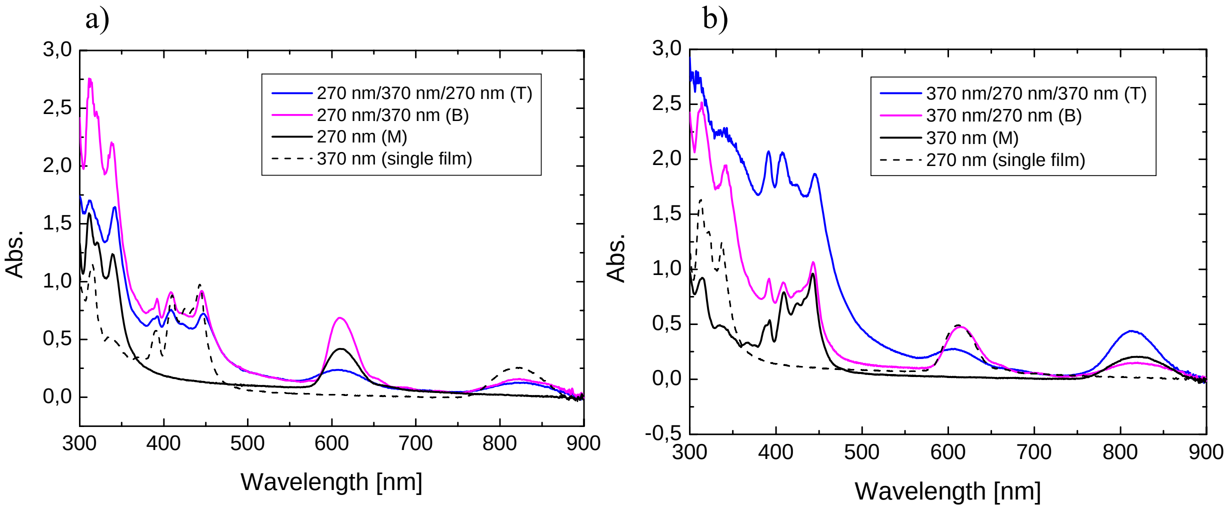

Figure 4.10. Transmission spectra of three-layer opal film ABA formed by 370 and 270 nm PMMA spheres in comparison with its bi-layer and single opal films: a) 270 nm/370 nm/270 nm, b) 370 nm/270 nm/370 nm.

In order to investigate the influence of the position ratio of the Bragg diffraction peaks from different crystalline layers on the interference of these bands in multilayer opals, multilayer opals were also prepared from other sphere size combinations. Fig. 4.11 shows the transmission spectra of two multilayer opal samples with the same ABA structure but slightly different layer thickness, their A and B layer were made of the PMMA spheres of the diameters of 420 and 370 nm, respectively. Unfortunately the stop band of the A layer exceeds the measure range of the UV-vis spectrometer in our lab and only its high order bands could be recorded. In this case the high order bands from A and B layers lie close to each other. In Fig. 4.11a the most high order bands of the spectra from each individual layer A and B can be clearly seen in the spectra of their bi-layer and three-layer opal films. But in Fig. 4.11b the high order bands from the monolayer opal disappeared in the spectrum of the bi-layer opals. It seems that the thickness of the individual layers could influence the optical property of the multilayer opals. Fig. 4.12 shows the transmission spectra of several bi-layer (Fig. 4.12a-d) and three-layer (Fig. 4.12e) opal samples with different individual layer thickness. The amplitude and shape of the high order band peaks from the multilayer film spectra are dependent on their amplitude and shape in monolayer opal and also on thickness of the second layer opal (Fig. 4.12a-d). Fig. 4.12e shows transmission spectra from three three-layer opal films (T1, T2, and T3) with different middle layer thickness. It is evident that the high order bands can be clearly seen in the spectra of the samples, whose B layer is relative thin (spectra T1 and T2).

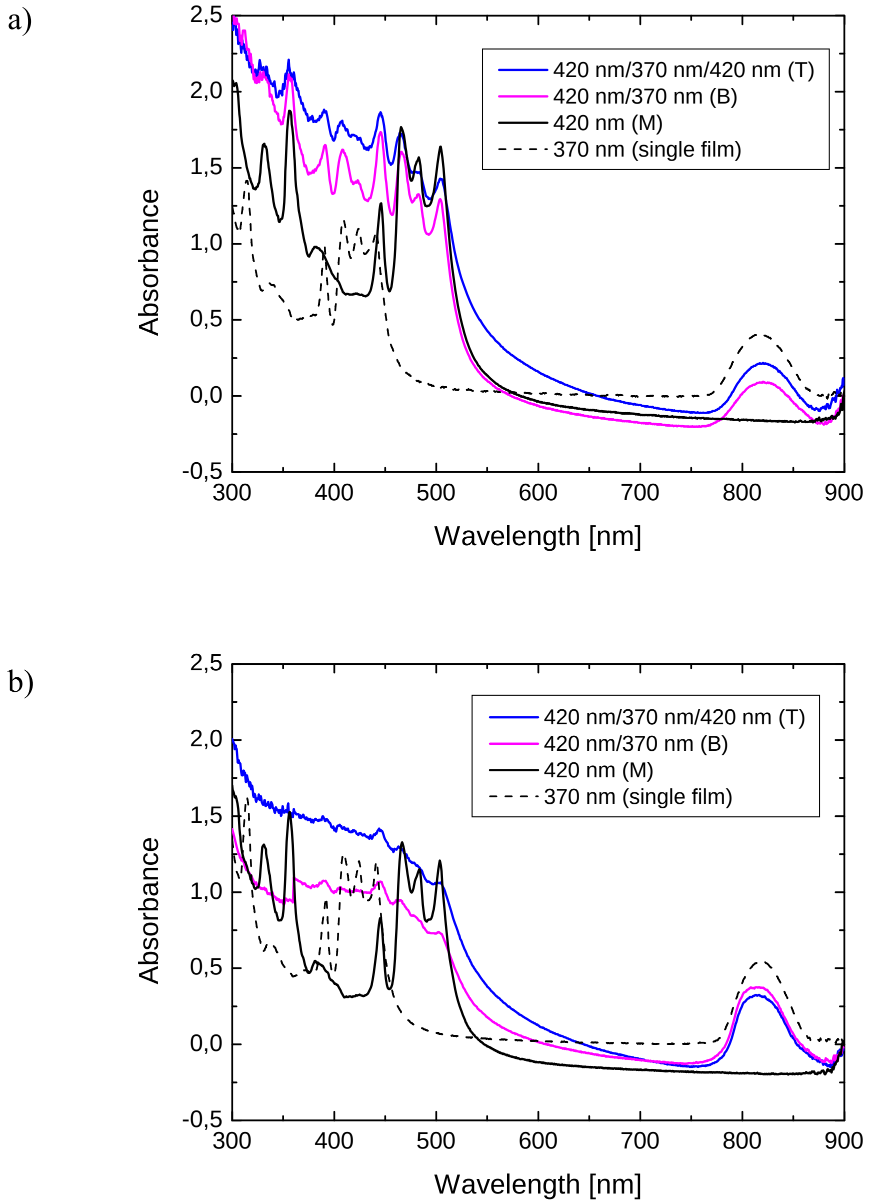

Figure 4.11. Transmission spectra of two multilayer opal samples with the same ABA structure but with slightly different layer thickness, their A and B layer were made of the PMMA spheres of diameters of 420 and 370 nm, respectively. The black lines represent spectra from the monolayer opal (M), while the magenta lines show the double overlapped multilayer (B) and the blue lines represent the triple overlapped multilayer (T). The black dash lines represent the single opal layers which were made of the same spheres and had the similar thickness as that of the second opal layer in the multilayer films.

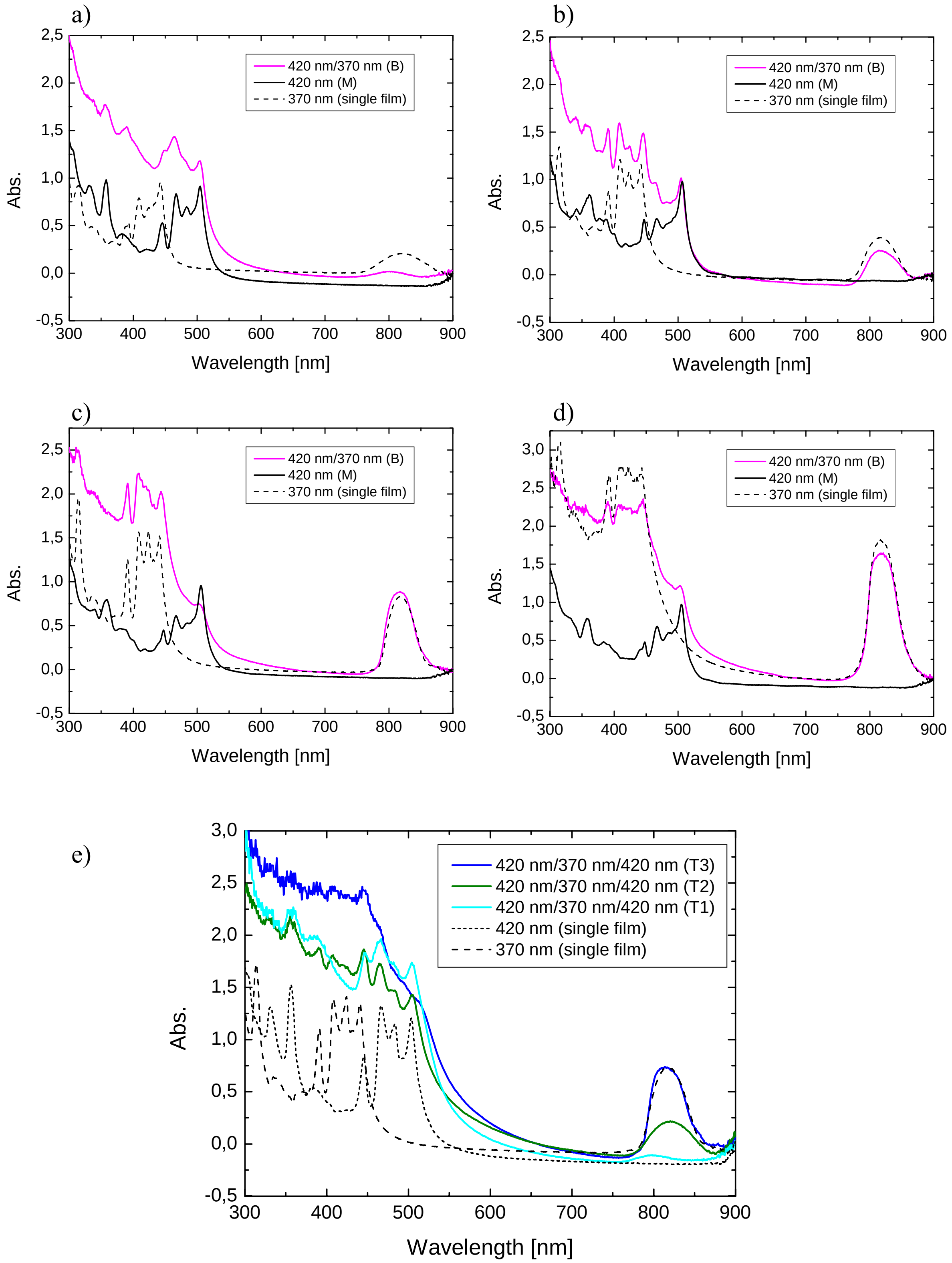

Figure 4.12. Transmission spectra of the multilayer PMMA opal films. The solid lines represent spectra from multilayer films, while the black dash and dot lines show the single opal films: a)-d) Spectra from bi-layer (420 nm/370 nm) films, e) spectra from three-layer (420 nm/370 nm/420 nm) films.

Fig. 4.13 shows transmission spectra of a tri-layer opal film composed of the same A and B layer as described above (Fig. 4.11 and 4.12) but in reverse order, namely BAB instead of ABA. The magenta and blue line represent spectra from bi-layer and tri-layer opaline film respectively, while the black dash and dot line show the single opaline films. However in this case because the stop band of middle layer exceeds the measure range it was not possible to estimate the layer thickness. As shown in Fig. 4.13 it is remarkable that the bandwidth of the Bragg diffraction in the spectrum of the multilayer opals is comparable with that of the single opal film. This observation has been also obtained from other multilayer opal samples (Figs. shown above). This means that the narrow spectral feature was in fact formed from multilayer opals as a result of interface effect if we consider that the opal quality of multilayer opals was not as good as that of single opal film, because of their smaller crystallites and more cracks.

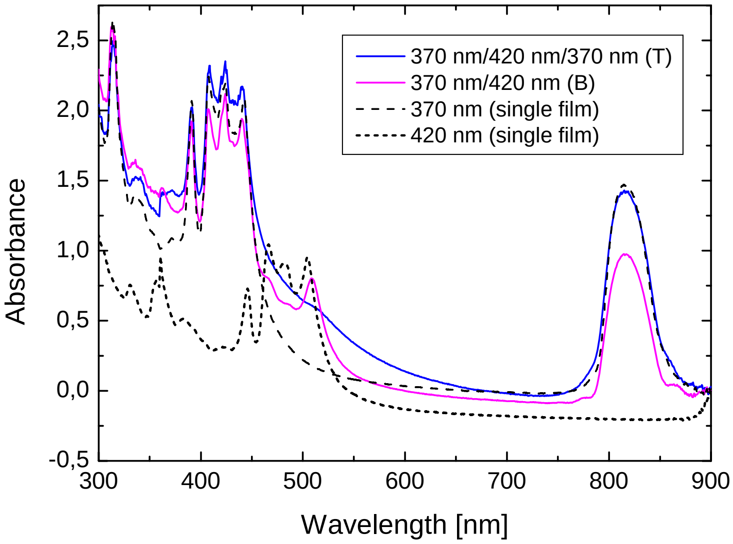

Figure 4.13. Transmission spectra of a three-layer (370 nm/420 nm/370 nm) opal sample. The magenta and blue line represent spectra from bi-layer and three-layer opal film respectively, while the black dash and dot line show the single opal films.

Transmission and reflectance spectra of another tri-layer (370 nm/420 nm/370 nm) opal sample measured by the Fraunhofer Institute in Golm are shown in Fig. 4.14a. The Bragg diffraction peak (930 nm) of the middle layer made of 420 nm spheres was very weak as shown in the spectra but no deep diffraction minima as a result of a plane-defect transmission were observed in this frequency range; presumably this layer was too thin to be able to be defined properly. It is remarkable, however, that strong enhancement of the Fabry-Pérot oscillations was observed from the spectra of triple-film opals in comparison with that of single film opals (Fig. 4.14b and c). The same observation has been also obtained from other multilayer opal samples.

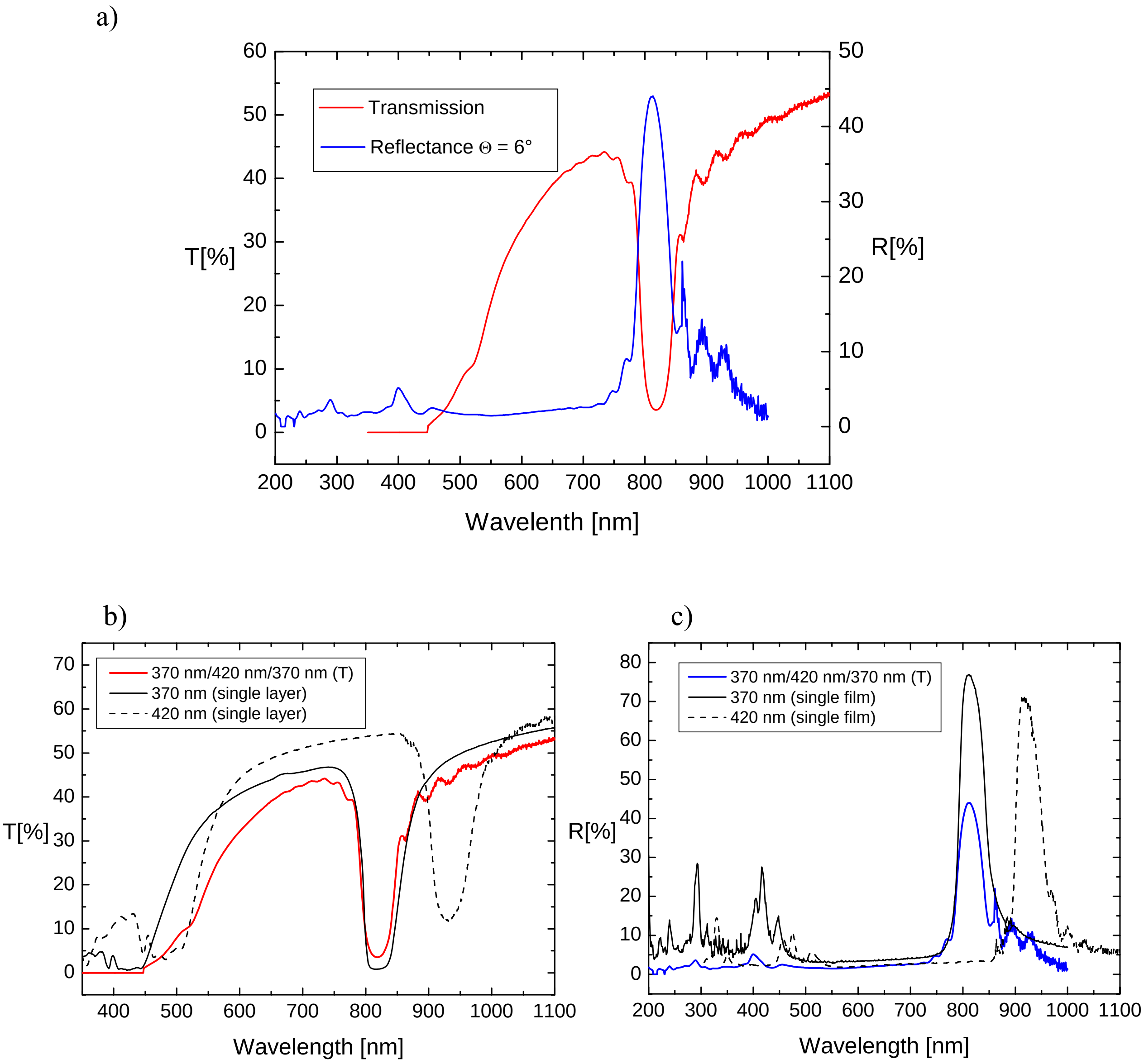

Figure 4.14. a) Transmission and reflectance spectra of a tri-layer (370 nm/420 nm/370 nm) opal sample. b) Comparison of the transmission spectrum of tri-layer opals with that of the single film opals. c) Comparison of the reflectance spectrum of tri-layer opals with that of the single film opals.

The angular resolved transmission measurements for the multilayer opals were performed in the Light Technical Institute of the University of Karlsruhe. The angular dispersion of the stop band was studied by changing the angle of incidence Θ between the beam and the (111) axis of the fcc crystal from 0° to 60°. Fig. 4.15 shows the angular resolved transmission spectra of a tri-layer (420 nm/370 nm/420 nm) opal film. The comparison of the spectra between multilayer and single layer opals for the angle Θ = 10°, 20°, 30°, 40°, 50°, and 60° is shown in Fig. 4.16. It is remarkable that the Bragg diffraction peaks shifted at the high angle to blue (Fig. 4.16e and f).

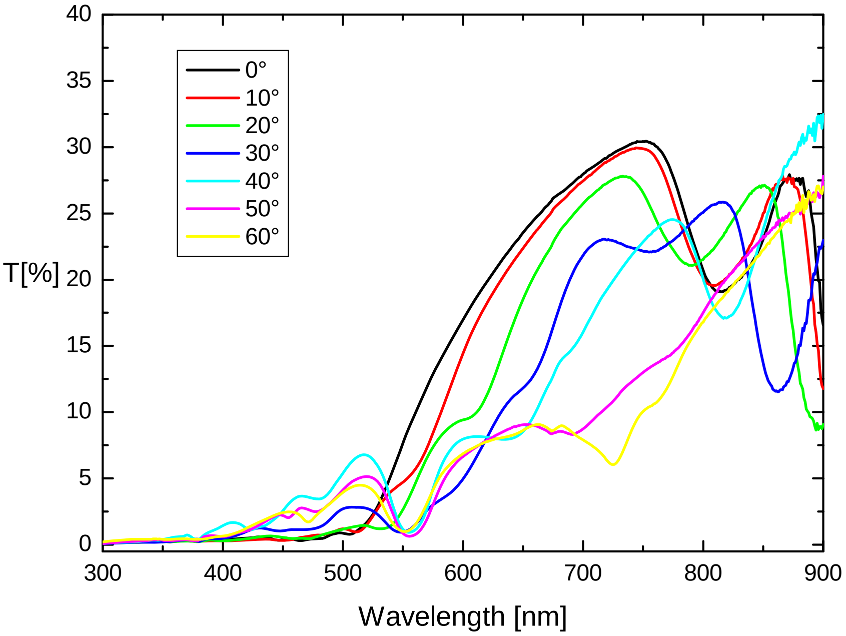

Figure 4.15. Angular resolved transmission spectra of a tri-layer (420 nm/370 nm/420 nm) opal film from angle Θ = 0° to 60° with a 10° step.

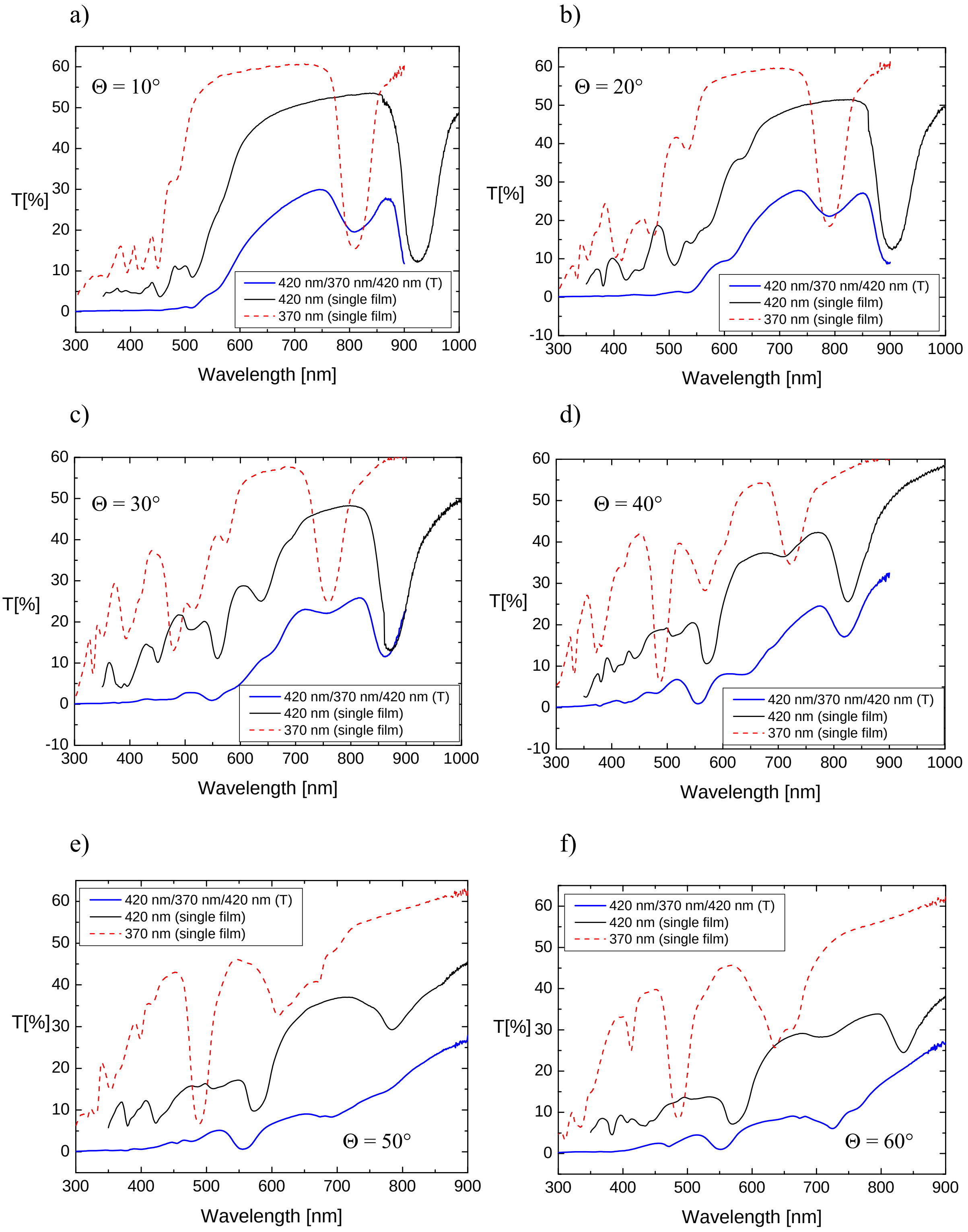

Figure 4.16. Comparison of the angular resolved transmission spectra between tri-layer opal film and single opal layer film: a) Θ = 10°, b) Θ = 20°, c) Θ = 30°, d) Θ = 40°, e) Θ = 50°, f) Θ = 60°.

4.3 TiO_2 Sandwich Opals

The optical effect of the strong anisotropy of reflectance and emission with respect to the interface plane is also expected from the hetero-opals made from materials of different dielectric constants that combine band gaps of different width and dispersion. In order to get such hetero-opals TiO_2 nanoparticles with a diameter of about 5 nm were used. These TiO_2 particles were prepared by M. Nawaz Tahir from the Inorganic Chemical Institute of the University of Mainz. The surface of these TiO_2 particles was modified and they were stable in water. Fig. 4.17a shows a picture of a thin TiO_2 film made from the TiO_2 particle suspension on a glass substrate by the vertical deposition method using a lifting machine as described above. Similarly the TiO_2 film was also formed on the top of opal film made of the PMMA spheres of 370 nm diameter (Fig. 4.17b). Fig. 4.18 shows SEM images of cross-section of a bi-layer film. A well defined TiO_2 film about 160 nm thick can be clearly seen in Fig. 4.18. However, in this case the interstitial of the PMMA opal film on the bottom were also infiltrated from the TiO_2 particles (Fig. 4.18) as a side product from preparing the middle layer. A tri-layer film was formed by depositing PMMA spheres on the top of the bi-layer film. Fig. 4.19 shows SEM images of a cross-section of this tri-layer film, in which the top layer was a PMMA opal film made of spheres of 370 nm diameter, the middle layer was made of TiO_2 particles with a diameter of about 5 nm, and the bottom layer was composed of the same PMMA opals as that of the top layer but infiltrated with TiO_2 particles.

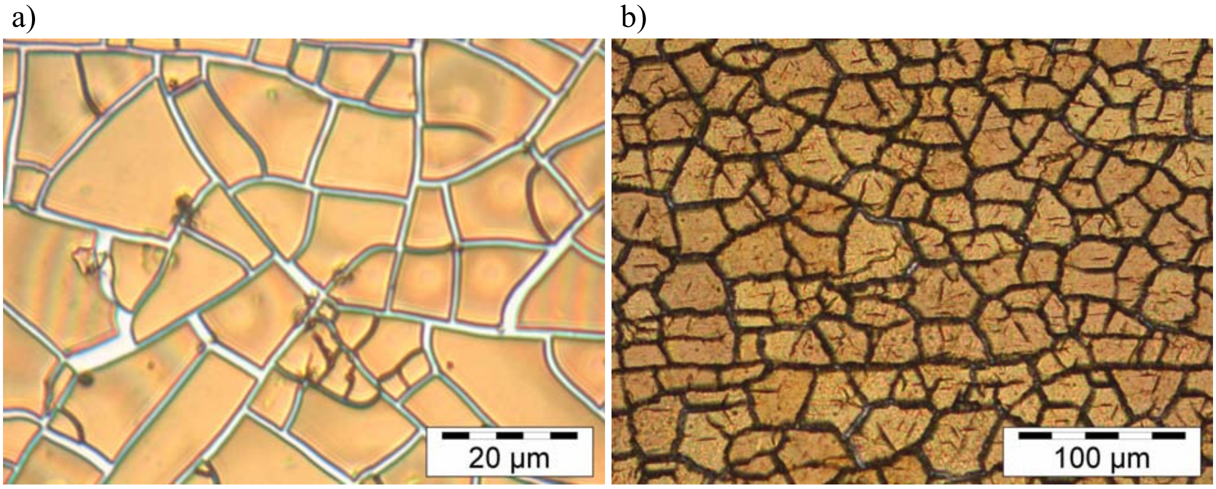

Figure 4.17. Optical microscopy of a thin TiO_2 film made of the TiO_2 particles of a diameter of about 5 nm: a) TiO_2 film on a glass substrate. b) TiO_2 film on the top of an opal film composed of the PMMA spheres with a diameter of 370 nm.

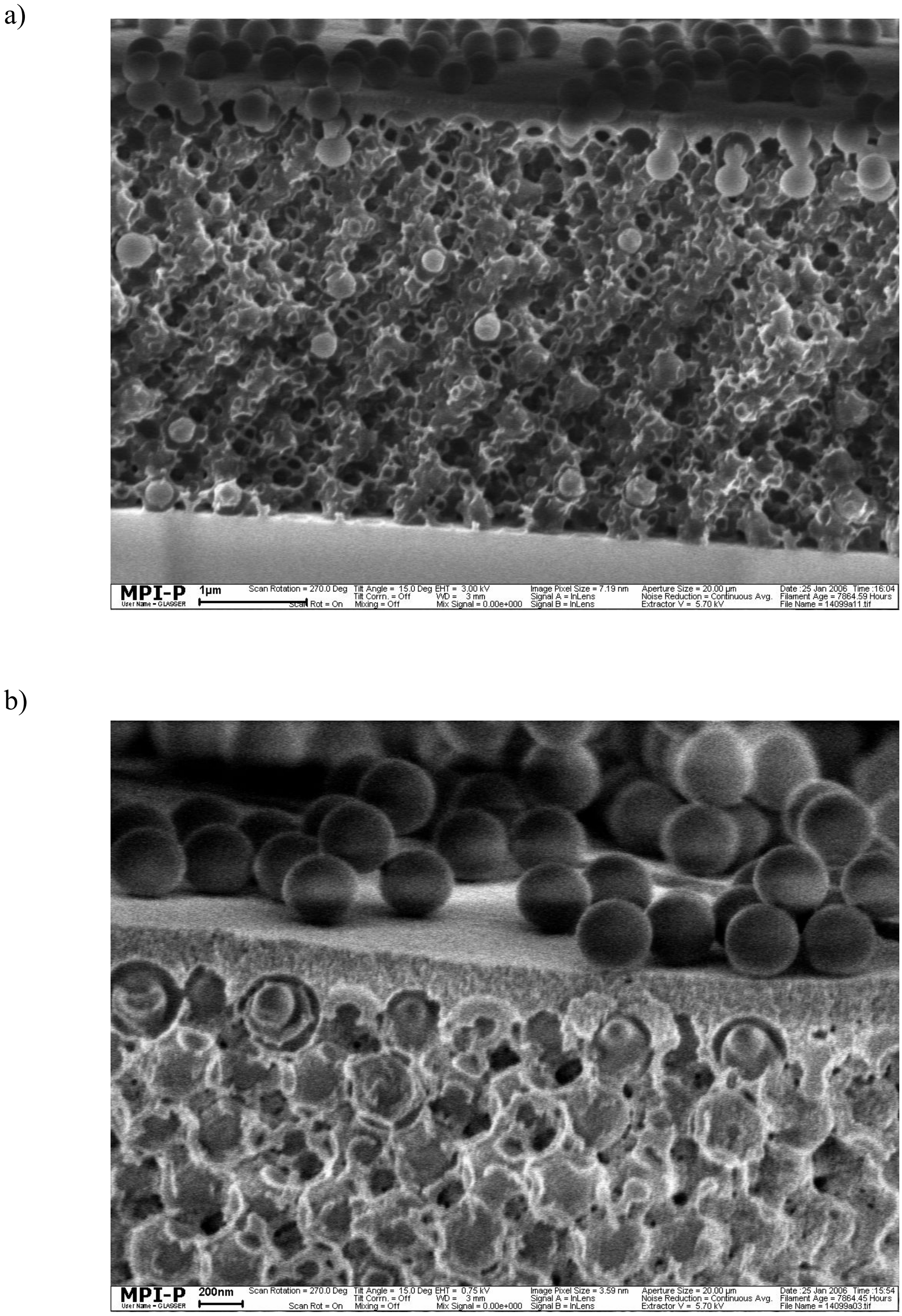

Figure 4.18. SEM images of a cross-section of the bi-layer film, whose top layer was made of TiO_2 particles with a diameter of about 5 nm and bottom layer was PMMA opals (sphere diameter 370 nm) that were infiltrated with the TiO_2 particles (same TiO_2 particles as the top layer): a) Low magnification, b) high magnification.

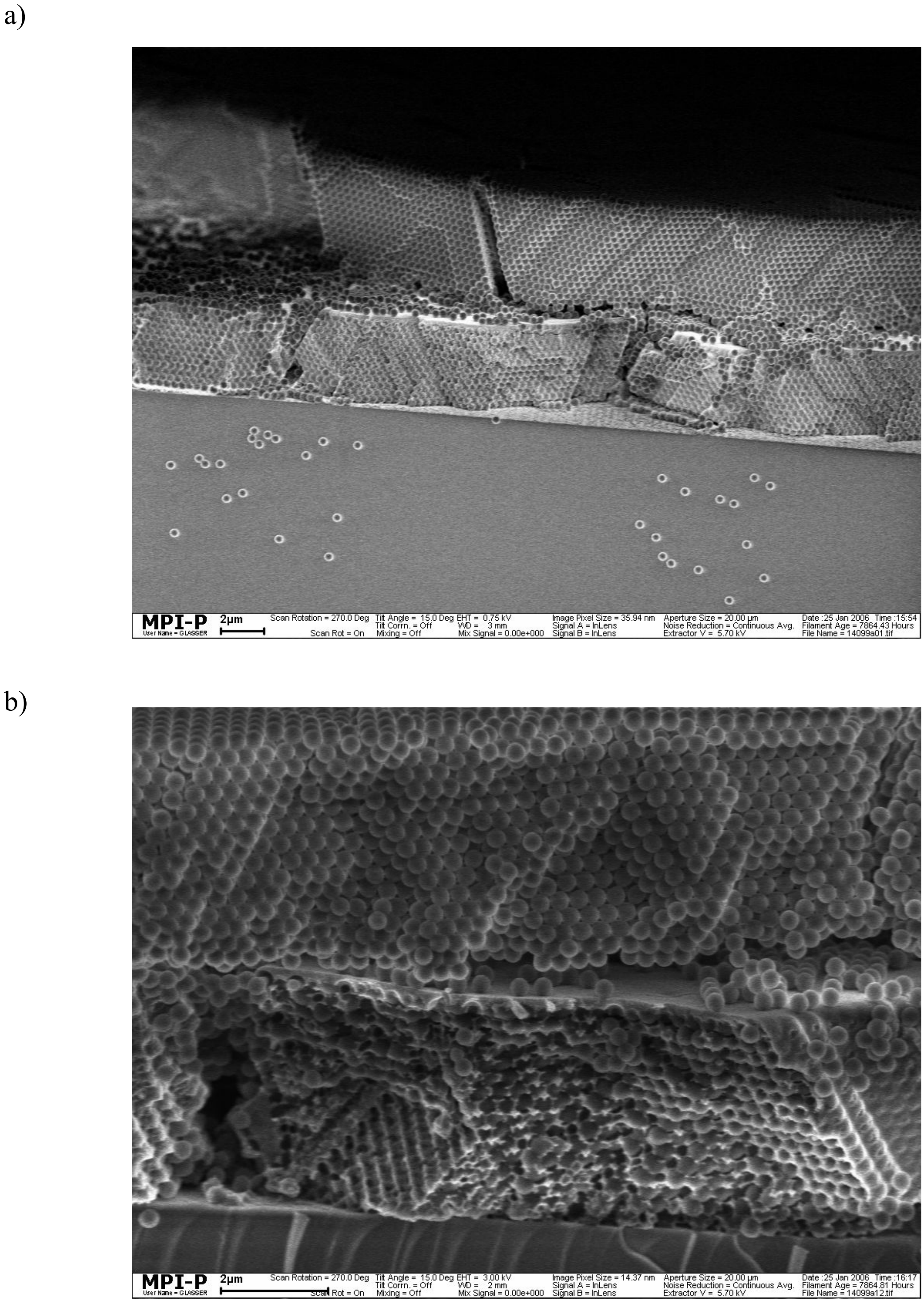

Figure 4.19. SEM images of cross-section of the tri-layer film, in which the top layer was the PMMA opal film made of spheres of 370 nm diameter, the middle layer was made of TiO_2 particles with a diameter of about 5 nm, and the bottom layer was composed of same PMMA opals as the top layer but infiltrated with TiO_2 particles: a) Low magnification, b) high magnification.

For the optical characterization of the TiO_2 hetero-opal transmission measurements were performed by the UV-vis spectrometer using incident light beam normal to the substrate surface (in the (111) direction) at a range of 300 to 900 nm. In this wave range a weak maximum (362 nm) of the transmission spectrum of single TiO_2 film has been observed (Fig. 4.20). Fig. 4.21 shows the transmission spectrum of a bi-layer film, whose bottom layer was a TiO_2 particle infiltrated PMMA opal with a sphere diameter of 370 nm (TiO_2-opal) film and whose top layer was a thin TiO_2 film in comparison with the spectrum of its original monolayer PMMA opals (air-opal) and the single TiO_2 film. In Fig. 4.21a it can be seen that the stop band peak (846 nm) from TiO_2-opal shifts to red towards the one (813 nm) from air-opal because of the increase of effective refractive index by loading the TiO_2 particles in the opal voids. The Bragg condition $\lambda_{Bragg} = 2n_{eff}d$, where $d = 0{,}816D$ is the interplane distance in the (111) direction, allows extraction of the effective refractive index value of $n_{eff} = 1.40$ for the TiO_2-opal. The refractive index of the composite can be estimated using simplified effective medium approach as $n_{eff} = \sum_i n_i f_i$, where i is the index of a component and f_i the volume fraction of this component. Correspondingly, the volume fraction of the deposited TiO_2 particles can be estimated as $f_{TiO_2} \approx 4\%$ for $n_{TiO_2} = 2$ (anatase titania). However, other observations of the spectra from such TiO_2-opal samples have been also obtained, for example, Fig. 4.21b represents a spectrum that no shift was observed, presumably the TiO_2 particle content was too low or they were not distributed homogenously in the opals. Fig. 4.21c shows the spectrum where the stop band shifts to blue which indicated a TiO_2 replica character.

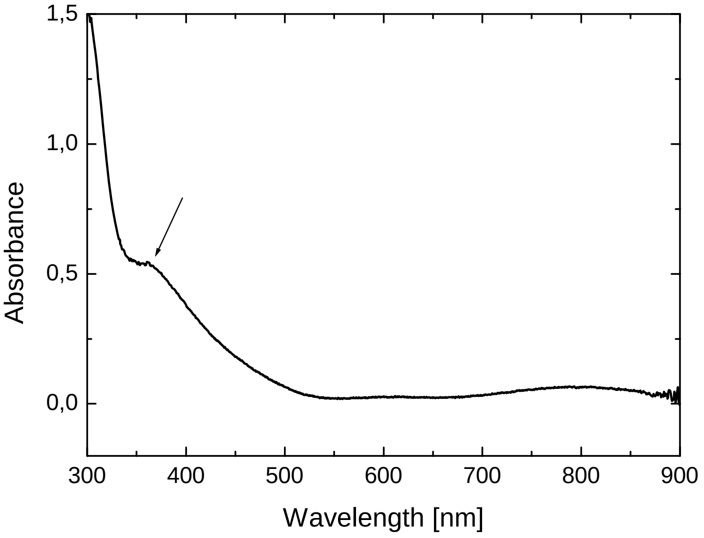

Figure 4.20. Transmission spectrum of single TiO_2 film made of TiO_2 particles with a diameter of about 5 nm.

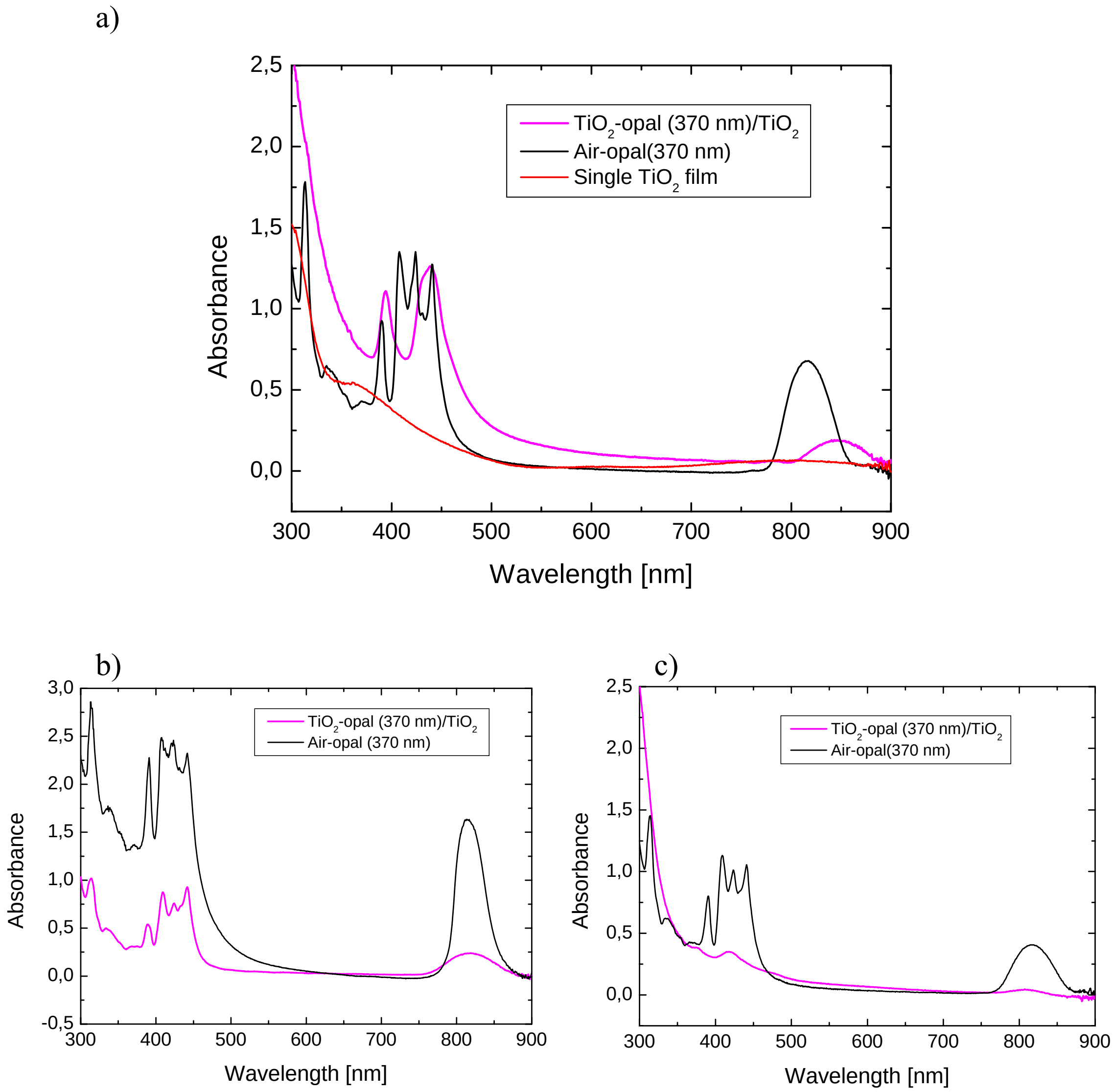

Figure 4.21. Transmission spectra of three bi-layer film samples, whose bottom layer was a TiO_2 particle infiltrated PMMA opal with a sphere diameter of 370 nm (TiO_2-opal) film and whose top layer was a thin TiO_2 film, in comparison with the spectra of the single films (air-opal and TiO_2 film): a) Red shift of the TiO_2-opal stop band, b) no shift, c) blue shift.

It is remarkable that the amplitude of the stop band of opals reduced dramatically after infilling TiO_2 particle (Fig. 4.21). This is a result of decreasing the refractive index contrast ratio and eventually also inhomogeneous TiO_2 particle distribution. Fig. 4.22 shows transmission spectra of three tri-layer (TiO_2-opal/TiO_2/air-opal) hetero-opal samples in comparison with the single opal films. These hetero-opals possessed a wider and asymmetric stop band as shown in Fig. 4.22. No sharp deep diffraction minima as a result of a plane-defect transmission were observed in the stop band. However, at the wave range of 300 to 350 nm very strong resonances were recorded (Fig. 4.22). This anomalous phenomenon has only been observed from the tri-layer (TiO_2-opal/TiO_2/air-opal) hetero-opals and presumably is the specific of hetero-opal effects as a consequence of the coherent interference between the high order bands of PMMA opal with the band edge of the TiO_2 film. The transmission spectra of the tri-layer (TiO_2-opal/TiO_2/air-opal) hetero-opals at different angles Θ between the incident beam and the normal to the (111) plane are given in Fig. 4.23 (these measurements were done in our lab and the Θ values were not exact). It is evident that the anomalous strong absorption can be also observed in the angular resolved spectra. This is only a primary study of the optical behaviour of these hetero-opals and further investigation is in progress.

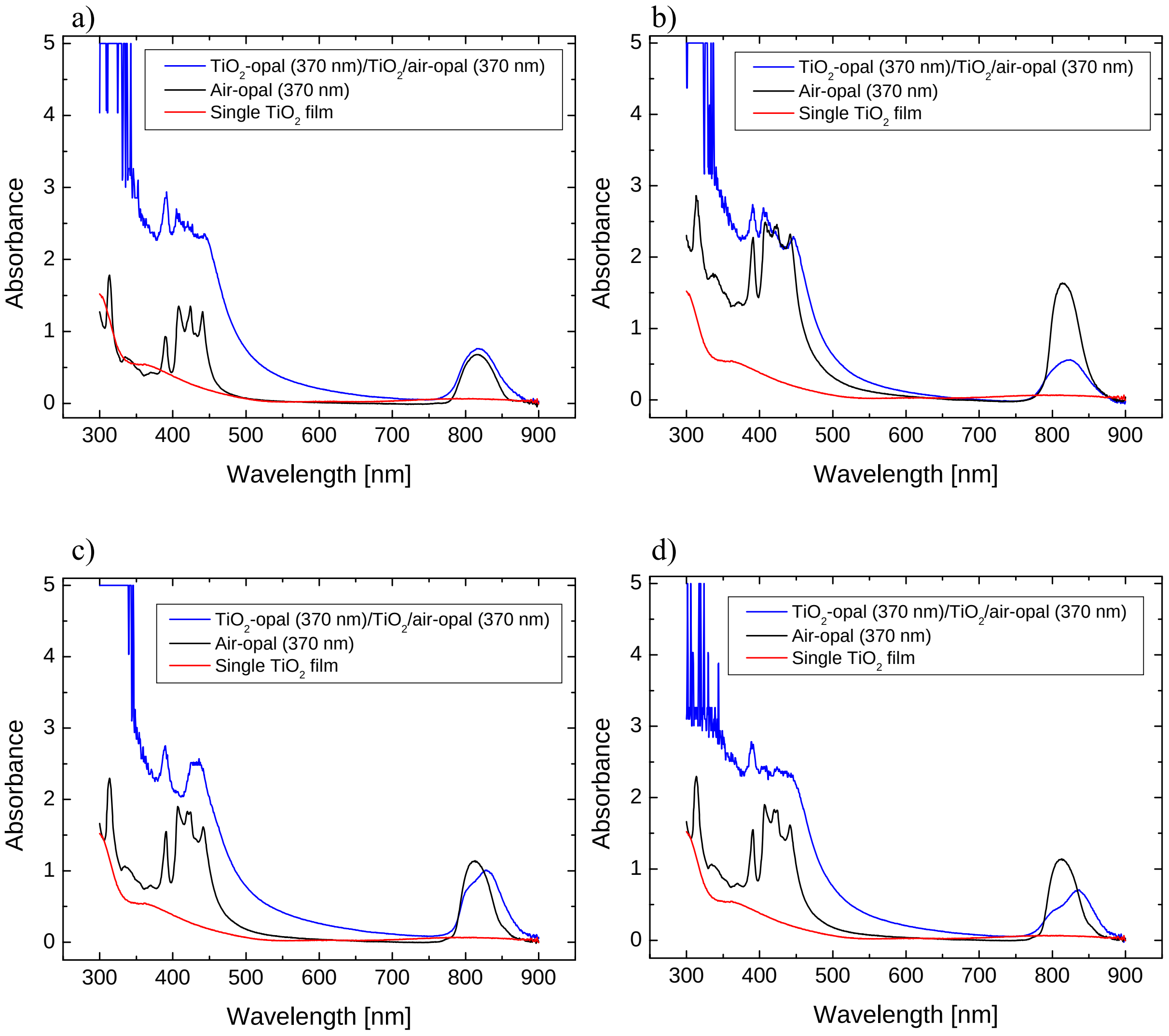

Figure 4.22. Transmission spectra of tri-layer (TiO_2-opal/TiO_2/air-opal) hetero-opal samples in comparison with the single layer type films: a) and b) Spectra from two individual samples, c) and d) spectra from the same sample but in different positions.

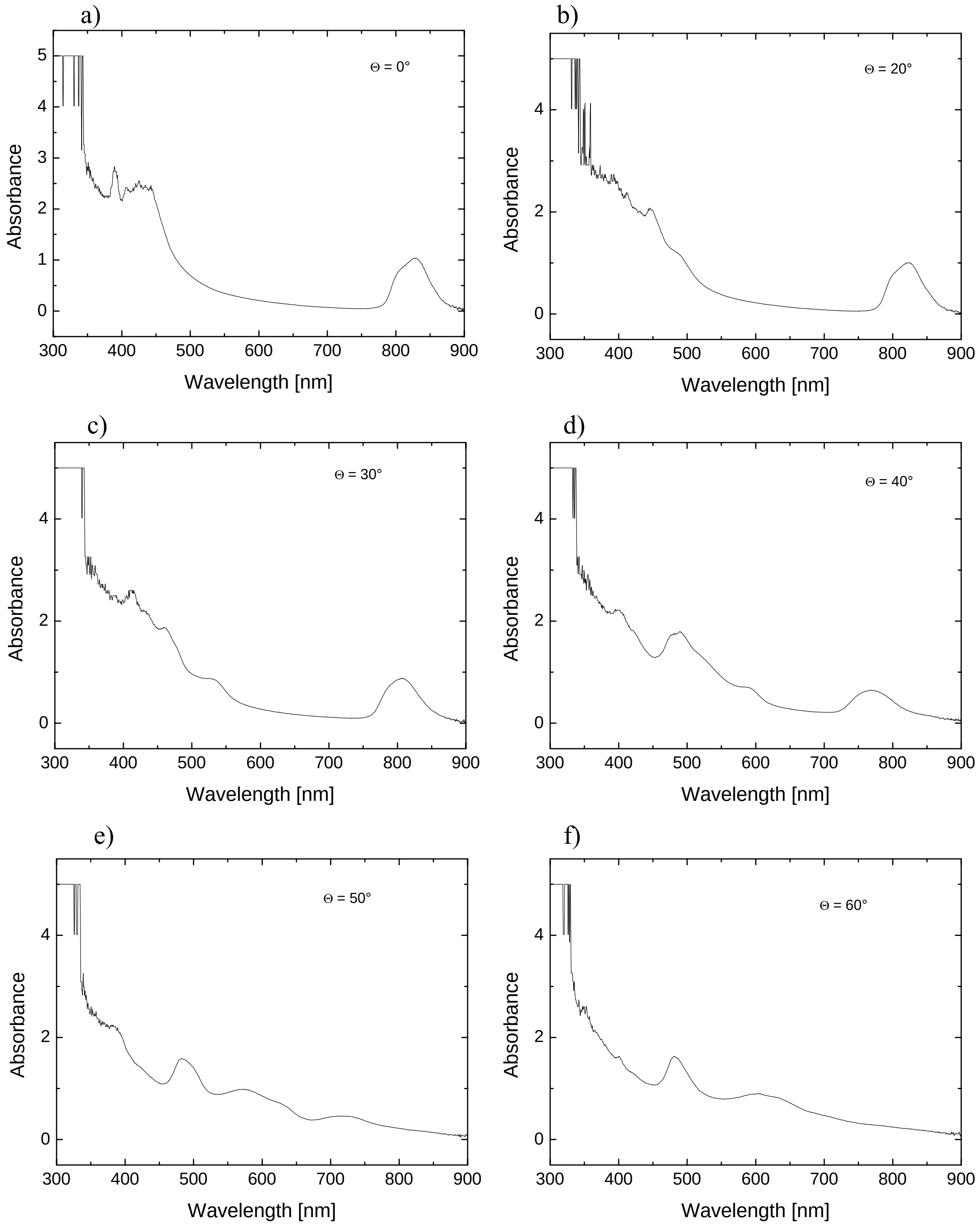

Figure 4.23. Transmission spectra of the tri-layer (TiO_2-opal/TiO_2/air-opal) hetero-opals at different angles Θ between the incident beam and the normal to the (111) plane.

In addition, Fig. 4.24a shows the transmission spectrum of a bi-layer film, whose bottom layer was TiO_2 film and top layer was PMMA opals, in comparison with that of single type films. The stop band of this bi-layer film shifts to red as shown in Fig. 4.24a but the reason for this is not clear. It is interesting that similar spectrum has been found from a tri-layer (TiO_2-opal/TiO_2/air-opal) film (Fig. 4.24b), probably the TiO_2 particles faction of the TiO_2-opal layer was relatively high and the refractive index contrast between opal and medium was too low to result in a Bragg diffraction.

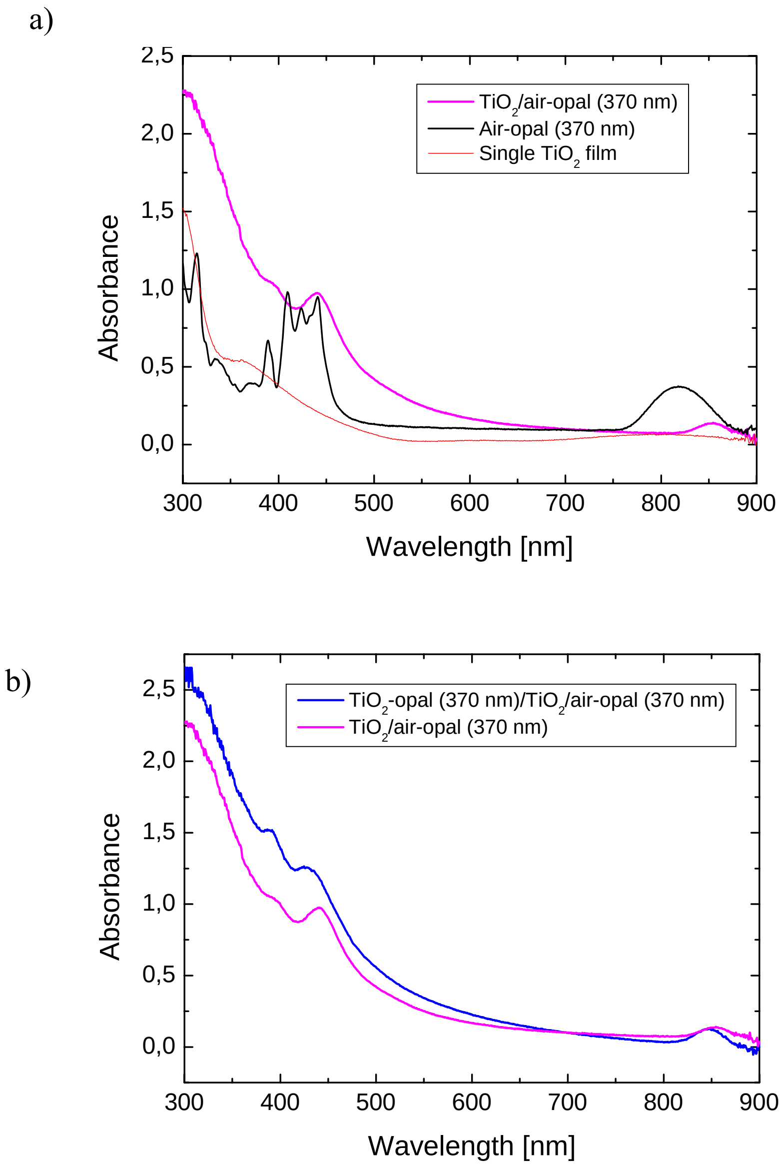

Figure 4.24. Transmission spectrum of a bi-layer film, whose bottom layer was TiO_2 film and top layer was PMMA opals, in comparison with: a) single type films, b) a tri-layer (TiO_2-opal/TiO_2/air-opal) film.

5. Fabrications of Inverse Opals

Self-assembly of monodisperse microspheres into opal structures offers an attractive possibility to be used as templates for the fabrication of photonic materials, owing to its simplicity, flexibility, and low cost. These colloidal crystal templates can be infiltrated with the high refractive index materials for fabrication of full bandgap materials, much more, however, with a variety of ferroelectric, nonlinear, and photorefractive materials, thus permitting the creation of composites for optoelectronic applications. Recently opals were infiltrated with semiconductors,[42,43,136,137,138,139,140] titanium dioxide,[141,142,143] SnS_2,[144] liquid crystal[55,145] or conjugated polymer.[146,147] Therefore, template-directed synthesis is a convenient and versatile method for generating porous materials. Fabrication based on this approach is remarkable not only for its simplicity but also for its fidelity in transferring the structure from the template to the replica. The size of the pores and the periodicity of the porous structures can be controlled precisely and readily tuned by changing the size of the colloidal spheres.

It is well known that the photonic crystal properties of the final structures are strongly dependent on both the quality and uniformity of the initial opal template and the filling process. Zakhidov et. al. has reported[148] that the infiltration step either completely fills the void volume of the opal spheres or coats the surfaces of the void space depending on the interface energies between the different materials involved and on the mechanical properties of the transition states of the formed materials, thereby resulting (after latex spheres extraction) in either a volume-templated inverse opal or a surface-templated inverse opal. Most replicas from colloidal crystal templates were prepared by the sol-gel process. A large disadvantage of this process consists in the high percentage of volume shrinkage during the solidification of the gel as a result of solvent evaporation. Even by multiple filling it was not possible so far to obtain 100 % infiltration of the interstitial spaces of the opal templates. Thus, replica which were obtained by a sol-gel based process are usually brittle and inhomogeneous and do not fulfill the demands with respect to optical, mechanical, and sometimes thermal stability. Therefore, the preparation of high quality and robust photonic opal replica still remains a challenge.

In this chapter it is shown how a large-area, high quality and robust photonic opal replica from an inorganic-organic hybrid material (ORMOCER®) was prepared by using the template-directed method, in which a high quality polymer opal template was fabricated and infiltrated with a neat inorganic-organic ORMOCER® oligomer, which can be photopolymerized within the opaline voids leading to a fully-developed replica structure with a filling factor of nearly 100%. This opal replica is structurally homogeneous and thermally and mechanically stable. The high quality of the 3D structure is confirmed by optical studies and SEM microscopy. Fabrication of silicon replica from silica opals on patterned substrate and inverse opals of other different materials are also introduced in the following chapter.

5.1 Inverse Opals from Inorganic-Organic Hybrid Polymer (ORMOCER®)

Silicate-based inorganic-organic hybrid polymers (ORMOCER® s)[**] are very promising materials for photonic applications such as waveguides due to their outstanding properties resulting from their inorganic and organic units and their widely tunable material properties.[149] This allows one either to apply them, for example, in optical interconnects or waveguides, in microoptics, or in electro-optical applications.[150] For this study a hybrid polymer – henceforth referred to as OC-I – with a resin's refractive index of 1.5355 (@ 587 nm), acquired from the Fraunhofer Institute in Würzburg was used. Originally, this material is used as core for waveguide applications, where another hybrid polymer with a lower refractive index acts as cladding material.[151] The material has negative resist behavior which allows one to pattern it by UV irradiation and by two-photon polymerization using femtosecond lasers, where the latter method was applied to generate 3D microstructures including 3D photonic crystals.[152] The thermal stability of these inorganic-organic hybrid polymers can be as high as 415 °C,[153] and they are chemically and mechanically highly stable.

5.1.1 Fabrication of ORMOCER® Replica

As the colloidal crystal template PMMA opaline films on a glass substrate were used, which were prepared by the vertical self-assembly method using a drawing machine as described in Chapter 2.3.2. The superior quality of PMMA opaline films is one of the most important prerequisites to obtain high quality replica. In the next step, the interstitial spaces of opal templates were infiltrated drop by drop with the solvent-free, initiator-containing OC-Ioligomers at 80°C. The viscose oligomer liquid penetrated the voids of the colloidal crystal by capillary forces. After infiltrating the opal template, the samples were degassed for about

---

[**] registered by the Fraunhofer-Gesellschaft für Angewandte Forschung e.V., Germany.

10 min in a vacuum oven. Before UV exposure, the samples were heated again for 2 min at 80°C on a flat metal plate, cooled down and subsequently exposed for 30s to initiate the organic photopolymerization. Finally, a thermal curing step was carried out in an oven at 150°C for 3 hours. Afterwards, the very hot samples were cooled down slowly to room temperature in the air. The final step in the fabrication of hybrid polymer opal replicas was the removal of the template with an organic solvent, e.g. tetrahydrofuran. The sample was immersed in the organic solvent for several hours. During this step the PMMA spheres were dissolved and the resulting OC-I replica showed strongly iridescent colors. Fig. 5.1 shows the photographs of OC-I replica made of PMMA opal template with a sphere diameter of 370 nm (Sample No. 5). It is remarkable that the obtained large scale (cm^2 size) replica films can easily be handled as free films with a pair of tweezers.

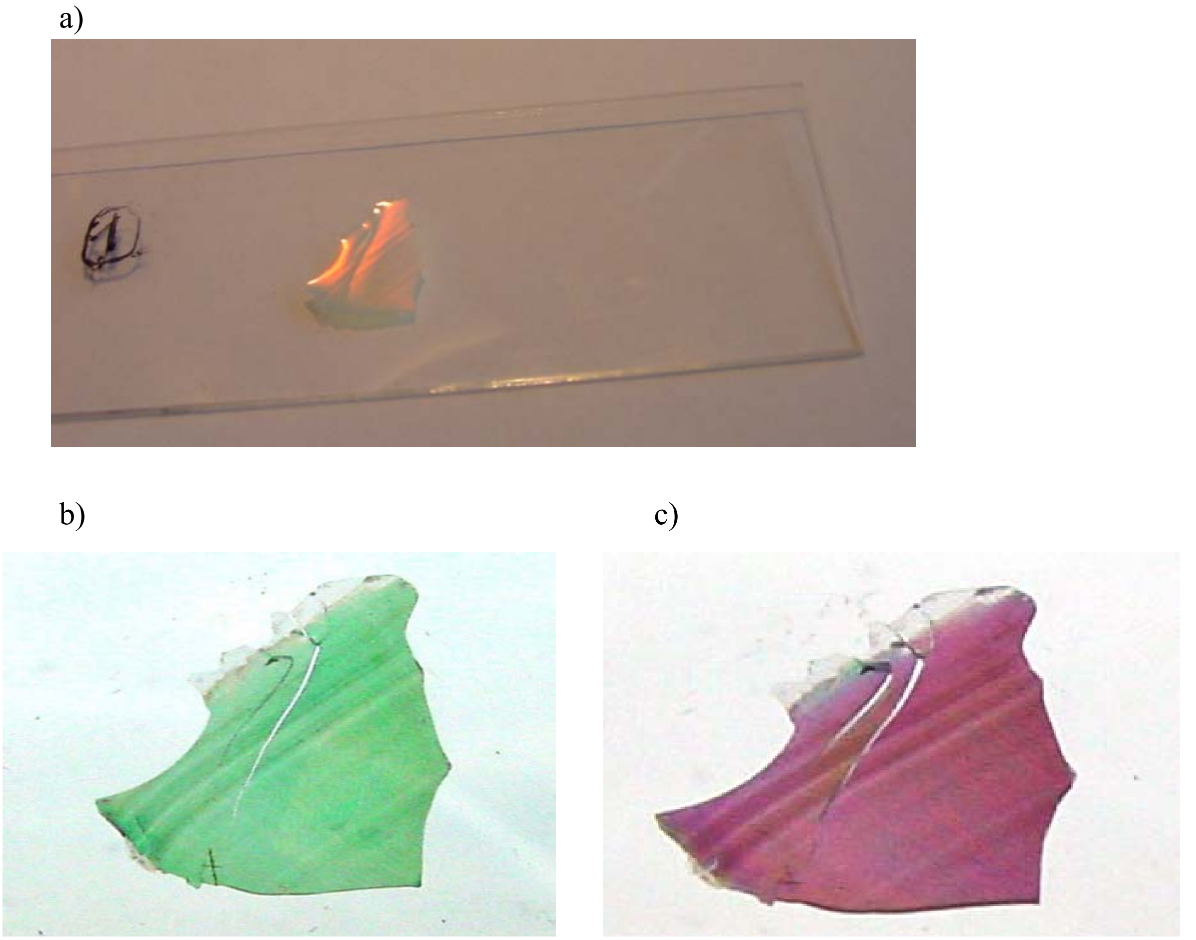

Figure 5.1. Photographs of OC-I replica made from PMMA opal template with a sphere diameter of 370 nm: a) Taken by reflection; b) Taken by transmission on the level; c) Taken by transmission tilted. These photos were taken by Dr. Jürgen Wagner in Golm.

5.1.2 Structural Characterization by SEM Method

Figure 5.2 shows the SEM image of the top view of the OC-I replica made from the PMMA opal template having a sphere diameter of 370 nm. A nearly perfect hexagonal arrangement of the air spheres can clearly be seen and a simple reconstruction of the position of the spheres confirms the fcc lattice with the (111) plane normal to the surface of the template. The dark spots indicated with an arrow in Fig. 5.2 are the connections between the air spheres and the nearest-neighbour air spheres in the layer below, called windows. The windows correspond to points where the latex spheres in the template were touching each other by sintering. In Fig. 5.2 they are arranged in a triangular pattern, since along the axie of the (111) plane normal to the surface direction each sphere rests on three neighbours below. However, quite a lot less than three windows inside each void have been observed (Fig. 5.3). In addition Figs. 5.2 and 5.3 shown that the interstitial space among opal spheres were fully infiltrated from OC-Ioligomers. This indicated that the OC-I replica is a volume-templated inverse opal.

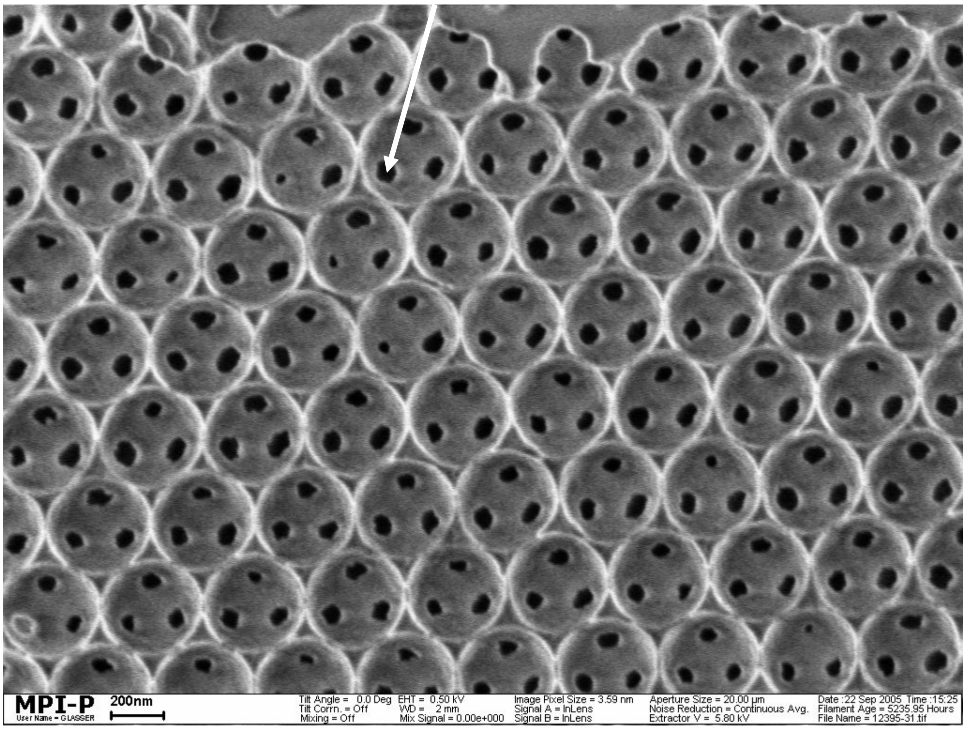

Figure. 5.2. Representative SEM image of the top view of the OC-I replica made from the PMMA opal template having a sphere diameter of 370 nm.

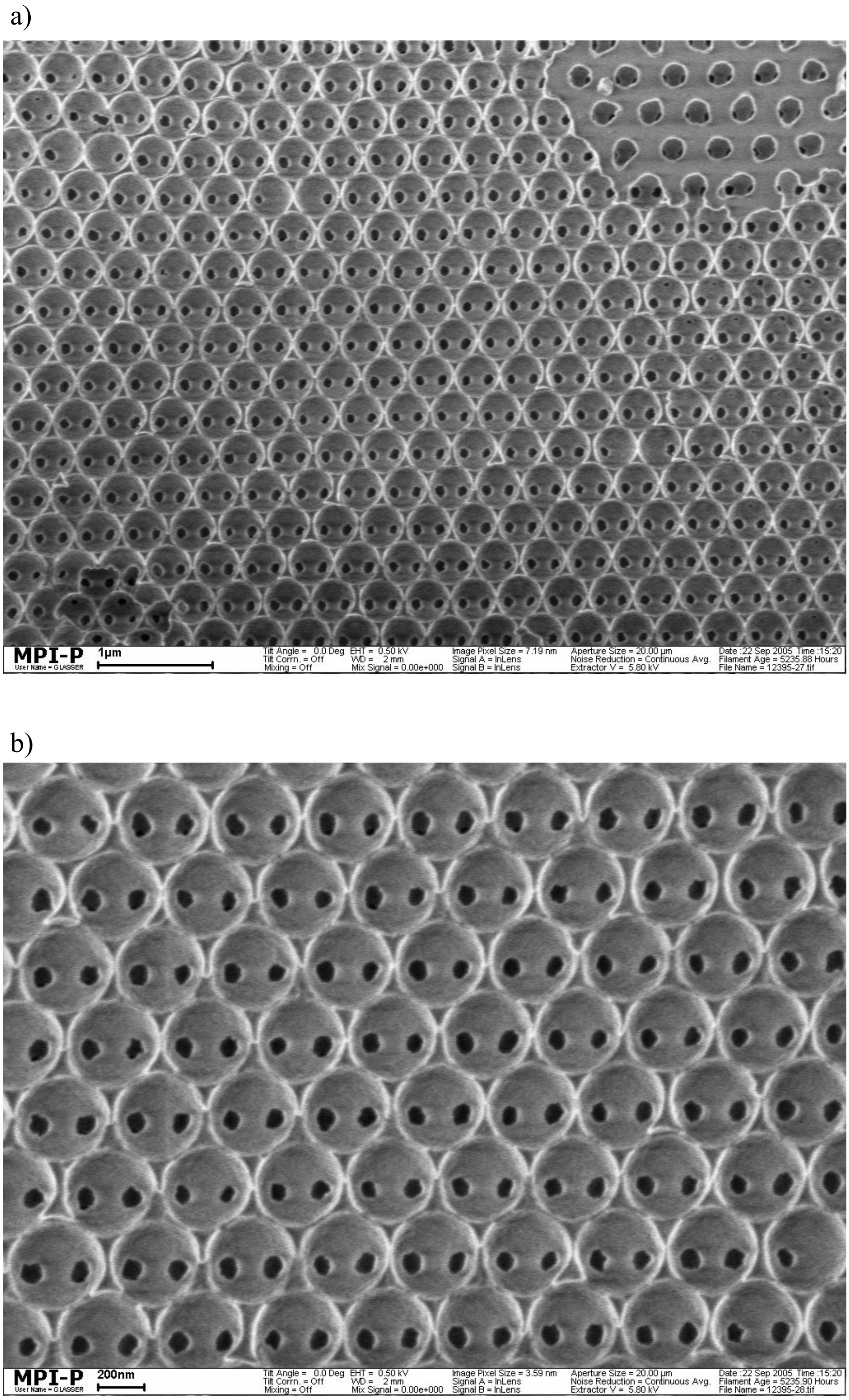

Figure 5.3. Representative SEM image of the top view of the OC-I replica made from the PMMA opal template having a sphere diameter of 370 nm: a) Low magnification; b) high magnification.

Figure 5.4 shows the SEM image of the cross-section of the replica. This picture nicely demonstrates the well formed replica structure in depth. The SEM study reveals that the OC-I replica keeps the 3D crystalline order of the initial template very precisely. The lattice constant is also close to that of the opal template. A quantitative analysis of the SEM images of the (111) plane for the template and the replica results in an average distance of the lattice sites of (387±5) nm and (383±10) nm, respectively.

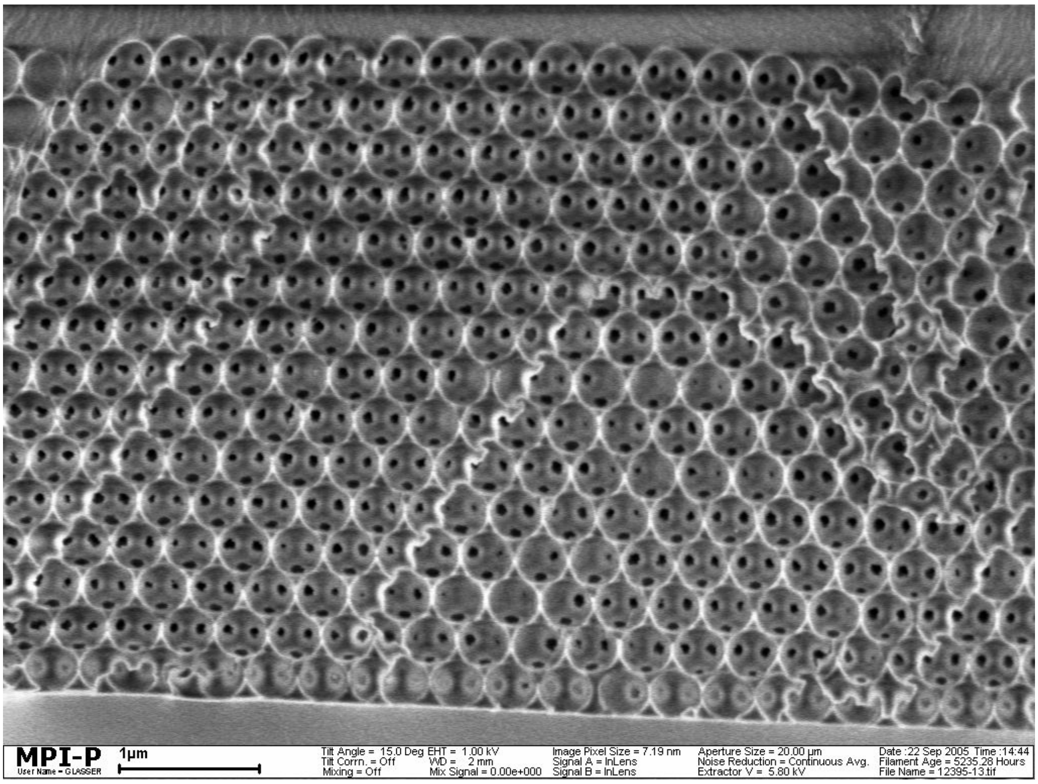

Figure 5.4. Representative SEM image of cross-section of the OC-I replica made from the PMMA opal template having a sphere diameter of 370 nm.

5.1.3 Optical Property of ORMOCER Replica

The photonic properties of the OC-I replica were studied using transmission and reflectance spectroscopy. These are powerful and easily processable tools to characterize the 3D structure quality of inverse opals manifested in the attenuation of the (111) Bragg peak, the appearance of Fabry-Pérot resonances and well-defined peak angle dependences according to the Bragg condition. Moreover, experimental data of the photonic material such as effective refractive index or film thickness (number of layers) can be obtained from these measurements. Spectra were recorded in Golm with a Perkin-Elmer Lambda 2 spectrophotometer using accessories for specular reflectance (6°) and for variable angle transmission (0-60°) or reflectance (15-75°). Fig. 5.5 shows optical transmission ($\Theta = 0°$) and reflectance ($\Theta = 6°$) spectra of the opal template (370 nm spheres) and the OC-I replica. The stop bands of OC-I replica shift to blue and they are wider than that of the opal template. The relative bandwidth value is 0.094 for OC-I replica and 0.060 for the template respectively. The spectra at different angles Θ between the incident beam and the normal to the (111) plane are given in Fig. 5.6. The position of the (111) Bragg band in transmission and reflectance spectra of the replica at various angles of incidence is shown in Fig. 5.7.

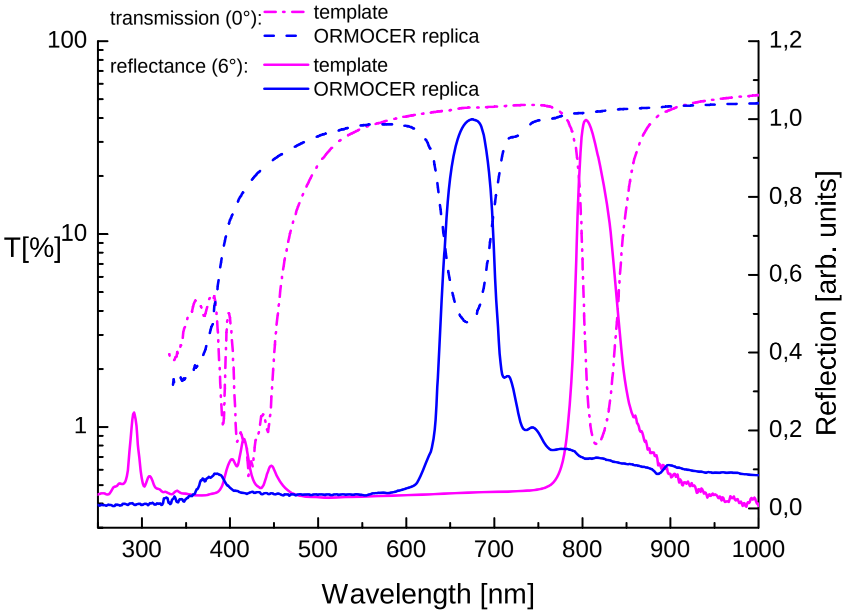

Figure 5.5. Optical transmission ($\theta = 0°$) and reflectance ($\theta = 6°$) spectra of the opal template having a sphere diameter of 370 nm and the OC-I replica.

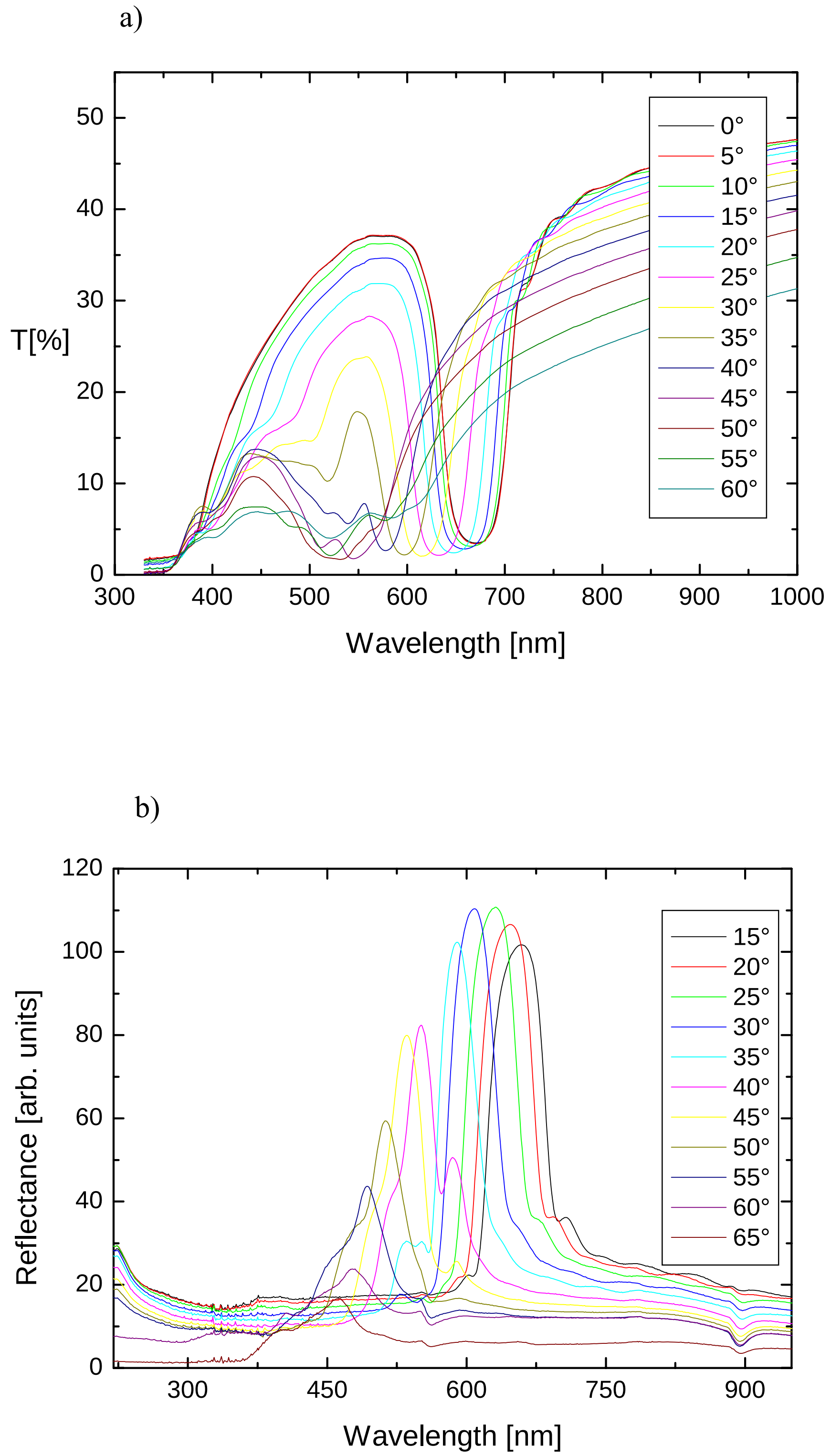

Figure 5.6. a) Angle resolved transmission spectra of OC-I replica from PMMA opals with 370 nm diameter spheres for angles between 0° and 60° with a 5° step. b) Angle resolved reflectance spectra of OC-I replica for angles between 15° and 65° with a 5° step.

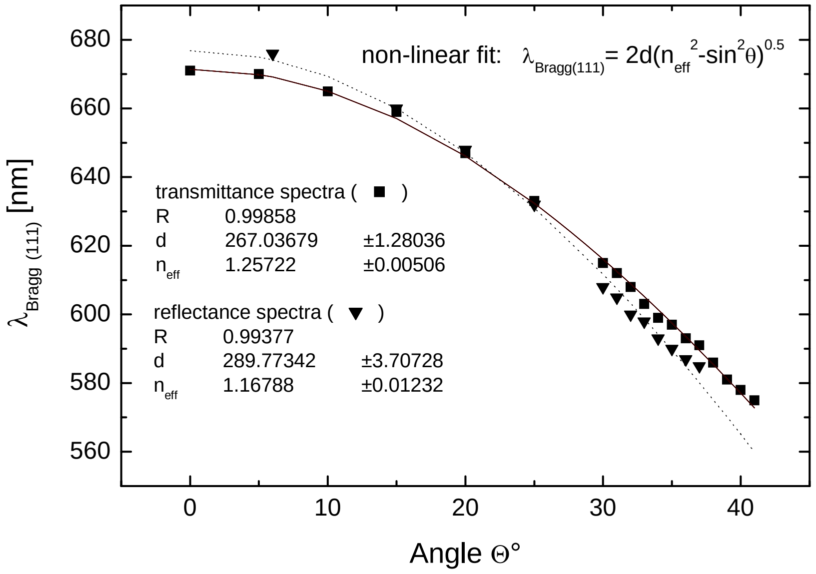

Figure 5.7. Position of the (111) Bragg band in transmission (■) and reflectance (B▼) spectra of the OC-I replica from PMMA opals with 370nm diameter spheres at various angles of incidence (Θ). Non-linear fit to the Bragg equation: The lattice constant d = 267 nm (D = 327 nm) and the effective refractive index n_{eff} = 1.257 from transmission spectra; d = 290 nm (D = 355 nm) and n_{eff} = 1.168 from reflectance spectra.

For samples prepared with 370 nm PMMA spheres (Fig. 5.5) multiple stop bands could be indexed to different sets of planes for the reflectance spectra (6°) of the colloidal crystal template at 806nm (111), 447nm (220), 415nm (222), 402nm (311), 291nm (400) and the OC-I replica at 675nm (111) and 380nm (220), which corresponded well to the calculated wavelengths. However, reflection bands corresponding to (200) were missing at small angles of incidence.

From angle-dependent reflectance of the (111) Bragg band (Fig. 5.7) the non-linear fit to the Bragg equation leads to d = 295 nm (D = 355 nm) and n_{eff} = 1.168. The effective refractive index (n_{eff}) can also be determined by $n_{eff}^2 = n_{walls}^2 \Phi + n_{voids}^2 (1 - \Phi)$, where Φ is the volume fraction of the solid wall material, n_{walls} is the refractive index of the wall material, and n_{voids} is the refractive index of the void space. A solid volume fraction of 0.26 is predicted for an exact inverse replica of close-packed fcc templates. For a fully-developed hybrid polymer replica (n_{walls} = 1.5355, n_{voids}=1) n_{eff} = 1.163 is obtained. The experimental value fits well to this calculation, and this reveals that the resulting inverse opal structure is fully-developed with a filling factor of nearly 100%.

The observation of well-defined Fabry-Pérot resonances in the vicinity of the (111) Bragg band by reflectance (or transmission) spectroscopy (Fig.5.6) also indicates the high structural order of the opal replica. Fabry-Pérot fringes are very sensitive to disorder and the deviation of film thickness is not more than 10 % at the area of the spectrometer beam. Moreover, the film thickness and the number of layers can be calculated from the distance between the fringes[92] resulting in an average of 18 to 20 layers (Fig. 5.8) for the sample prepared with 370 nm PMMA spheres over the large area of the spectrometer beam compared to 15 layers for the cross-section in SEM (Fig.5.4).

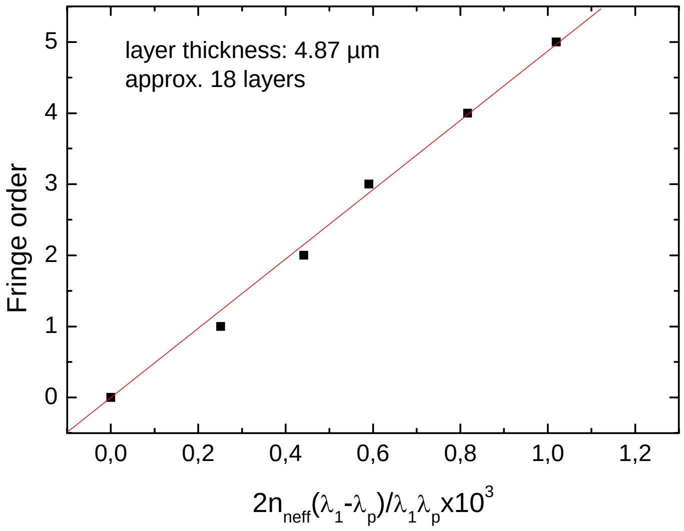

Figure 5.8. Calculation of film thickness based on Fabry-Pérot fringes from the reflectance spectrum at Θ = 15° (18 layers).

A splitting of (111) Bragg resonance in transmission and reflection was observed for angles of incidence between Θ = 36° and 43°. This behavior is attributed to the (200) Bragg reflection if the specular conditions are fulfilled for both (111) and (200) sets of planes. Thus, double peaks appear in the vicinity of the crossing between the two Bragg conditions (Fig. 5.9).

a)

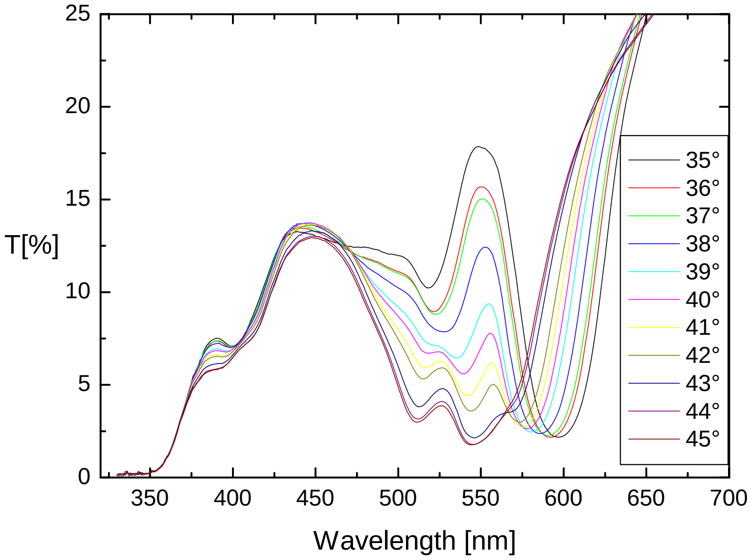

b)

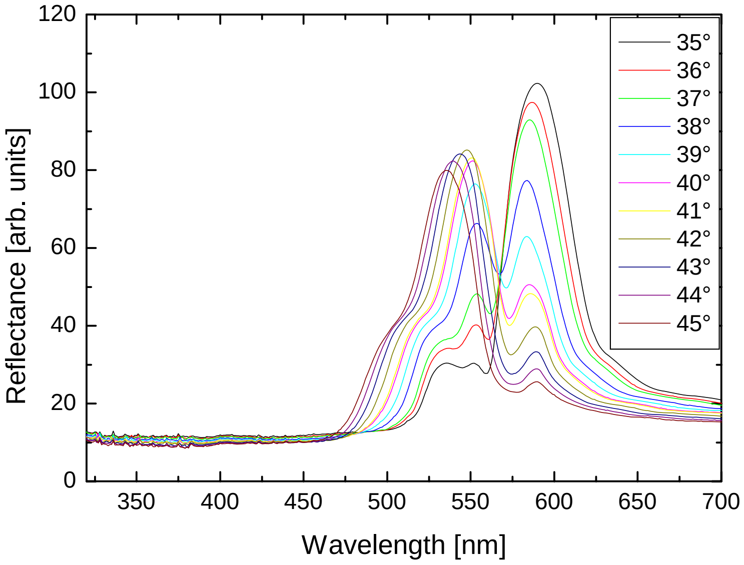

Figure 5.9. Angle dependent spectra of OC-I replica made from PMMA template with a sphere diameter of 370 nm at a angle range between 35° to 45°: a) Transmission spectra, b) reflectance spectra.

Based on fcc model calculation[99b,113] ($\alpha = 54.74°$) including experimental data for n_{eff} and D from reflectance peak angle dependence, the crossing is predicted at 38°. In Fig. 5.10, both peaks' wavelengths of (111) and (200) bands are plotted against Θ along with the calculated angular dependence of the (111) and (220) Bragg reflections (solid and dashed lines, respectively) of a fcc structure. This figure was made from Dr. Jürgen Wagner from

Fraunhofer Institute in Golm. As shown in Fig. 5.10, this calculated line fits well to the experimental result and reveals the high degree of fcc order.

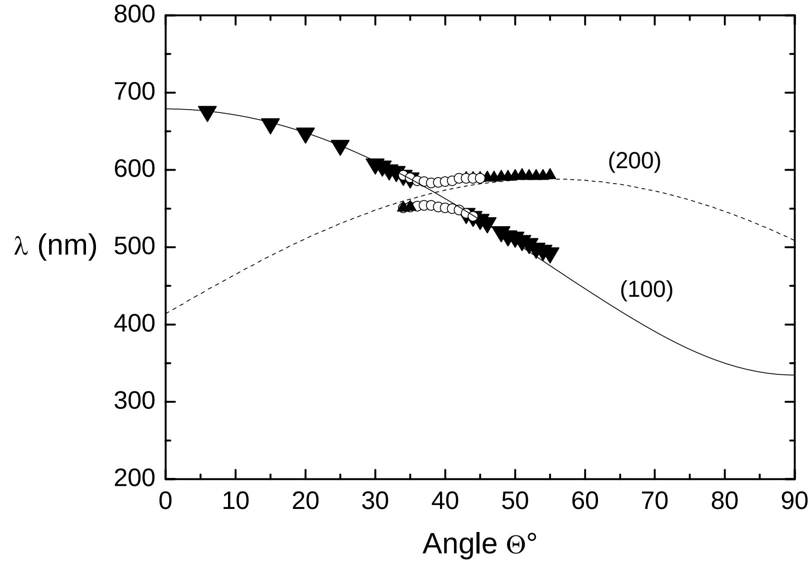

Figure 5.10. Bragg peaks λ of (111) and (200) bands plotted against Θ ((111) plane (▼), (200) plane (▲), splitting range (○)) and their calculated angular dependence in an fcc packing (solid and dashed line, respectively).

Fig. 5.11 shows the comparison of the transmission spectra at the angle Θ = 45° (Fig. 5.11a) and 55° (Fig. 5.11b) from two opal templates, one made of Sample No. 3 (sphere diameter 270 nm), another made of Sample No. 5 (sphere diameter 370 nm), and OC-I replica made from opal template having a sphere diameter of 370 nm (Sample No. 5). It is remarkable that for opal templates with different sphere sizes their angular dependent spectra have the same shapes and only the positions of the different bands are shifted. But in comparison with the opal template the angular dependent spectrum of OC-I replica is not only different in the positions of the bands, but also in the shape. However, interesting is that the similar shape spectra of OC-I replica in comparison with the template have been found at different angles (Fig. 5.12). It can be seen in Fig. 5.12 that the angular transmission spectra of OC-I replica for angles between 40° and 50° are similar to that of the opal template having a sphere diameter of 370 nm at the angle range of 50° to 60° and the similarity of these spectra has also been found between OC-I replica at the angles 50°-60° and opal template at the angles 60°-70°.

a)

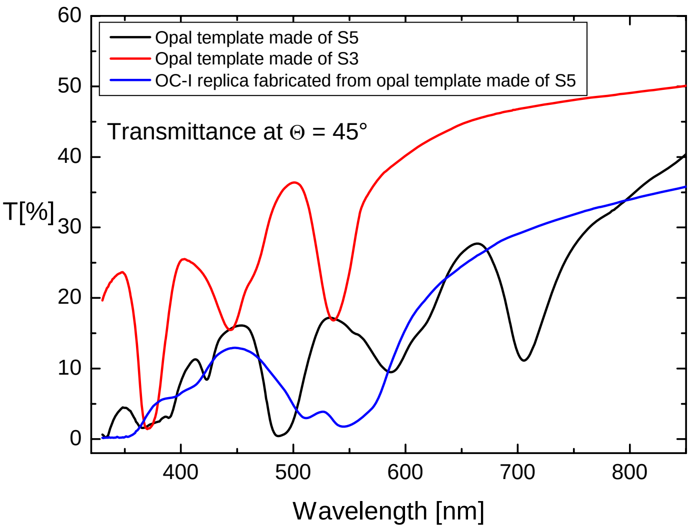

b)

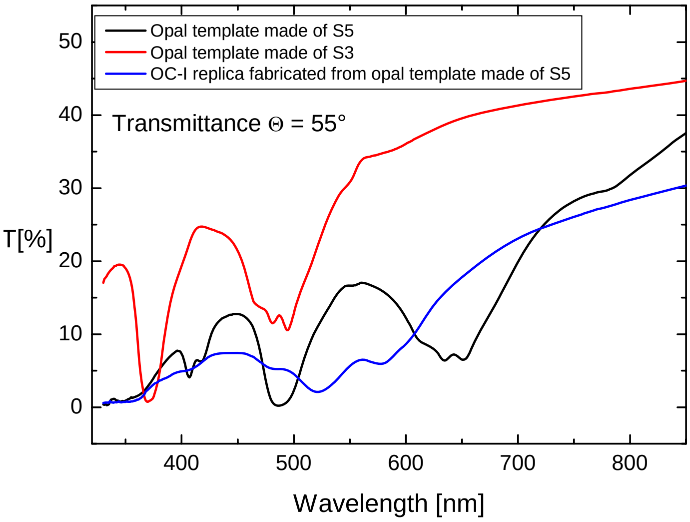

Figure 5.11. Comparison of the transmission spectra from two opal templates, one made of Sample No. 3 (sphere diameter 270 nm), another made of Sample No. 5 (sphere diameter 370 nm), and OC-I replica made from opal template with a sphere diameter of 370 nm (Sample No. 5): a) At the angle Θ = 45° , b) at the angle Θ = 55°.

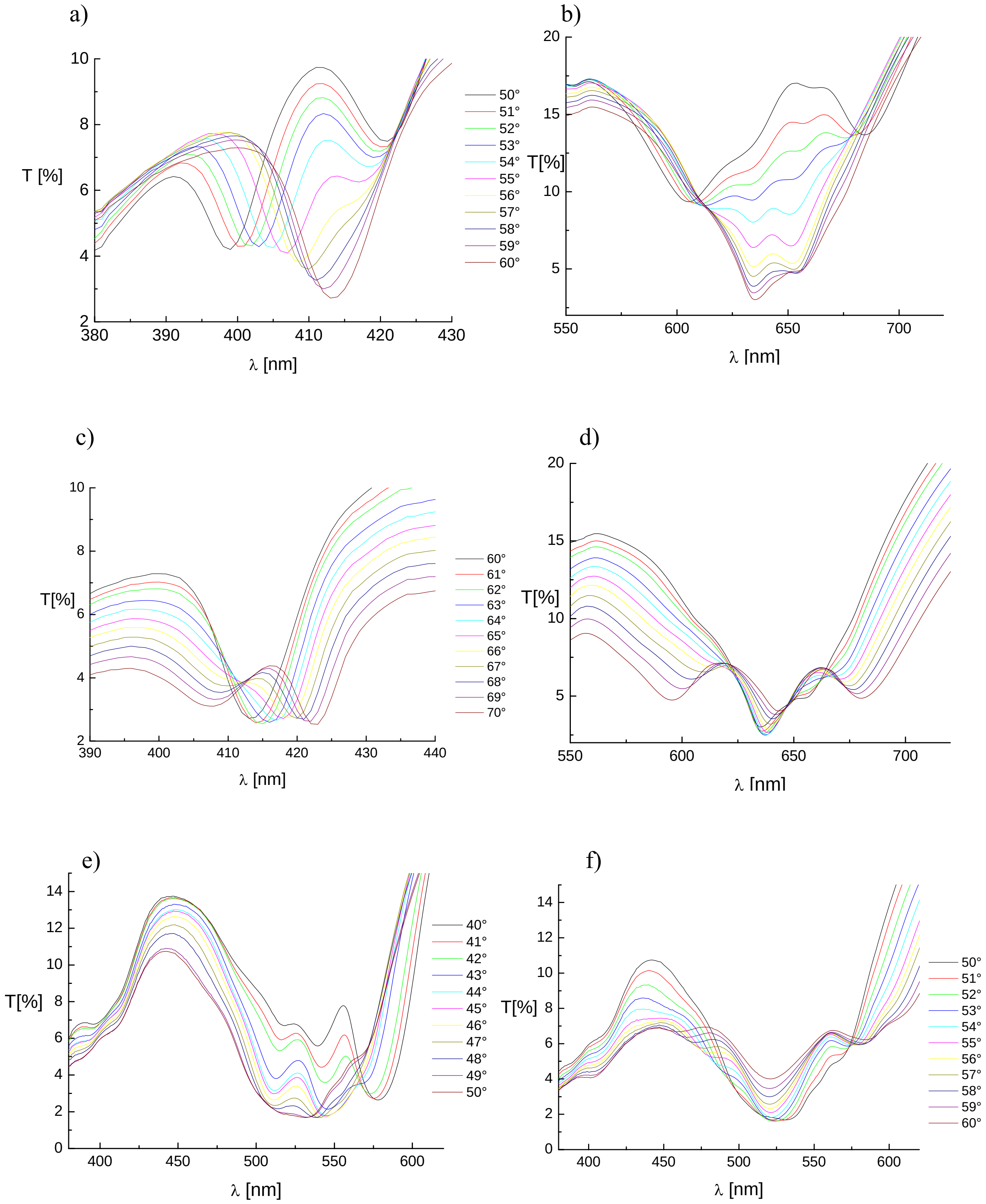

Figure 5.12. Comparison of the transmission spectra of the opal template made of Sample No. 5 (sphere diameter 370 nm) with that of its OC-I replica: a-d) Transmission spectra from opal template for angles between 50° and 70°, e-f) transmission spectra from OC-I replica for angles between 40° and 60°.

5.2 Fabrication of Silicon Replica on Patterned Substrates

The silica opals on patterned substrates as described in Chapter 3 were used as templates for the fabrication of silicon replica. The voids of the opal samples were filled with silicon by using the thermal chemical vapor deposition (CVD) technique, in which the CVD-reactor consisted of a quartz tube with an external heater, through which a gas mixture of SiH_4 (5%) and Ar was passed. An opal plate was placed perpendicular to gas flow. The reactor design excluded gas flow around a sample. As a result of silane thermal decomposition a silicon film was deposited on the inner surface of opal voids. The conditions of decomposition were isothermal.[154] Finally, the inverse opal was obtained by etching out SiO_2 opals in a dilute HF aqueous solution. The fabrication of silicon replica was performed in the Ioffe Physical Technical Institute in St.-Petersburg Russia. The silicon replica structure was characterized by SEM. Fig. 5.13 and 5.14 show the SEM images of the top view of the silicon replica made from silica opals with a sphere diameter of 890 nm on a patterned substrate in different magnifications. Although the sample surface was broken somewhere during to removal of the covered silicon layer (Fig. 5.13), the good hexagonal arrangement of the voids clearly can be seen and indicates that the inverse opals remained the fcc structure of silica opal template.

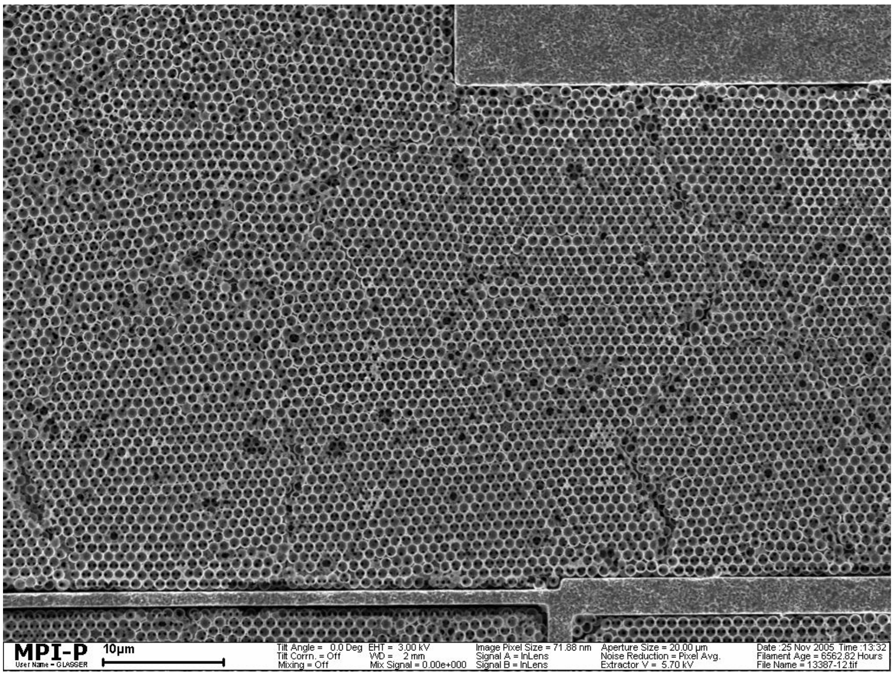

Figure 5.13. SEM image of the top view of the silicon replica made from silica opals with a sphere diameter of 890 nm on a patterned substrate in low magnification.

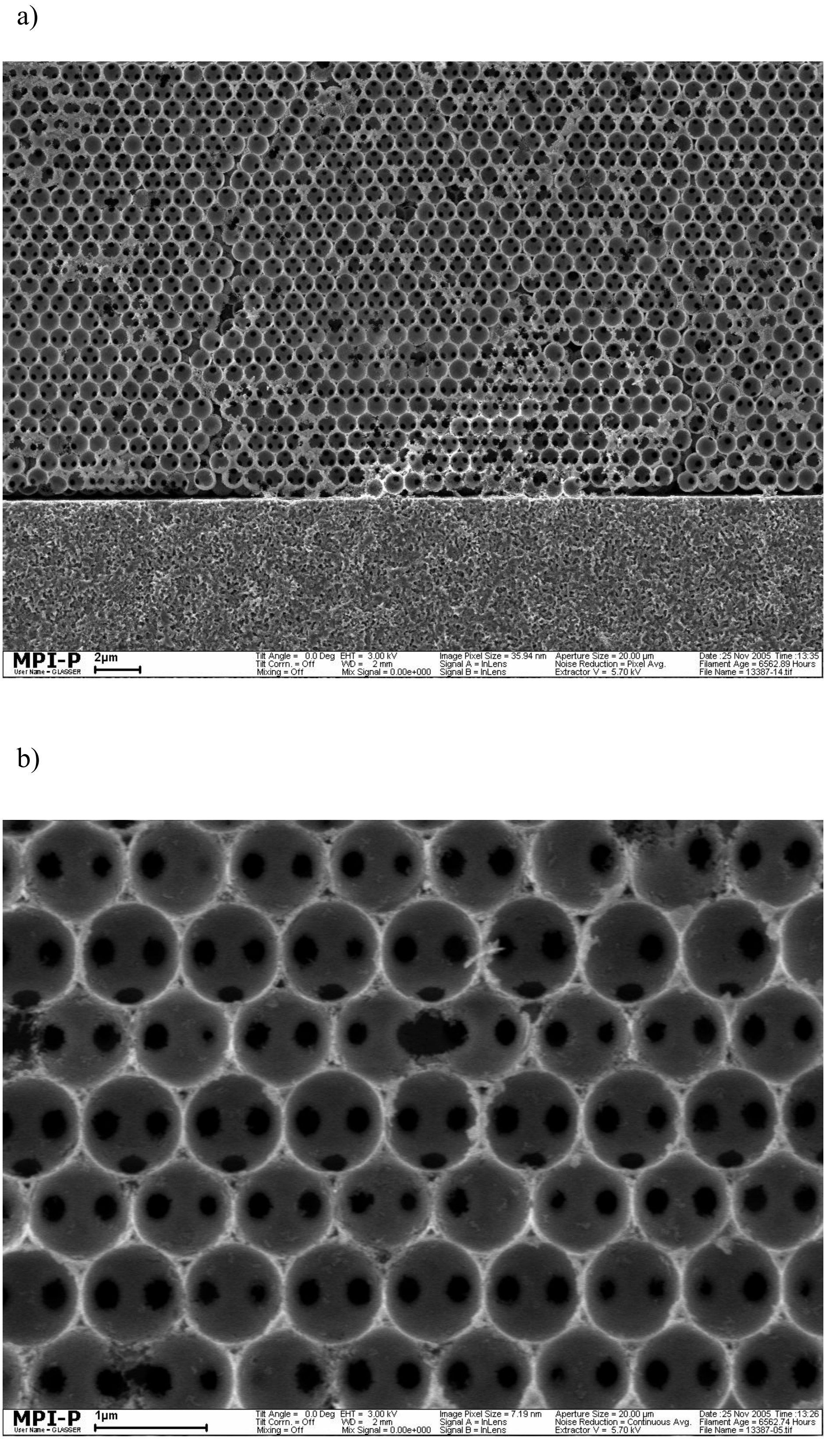

Figure 5.14. SEM images of the top view of the silicon replica made from silica opals (sphere diameter 890 nm) on a patterned substrate: a) Low magnification, b) high magnification.

Fig. 5.15 shows SEM images of the cross-section of the silicon replica made from silica opals with a sphere diameter of 890 nm on a patterned substrate. These pictures reveal that silicon growth takes place layer by layer in the sphere surface of the silica opal, producing a surface-templated inverse opal. The layer thickness was about 100 nm.

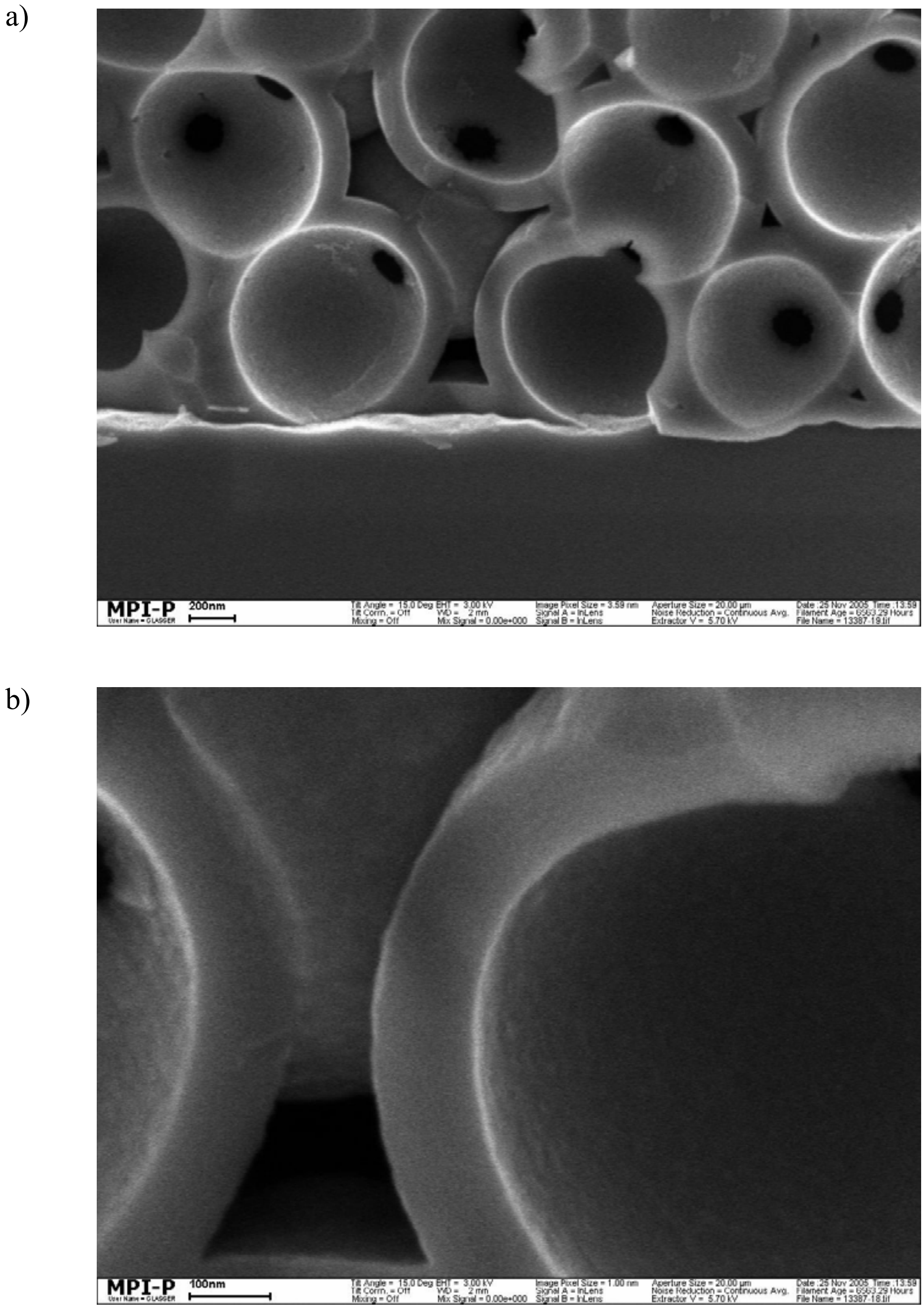

Figure 5.15. SEM images of the cross-section of the silicon replica made from silica opals (sphere diameter 890 nm) on a patterned substrate: a) Low magnification, b) high magnification.

5.3 Inverse Opals as Catalyst Supports in Micro Reactors

Using PMMA opals as templates has also been successfully applied to the fabrication of 3D macroporous structures from other different materials. One of the interesting applications of these inverse opals is as catalyst or catalyst support for the micro-structured reactors owing to their large surface area. In porous structures at microscale the mass and heat transport is much larger than those at macroscale, as a result of the shorter distances and the large surface area to volume ratios.[155] This provides the possibility to fix a sufficient number of active sites in the micro space for heterogeneously catalyzed reactions, for example, steam reforming, water gas shift, preferential carbon monoxide oxidation, or hydrocarbon catalytic combustion, etc.. The micro reactors could be realized by using inverse opals as the catalyst supports on the micro channels, over which active transition metal or noble metal nano-sized species were anchored onto these supports. Fig. 5.16 shows the picture of PMMA opals with a sphere diameter of 370 nm (Sample No. 5) in metal micro channels. Fig. 5.17 and 5.18 show photographs and SEM images of several examples of inverse opals that were fabricated by Dr. Guan Guqing from the Institut für Mikrotechnik Mainz GmbH. These inverse opals were made of PMMA opals having a sphere diameter of 370 nm (Sample No. 5) by sol-gel process. They could serve either as catalyst supports or also as a catalyst itself (Fig. 5.18a, 5.18b, and 5.18c). Catalytic test for Pt based inverse opals in propane combustion at low temperature revealed excellent reactivity and stable activity of the promoted catalysts.[156] The reactivity of such catalysts was also observed for the preferential carbon monoxide oxidation.[157]

Figure 5.16. Picture of PMMA opals with a sphere diameter of 370 nm in metal micro channels.

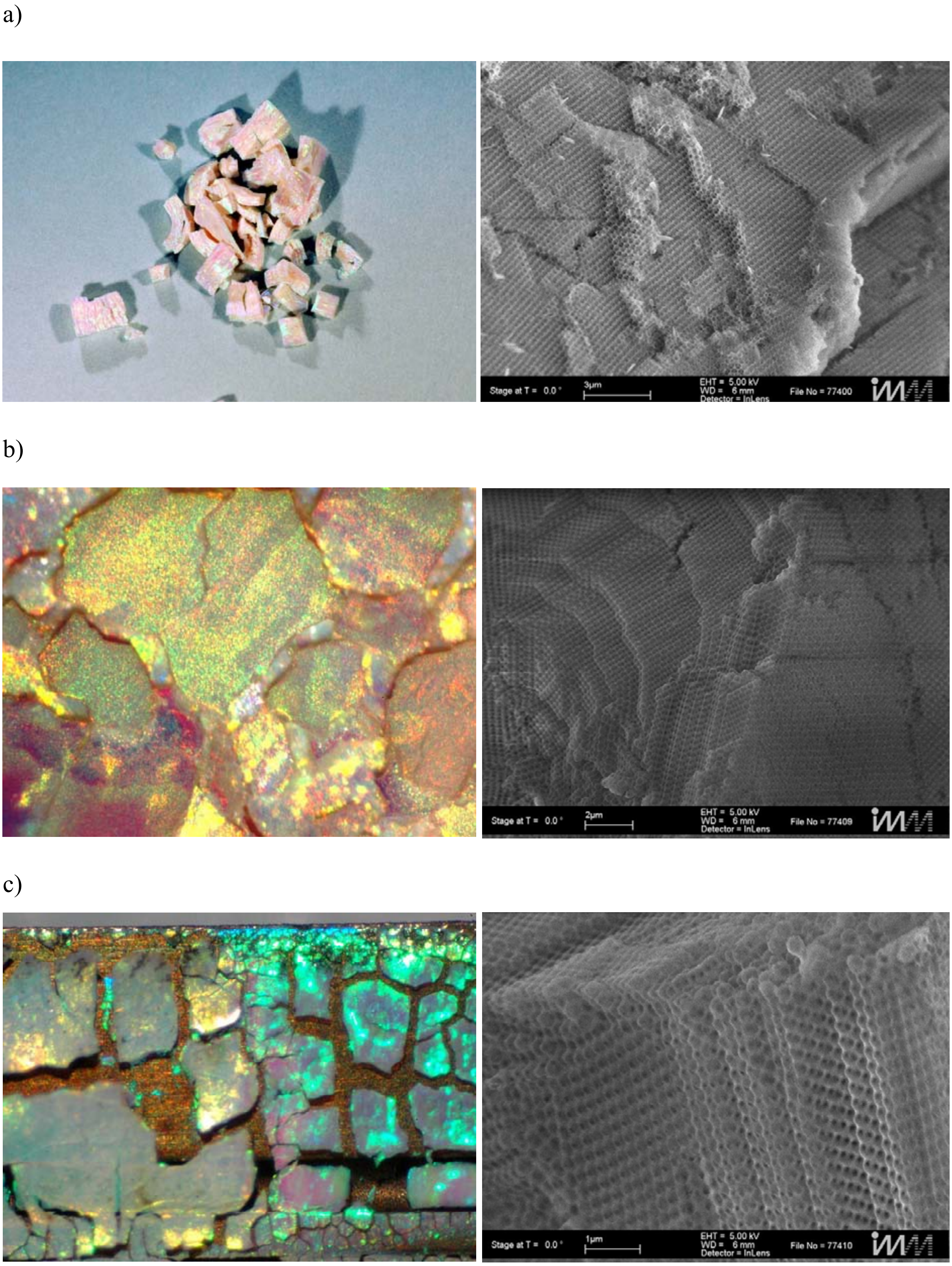

Figure 5.17. Photographs and SEM images of inverse opals made of PMMA opals (sphere diameter 370 nm): a) CeO2(10%)-SiO2(90%)-inverse opals, b) CeO2 (15%)SiO2(85%) – inverse opals, c) SiO2-inverse opals.

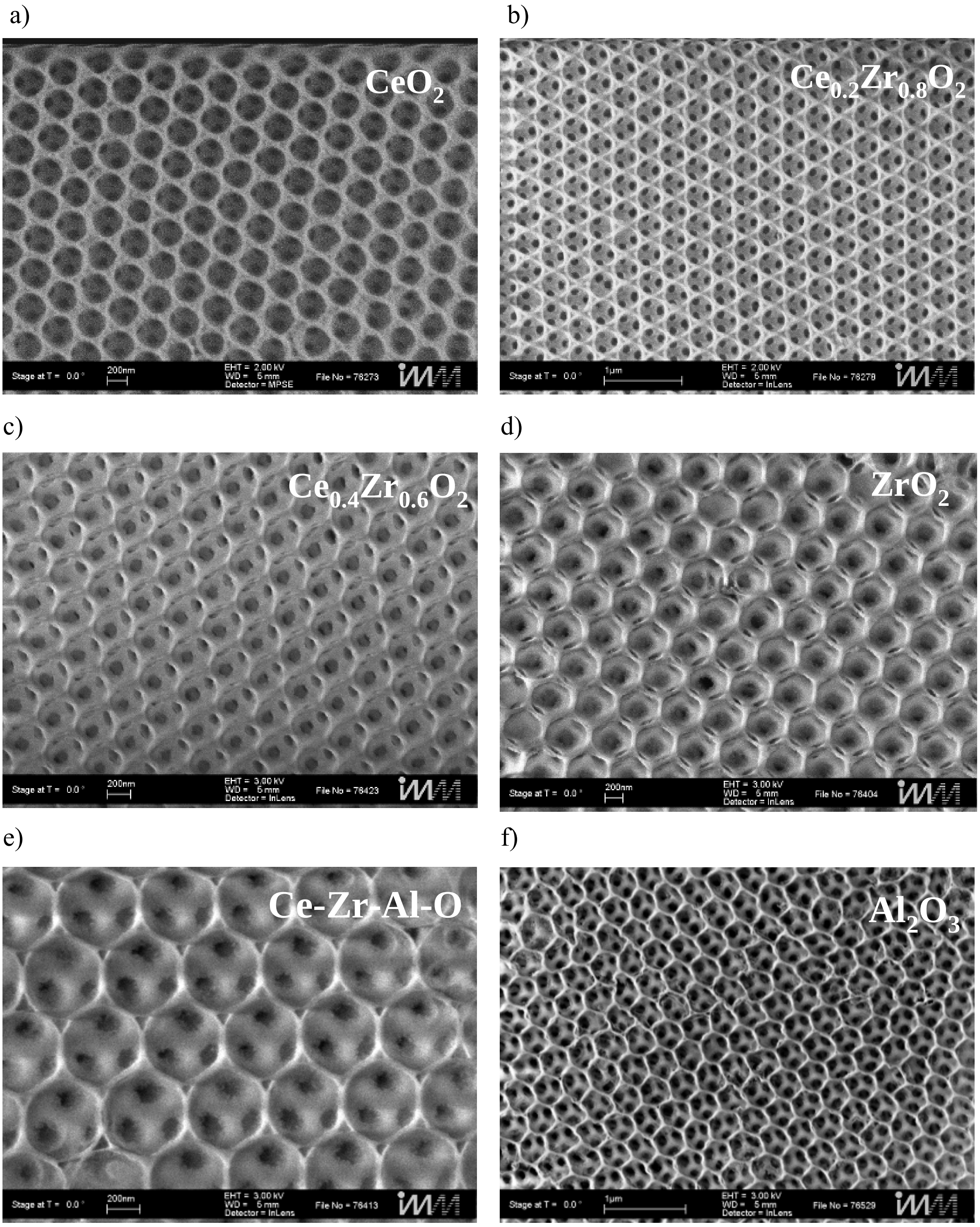

Figure 5.18. SEM images of inverse opals made of PMMA opals (sphere diameter 370 nm): a) CeO_2, b) $Ce_{0.2}Zr_{0.8}O_2$, c) $Ce_{0.4}Zr_{0.6}O_2$, d) ZrO_2, e) Ce-Zr-Al-O, f) Al_2O_3.

6. Summary

In this present work high quality PMMA opals with different sphere sizes, silica opals from large size spheres, multilayer opals, and inverse opals were fabricated. For preparation of PMMA opals highly monodisperse PMMA spheres were synthesized and characterized. For crystallization of large size silica spheres a new crystallization method was developed. The opal quality was determined by SEM studies and optical experiments. The optical properties of these colloidal crystals were also investigated intensively.

The prerequisite for fabrication of high quality colloidal crystals is the preparation of highly monodisperse colloids. PMMA spheres with the diameter range of 180 to 500 nm were synthesized by surfactant-free emulsion polymerization. The sphere sizes were determined from the position of the stop band obtained by UV-Vis-Spectroscopy. By careful control of the reaction conditions, for example, the reaction temperature, the concentration of reactants, PMMA spheres with desired size and very narrow size contribution were obtained. The polydispersity for PMMA spheres with a diameter smaller than 400 nm is smaller than or close to 2% determined by dynamic light scattering. The spheres quality can be also controlled by examining the opal film quality.

For self-assembly of PMMA colloids the vertical deposition method by a drawing device was mostly used in this present work. This technique has been proven by its versatility and flexibility. By using this method large-area and well-ordered PMMA crystalline films with a homogenous thickness were produced on the glass substrates and patterned silicon substrates. The thickness of these crystalline films is 5-10 µm (about 10-50 layers) controlled by suspension concentration, sphere size, and withdrawing speed. SEM studies show that the PMMA opals possess excellent fcc close-packed structure. Optical experiments have confirmed the high quality of these PMMA photonic crystals. One of the important criteria for high quality is the detection of well resolved high-energy bands of the transmission and reflectance spectra of the opaline films. This could be very useful as a model for the investigation of the behaviour of the photonic band structure in the high-energy region which is very interesting for the optoelectronic applications. Moreover, these high quality PMMA opals are excellent templates for fabrication of high-grade 3D photonic crystals (inverse opals).

For fabrication of high quality opaline photonic crystals from large silica spheres (diameter of 890 nm), self-assembled in hydrophilic trenches of silicon wafers a novel technique has been developed, in which the crystallization was performed by using a drawing apparatus (providing control of the crystallization speed) in combination with stirring (providing counterbalancing of the sedimentation). The achievements comprise a spatial selectivity of opal crystallization without special treatment of the wafer surface, a filling of the trenches up to the top, leading to a spatially uniform film thickness, particularly an absence of cracks within the size of the trenches, and finally a good three-dimensional order of the opal lattice even in trenches with a complex confined geometry, verified using optical measurements. The opal lattice was found to match the pattern precisely in width as well as depth, providing an important step towards applications of opals in integrated optics.

The influence of the trench structure and surface property on the crystallization of colloidal crystals on the patterned silicon substrate has been also investigated. Microspectroscopy studies show no significant quality difference of opals made in trenches with different geometries.

Multilayer opals from PMMA spheres of different sizes were produced by sequential crystallization procedure, in which each single opal layer was fabricated by vertical deposition technique using a drawing device. Double and triple layer PMMA opals were prepared from different sphere size combinations. SEM studies indicate that the multilayer opals were composed from highly ordered opaline films and possessed good interfacial packing of the spheres. Optical properties of these multilayer opals have been investigated. Studies of the transmission in triple-layer hetero-opal revealed that its optical properties cannot only be considered as the linear superposition of two independent photonic bandgaps. The remarkable interface effect is the narrowing of the transmission minima.

Hetero-opals were also prepared by introducing TiO_2 particles, which were composed from the PMMA opal film infiltrated with TiO_2 particles, TiO_2 film, and bare PMMA opal film. Their transmission spectra show anomalous strong resonances at the wavelength range of 300 to 350 nm, presumably as a consequence of the coherent interference between modes from PMMA opal and TiO_2 film at the interface. Further investigation of the optical behaviour of these hetero-opals is in progress.

For fabrication of inverse opals, large-area, high-quality, and robust photonic opal replicas from silicate-based inorganic-organic hybrid polymers (ORMOCER® s) were prepared by using the template-directed method, in which a high quality PMMA opal template was fabricated and infiltrated with a neat inorganic-organic ORMOCER® oligomer, which can be photopolymerized within the opaline voids leading to a fully-developed replica structure with a filling factor of nearly 100%. This opal replica is structurally homogeneous, thermally and mechanically stable and the large scale (cm^2 size) replica films can be handled easily as free films with a pair of tweezers. The high quality of the 3D structure is confirmed by optical studies and SEM microscopy revealing a high degree of fcc close-packed order. This successful example for the fabrication of opal replica demonstrates an attractive way to create new composites by inverse opals from a variety of ferroelectric, nonlinear or photorefractive materials for optoelectronic applications.

In addition, by using PMMA opal template microporous catalysis materials with inverse opal structure in the micro channels were obtained. The inverse opal structure could enhance the mass transfer, increase the surface area, and highly disperse the active elements. They are very suitable when used as catalyst or catalyst support in microreactors and have extensive applications in this field.

7. Experimental Part

7.1 Syntheses of PMMA spheres

The PMMA spheres were synthesized by surfactant-free emulsion polymerization. The monomer methyl methacrylate (MMA) and initiator potassium peroxodisulfate were purchased from Acros and Fluka respectively. The MMA monomers were used without further purification .The deionized water was used directly from a Milli-Q-system (Millipore).

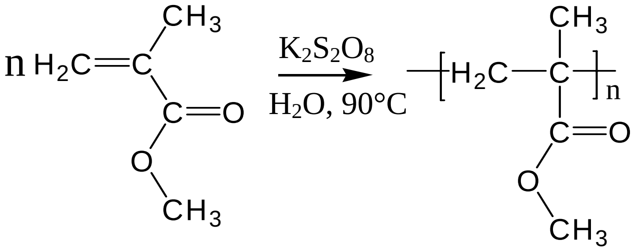

7.1.1 Preparation of PMMA spheres of a diameter smaller than 500 nm

A 2000 ml three-necked flask was charged with 1200 ml deionized water. The flask was sealed with a septum and flushed with nitrogen for 1h. At the same time the flask was heated in an oil bath to 90°C. As the temperature was constant, 200 ml (1.87 mol, dependent on the sphere size) MMA monomer were added. The mixture was heated further for 5 min at 90°C. Then the nitrogen flux was turned off and 40 ml (14.8 mmol) of a 10 wt.-% aqueous solution of potassium peroxodisulfate, which was also flushed with nitrogen and heated to 90°C, were added and the polymerization started at once. The reaction’s mixture was stirred at about 400 rpm by a KPG-mixer during the whole procedure.

For the controlling of the reaction 0.1 ml reaction solution was taken from the flask after 60 min polymerization. The liquid sample obtained was spread into a glass substrate and formed a color film by drying it in the air. This was repeated every 30 mins until the colour of the samples did not change. The reaction took about 2 hours and then was stopped with air. The suspension (reaction product) was stirred for another 20 min in this opened flask.

For purification the warm reaction suspension was filtered through a standard paper filter to separate solids of the agglomerated bulk polymers. Then the suspension was centrifuged, at first three times for 5 min at 4500 rpm to get the large PMMA spheres (or small agglomerations). After that the solution was centrifuged at least three times at 4500 rpm for from 30 min to 2 h depending on the sphere size until a clear water solution above the iridescent deposits was obtained. The liquid phase was separated and the deposits were redispersed in deionized water again. The aqueous suspension was stored with 20 to 30 vol.-% solid content. The reaction yield was estimated at about 70 to 90 %.

The sphere sizes were controlled by adjusting the ratio of monomer to water (Table 2.1) under the same reaction conditions as described above.

7.1.2 Preparation of PMMA spheres of a diameter larger than 500 nm

The PMMA spheres of a diameter larger than 500 nm were synthesized by the continuous subsequent addition of monomers during the polymerization process. A 500 ml three-necked flask was charged with 180 ml deionized water. The flask was sealed with a septum and flushed with nitrogen for 30 min. The flask was heated in an oil bath to 90°C. As the temperature was constant, 45 ml (0.42 mol) MMA monomer were added and the mixture was heated further for 5 min at 90°C. Then the nitrogen flux was turned off and 15 ml (5.55 mmol) of a 10 wt.-% aqueous solution of potassium peroxodisulfate, which was also flushed with nitrogen and heated to 90°C, were added to start polymerization. The reaction’s mixture was stirred at about 400 rpm by a KPG-mixer during the whole procedure. After 1 h polymerization 14 ml (0.13 mol) MMA were added and other 16 ml (0.15 mol) and 18 ml (0.17 mol) MMA were added successively at a time interval of 30 min. The work-up was performed as described above, except the centrifugations, which were done more than 10 times for 30 min at 4500 rpm because of the existence of a small faction of very fine spheres (second seeds).

7.2 Fabrication of colloidal opals

7.2.1 Pre-treatment of substrates

The glass substrates (26x76 mm, ca. 1mm thick) were hydrophilized during 2 h in a bath of a 7.5 M sodium hydroxide aqueous solution. Then they were rinsed well with water and dried in the air.

The silicon substrates (ca. 15x50 mm) were cleaned by immersion into a 7:3 solution of sulphuric acid (98%) and hydrogen peroxide (35%) for 20 min, followed by copious rinsing with de-ionized water. The substrates were then hydrophilized in a 1:1:5 mixture of hydrogen peroxide (35%), ammonia (28-30%), de-ionized water at 65°C for 20 min. Finally they were rinsed carefully with de-ionized water and dried in a stream of nitrogen.

7.2.2 Preparation of PMMA opaline films

The particle suspensions were diluted with de-ionized water to desired concentration, typically 1.5-5 vol.-%.

7.2.2.1 Horizontal crystallization

For the preparation of very thin opaline film (less than 15 layers) two or three drops of 1.5-2 vol.-% PMMA sphere suspension were spread onto a glass substrate and the thin liquid layer was left to dry in the air. For fabrication of the opaline films with a thickness more than 15 layers 2-10 vol.-% suspensions were used. In this case the liquid film was dried in a chamber, in which the relative humidity was set to about 98% and controlled by using a saturated potassium nitrate solution,[82] under the normal pressure at the room temperature for from several days to a week.

7.2.2.2 Vertical crystallization

The drawing device is a home-made apparatus based on a step motor enabling withdrawing speeds in the range of several 100 nm/s. In a representative procedure, a hydrophilized glass substrate was immersed vertically into a home-made glass container (diameter ca. 4 cm, higher 11 cm) filled with about 50 ml suspension. The substrate was withdrawn with the drawing machine at a controlled speed (typically 200 nm/s). The suspension concentration for vertical crystallization using a drawing device is 1.5-5 vol.-%. The opal film thickness can be controlled by varying of the suspension concentration and withdrawing speeds. Similarly the crystallization was also performed on silicon substrates both flat and patterned. The whole apparatus was placed in a box or in a very small room to protect the experiment from air drafts. The temperature for the experiments was about 21°C (room temperature).

7.2.3 Fabrication of silica opals from large size spheres

7.2.3.1 Purification of the large SiO_2 spheres

In order to separate the small spheres the silica sphere suspension was centrifuged for 5 min at about 500 rpm. The liquid phase was separated and the deposits were redispersed in de-ionized water. This was repeated more than 5 times until the liquid phase was very clear. Then the suspension was diluted with de-ionized water in a 2 l beaker and stood still for about one night. The liquid phase was separated very carefully. The deposits at the bottom were diluted with de-ionized water again. The same procedure was repeated several times to ensure that the most doublet spheres were eliminated. The other dirt was removed by sequential and multiple filtering through a filter paper with a pore diameter of 5 µm. The silica sphere quality was determined by SEM.

7.2.3.2 Crystallization of large silica spheres

For crystallization of silica spheres ethanol (99.8%, Roth) was used as a solvent. The silica spheres were washed with ethanol three times by centrifuging. They were diluted with ethanol to a 2-5 vol.-% concentration. However, it was difficult to determine exactly the suspension concentration in this case because the ethanol evaporated very quickly. The patterned silicon substrates were immersed vertically into the silica sphere suspension and withdrawn with the drawing device at a withdrawing speed of 200 nm/s. In order to prevent sedimentation of the large silica spheres, a spinning magnetic bar at the bottom of the container was added with slow stirring at 100 rpm. In this set-up, the surface of the suspension has to be far way enough from the spinning bar, so as to ensure that the suspension in the region of the meniscus contacting the substrate is maintained in a quiet state. The experiments were done at the room temperature and normal atmospheric pressure.

7.3 Fabrication of multilayer opals

The multilayer opals were fabricated by successive depositions. Each single opal film was prepared by vertical deposition using a drawing device. After each individual film was deposited the film was air-dried for at least 24 h and sintered at 80°C-95°C depending on the sphere sizes (smaller spheres at 80°C and larger ones at 95°C) for about 3 hours. Then a next opaline film was crystallized on top of the first one and so the procedure was repeated.

7.4 Fabrication of ORMOCER® replica

The voids of opal templates were infiltrated drop by drop with the solvent-free, initiator-containing OC-Ioligomers at 80°C in a sallow room. After infiltrating the opal template, the samples were degassed for about 10 min in a vacuum oven. Before UV exposure, the samples were heated again for 2 min at 80°C on a flat metal plate, cooled down and subsequently exposed at a wavelength of 280-400 nm for 30s to initiate the organic photopolymerization. For the final polymerization the samples were carried out in an oven at 150°C for 3 hours. Afterwards, the very hot samples were cooled down slowly to room temperature in the air. For the development of opal template organic solvent tetrahydrofuran or Acetone was used. The samples were immersed in the organic solvent for 3 h. Then the organic solvent was changed with a fresh one. This was repeated several times.

The ORMOCER® used for this work had a resin’s refractive index of 1.5355 (@ 587 nm) and was acquired from Dr. Ruth Houbertz from the Fraunhofer Institute in Würzburg.

7.5 Characterization

7.5.1 UV-Vis-Spectroscopy

Optical characterization was performed using a UV-2102-PC UV-visible spectrometer from Shimadzu. Absorbance, defined as – log(I/I_0) with I the transmitted intensity for impinging intensity I_0, spectra were collected using incident light beam with a spot size of about 6 x 3 mm^2 normal to the substrate surface (perpendicular to the (111)-plane) at a range from 300 to 900 nm.

Transmission and reflectance measurements were done by Dr. Jürgen Wagner at the Fraunhofer Institute in Golm. Spectra were recorded with a Perkin-Elmer Lambda 19 UV/VIS/NIR Spectrometer and a Perkin-Elmer Lambda 2 spectrophotometer.

7.5.2 Scanning electron microscopy (SEM)

The SEM measurements were performed by Gunnar Glaßer at the Max Plank Institute for Polymer Research. SEM images were taken with a ZEISS Gemini 1530 at acceleration voltages of 0.5-1 kV.

References

[1] Joannopoulos, J. D.; Villeneuve, P. R.; Fan, S. *Nature* **1997**, *386,* 143.

[2] Yablonovitch, E. *Phys. Rev. Lett.* **1987**, *58,* 2059.

[3] John, S. *Phys. Rev. Lett.* **1987**, *58,* 2468.

[4] Arsenault, A.; Fournier-Bidoz, S.; Hatton, B.; Míguez, H.; Tétreault, N.; Vekris, E.; Wong, S.; Yang, S. M.; Kitaev, V.; Ozin, G. A. *J. Mater. Chem.* **2004**, *14,* 781.

[5] a) John, S. *Phys. Today* **1991**, *May*, 32.
b) Yablonovitch, E. *J. Opt. Soc. Am. B* **1993**, *10,* 283.

[6] a) *Photonic Band Gap Materials* (Ed: Soukoulis, C. M.), Kluwer, Boston, MA **1996**.
b) Scherer, A.; Doll, T.; Yablonovitch, E.; Everitt, H. O.; Higgins, J. A., a special issue in *J. lightwave Technol.* **1999**, *17,* 1928.

[7] Xia, Y.; Gates, B.; Yin, Y.; Lu, Y. *Adv. Mater.* **2000**, *12*, 693.

[8] Hinton, H. E.; Gibbs, D. F. *J. Insect. Physiol.* **1969**, *15*, 959.

[9] Sanders, J. V. *Nature* **1964**, *204*, 1151.

[10] Joannopoulos, J. D.; Meade, R. D. ; Winn, J. N. *Photonic Crystal s : molding the flow of light*, Princeton Unversity Press, Princeton, NJ **1995**.

[11] Sakoda, K. *Optical Properties of Photonic Crystals*, Springer Series in Optical Sciences, Vol. 80, Springer, Berlin **2001**.

[12] López, C. *Adv. Mater.* **2003**, *15*, 1679.

[13] Wang, T. C.; Cohen, R. E.; Rubner, M. F. *Adv. Mater.* **2002**, *14*, 1534.

[14] Birner, A.; Wehrspohn, R. B.; Gösele, U. M.; Busch, K. *Adv. Mater.* **2001**, *13,* 377.

[15] Chigrin, D. N.; Lavinenko, A. V.; Yarotsky, D. A.; Gaponenko, S. *Appl. Phys.* **1999**, *68,* 25.

[16] Lin, S. Y.; Chow, E.; Hietala, V.; Villeneuve, P. R.; Joannopoulos, J. D. *Science,* **1998**, *282,* 274.

[17] Birner, A.; Busch, K.; Müller, F. *Phys. Blätter,* **1999**, *55*, 27.

[18] Kramper, P.; Birner, A.; Agio, M.; Soukoulis, C. M.; Müller, F.; Gösele, U.; Mlynek, J.; Sandoghar, V. *Phys. Rev. B.* **2001**, *64,* 233102.

[19] Steinhart, M.; Wendorff, J. H.; Greiner, A.; Wehrspohn, R. B. *Science,* **2002***, 296,* 1997.

[20] Grüning, U.; Lehmann, V.; Ottow, S.; Busch, K. Appl. Phys. Lett. **1996**, *68*, 747.
Grüning, U.; Lehmann, V.; Eberl, U. Phys. Bl. **1996**, *52*, 661.

[21] John, S.; Rangarajan, R.; *Phys. Rev. B* **1988**, *38,* 101.

[22] Busch, K.; John, S. *Phy. Rev. E* **1998**, *58*, 3896.

[23] Ho, K. –M.; Chan, C. T.; Soukoulis, C. M. *Phys. Rev. Lett.* **1990**, *65*, 3152.

[24] Yablonovitch, E.; Gmitter, T. J.; Leung, K. M. *Phys. Rev. Lett.* **1991**, *67*, 2295.

[25] Ho, K. –M.; Chan, C. T.; Soukoulis, C. M.; Biswas, R., Sigalas, M. *Solid State Commun.* **1993**, *89*, 413.

[26] Chan, C. T.; Datta, S.; Ho, K. –M.; Soukoulis, C. M. *Phys. Rev. B* **1994**, *50*, 1988.

[27] Fan, S.; Villeneuve, P. R.; Meade, R. D.; Joannopoulos, J. D. *Appl. Phys. Lett.* **1994**, *65*, 1466.

[28] Leung, K. M. *Phys. Rev. B* **1997**, *56*, 3517.

[29] Özbay, E.; Tuttle, G.; McCalmont, J. S.; Biswas, R.; Soukoulis, C. M.; Ho, K. –M. *Appl. Phys. Lett*. **1995**, *67*, 1969.

[30] Brown, E. R.; Parker, C. D.; McMahon, O. B. *Appl. Phys. Lett.* **1994**, *64,* 3345.

[31] Cheung, S. D.; Biswas, R.; Özbay, E.; McCalmont, J. S.; Tuttle, G.; Ho, K. –M. *Appl. Phys. Lett.* **1995**, *67,* 3399.

[32] Sigalas, M.; McCalmont, J. S.; Ho, K. –M.; Tuttle, G. *Appl. Phys. Lett.* **1996**, *68,* 3525.

[33] Mekis, A.; Chen, J. C.; Kurland, I.; Fan, S.; Villeneuve, P.; Joannopoulos, J. D. *Phys. Rev. Lett.* **1996**, *77*, 3787.

[34] Lin, S. –Y.; Hietala, V. M.; Lyo, S. K.; Zaslavsky, A. *Appl. Phys. Lett.* **1996**, *68,* 3233.

[35] Sakoda, K.; Ueta, T.; Ohtaka, K. *Phys. Rev. B* **1997**, *56*, 905.

[36] Lin, S. Y.; Fleming, J. G.; Hetherighton, D. L.; Smith, B. K.; Biswas, R.; Ho, K. M.; Sigalas, M. M.; Zubrzycki, W.; Kurtz, S. R.; Bur, J. *Nature*, **1998**, *394*, 251.

[37] Noda, S.; Tomoda, K.; Yamamoto, N.; Chutinan, A. *Science*, **2000**, *289*, 604.

[38] Sharp, D. N.; Campbell, M.; Dedman, E. R.; Harrison, M. T.; Denning, R. G.; Turberfield, A. *J. Optical Quantum Electronics*, **2002**, *34*, 3.

[39] Campell, M.; Sharp, D. N.; Harrison, M. T.; Denning, R. G.; Turberfield, A. J. *Nature*, **2000**, *404*, 53.

[40] Shoji, S.; Kawata, S. *Appl. Phys. Lett*, **2000**, *76*, 2668.

[41] Joannopoulos, J. D. *Nature*, **2001**, *414*, 257.

[42] Blanco, A.; Chomski, E.; Grabtchak, S.; Ibisate, M.; John, S.; Leonard, S. W.; López, C.; Meseguer, F.; Miguez, H.; Mondia, J. P.; Ozin, G. A.; Toader, O.; van Driel, H. M. *Nature*, **2000**, *405*, 437.

[43] Miguez, H.; Chomski, E.; Garcia-Santamaria, F.; Ibisate, M.; John, S.; López, C.; Meseguer, F.; Mondia, J. P.; Ozin, G. A.; Toader, O.; van Driel, H. M. *Adv. Mater.* **2001**, *13*, 1634.

[44] Miguez, H.; Yang, S. M.; Tétreault, N.; Ozin, G. A. *Adv. Mater.* **2002**, *14*, 1805.

[45] Foresi, J. S.; Villeneuve, P. R.; Ferrera, J.; Thoen, E. R.; Steinmeyer, G.; Fan, S.; Joannopoulos, J. D.; Kimierling, L. C.; Smith, H. I.; Ippen, E. P. *Nature* **1997**, *390*, 143.

[46] Palacios-Lidon, E; Galisteo-Lopez, J. F.; Juarez, B. H.; Lopez, C.; *Adv. Mater.* **2004**, *16*, 341.

[47] Tétreault, N.; Mihi, A.; Miguez, H.; Rodriguez, I.; Ozin, G. A.; Meseguer, F.; Kitaev, V. *Adv. Mater.* **2004**, *16*, 346.

[48] Tétreault, N.; Arsenault, A. C.; Mihi, A.; Wong, S.; Kitaev, V.; Manners, I.; Miguez, H.; Ozin, G. A. *Adv. Mater.* **2005**, *17*, 1912.

[49] Wostyn, K.; Zhao, Y.; de Schaetzen, G.; Hellemans, L.; Matsuda, N.; Clays, K.; Persoons, A. *Langmuir* **2003**, *19*, 4465.

[50] Zhao, Y.; Wostyn, K.; de Schaetzen, G.; Clays, K.; Hellemans, L.; Persoons, A.; Szekeres, M.; Schoonheydt, R.A. *Appl. Phys. Lett.* **2003**, *82*, 3764.

[51] Massé, P.; Reculusa, S.; Clays, K.; Ravaine, S. *Chem. Phys. Lett.* **2006**, *422*, 251.

[52] Jonsson, F.; Sotomayor Torres, C. M.; Seekamp, J.; Schiedergers, M.; Tiedemann, A.; Ye, J.; Zentel, R. *Microelectronic Engineering* **2005**, *78*, 429

[53] Miyazaki, H. T.; Miyazaki,H.; Ohtaka, K.; Sato, T. *J. Appl. Phys.* **2000**, *87*, 7152.

[54] Cai, W.; Piestun, R. *Appl. Phys. Lett.* **2006**, *88*, 111112.

[55] Yoshino, K.; Shimoda, Y.; Kawagishi, Y.; Nakayama, K.; Ozaki, M. *Appl. Phys. Lett.* **1999**, *75*, 932.

[56] Shimoda, Y.; Ozaki, M.; Yoshino, K. *Appl. Phys. Lett.* **2001**, *79*, 3627.

[57] Ozaki, M.; Shimoda, Y.; Kasano, M.; Yoshino, K. *Adv. Mater.* **2002**, *14*, 514.

[58] Kubo, S.; Gu, Z. Z.; Takahashi, K.; Ohko, Y.; Sato, O.; Fujishima, A. *J. Am. Chem. Soc.* **2002**, *124*, 10950.

[59] Yoshino, K.; Lee, S. B.; Tatsuhara, S.; Kawagishi, Y.; Ozaki, M.; Zakhidov, A. A. *Appl. Phys. Lett.* **1998**, *73*, 3506.

[60] Petrov, E. P.; Bogomolov, V. N.; Kalosha, I. I.; Gaponenko, S. V. *Phys. Rev. Lett.* **1998**, *81*, 77.

[61] Romanov, S. G.; Maka, T; Sotomayor Torres, C. M.; Müller, M.; Zentel, R. *Appl. Phys. Lett.* **1999**, *75*, 1057.

[62] Frolov, S. V.; Vardeny, Z. V.; Zakhidov, A. A.; Baughman, R. H. *Opt. Commun.* **1999**, *162*, 241.

[63] Shkunov, M. N.; Vardeny, Z. V.; DeLong, M. C.; Polson, R. C.; Zakhidov, A. A.; Baughman, R. H. *Adv. Funct. Mater*. **2002**, *12*, 21.

[64] Hu, Z.; Lu, X.; Gao, J. *Adv. Mater.* **2001,** *13*, 1708.

[65] Asher, S. A.; Sharma, A. C.; Goponenko, A. V.; Ward, M. M. *Anal. Chem.* **2003**, *75*, 1676.

[66] Lyon, L. A.; Debord, J. D. *J. Phys. Chem.* **2000,** *104*, 6327.

[67] Lee, K.; Asher, S. A. *J. Am. Chem. Soc.* **2000,** *122*, 9534.

[68] Gates, B.; Park, S. H.; Xia, J. *Adv. Mater.* **2000,** *12*, 653.

[69] Holtz, J. H.; Asher, S. A. *Nature* **1997,** *389*, 829.

[70] a) Pieranski, P. *Contemp. Phys.* **1983**, *24*, 25.
b) van Megan, W.; Snook, I. *Adv. Colloid Interface Sci.* **1984**, *21*, 119.
c) Gast, A. P.; Russel, W. B. *Phys. Today* **1998**, December, 24.
d) From Dynamics to Devices: *Directed Self-Assembly of Colloidal Materials* (Ed: D. G. Grier), a special issue in MRS Bull. **1998**, *23*(10), 21.

[71] a) Matijevic, E. *Acc. Chem. Res.* **1981**, *14*, 22.
b) Fine Particles (Ed: E. Matijestic), a special issue in MRS Bull. **1989**, *14*(12), 18.
c) Matijestic, E. *Chem. Mater.* **1993**, *5*, 412. d) Matijevic, E. *Langmuir* **1994**, *10*, 8.

[72] Stöber, W.; A. Fink, A. *J. Colloid Interface Sci*. **1968**, *26*, 62.

[73] Iler, R. K. *The Chemistry of Silica,Wiley,* New York **1979**.

[74] Arshady, R. *Colloid Polym. Sci.* **1992**, *270*, 717.

[75] a) *Emulsion Polymerization* (Ed: Piirma, I.), Academic, New York **1982**.
b) *Science and Technology of Polymer Colloids* Vol. II (Eds: Poehlein, G. W.; Ottewill, R. H.; Goodwin, J. W.), Martinus Nijhoff, Boston, MA **1983**.
c) Distler, D. (editor), *Wäßrige Polymerdispersionen*, WILEY-VCH,Weinheim **1999**.

[76] Goodwin, J. W.; Hearn, J.; Ottewill, R. H. *Colloid Polym. Sci.* **1974**, *252*, 464.

[77] Goodwin, J. W.; Ottewill, R. H.; Pelton, R.; Vianello, G.; Yates, D. E. *Brit. Polym. J.* **1978**, *10*, 173.

[78] Egen, M.; Zentel, R.; Ferrand, P.; Eiden, S.; Maret, G.; Caruso, F. in: ‘‘*Photonic Crystal – Advances in Design, Fabrication, and Characterization*’’, Busch, K.; Lölkes, S.; Wehrspohn, R.; Föll, H. Eds., Wiley-VCH, Weinheim **2004**.

[79] Müller, M.; Zentel, R.; Maka, T.; Romanov, S. G.; Sotomayer-Torres, C. M. *Chem. Mater.* **2000**, *12*, 2508.

[80] Egen, M.; Zentel, R. *Chem. Mater*. **2002**, *14*, 2176.

[81] Egen, M.; Zentel, R. *Macromol. Chem. Phys.* **2004**, *205*, 1479.

[82] Egen, M. "*Funktionale dreidimensionale Photonische Kristalle aus Polymerlatizes*", Ph. D. Thesis, Uni-Mainz, Germany **2003**.

[83] Egen, M.; Braun, L.; Zentel, R.; Tännert, K.; Frese, P.; Reis, O.; Wulf, M. *Macromol. Mater. Eng*. **2004**, *289*, 158.

[84] Davis, K. E.; Russel, W. B.; Glantschnig, W. J. *Science* **1989**, *245*, 507.

[85] Salvarezza, R. C.; Vazquez, L.; Míguez, H.; Mayoral, R.; López, C.; Meseguer, F. *Phys. Rev. Lett.* **1996**, *77*, 4572.

[86] Vlasov, Yu. A.; Astratov, V. N.; Baryshev, A. V.; Kaplyanski, A. A.; Karimov, O. Z.; Limonov, F. M. *Phys. Rev. E* **2000**, *61*, 5784.

[87] Vlasov, Yu. A.; Deutch, M.; Norris, D. J. *Appl. Phys. Lett.* **2000**, *76*, 1627.

[88] Trau, M.; Saville, D. A.; Aksay, I. A. *Science* **1996**, *272*, 706.

[89] Holgado, M.; Garcia-Santamaria, F.; Blanco, A.; Ibisate, M.; Cintas, A.; Miguez, H.; Serna, C. J.; Molpeceres, C.; Requena, J.; Mifsud, A.; Meseguer, F.; López, C. *Langmuir* **1999**, *15*, 4701.

[90] van Blaaderen, A.; Ruel, R.; Wiltzius, P. *Nature* **1997**, *385*, 321.

[91] Vickreva, O.; Kalinina, O.; Kumacheva, E. *Adv. Mater.* **2000**, *12*, 110.

[92] Jiang, P.; Bertone, J. F.; Hwang, K. S.; Colvin, V. L. *Chem. Mater.* **1999**, *11*, 2132.

[92] Vlasov, Y. A.; Bo, X. Z.; Sturm, J. C.; Norris, D. J. *Nature* **2001**, *414*, 289.

[94] Denkov, N. D.; Velev, O. D.; Kralchevsky, P. A.; Ivanov, I. B.; Yoshimura, H.; Nagayama, K. *Langmuir* **1992**, *8*, 3183.

[95] (a) Deegan, R. D.; Bakajin, O.; Dupont, T. F.; Huber, G.; Nagel, S. R.; Witten, T. A. *Nature* **1997**, *389*, 827. (b) Deegan, R. D.; Bakajin, O.; Dupont, T. F.; Huber, G.; Nagel, S. R.; Witten, T. A. *Phys. Rev. E* **2000**, *62*, 756.

[96] Gu, Z. Z.; Fujishima, A.; Sato, O. *Chem. Mater.* **2002**, *14*, 760.

[97] Egen, M.; Voss, R.; Griesebock, B.; Zentel, R.; Romanov, S. G.; Sotomayor Torres, C. M. *Chem. Mater.* **2003**, *15*, 3786.

[98] Yang, S. M.; Míguez, H.; Ozin, G. A. *Adv. Funct. Mater.* **2002**, *12*, 425.

[99] a) Mayoral, R.; Requena, J.; Moya, J. S.; López, C; Cintas, A.; Míguez, H.; Meseguer, F.; Vazquez, L.; Holgado, M.; Blanco, A. *Adv. Mater.* **1997**, *9*, 257.
b) Míguez, H.; López, C.; Mesequer, F.; Blanco, A.; Vazquez, L.; Mayoral, R.; Ocana, M.; Fornes, V.; Mifsud, A. *Appl. Phys. Lett.* **1997**, *71*, 1148.
c) López, C.; Vazquez, L.; Meseguer, F.; Mayoral, R.; Ocana, M.; Míguez, H. Superlattices Microstruct. **1997**, *22*, 399.

[100] Musikhin, Y. G.; Bert, N. A.; Bogomolov, V. N.; Prokofiev, A. V. *Phys. Lett. A* **1996**, *222*, 349. b) Vlasov, Y. A.; Astratov, V. N.; Karimov, O. Z.; Kaplyanskii, A. A.; Bogomolov, V. N.; Prokofiev, A. V. *Phys. Rev. B* **1997**, *55*, R13 357.

[101] Mei, D.; Liu, H.; Cheng, B.; Li, Z.; Zhang, D. *Phys. Rev. B* **1998**, *58*, 35.

[102] Bertone, J. F.; Jiang, P.; Hwang, K. S.; Mittleman, D. M.; Colvin, V. L. *Phys. Rev. Lett.* **1999**, *83*, 300.

[103] Joannopoulos, J. D. http://ab-initio.mit.edu/photos/micropolis.html.

[104] Fischer, J. P. Kunstharz Nachrichten, Zeitschrift Hoechst AG, **1993**, *28*, 12.

[105] Mastersizer-measurements were done from the Celanese Emulsion GmbH company by using Malvern Mastersizer Microplus Instrument. Reference to this method: Kippax, P. *Pharmaceutcal Technology Europe*, **2005** *17*, 32-29.

[106] Fischer, J. P.; Schäfer, R. Kunstharz Nachrichten, Zeitschrift Hoechst AG, **1993**, 29, 48.

[107] Woodcock, L. V. *Nature* **1997**, *388*, 235.

[108] Perrin, J. *Ann. Chem. Phys.* **1909**, *18*, 5.

[109] Míguez, H.; Meseguer, F.; López, C.; Mifsud, A.; Moya, J. S.; Vázquez, L. *Langmuir* **1997**, *13*, 6009.

[110] Romanov, S. G.; Fokin, A. V.; Alperovich, V. I.; Johnson, N. P.; De La Rue, R. M. *Phys. Status Solidi B* **1997**, *164*, 169.

[111] Romanov, S. G.; Maka, T.; Sotomayor Torres, C. M.; Müller, M.; Zentel, R.; Cassagne, D.; Manzanares-Martinez, J.; Jouanin, C. *Phys. Rev. E* **2001**, *63*, 056603.

[112] Schroden, R. C.; Al-Daous, M.; Blanford, C. F.; Stein, A. *Chem. Mater.* **2002**, *14*, 3305.

[113] Kittel, C. *Introduction to Solid State Physics*, 8th Edition, Wiley, **2004.**

[114] Wostyn, K.; Zhao, Y.; Yee, B.; Clays, K.; Persoons, A. *J. Chem. Phys.* **2003**, *118*, 10752.

[115] Unger, K.; Giesche, H.; Kinkel, J. DE 35 34143A1 Kugelförmige Silica Partikel, Merck Patent GmbH, 25. Sept. **1985**.

[116] Kaiser, C.; Hanson, M.; Giesche, H.; Kinkel, J.; Unger, K. K. In *Nonporous Silica Microsheres in the Micron and Submicron Range: Manufacture, Characterization and Application*; Pelizetti, E., Ed.; Fine Particle Science and Technology from Micro to Nanoparticles, NATO AST Series Kluwer Academic Publishers: Dordrecht, NL, **1996**, 71-84.

[117] Lin, Y.; Herman, P. R.; Valdivia, C. E.; Li, J.; Kitaev, V.; Ozin, G. A. *Appl. Phys. Lett.* **2005**, *86*, 121106.

[118] Schöpe, H. J.; Barreira Fontecha, A.; König, H.; Marques Hueso, J.; Biehl, R. „*Fast Microscopic Method for Large Scale Determination of Structure, Morphology, and Quality of Thin Colloidal Crystals*", *Langmuir* **2005,** in press.

[119] Song, B. -S.; Noda, S.; Asano, T.; Akahane, Y. *Nature Materials* **2005**, *4*, 207.

[120] Serbin, J.; Ovsianikov, A.; Chichkov, B. N.; *Opt. Express* **2004**, *12*, 5221.

[121] Yang, P.; Deng, T.; Zhao, D.; Feng, P.; Pine, D.; Chmelka, B. F.; Whitesides, G. M.; Stucky, G. D. *Science* **1998**, *282*, 2244-2246.

[122] Ozin, G. A.; Yang, S. M. *Adv. Funct. Mater.* **2001**, *11*, 95.

[123] Yin, Y.; Xia, Y. *Adv. Mater*. **2002**, *14*, 605).

[124] Ferrand, P.; Egen, M.; Griesebock, B.; Ahopelto, J.; Müller, M.; Zentel, R.; Romanov, S. G.; Sotomayor Torres, C. M. *Appl. Phys. Lett.* **2002**, *81*, 2689.

[125] Fustin, C. –A.; Glasser, G.; Spiess, H. W.; Jonas, U. *Adv. Mater.* **2003**, *12*, 1025.

[126] Wong, S.; Kitaev, V.; Ozin, G. A. *J. Am.Chem.Soc.* **2003**, *125*, 15589.

[127] Fustin, C. –A.; Glasser, G.; Spiess, H. W.; Jonas, U. *Langmuir* **2004**, *20*, 9114.

[128] Ye, J.; Zentel, R.; Arpiainen, S.; Ahopelto, J.; Jonsson, F.; Romanov, S. G.; Sotomayor Torres, C. M. "*Integration of self-assembled three-dimensional photonic crystals onto structured silicon wafer*", *Langmuir* **2006,** in press.

[129] Mıguez, H.; Yang, S. M.; Ozin,G. A. *Langmuir***, 2003**, *19,* 3479-3485.

[130] Gaponik, N.; Eychmüller, A.; Rogach, A. L.; Solovyev, V. G.; Sotomayor Torres, C. M.; Romanov, S. G. *J. Appl. Phys.* **2004**, *95*, 1029.

[131] Romanov, S. G.; Gaponik, N.; Eychmüller, A.; Rogach, A. L.; Solovyev, V. G.; Chigrin, D. N.; Sotomayor Torres, C. M. "*Light emitting opal-based photonic crystal heterojunctions*", in Photonic Crystals, eds. K. Busch, K.; Lölkes, S.; Wehrspohn, R.; Föll, H. Wiley-VCH, Weinheim **2004**, 132-152.

[132] Rengarajan, R.; Jiang, P.; Larrabee, D. C.; Colvin, V. L.; Mittleman, D. M.; *Phys. Rev. B* **2001**, *64*, 205103.

[133] Romanov, S. G.; Sotomayer Torres, C. M.; Ye, J.; Zentel, R. E-MRS Symposium I, Strasbourg, **2005**.

[134] Worawut, K.; Romanov, S. G.; Sotomayer Torres, C. M.; Ye, J.; Zentel, R. in progress.

[135] Jiang, P.; Gordana, N. O.; Roxana, N.; Mittleman, D. M.; Colvin, V. L. *Adv. Mater.* **2001**, *13*, 389.

[136] Astratov, V. N.; Bogomolov, V. N.; Kaplyanskii, A. A.; Prokofiev, A. V.; Samoilovich, L. A.; Samoilovich, S. M.; Vlasov, Y. A. *Nuovo Cimento* **1995**, *D 17*, 1349.

[137] Astratov, V. N.; Vlasov, Y. A.; Karimov, O. Z.; Kaplyanskii, A. A.; Musikhin, Y. G.; Bert, N. A.; Bogomolov, V. N.; Prokofiev, A. V. *Phys. Lett.* **1996**, *A 222*, 349; *Superlattices Microstruct*. **1997**, *22*, 393.

[138] Blanco, A.; Lopez, C.; Mayoral, R.; Miguez, H.; Mesequer, F.; Mifsud, A.;Herrero, *J. Appl. Phys. Lett.* **1998**, *73*, 1781.

[139] Romanov, S. G.; Fokin, A. V.; De La Rue, R. M. *Appl. Phys. Lett.* **1999**, *74*, 1821.

[140] Vlasov, Y. A.; Yao, N.; Norris, D. J. *Adv. Mater.* **1999**, *11*, 165.

[141] Wijnhoven, J.; Vos, W. L. *Science* **1998**, *281*, 802.

[142] Thijssen, M. S.; Sprik, R.; Wijnhoven, J. E. G. J.; Megens, M.; Narayanan, T.; Lagendijk, A.; Vos, W. L. *Phys. Rev. Lett.* **1999**, *83*, 2730.

[143] Richel, A.; Johnson, N. P.; McComb, D. W. *Appl. Phys. Lett.* **2000**, *76*, 1816.

[144] Romanov, S. G.; Maka, T.; Sotomayor Torres, C. M.; Müller, M.; Zentel, R. *Appl. Phys. Lett.* **2001**, *79*, 731.

[145] Kang, D.; Maclennan, J. E.; Clark, N. A.; Zakhidov, A.A.; Baughmann, R. H. *Phys. Rev. Lett.* **2001**, *86*, 4052.

[146] Yoshino, K.; Tatsuhara, S.; Kawagishi, Y.; Ozaki, M.; Zakhidov, A. A.; Vardeny, Z. V. *Appl. Phys Lett.* **1999**, *74*, 2590.

[147] Deutsch, M.; Vlasov, Y. A.; Norris, D. J. *Adv. Mater.* **2000**, *12*, 1176.

[148] Zakhidov, A. A.; Ray H. Baughman, R. H.; Zafar Iqbal, Z.; Cui, C.; Khayrullin, I.; Dantas, S. O.; Marti, J.; Ralchenko, V. G. *Science* **1998**, *282*, 897.

[149] Popall, M.; Dabek, A.; Robertsson,M. E.; Valizadeh, S.; Hagel, O. J.; Büstrich, R.; Nagel, R.; Cergel, L.; Lambert, D.; Schaub, M. *Mol. Cryst. & Liq. Cryst.* **2000**, *354*, 123.

[150] Robertsson, M. E.; Hagel, O. –J.; Gustafsson, G.; Dabek, A.; Popall, M.; Cergel, L.; Wennekers, P.; Kiely, P.; Lebby, M.; Lindahl, T. *ECTC* **1998**, 1413.

[151] Houbertz, R.; Domann, G.; Cronauer, C.; Schmitt, A.; Martin, H.; Park, J. –U.; Fröhlich, L.; Buestrich, R.; Popall, M.; Streppel, U.; Dannberg, P.; Wächter, C.; Bräuer, A. *Thin Solid Films* **2003**, *442*, 194.

[152] Serbin, J.; Egbert, A.; Ostendorf, A.; Chichkov, B. N.; Houbertz, R.; Domann, G.; Schulz, J.; Cronauer, C.; Fröhlich, L.; Popall, M. *Optics Letters* **2003**, *28*, 301.

[153] Fröhlich, L.; Houbertz, R.; Jacob, S.; Popall, M.; Müller-Fiedler, R.; Graf, J.; Munk, M.; von Zychlinski, H. *Mater. Res. Soc. Symp.* **2002**, *726*, 349.

[154] Bogomolov, V. N.; Feoktistov, N. A.; Golubev, V. G.; Hutchison, J. L.; Kurdyukov, D. A.; Pevtsov, A. B.; Schwarz, R.; Sloan, J.; Sorokin, L. M. *J. Non-Cryst. Solids* **2000**, *266-269*, 1021.

[155] Sung, I. K.; Mitchell, C. M.; Kim, D. P.; Kenis, P. J. A. *Adv. Funct. Mater.* **2005**, *15*, 1336.

[156] Guan, G.; Zapf, R.; Kolb, G.; Men, Y.; Hessel, V.; Loewe, H.; Ye, J.; Zentel, R. "*Low temperature catalytic combustion of propane over Pt-based catalyst with inverse opal microstructure in microchannel reactor*",*Chem. Commun.* **2006**, in press.

[157] Guan, G.; Zapf, R.; Kolb, G.; Hessel, V.; Löwe, H.; Men, Y.; Ye, J.; Zentel, R. „*Preferential CO Oxidation over Catalysts with Well-defined Inverse Opal Structure in Microchannels*", *Adv. Mater.* **2006**, accepted.